

**ATOMIC-SCALE IN-SITU TEM STUDY ON THE PHASE TRANSITIONS DURING
RAPID SOLIDIFICATION AND LI-ION BATTERY OPERATION**

by

Li Zhong

B.S., Beihang University, 2006

M.S., Beihang University, 2009

Submitted to the Graduate Faculty of
Swanson School of Engineering in partial fulfillment
of the requirements for the degree of
Doctor of Philosophy

University of Pittsburgh

2015

UNIVERSITY OF PITTSBURGH
SWANSON SCHOOL OF ENGINEERING

This dissertation was presented

by

Li Zhong

It was defended on

November 20, 2015

and approved by

Brian Gleeson, PhD, Professor, Department of Mechanical Engineering and Materials Science

William S. Slaughter, PhD, Associate Professor, Department of Mechanical Engineering and
Materials Science

Guofeng Wang, PhD, Associate Professor, Department of Mechanical Engineering and
Materials Science

Tevis Jacobs, PhD, Assistant Professor, Department of Mechanical Engineering and Materials
Science

Guangyong Li, PhD, Associate Professor, Department of Electrical and
Computer Engineering

Dissertation Director: Scott X. Mao, PhD, Professor, Department of Mechanical Engineering
and Materials Science

Copyright © by Li Zhong

2015

ATOMIC-SCALE IN-SITU TEM STUDY ON THE PHASE TRANSITIONS DURING RAPID SOLIDIFICATION AND LI-ION BATTERY OPERATION

Li Zhong, PhD

University of Pittsburgh, 2015

Phase transitions in nanomaterials are the basis for their broad applications. However, due to the short length and fast kinetics at the nanoscale, gaining a mechanistic understanding of such transient processes is extremely challenging. In this dissertation, in-situ transmission electron microscopy (TEM) studies have been performed to reveal the atomic-scale processes during vitrification of metallic liquids and to uncover the reaction and degradation mechanisms in lithium-ion battery electrodes.

It has been a long-standing goal for scientists to vitrify single-element metallic liquids. Here, we report an experimental approach that successfully vitrifies melts of pure refractory body-centered cubic metals by achieving an unprecedented high liquid quenching rate of 10^{14} Ks⁻¹. The availability of monatomic metallic glasses being the simplest glass formers offers unique possibilities to study the structure-property relationships of glasses. Distinctive tendencies towards shear localization have been observed in sub-100-nm metallic glasses, which may shed light on the relationship between atomic structure and mechanical property of metallic glasses.

Phase transitions in anode materials during battery operation often induce large volume change and pulverization. By building a nanobattery inside the TEM, the plasticity and strain accommodation in one-dimensional anode materials during lithiation/delithiation were, for the first time, visualized under atomic-scale resolution. Lithiation of SnO₂ nanowires was initiated

by preferred lithium insertion along the (020) plane, which developed into multiple reaction fronts where stress-driven dislocation plasticity was found to be a precursor towards solid-state amorphization.

Revealing the thermodynamics and kinetics in intercalation compounds has been technically challenging, due to the subtle structural changes associated with lithium intercalation/extraction. By tracking the evolution in the electron diffraction pattern of a multi-particle system consisting of 200-300 nanoparticles, we found that the lithiation of anatase TiO_2 , previously believed to be biphasic, switches to a single-phase reaction with a high lithiation rate up to 60 C when the crystal size decreases to 20 nm.

This dissertation provides a novel non-equilibrium processing methodology for investigating the fast kinetics and structures of supercooled liquids under deep quench, and advances the fundamental understanding of the mechanical degradation and the size-dependent kinetics and thermodynamics in nanostructured electrode materials.

TABLE OF CONTENTS

PREFACE.....	XXII
1.0 INTRODUCTION	1
2.0 BACKGROUND.....	5
2.1 CAPTURING PHASE TRANSITIONS WITH IN-SITU TEM.....	5
2.2 IMPORTANT ASPECTS FOR VITRIFYING METALLIC LIQUIDS	7
2.2.1 Thermodynamics and kinetics during rapid solidification	7
2.2.2 Glass forming ability.....	9
2.2.3 The search for monatomic metallic glasses	11
2.3 MECHANISMS GOVERNING THE PERFORMANCES OF LI-ION BATTERIES.....	15
2.3.1 Mechanical degradation in high-capacity anodes.....	15
2.3.2 Phase evolutions in intercalation compounds.....	17
2.3.3 Previous in-situ studies on LIBs	19
2.3.4 Difficulties associated with in-situ TEM observation.....	21
2.4 MOTIVATION AND OBJECTIVES	23
3.0 MATERIALS AND EXPERIMENTAL PROCEDURES	25
3.1 MATERIALS	25
3.1.1 High-purity bcc and fcc metals.....	25
3.1.2 Pd₇₉Ag_{3.5}P₆Si_{9.5}Ge₂ and Cu₅₀Zr₅₀ metallic glasses.....	27

3.1.3	Single crystalline SnO ₂ nanowires.....	28
3.1.4	Polycrystalline anatase TiO ₂ nanowires.....	29
3.1.5	Single crystalline anatase TiO ₂ nanowires.....	30
3.2	EXPERIMENTAL PROCEDURES	32
3.2.1	Experimental configurations.....	32
3.2.2	Calibration of the transient electric pulses.....	34
3.2.3	Metallic glass microstructure characterization.....	35
3.3	SIMULATION METHODS.....	35
4.0	FORMATION OF MONATOMIC METALLIC GLASSES THROUGH ULTRAST LIQUID QUENCHING.....	37
4.1	INTRODUCTION	38
4.2	EXPERIMENTAL APPROACHES	39
4.3	EXPERIMENTAL RESULTS	40
4.3.1	Formation of monatomic metallic glasses from melts of pure metals.....	40
4.3.2	Controlled competition between vitrification and crystal growth	52
4.3.3	Tensile deformation of sub-100-nm-sized metallic glasses.....	55
4.4	DISCUSSION.....	61
4.4.1	Minimization of possible contaminations	61
4.4.2	Opportunity for revealing the structure-ductility relationship in MGs ...	64
4.5	CONCLUSIONS.....	68
5.0	IN-SITU TEM OBSERVATION ON LITHIATION/DELITHIATION OF TIN DIOXIDE NANOWIRES.....	70
5.1	INTRODUCTION	71
5.2	EXPERIMENTAL APPROACHES	72
5.3	EXPERIMENTAL RESULTS	74

5.3.1	Lithiation/delithiation of SnO ₂ NWs in an end-contact geometry	74
5.3.2	Lithiation of SnO ₂ NWs in a flooding geometry	79
5.4	DISCUSSION.....	87
5.5	CONCLUSIONS	88
6.0	IN-SITU OBSERVATION OF NON-EQUILIBRIUM SINGLE-PHASE LITHIATION IN ANATASE TITANIUM DIOXIDE NANOPARTICLES	89
6.1	INTRODUCTION	90
6.2	EXPERIMENTAL APPROACHES	91
6.3	EXPERIMENTAL RESULTS	92
6.3.1	Lithiation of TiO ₂ nanoparticles via a single-phase reaction.....	92
6.3.2	Two-phase lithiation in single crystalline anatase TiO ₂ NWs.....	101
6.4	DISCUSSION.....	104
6.5	CONCLUSIONS	108
7.0	SUMMARY AND CONCLUSIONS	110
8.0	OUTLOOK.....	113
8.1	DISPLACIVE VS. DIFFUSIVE PLASTICITY IN NANOCRYSTALS	114
8.2	DEFORMATION TWINNING NUCLEATION AND GROWTH IN BCC NANOCRYSTALS	116
APPENDIX A		119
BIBLIOGRAPHY		125

LIST OF TABLES

Table 2.1 Summaries of bulk metallic glass alloys with critical size ≥ 10 nm.	11
Table 2.2 Vapor pressure of several widely used solvents around RT.	22
Table 3.1 Impurities in bcc metals.	26
Table 3.2 Calibration of the applied square electric pulse.	34

LIST OF FIGURES

- Figure 2.1** Magnified area from a movie image acquired at $\sim 750\text{ C}^\circ$ showing the contrast perturbations in the liquid parallel to the (0006) planes in alumina. The atom positions in the Al_2O_3 (red for oxygen and yellow for aluminum) were determined by contrast matching between simulated and experimental images at different objective lens defocus and specimen thickness values. The first layer of liquid atoms is shown schematically. The white line is an average-intensity line scan perpendicular to the interface. The numbers indicate the minima in intensity, which for the negative numbers correlate to the columns of atoms in the sapphire and for the positive numbers correlate to the intensity perturbations in the Al. The two black points at 1 and 2 indicate identified layers of ordered liquid Al. 6
- Figure 2.2** Crystallization velocities as a function of the normalized temperature for (a) Mo, (b) Fe, (c) Pt, and (d) Ag. Gray squares correspond to (110) face and black triangles correspond to the (100) face. Scaled temperatures should be multiplied by $T_m=3570\text{ K}$ for Mo, $T_m=1880\text{ K}$ for Fe, $T_m=2230\text{ K}$ for Pt, and $T_m=1170\text{ K}$ for Ag. 12
- Figure 2.3** Fast fracture of a free-standing 620-nm Si nanoparticle during chemical lithiation in one minute. (a-e) Time sequence of crack initiation and growth. (f) EDP indicating formation of polycrystalline $\text{Li}_{15}\text{Si}_4$ as the fully lithiated phase. 16
- Figure 2.4** Free energy and atomic configurations along the single-phase LiFePO_4 transformation path. (a) Zero-temperature mixing energies (black circles) calculated from first principles of 245 different Li/vacancy and electron/hole configurations in Li_xFePO_4 ($0 < x < 1$) show the existence of several low formation energy structures. The non-equilibrium free energy curve at room temperature determined by canonical Monte Carlo simulations (solid red) using small simulation cells ($2 \times 3 \times 3$ unit cells), as well as the least squares cubic spline fit of the Monte Carlo data (dashed blue) both plateau at $\sim 15\text{ meV}$ per formula unit (f.u.) within $\sim 0.05 < x_{\text{Li}} < 0.9$. (b) Snapshots of Li (green atoms) and Fe^{2+} (brown atoms) configurations in Monte Carlo simulations at room temperature for $x_{\text{Li}} = 0.2, 0.4, 0.6, 0.8$ show the succession of single-phase states with some local ordering. Adjacent (010) planes containing Li/vacancy are shown in green. 18

Figure 2.5 X-ray tomography. (a) Unprocessed cross-sectional tomogram showing individual SnO particles in the electrode with high resolution and good contrast against a low-attenuating carbon black, binder, and electrolyte phase. Att. coeff, attenuation coefficient. (b) A series of cross sections through two particles demonstrates a core-shell process, volume expansion, and particle fracture during the initial reduction and particle redensification during subsequent oxidation. mAhg⁻¹, milliampere hours per gram. 20

Figure 3.1 Nano-tips as specimens in the liquid-quenching experiment. 27

Figure 3.2 Cross-section of the nanowire and their growth direction. (A-C) Scanning electron microscopy (SEM) micrographs showing the cross-section of the nanowire is either polygonal (A), or rhombic (B-C), or hexagonal (C). (D) A high resolution transmission electron microscopy (HRTEM) image showing the nanowire growth direction is [011]. Inset is a Fast Fourier Transformation of the HRTEM image. 29

Figure 3.3 Morphology of pristine poly-crystalline anatase TiO₂ nanowires (NWs). (a-b) Bright-field and dark-field TEM images of several poly-crystalline TiO₂ NWs, representing randomly oriented component crystallites. (c) A close-up view of a typical TiO₂ NW, showing that the crystallites are about 20 nm in diameter, randomly oriented, and loosely packed. (d) Size distribution of more than 300 component crystallites with most of them being 10–25 nm. 30

Figure 3.4 Morphology and structure of single crystalline anatase TiO₂ NWs. (a) A typical TiO₂ NW with growth direction of <100> viewed from the <010> direction. Some defects are visible. (b) HRTEM showing a well-defined tetragonal phase. A 5-nm-thick amorphous carbon layer was deposited to the surface of the NW to increase the electronic conductivity. (c) Cross-sectional view of one NW along its growth direction (that is, [100]). Most of the surface facets are low-index planes such as {011} and {004}. (d) Corresponding EDP of the nanowire cross-section shown in (c). 31

Figure 3.5 Schematic illustration of the Nanofactory TEM-STM platform. 33

Figure 4.1 Illustration of an ultrafast liquid-quenching approach. (a-c) Schematic drawing of the experimental configuration. Two protruded nano-tips are brought into contact with each other (a), which are melted by applying a short square electric pulse with duration around 3.7 ns and voltage in the range of 0.5–3 V (b). Heat dissipates rapidly through the two bulk substrates (indicated by two red arrows), vitrifying the melting zone to form monatomic MGs (c). (d-e) High resolution TEM images showing two contacting tantalum nano-tips (d) forming a tantalum MG (e) after applying a 0.8 V, 3.6 ns electric pulse. The glass-crystal interfaces (GCIs) are denoted by yellow dotted curves. (f-h) FFTs confirming a 20 nm long, 15 nm thick fully vitrified region (g) bounded by

two crystalline substrates viewed along the $\langle 100 \rangle$ (f) and $\langle 110 \rangle$ (h) crystallographic orientations, respectively. 41

Figure 4.2 Controllable geometries by tuning the electric pulse and by coupling with tensile/compressive stress. A tantalum MG with diameter close to 100 nm is obtainable under an electric pulse with voltage above 2 V (left). A nanowire with an aspect ratio of 4 was formed by applying tensile loading during liquid quenching (right). The GCIs are indicated by yellow dotted curves..... 42

Figure 4.3 Formation and RT stability of vanadium MG. (a) TEM image of two crystalline vanadium nano-tips in contact with each other. (b) Formation of a 75 nm long, 80 nm thick vanadium MG under a 1.26 V, 3.6 ns electric pulse. The as-formed vanadium MG was sandwiched by two crystalline substrates with two GCIs (denoted by yellow dotted curves). (c-d) Thermal stability test on vanadium MG at RT, where amorphous vanadium was found stable after 56 hours. In order to protect vanadium from oxidation, a 5 nm thick amorphous carbon layer was coated to the surface of the vanadium MG. The reduced length of the vanadium MG in d is due to a slight change in the viewing angle. (e) High resolution image of the vanadium MG relaxed for 56 h, exhibiting typical amorphous characteristics. (f) Electron diffraction pattern of vanadium MG, showing diffusive amorphous halos and a diffusive background. The bright diffraction spots originate from bcc vanadium due to the fact that the aperture was not small enough to exclude the neighboring crystalline vanadium substrate. 43

Figure 4.4 Formation of molybdenum MG by ultrafast quenching. (a) TEM image of two contacting molybdenum nano-tips with a well-defined bcc structure viewed along the $\langle 111 \rangle$ zone axis (inset in a). (b-e) Mo MG formation and growth under a series of vitrification pulses. The GCIs (indicated by yellow dotted curves) moved a step away from each other after each pulse (denoted by two yellow arrows in b), resulting in the growth of the Mo MG. The amorphous structure is corroborated by the diffuse halos in the FFT (inset in e)..... 44

Figure 4.5 Formation and spontaneous crystallization of tungsten MG. (a) High resolution TEM image of the original crystalline tungsten nano-tip viewed along $\langle 100 \rangle$ zone axis. (b) Formation of tungsten MG in the tungsten nano-tip under a vitrification pulse. An atomically rough and diffuse GCI was identified, where the transition zone from amorphous to bcc tungsten was about 1–2 nm thick (the region between the two dotted yellow curves) (c-e) In-situ TEM observation of spontaneous crystallization of tungsten MG. Tungsten MG is found to be unstable at RT, undergoing spontaneous crystallization to a well-defined bcc structure. 45

Figure 4.6 Structure and thermal stability of tantalum MG. (a) TEM morphology of a typical Ta MG with length of ~90 nm and diameter of ~60 nm. The GCIs are indicated by yellow dotted curves. (b) Electron diffraction of Ta MG, as-quenched (b left) versus relaxed

for approximately 8 h (b right). (c) A comparison of the structure factors of the as-formed, 8 h relaxed and simulated Ta MGs. All three curves show very similar peak positions, including well separated second (q_2) and third peaks (q_3) (indicated by cyan arrows). The ratios of peak positions are the same for the relaxed and simulated structure, where $q_2/q_1=1.69$ and $q_3/q_1=1.99$ 46

Figure 4.7 Cooling rate and crystal growth rate estimated by AtC computer simulation. (a) Atomic temperature distribution of a tantalum nanowire with dimension 85 nm×40.8 nm×13.6 nm at time zero when Joule heating is instantly stopped. The 32×12×6 finite-element meshes were used to simulate the electron temperature field in the TTM. The electron temperature on both sides of the nanowire was kept constant at 300 K. (b) Evolution of atomic temperature distribution along the x direction of the Ta nanowire during the cooling process. (c) Cooling rate as a function of temperature in liquid tantalum (the middle section within 5 nm along the x direction). The highest cooling rate at the initial stage of quenching reaches as high as 10^{14} Ks⁻¹. (d) Crystal growth rate at the LCIs of the (100) (orange squares) and (110) (cyan circles) crystallographic planes, respectively, based on classic MD simulation. The simulation details for crystal growth from the melt are similar to previous research²⁴⁵. 48

Figure 4.8 Glass transition temperature T_g of tantalum from MD simulation. Both the enthalpy change and the volume change as a function of temperature indicate T_g is close to 1650 K..... 49

Figure 4.9 Dynamic vitrification process in liquid Ta revealed by atoms-to-continuum computer simulation. (a) Atomic configuration showing a 35 nm long liquid zone of tantalum after Joule heating (at $t=0$ ps). The atoms are colored based on their degree of disorder represented by local bond-orientational order parameter²⁴⁶ q_6 . The red color corresponds to liquid tantalum after Joule heating. (b) Atomic configuration showing the formation of a 30 nm long tantalum MG segment after quenching ($t=150$ ps). The average temperature of the tantalum nanowire is close to RT at $t=150$ ps. The inset highlights the interface structure between amorphous and bcc Ta. (c) A Time-Temperature-Transformation diagram derived from isothermal MD simulations, outlining approximately the formation condition of Ta MG. The crystal zone is estimated based on the crystal growth rates of the (100) plane (cyan circles) and the (110) plane (orange squares). The red solid line indicates the temperature evolution of the moving LCI (and later on GCI) during cooling. 50

Figure 4.10 Vitrification of liquid tantalum under a heating flux terminated within 0.4 ns by AtC computer simulation. (a) Atomic configuration of the tantalum nanowire after Joule heating. A 35 nm long melting zone was formed before quenching (atoms colored with red). (b) A 18 nm region in the middle of the melting zone is vitrified to a glassy state after being quenched to RT. (c) Cooling rate as a function of temperature in the middle region of the melting zone during quenching. The cooling rate varied between 3×10^{13} Ks⁻¹ at 4200 K and 10^{13} Ks⁻¹ at T_g 51

Figure 4.11 Reversible crystallization-vitrification phase changes of tantalum MG. (a) Formation of a 40-nm-thick, 50-nm-long tantalum MG under a 3.6 ns, 1.26 V electric pulse. The two GCIs are indicated by yellow dotted curves and labeled as A and B, respectively. (b-c) Controlled gradual crystallization under a series of pulses with 3.6 ns in duration and 0.91 V in amplitude. Crystallization proceeded with crystal growth at GCI B (indicated by a yellow arrow), and completed after 6 crystallization pulses (inset in c). (d) A second vitrification pulse resulted in the formation of a Ta MG similar to (a). (e-f) Close-up views of the atomically rough and diffuse GCIs during a phase-change cycle. A schematic drawing with cyan dotted lines along one set of the (110) planes is presented in f to show the gradual breakdown of the long-range order across the GCI..... 53

Figure 4.12 Controlled gradual crystallization under a series of crystallization pulses. The GCIs are marked with yellow dotted curves their move directions are indicated by yellow arrows..... 54

Figure 4.13 Shear-dominated deformation in Ta MG under a strain rate of 10^{-3} s^{-1} . (a) A hybrid Ta nanowire with the left half being Ta MG and the right half being bcc Ta. This hybrid nanowire was fabricated by forming a Ta MG nanowire at first, followed by controlled gradual crystallization to move one of the GCIs (outlined by yellow dotted curves) to the middle of the nanowire (marked by a green arrow), which is used as a reference for tracking the deformation of Ta MG. The strain rate was around $2 \times 10^{-3} \text{ s}^{-1}$. (b) Elastic deformation to a strain close to 5%. (c) Onset of necking shortly after yielding (pointed out by a pair of purple arrow heads). (d) Nucleation of a major shear. (e) Subsequent deformation through gradual growth of a shear offset along $\sim 52^\circ$ off the tensile loading direction. (f) Fracture at an overall strain of 37%. The inset is a schematic drawing of the non-edge-on shear plane. During the whole deformation, no plasticity has been observed in bcc Ta on the right. (g) Contours outlining the shape change of the Ta MG during deformation shown in (a-c) (marked by yellow, cyan and purple contours, respectively). The deformed region in Ta MG is measured to be 28 nm. (h) Stress-strain curve estimated by using crystalline Ta as a strain gauge. The red arrows marked the data points collected from (c) and (d), which correspond to the onset of necking and shear localization, respectively..... 56

Figure 4.14 Completely ductile necking in $\text{Pd}_{79}\text{Ag}_{3.5}\text{P}_6\text{Si}_{9.5}\text{Ge}_2$ MG under a strain rate of $6 \times 10^{-3} \text{ s}^{-1}$. (a) A 52-nm-wide pristine Pd-based MG formed by applying a transient electric pulse on two contacting nanotips. (b) Uniform deformation of the Pd-based MG. (c-f) Completely ductile necking throughout the deformation process. (g-h) Contour evolution during deformation. The length of the deformed region is $L=L_1-L_2-L_3=32$ nm. The contour of the deformed region is outlined by blue dotted lines in (a). (i) Strain (magenta squares) and diameter change (cyan circles) with respect to time. D_0 and D_{\min} represent the minimum diameter of the MG before and during deformation, respectively. (j) $(1 + \varepsilon) \left(\frac{D_{\min}}{D_0}\right)^2$ as a function of the overall strain (ε). According to

equations (4.1) and (4.2), the onset of necking is estimated to be around a strain of 12%. 57

Figure 4.15 Necking in a sense of shear in $\text{Cu}_{50}\text{Zr}_{50}$ MG under a strain rate of $3.5 \times 10^{-3} \text{ s}^{-1}$. (a) Pristine $\text{Cu}_{50}\text{Zr}_{50}$ MG with a diameter of 52 nm and a deformed length of 35 nm. (b-c) Early necking in a sense of shear, where necking proceeded inside a shear band. (d-e) Fracture before being drawn to a point. The inset in (e) is a close-up view of the both tips after fracture. (f) Strain (magenta squares) and diameter change (cyan circles) with respect to time. D_0 and D_{\min} represent the minimum diameter of the MG before and during deformation, respectively. (g) Strain at which necking sets in is estimated to be 8% based on equations (4.1) and (4.2). 59

Figure 4.16 Shear localization in Pd-based MG with ‘large’ size under a strain rate of $6 \times 10^{-3} \text{ s}^{-1}$. (a) Pristine Pd-based MG with a diameter of 400 nm. (b-c) Nucleation of multiple shears at the early stage of deformation. The inset in (b) is a close-up view of nucleation of the first shear. (d-e) Fracture by shear along a non-edge-on plane, as evidenced by the abrupt contour of the necking region (outlined by blue dotted curves). 60

Figure 4.17 Electron energy-loss spectroscopy spectra of oxygen in tantalum. An oxygen K-edge was identified around 530 eV energy loss from tantalum that was exposed to air for approximately 10 minutes (red curve). In contrast, no O K-edge was detected in both Ta MG and crystal (cyan curve) when the Ta nano-tips were processed in a helium-protected environment and deoxidized by Joule heating before the liquid-quenching experiment, indicating that the oxygen concentration in the Ta MG was below the detection limit of EELS, which is ~ 1000 ppm in atomic ratio²⁵⁰ (i.e., ~ 100 ppm in weight percentage). 62

Figure 4.18 High-resolution TEM image showing the clean surface of an original Ta nano-tip specimen. 62

Figure 4.19 Glassy state throughout the deformation. (a) High-resolution TEM image showing a fully amorphous region after deformation. (b-c) Comparison of electron diffraction patterns of Pd-based MG before (b) and after (c) deformation, where no crystallization was identified. 65

Figure 4.20 Completely ductile necking of an 88-nm-wide Pd-based MG under a strain rate of $3 \times 10^{-3} \text{ s}^{-1}$. The electron beam was blanked throughout the deformation except for recording images every dozens of seconds. 65

Figure 4.21 Local symmetry of MGs obtained by nanobeam diffraction. Some diffraction spots on the second diffraction ring are highlighted with magenta arrow heads. Pd-based MG exhibits a relatively well-defined 5-fold symmetry compared to the CuZr (b) and Ta (c) MGs..... 67

Figure 5.1 Building a nano-battery inside a TEM, which consists of a single SnO₂ nanowire anode, an ionic liquid electrolyte, and a bulk LiCoO₂ cathode. 73

Figure 5.2 Time-lapse structure evolution of a SnO₂ nanowire anode during charging at –3.5 V against a LiCoO₂ cathode. The initially straight nanowire (a-b) became significantly twisted and bent after charging (c-r). The chemical reaction front progressed along the nanowire’s longitudinal direction, with the front clearly visible, as pointed out by arrowheads in (d) to (r). The red line in (a) to (n) marks a reference point to track the change of the nanowire length. (o) to (r) are sequential high-magnification images showing the progressive migration of the reaction front, swelling, and the twisted morphology of the nanowire after the reaction front passed by. The big dark particle in the middle of (n) is an island of gelled ILE. Because of the long cumulative electron beam exposure time during the recording of TEM images, the ILE front became gelled (with high viscosity) at this spot. 75

Figure 5.3 Structural and phase characterization of another SnO₂ NW anode during charging at –3.5 V against the LiCoO₂ cathode. (a) TEM micrograph of the nanowire containing a reaction front (dislocation cloud) separating the reacted (amorphous) and non-reacted (single crystal SnO₂) sections. (b-e) EDPs from the different sections of the nanowire. The pristine nanowire was single crystalline and the corresponding EDP (b) can be indexed as the [111] zone axis of rutile SnO₂. The EDP from the dislocation zone (c) shows a spot pattern superimposed on a diffuse scattering background. The EDP from an area immediately after the reaction front (d) shows an amorphous halo. The EDP from an area far away from the reaction front (e) shows diffraction rings superimposed on a diffuse amorphous halo. The diffraction rings can be indexed as tetragonal Sn (black indices) and a Li_xSn compound such as hexagonal Li₁₃Sn₅ (orange indices). (f) A high-resolution TEM image from a charged nanowire showing Sn nanoparticles dispersed in an amorphous matrix. 76

Figure 5.4 TEM images revealed a high density of dislocations emerging from the reaction front (marked by chevron-shaped dotted lines). As the dislocation front propagated, the crystalline contrast changed to gray amorphous contrast instantaneously, and the nanowire diameter increased immediately. (a-f) and (g-h) are two sets of time-lapsed TEM images showing the high density of dislocations that appeared at the reaction front and the migration of the reaction front..... 77

Figure 5.5 TEM images of a lithiated SnO₂ NW before (a) and after (b) delithiation. The NW was biased at –0.05 V versus the LiCoO₂ cathode. (c-f) Time-lapse EDPs of the same

area as outlined in (a) and (b), showing the structural evolution of the nanowire during delithiation. The initial nanowire consisted of Li_xSn , Sn and Li_2O (c and d). After 12417s of discharging, only Sn (diffraction rings in f) and amorphous Li_2O were present (amorphous halo in f). After discharging, the diameter of the NW was reduced from 183 nm to 154 nm. 79

Figure 5.6 Schematic illustration of end-contact and side-contact configurations. 80

Figure 5.7 Structural evolution of a SnO_2 NW anode in a flooding geometry during charging at -3.5 V with respect to the LiCoO_2 cathode. (a) A $45\text{-}\mu\text{m}$ -long and 220-nm -thick pristine SnO_2 NW with single crystalline structure (o). (b) Flooding geometry in which about $1/3$ of the NW was immersed in the ILE. (c-k) Sequential images showing the morphology change during charging. The reaction front (indicated by the red arrowheads) progressed continuously along the NW's axial direction. (l) Lithiated nanowire after the ILE was withdrawn. Similar morphology was observed for both the flooded and the nonflooded segments. The corresponding EDPs of nonflooded (m) and flooded (n) segments showed almost identical structure after lithiation. 81

Figure 5.8 Multiple stripes formation in flooded SnO_2 nanowire anodes during charging at -3.5 V against the LiCoO_2 cathode. (a) Pristine single crystalline nanowire and its corresponding EDP (g) which can be indexed to the $[10\bar{1}]$ zone axis of the rutile SnO_2 . (b-c) Multiple stripes formed after lithiation. A set of parallel stripes with dark contrast inclined 61° to the side surface of the nanowire. The corresponding EDP (h) showed single-crystal diffraction spots superimposed on a diffuse scattering background. Morphology (d-f) and the corresponding EDPs (i-k) after further lithiation. After further lithiation, the stripes disappeared completely and the nanowire underwent both elongation and swelling. The corresponding EDP (j-k) showed that the SnO_2 nanowire has been reduced to $\text{Sn}+\text{Li}_2\text{O}+\text{Li}_x\text{Sn}$. Note the images shown in (b-f) were captured from five different nanowires immersed in the ILE for different periods of time and were all viewed along the $[10\bar{1}]$ direction. 83

Figure 5.9 Microstructure of the lithiation induced multiple stripes in SnO_2 nanowires. (a-b) Low and high magnification images of the charged (a) and pristine (b) nanowire. The nanowire was viewed along the $[10\bar{1}]$ zone axis. Stripes inclining 61° to the (111) planes of the nanowire are parallel to the (020) plane. (c-d) Raw and Fourier filtered HRTEM images of the multiple stripes. (d) High magnification image of the framed area in (c), showing dislocations with Burgers vector $[001]$ or $[100]$ in the stripes. (e-f) Images of the nanowire after further lithiation. (f) is a high magnification image of the framed area in (e), showing a high density of stripes formed after prolonged lithiation. (g-h) Raw and Fourier filtered HRTEM images of another nanowire after lithiation, showing a high density of dislocations with Burgers vectors of $[100]$ and $[001]$, and even disordering. The viewing direction was the $[1\bar{1}0]$ zone axis. 84

Figure 5.10 EDPs from the striped nanowire indicated lattice expansion caused by lithiation. Structural evolution was viewed along the $[10\bar{1}]$ zone axis. (a) Stripes parallel to the (020) plane formed after initial lithiation. (b-d) The (020) diffraction spot was split into two with different d-spacings (insets in c and d), with the brighter spot corresponding to a d-spacing of 2.36 Å, matching that of the (020) plane in the pristine structure, while the darker spot having a d-spacing of 2.49 Å, indicating a 5.5% lattice expansion induced by lithiation. (e) Schematic illustration of lithium intercalation along [001] in the (020) plane in a side-contact geometry. The nanowire's growth direction is [011].
 86

Figure 6.1 Structural evolution of TiO₂ during lithiation. (a-b) Morphology changes of a polycrystalline anatase TiO₂ NW before (a) and after lithiation (b). (c) EDPs of polycrystalline TiO₂ before (top) and after (bottom) lithiation, showing the original tetragonal anatase TiO₂ has been converted to orthorhombic Li_xTiO₂. (d) Integrated intensity from time-lapse EDPs. A two-stage lithiation mechanism was observed. In the first stage (0 s to 4297 s), both diffractions from TiO₂ and Li_xTiO₂ (with x close to 0.5) were detected, indicating the coexistence of two phases. At the end of this stage, the TiO₂ NW has been fully converted to Li_{0.5}TiO₂, corresponding to the purple diffractogram. At the second stage (after 4297 s), the continuous displacement of the Li_xTiO₂ {200} peak was characteristic of a solid solution with increasing lithium content (0.5 < x < 1). Cyan and magenta vertical solid lines indicate the expected peak positions of TiO₂ and Li_{0.5}TiO₂, respectively. (e) Displacement of the {200} diffraction peak with respect to time. (f) A magnified view of the {200} diffraction peak (rectangular region in d). Cyan arrows indicate several small peaks at the left edge... 93

Figure 6.2 Comparison of morphologies before and after lithiation. (a) Pristine TiO₂ NW. (b) After lithiation, the same NW showed similar morphology with no significant changes in the crystallite size. A Li₂O surface layer was formed after lithiation..... 94

Figure 6.3 Structural evolution of single crystalline anatase TiO₂ NWs during lithiation. Both Li_{0.5}TiO₂ and TiO₂ phases were detected, with the former growing progressively at the expense of the latter. Unlike the case in polycrystalline TiO₂ NWs, no additional diffraction intensities were captured between Li_{0.5}TiO₂ {020} and TiO₂ {200}. Cyan and magenta vertical solid lines indicate the expected peak positions of TiO₂ and Li_{0.5}TiO₂, respectively..... 95

Figure 6.4 Continuous displacement of diffraction intensities from individual TiO₂ particles during the first-stage lithiation. (a) Time-lapse EDPs of {004} diffraction spots from three individual particles (named by Arabic 1, 2, and 3, respectively). Bragg spots 1 and 2 (marked by yellow and magenta arrows, respectively) shifted from the {004} diffraction ring of TiO₂ (Cyan dotted arc) towards that of Li_{0.5}TiO₂ (brown dotted arc) upon progressive lithium incorporation. After 69 s, the third spot also began to shift (indicated by an orange arrow). Finally, all three Bragg spots reached the Li_{0.5}TiO₂

{004} diffraction ring after ~200 s. The circles in the last frame indicate the original positions of the three diffraction spots while arrows indicate the displacement of these diffraction intensities, which are indicative of a single-phase reaction path. (b) Intensity profiles of Bragg spots 1 and 2 (top) and their displacement with respect to time (bottom). It took ~3 minutes to lithiate TiO₂ particles to Li_{0.5}TiO₂, which showed much higher rate compared to the overall lithiation of the poly-crystalline NWs..... 97

Figure 6.5 Continuous shifting of a diffraction spot from an individual TiO₂ crystallite. The Bragg spot (marked by a yellow arrow) moved from TiO₂ {200} (marked by cyan dotted arc) towards Li_{0.5}TiO₂ {020} (marked by brown dotted arc). It was half way towards Li_{0.5}TiO₂ {020} after 49 s. 98

Figure 6.6 Structure changes of a single TiO₂ crystallite induced by lithium insertion. (a-b) High-resolution TEM images of one TiO₂ nanocrystal before (a) and during (b) lithiation, showing a ~5% increase in the {011} lattice spacing. c-e, Corresponding fast Fourier transformations (FFTs) before (c) and after (e) lithiation, representing the microstructure changes caused by lithiation. Both an increase in the {022}/{011} lattice spacing and a slight rotation have been observed (d) by superimposing diffraction patterns before (cyan) and during (magenta) lithiation. Additional diffraction spots (marked by yellow circles in c) came from another overlapping particle..... 99

Figure 6.7 Reaction time distribution for individual TiO₂ crystallites to be lithiated to Li_{0.5}TiO₂ nanocrystals. The examined crystallites were lithiated within 1–6 min, corresponding to a rate of 10–60 C. 100

Figure 6.8 Two-phase lithiation in single crystalline TiO₂ NWs. (a) A pristine single crystalline TiO₂ NW diameter around 100 nm. (b-d) Phase boundary migration upon lithiation viewed along the <010> direction. Red arrow heads mark the reaction front and cyan arrows indicate phase boundary (marked by yellow dotted lines in b) movement upon further lithiation. Olive arrows denote a surface step as a reference for tracking the movement of the interface. (e-h) Structural evolution of the two-phase system corresponding to the lithiation progresses in (a-d). The insets in e–h are magnified views of the {004} diffraction spot. The d-spacing decrease from TiO₂ to Li_{0.5}TiO₂ in the c direction was ~4%. (i) Dark-field TEM image of the NW in (d) using Li_{0.5}TiO₂ g₀₀₄ diffraction condition. (j) Close-up view of the phase boundary region (rectangle in d). The thickness of the Li_{0.5}TiO₂ phase was ~20 nm. (k-l) Morphology (k) and structure (l) of a reaction front in a partially lithiated TiO₂ NW viewed along <111> zone axis. The magnified view of the 2 $\bar{2}$ 0 diffraction spot (l, right) also reflected both TiO₂ and Li_{0.5}TiO₂. (m-n) Original (m) and Fourier-filtered (n) HRTEM images of the reaction front tip (rectangle in k). 103

Figure 6.9 Schematic illustration of the single-phase lithiation process in anatase TiO₂ NWs composed of 20 nm crystallites. Cross-sections of the poly-crystalline TiO₂ NWs are depicted. The overall lithiation of the NW is slow (marked by pink arrow heads), proceeding by rapid lithiation of individual crystallites (enclosed in a green rectangle). The single-phase lithiation process inside each nanocrystal is too fast to be revealed by either ex-situ studies or in-situ X-ray and neutron diffractions, which makes TiO₂ crystallites appear to be either lithiated or unlithiated. Therefore, only the sluggish overall lithiation was captured by previous studies. The rapid lithiation inside individual crystallites as well as the metastable nature of Li_{0.5}TiO₂ makes the overall lithiation of TiO₂ NWs resemble an equilibrium two-phase reaction featured by a two-phase interface (marked by yellow dotted curves). 105

Figure 6.10 lithium concentration distributions in a TiO₂ crystallites (when $t=100$ s) at diffusion coefficients of 10^{-17} cm²s⁻¹ (typical for nanosized TiO₂ particles) and 10^{-13} cm²s⁻¹ (typical for micron-sized TiO₂ particles), respectively. The former leads to phase separation while the latter enables uniform lithium distribution. 106

Figure 8.1 Surface diffusive plasticity during tensile deformation of a 20-nm Ag nanocrystal. (a-f) Surface diffusion assisted lateral movement of the steps on a Ag nanocrystal {111} surface. Dislocations (pointed by white arrows in a and e) were continuously emitted from the corner enclosed in a cyan circle in a, leading to the formation of surface steps, which quickly moved away from the highly stressed region. Each surface step is tracked by arrows with a specific color. g, Lateral displacement versus time measured from four surface steps, where steps 1-3 correspond to step movements tracked by purple, blue, and red arrows, respectively. The green curve is measured from another surface step that is not shown. (h) Schematic illustration of surface diffusion by sequential hopping of the atoms at a surface step. 115

Figure 8.2 Reluctant twin growth in a Ta nanocrystal with size above 20 nm. (a) An as-formed 23-nm wide Ta NW under tensile loading along the [001] direction. (b) Nucleation of a twin embryo with a minimum thickness of six (112) layers and a width of 8 nm (inset in b). (c-h) Slow growth of the deformation twin. The twin boundaries are tracked by yellow dotted lines. Note that the lower twin boundary is inclined, which is curved by intersecting the side surface of the Ta NW. Most regions of the twin lamella exhibited Moiré patterns (cyan dots in d) formed by overlapping of the matrix and the twin. The Moiré-patterned region developed to an approximately elliptical shape (outlined by cyan dotted lines in f), matches the projection of an inclined plane, for example the (101) plane. Meanwhile, a second set of Moiré pattern developed at the upper twin boundary (enclosed by a magenta dotted curves in f and g), due to the formation of an inclined (011) boundary. The lattice strain following twin growth (pointed out by red arrows in c and g) was finally accommodated by penetration of the twin through radial direction of the NW, which was accompanied by an abrupt shape change in the NW (h). The FFT (inset in h) clearly demonstrates a diffraction pattern of a {112} twin. (i) High resolution TEM image of the deformation twin containing a high density of

dislocations. Moiré-patterns were found at both twin boundaries (indicated by cyan arrow heads)..... 117

PREFACE

I would like to extend my sincere acknowledgement to all those who helped me during my pursuit for a PhD degree. My deepest gratitude goes first and foremost to my advisor Dr. Scott X. Mao, for his patient guidance and constant support. His professional instructions and encouragement have walked me through the entire period of my PhD study and offer me the opportunity for further pursuing an academic career in the future.

My sincere gratitude also goes to my collaborators: Dr. Jianyu Huang for his guidance and support; Dr. Hongwei Sheng at George Mason University, for his brilliant work and helpful discussions on revealing the multi-physics during rapid solidification; Dr. Chongmin Wang at Pacific Northwest National Laboratory, for his helpful on building a nanobattery inside the TEM; Dr. Yang Liu, who is now at Carolina State University, for his help and discussion on the size-dependent lithiation mechanisms in TiO_2 ; Dr. Weiqiang Han, who is now at Ningbo Institute of Materials Technology and Engineering in China, and Yang Zhao at Beihang University, for providing excellent specimens. I would also like to express my sincere gratitude to my committee members: Dr. Brian Gleeson, Dr. William Slaughter, Dr. Guofeng Wang, Dr. Tevis Jacobs, and Dr. Guangyong Li for their help, insightful discussion and advice on both my research and dissertation.

My next acknowledgement goes to Dr. Xiaohua Liu (now at Enevate Corporation), Anthony J. Coley, Dr. John Sullivan and Dr. Katherine Jungjohann from Sandia National Laboratory; Dr. Pengfei Yan and Dr. Langli Luo at Pacific Northwest National Laboratory; and Dr.

Yimei Zhu, Dr. Dong Su and Dr. Feng Wang at Brookhaven National Laboratory, for their generous help, inspiring discussion and technical assistance during my research.

I am also indebted to my wonderful colleagues and friends, especially my group member Junhang Luo, He Zheng, Liqiang Zhang, Jiangwei Wang and Yang He, for their helpful discussion and support on my research; Yu Gong, Yinkai Lei, Pu Zhang, Qingcheng Yang, Kexi Liu, and Zhenyu Liu at University of Pittsburgh, Wentao Liang at Northeastern University, Chenzhi Wang at InDepth Engineering Solutions, for their help in both my everyday life and PhD research.

Finally, from the bottom of my heart, I would like to thank my family, especially my beloved wife Yuexian Gong. Their unconditional love, support, sacrifice and encouragement have been and will always be the motivation for me to advance.

1.0 INTRODUCTION

Nanomaterials often exhibit superior physical and chemical properties compared to their bulk counterparts¹⁻¹⁰, and therefore hold great promise in various applications such as energy storage devices¹⁰⁻²², biosensors²³⁻²⁶ and memristors²⁷⁻³¹. For example, recent investigations on the mechanical properties of nanosized metallic glasses (MGs) have reported increasing strength and ductility with decreasing specimen size, resulting in a transition from strong-yet-brittle to strong-and-ductile at the nanoscale³²⁻³⁷. Unfortunately, nanosized MGs are usually fabricated by focused ion-beam (FIB) milling, which tends to introduce contamination and lacks the ability to produce sub-100-nm sized MGs, while effective liquid-quenching approaches at the nanoscale have currently been lacking. To date, most bulk MGs are produced by liquid-quenching techniques such as die-casting, melt-spinning, and liquid splat-quenching. However, the mediocre accessible cooling rates in these vitrification techniques limit the glass formers to those consisting of multiple elements with distinctive atomic sizes and chemical affinities³⁸⁻⁴¹. At the nanoscale, however, ultrahigh cooling rates may be achieved by employing deliberately designed structures and geometries (e.g., by reducing interfaces that block the heat transport⁴² and by shortening the distance to heat reservoirs for facile heat dissipation), which leads to the formation of nanosized MGs with compositions outside the glass-forming zone defined by conventional vitrification techniques, and may even open up the possibility for vitrifying monatomic metallic liquids, which is otherwise extremely challenging due to their poor glass

forming ability (GFA) resulting from their negligible nucleation barrier and superfast crystallization kinetics under supercooled condition^{43,44}. Though promising, such success has not yet been demonstrated by laboratory efforts.

Moreover, the electrochemical performances of rechargeable lithium-ion batteries (LIBs), which is one of the most important energy storage devices that are widely applied in portable electronic devices and hybrid vehicles, have also been widely reported to benefit from nanostructured electrode materials^{10,18,19,45}, due to their large surface-to-volume ratio and reduced Li ion diffusion length. Nanostructured electrodes often demonstrates superior electrochemical performances compared to their micrometer-sized counterparts, such as higher energy density¹⁸, higher rate^{45,46}, and longer cycle life^{47,48}. Nevertheless, a bottleneck that preventing further improvement of the performance of LIBs is found to be mechanical degradation due to the large volume change and plasticity associated with phase transitions during battery operation⁴⁹⁻⁵³. Despite a long history of research, the detailed mechanism of such mechanical degradation is still not clear, due to the complexity in the battery reactions and the lack of techniques that can visualize the electrochemical reactions on the fly⁵⁴.

It is worth noting that among the broad applications of nanomaterials, many of them are based on phase transitions^{12,14,17,22,29-31}, which is defined as the transformation of a thermodynamic system from one state to another⁵⁵. To gain a mechanistic understanding of these complex physical-chemical processes, it is important to know not only the final phases, but also the transition pathways (that is, how the original phases are transformed to the final ones). Unfortunately, owing to the small volume and fast kinetics inside nanomaterials, such phase transitions are often transient processes that can only be revealed by molecular dynamics (MD) simulations⁵⁶⁻⁵⁸, which are frequently subject to validity issues due to their extremely fast time

scale and inaccuracies in the applied atomic potentials. Gaining direct experimental evidence of the rapid phase transitions, however, requires in-situ investigation techniques with both superior spatial and temporal resolutions to capture the microstructural and morphological evolutions along the transition paths, and thus has been a long-standing challenge for scientists. Recently, the development in in-situ transmission electron microscopy (TEM), with the ability to resolve the atomic structure and to operate on a time scale within a fraction of one second⁵⁹⁻⁶⁵, became a strong tool to address these challenges.

In this dissertation, in-situ TEM investigations have been performed on vitrification of melts from pure bcc metals and on electrochemical lithiation/delithiation of individual SnO₂ and anatase TiO₂ nanowires (NWs). With the help of a Nanofactory scanning tunneling microscopy (STM)-TEM specimen holder, phase transitions in nanosized materials under transient electric pulses (that is, ultrafast liquid quenching) and under constant biases (that is, lithiation/delithiation of electrodes) were atomically resolved. This dissertation is organized as follows:

In Chapter 2, strategies for stabilizing supercooled metallic liquids, the mechanisms governing the performances and degradation of both cathodes and anodes, and previous in-situ techniques applied to reveal the charge/discharge processes of LIBs are reviewed. Additionally, the motivation and objectives of this dissertation will be proposed.

Chapter 3 introduces the experimental procedures for sample preparation and for developing a nanobattery and an ultrafast liquid-quenching nanodevice inside the TEM.

Chapter 4 reports the formation of monatomic MGs from pure body-centered cubic (bcc) metals by an ultrafast liquid-quenching approach that achieves an unprecedentedly high cooling rate of $\sim 10^{14}$ Ks⁻¹. Combining both in-situ TEM observation and atomistic simulations, the

cooling process is found to be dependent on the competition between vitrification and crystal growth from metallic liquids at the liquid-crystal interface (LCA). This competition can be controlled by tuning the parameters of the applied electric pulses, leading to a novel phase-change phenomenon. The methodology created in this chapter leads to the formation of nanosized MGs with clean surfaces and tunable dimensions, which enables investigation on the intrinsic size-dependent mechanical property and, possibly, its connection to the atomic structure of MGs in the sub-100-nm regime.

In Chapter 5, the strain accommodation and plasticity during lithiation and delithiation of one-dimensional anodes are studied by using SnO₂ NWs as an example. Lithiation of the SnO₂ NW initiated by preferred lithium insertion along the (020) crystallographic plane, followed by formation of multiple reaction fronts propagating along the longitudinal direction of the NW. The microstructural and morphological evolutions during lithiation indicate large dislocation plasticity at the reaction front, which is a precursor to electrochemically-driven solid-state amorphization (ESA).

Chapter 6 focuses on the phase evolutions in intercalation compounds by using anatase TiO₂ as a model material. Size-dependent lithiation pathways are uncovered in TiO₂ NWs and nanoparticles, where anatase TiO₂, a classic intercalation system long believed to follow a two-phase lithiation path, switches to a single-phase reaction path when the crystal size drops below 20 nm. The in-situ electron diffraction approach developed in this chapter tackles the difficulties associated with tracking the subtle microstructural evolutions during lithium intercalation/extraction, which can be extended to studies on a variety of cathode materials.

At last, the results of this dissertation are summarized in Chapter 7, and future work as well as possible research directions is discussed and proposed in Chapter 8.

2.0 BACKGROUND

In this chapter, strategies for stabilizing supercooled metallic liquids as well as the mechanisms governing the performances and degradation of electrodes in LIBs will be briefly introduced. Additionally, previous efforts on the search for single-element MGs and in-situ investigation of lithiation/delithiation mechanisms will be reviewed and discussed.

2.1 CAPTURING PHASE TRANSITIONS WITH IN-SITU TEM

Phase transition is the transformation of a thermodynamic system from one state to another⁵⁵, which is the basis for many research fields, including high pressure physics^{66,67}, rapid solidification^{68,69} and electrochemistry^{70,71}. Phase transitions occur when the original phases become unstable in the given thermodynamic conditions⁵⁵, and are often accompanied by morphological and structural evolutions. Take the liquid quenching process for example, a crystalline metal is first melted, undergoing a solid to liquid phase transition, followed by solidification of the liquid to form a MG. After these phase transitions, the long range periodic sequence (that is, translational symmetry) in the original crystal changes to a disordered glassy state with only short-to-medium-range order⁷². In another case, electrochemically-driven solid-state amorphization is frequently observed during lithiation/delithiation of electrodes, especially

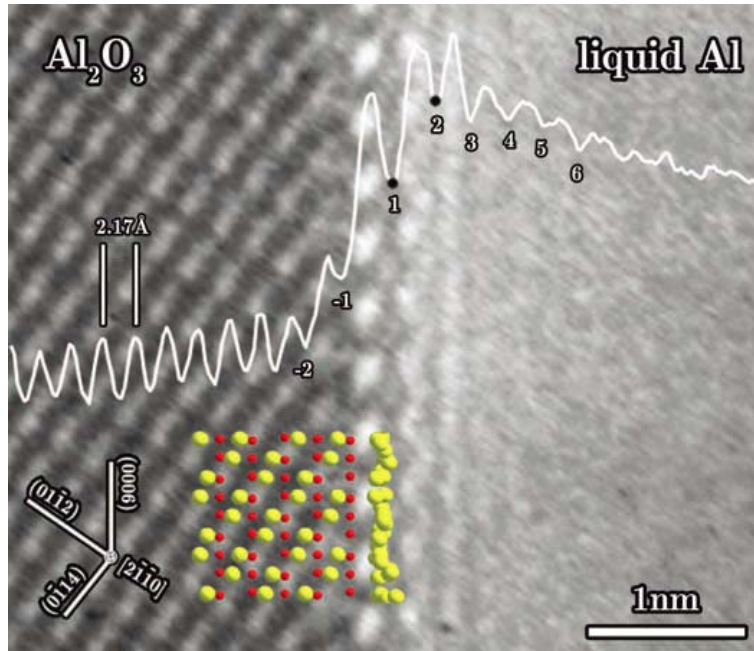


Figure 2.1 Magnified area from a movie image acquired at $\sim 750\text{ C}^\circ$ showing the contrast perturbations in the liquid parallel to the (0006) planes in alumina. The atom positions in the Al_2O_3 (red for oxygen and yellow for aluminum) were determined by contrast matching between simulated and experimental images at different objective lens defocus and specimen thickness values. The first layer of liquid atoms is shown schematically. The white line is an average-intensity line scan perpendicular to the interface. The numbers indicate the minima in intensity, which for the negative numbers correlate to the columns of atoms in the sapphire and for the positive numbers correlate to the intensity perturbations in the Al. The two black points at 1 and 2 indicate identified layers of ordered liquid Al.⁶⁰

in anode materials^{73,74}, which tends to induce large volume change upon cycling and thus catastrophic failure by cracking and pulverization.

The technique of in-situ TEM refers to a broad class of experiments where the dynamic response of a material to an externally applied stimulus is observed as it happens inside the microscope⁷⁵. With the power of resolving atomic-scale processes and a temporal resolution within a fraction of a second, in-situ TEM is capable of revealing the rapid phase transition processes at real time. Compared to conventional post-mortem TEM studies where only snapshots are allowed, in-situ TEM investigation can provide more critical information that bridges

the gaps between the snap shots, and has thus been widely applied to reveal the thermodynamics and kinetics in various phase transitions in nanomaterials, including nanostructure growth^{63,76-81}, crystal nucleation and growth from solution^{64,65,82,83}, gas-solid interaction⁸⁴⁻⁸⁹, phase-change-based memory devices⁹⁰⁻⁹², ferroelectric materials^{93,94}, crystallization and melting^{60,95-97}, temperature controlled phase transition^{98,99}, and stress or pressure induced phase transformation¹⁰⁰⁻¹⁰². One example that demonstrates the excellent resolving power of in-situ TEM is shown in Figure 2.1, where an ordered liquid phase was identified in Al liquid at the interface with sapphire.

In this dissertation, several novel experimental configurations have been developed to investigate the atomic-scale phase transition pathways in nanomaterials under different electric loading conditions: transient electric pulses for revealing the vitrification process during ultrafast liquid quenching; and constant biases for uncovering the mechanical degradation mechanism as well as size-dependent lithiation pathways in nanostructured electrodes.

2.2 IMPORTANT ASPECTS FOR VITRIFYING METALLIC LIQUIDS

2.2.1 Thermodynamics and kinetics during rapid solidification

Metallic glasses, also known as amorphous metals, are metallic solids that demonstrate a disordered structure with only short-to-medium-range order⁷². They excel in various chemical and physical properties including strength, soft magnetic property, corrosion resistance and thermo-plastic formability, and are therefore important materials over a wide range of applications¹⁰³. Recently, MGs with superior ductility¹⁰⁴ and toughness¹⁰⁵ have also been

reported, extending their functionality to serving as advanced engineering materials. Unlike their crystalline counterparts that possess long range orders (that is, translational symmetry) and are often thermodynamically favored, MGs are non-equilibrium or metastable materials, which are formed by non-equilibrium processing methods such as rapid solidification. During liquid quenching, the metals (typically alloys) are first heated to a temperature above their melting points, followed by fast quenching to bypass the glass transition temperature, so that atoms in the supercooled liquids are frozen before the onset of crystal nucleation and growth. Whether metallic liquids can be successfully vitrified depends on both the thermodynamics and kinetics during the cooling process.

From a thermodynamic perspective, the activation energy for forming crystal nuclei is mainly dictated by the free energy difference between the undercooled liquid and the corresponding crystalline state, which is the driving force for crystallization. Its value is determined by both the enthalpy of fusion and entropy of fusion, where a small enthalpy of fusion and a large entropy of fusion lead to a small free energy difference, therefore more stable supercooled liquids with low driving forces towards crystallization^{39,106}. An alloy composed of multiple elements is not only associated with a large entropy of fusion, but also accounts for an increased degree of dense random packing in undercooled liquid and thus a decrease in the enthalpy of fusion, imparting multi-component metallic liquids ideal MG formers¹⁰⁷. Indeed, small gaps in thermodynamic driving forces between several Zr-based MGs lead to dramatic differences in the critical cooling rates up to 4 orders of magnitude¹⁰⁸.

The kinetics during liquid-quenching is another important aspect that determines the GFA. Among a variety of parameters, viscosity is the most important one that describes the crystallization kinetics in supercooled liquids, and is reflected in a parameter named fragility¹⁰⁹,

which represents the change in the viscosity as a function of temperature above glass transition. A strong glass former (e.g., SiO₂) exhibits almost a linear increase of viscosity with decreasing temperature (that is, Arrhenius behavior), therefore keeping the liquid viscous over most of the undercooled regime. On the other hand, a fragile liquid shows an abrupt increase in the viscosity near the glass transition temperature while keeping a low viscosity over a wide temperature range below the melting point. As a result, strong liquids are better glass formers, due to their high viscosities that reduce the atomic mobility, kinetically suppressing the nucleation and growth of thermodynamically favored crystalline phases.

2.2.2 Glass forming ability

The GFA of MG formers is reflected in the magnitude of the critical cooling rate required for vitrification or, alternatively, the maximum accessible specimen thickness. While a cooling rate of 10⁵⁻⁶ Ks⁻¹ was required to form the first MG (i.e., the binary Au₇₅Si₂₅ MG)¹¹⁰, the lowest critical cooling rate obtained at present is around 0.1 Ks⁻¹ with a corresponding maximum sample thickness over ten centimeters¹¹¹. The most widely accepted universal criterion to determine the GFA is the reduced glass transition temperature:

$$T_{rg} = \frac{T_g}{T_m}, \quad (2.1)$$

where T_g is glass transition temperature and T_m is the melting point or liquidus temperature. Inoue interpreted this criterion in terms of three key factors⁴¹: a multicomponent system with three or more elements; significant differences in the atomic sizes between the main component elements; and a negative heat of mixing for the system. Although the first statement is no longer a necessary concern today as evidenced by the successful formation of various binary bulk

MGs^{112,113}, the above empirical rules still hold their ground, and are consistent with both the thermodynamic and kinetic requirements for MG formation as illustrated in Section 2.1.1. The basic idea is that a multicomponent system with distinctive atomic sizes destabilizes the crystalline phases by making them ‘too confuse to crystalize’¹¹⁴. Specifically, a complex glass former thermodynamically reduces the driving force for crystallization by increasing in the configurational entropy and, at the meantime, kinetically suppresses crystal growth by a more complex and efficient atomic packing that leads to limited atom mobility and, thus, a high viscosity in the undercooled liquid. Additionally, multicomponent systems with deep eutectics also improve GFA by reducing the melting point¹⁰³.

Several criteria based on equation 2.1 have been proposed to represent the GFA, where additional parameters are taking into account, including the crystallization temperature¹¹⁵ and the fragility of undercooled liquids^{116,117}. Recently, the GFA has also been connected to the density of amorphous phases in laboratory¹¹⁸, as well as to the maximum crystal growth rate and its corresponding temperature in undercooled liquids¹¹⁹. Additionally, more and more efforts have been devoted to reveal the atomic-scale origin of these empirical criteria^{112,120-123}.

In summary, excellent MG formers are generally alloys consisting of multiple elements with distinctive atomic sizes and chemical affinities, as evidenced in Table 2.1 where the best glass forming systems are among the ternary, quaternary and quinary alloys. In contrast, single-element metallic liquids have extremely low GFA, mainly due to their low viscosity and thus fast crystallization kinetics when undercooled. From this perspective, melts of bcc metals are better glass formers compared to those of fcc metals, since the crystal growth rates in the former are generally lower than those in the latter, especially at low temperatures. As depicted in Figure 2.2, the crystal growth rates for Pt and Ag keep significant even at zero temperature, indicating a

Table 2.1 Summaries of bulk metallic glass alloys with critical size ≥ 10 mm.¹²⁴

System	Alloy	Critical size (mm)	Year
Pd-based ^{125,126}	Pd ₄₀ Ni ₄₀ P ₂₀	10	1984
	Pd ₄₀ Cu ₃₀ Ni ₁₀ P ₂₀	72	1997
Zr-based ^{127,128}	Zr ₆₅ Al _{7.5} Ni ₁₀ Cu _{17.5}	16	1993
	Zr _{41.2} Ti _{13.8} Cu _{12.5} Ni ₁₀ Be _{22.5}	25	1996
Cu-based ^{129,130}	Cu ₄₆ Zr ₄₂ Al ₇ Y ₅	10	2004
	Cu ₄₉ Hf ₄₂ Al ₉	10	2006
RE-based ^{131,132}	Y ₃₆ Sc ₂₀ Al ₂₄ Co ₂₀	25	2003
	La ₆₂ Al _{15.7} Cu _{11.15} Ni _{11.15}	11	2003
Mg-based ^{133,134}	Mg ₅₄ Cu _{26.5} Ag _{8.5} Gd ₁₁	25	2005
	Mg ₆₅ Cu _{7.5} Ni _{7.5} Zn ₅ Ag ₅ Y ₅ Gd ₅	14	2005
Fe-based ¹³⁵⁻¹³⁷	Fe ₄₈ Cr ₁₅ Mo ₁₄ Er ₂ C ₁₅ B ₆	12	2004
	(Fe _{44.3} Cr ₅ Co ₅ Mo _{12.8} Mn _{11.2} C _{15.8} B _{5.9}) _{98.5} Y _{1.5}	12	2004
	Fe ₄₁ Co ₇ Cr ₁₅ Mo ₁₄ C ₁₅ B ₆ Y ₂	16	2005
Co-based ¹³⁸	Co ₄₈ Cr ₁₅ Mo ₁₄ C ₁₅ B ₆ Er ₂	10	2006
Ti-based ¹³⁹	Ti ₄₀ Zr ₂₅ Cu ₁₂ Ni ₃ Be ₂₀	14	2005
Ca-based ¹⁴⁰	Ca ₆₅ Mg ₁₅ Zn ₂₀	15	2004
Pt-based ¹⁴¹	Pt _{42.5} Cu ₂₇ Ni _{9.5} P ₂₁	20	2004

crystallization process with negligible activation energy. Mo and Fe, on the other hand, exhibit thermally activated crystal growth with infinitesimal rates at room temperature (RT)¹⁴². Although kinetic parameters, such as the viscosity and crystallization rate, can provide important implications for the GFA of monatomic MGs, they can only be experimentally measured within a very small temperature window below the melting point¹⁴³, which is attributed to the limited accessible cooling rates for reaching deep quench in these fragile liquids.

2.2.3 The search for monatomic metallic glasses

Vitrifying pure metal melts is extremely difficult due to their poor GFA¹⁴⁴, which has become a long-term scientific curiosity. To the best of our knowledge, laboratory demonstrations of formation of monatomic MGs by liquid quenching are rare, if at all, owing to the extremely

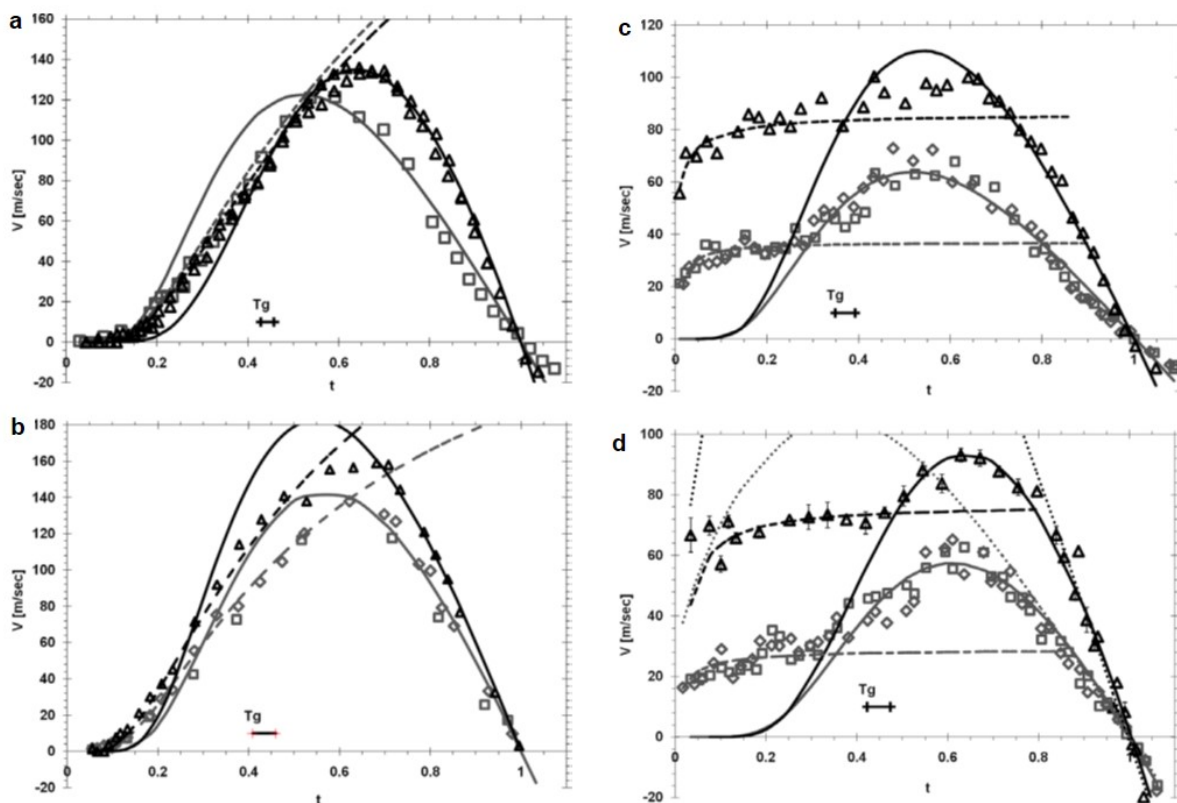


Figure 2.2 Crystallization velocities as a function of the normalized temperature for (a) Mo, (b) Fe, (c) Pt, and (d) Ag. Gray squares correspond to (110) face and black triangles correspond to the (100) face. Scaled temperatures should be multiplied by $T_m=3570$ K for Mo, $T_m=1880$ K for Fe, $T_m=2230$ K for Pt, and $T_m=1170$ K for Ag.¹⁴²

high critical cooling rates required for freezing atoms in such fragile liquids. Most reported successes on obtaining single-element MGs were based on alternative techniques other than liquid-quenching, which are summarized below.

The earliest method is vapor condensation onto substrates kept at a very low temperature. This technique allows deposition of thin amorphous films with pure metals such as Al, Ga, Sn, Bi, Pd, and Ni¹⁴⁵⁻¹⁴⁷. However, these films are kinetically unstable and show very limited resistance against crystallization even at very low temperatures¹⁵¹, for example 14 K for Ga to crystallize^{146,147}. Later, amorphous Ta films have been deposited using e-beam evaporation¹⁴⁸ and recently laser ablation (combined with gas condensation) succeeded in producing 1–3 nm

amorphous Fe nanoparticles¹⁴⁹. Beside vapor condensation, several other non-vitrification methods that produce monatomic MGs have also been reported. Ion irradiation of pure Ga at very low temperature induced fully amorphization of Ga¹⁵⁰, whose purity was compromised by a contamination layer¹⁵¹. In the 1990s, chemical methods, such as sonochemical synthesis, succeeded in the synthesis of amorphous Fe¹⁵² and Ni¹⁵³ powders with purity below 96%. Recently, deformation induced solid-state amorphization has also been reported to produce localized amorphous Ni in severely deformed regions¹⁵⁴. Unfortunately, the produced amorphous region is so localized that a mixture of nanocrystallites and amorphous domains is observed. Therefore it is generally believed that amorphous metals formed by these non-vitrification approaches can be kept stable only at low temperature by incorporation of impurities above a certain concentration¹⁴⁵, especially in the case of fcc metals, and thus can hardly be treated as true monatomic metallic glasses.

In contrast, vitrification of metallic liquids is a classic approach that produces bulk MGs with high purity. However, the accessible cooling rates by conventional quenching methods, such as die-casting¹⁵⁵, melt-spinning¹⁵⁶, and liquid splat-quenching¹⁵⁷ are in the range of 10^1 – 10^8 Ks⁻¹, which is not sufficient to reach the critical cooling rate around 10^{10} Ks⁻¹ for making pure amorphous metals¹⁵⁸. Therefore, new technological advancement has to be made in order to overwhelm the superfast kinetics in undercooled monatomic metallic liquids. Given that whether a glass can be formed depends on the competition between vitrification of the melts (cooling rate) and crystallization, there are two routes to promote the formation of MGs: either by suppressing crystallization (i.e., improving GFA) or by raising the cooling rate. Up to now, progresses have been made in only one example following the first route, which is vitrification of pure Ge liquid under very high static compressive pressure¹⁵⁹. However, the metallic phase of Ge is not stable

under ambient pressure, in which case the tendency and mechanism towards vitrification may be different from those in true metals¹⁶⁰. Moreover, this approach requires the materials to melt accompanied by a decrease in the volume and is thus not applicable to most of the metals.

Much more efforts have been made following the second route. In 1973, non-crystalline Ni foils were produced by splat quenching¹⁵⁷ at an estimated cooling rate above $2 \times 10^9 \text{ Ks}^{-1}$. However, amorphous regions were only found in the very thin edge of these foils, which may formed due to incorporation of oxygen and carbon impurities. In the late 1980s, a systematic study on the GFAs of metals was carried out by Kim *et al.* using an electrohydrodynamic atomization method¹⁶⁰. In their experiment, all the examined pure bcc metals, including Ta, W, V, Nb, Mo, and Fe, were found to solidify from melts to form amorphous nanoparticles at a cooling rate of $\sim 10^6 \text{ Ks}^{-1}$. This may be the only true experimental demonstration of successful vitrification of monatomic metallic liquids.

In summary, during the long-lasting search for monatomic MGs, various attempts have been made to produce monatomic amorphous samples, which are, however, often in geometrically confined forms (e.g., substrate-supported thin films and nano-sized powders) and are plagued with either purity¹⁵² or stability problems¹⁴⁶, offering limited potential for broader applications. Therefore, advanced techniques to fabricate high purity monatomic MGs with controllable geometries are highly appealing but yet to be developed.

2.3 MECHANISMS GOVERNING THE PERFORMANCES OF LI-ION BATTERIES

2.3.1 Mechanical degradation in high-capacity anodes

LIB delivers the highest specific energy (that is, the energy per unit weight) among the family of rechargeable batteries (e.g., Ni-Cd and Lead-acid batteries)⁵³. The present generation of LIB consists of graphite as anode and layered transition metal oxides, such as LiCoO₂ and LiFePO₄, as cathode, with lithium ions being repeatedly intercalated into and extracted from the electrode hosts during cycling. However, the energy density accessible by intercalation-type electrodes is inherently limited by their crystal structure (e.g., the lattice parameters and the amount of interstices) and the redox activity (that is, the number of exchangeable electrons), and thus cannot keep up with the pace of the rapidly growing demands for applications in hybrid vehicles and other portable electronic devices. Much efforts have been devoted to the search for new high-capacity electrode materials beyond intercalation compounds, and were mostly succeeded in finding metals, semimetals and transition metal oxides as promising anode materials to replace graphite. Most of these new materials react with lithium based on completely different mechanisms compared to intercalation, and can be categorized into either alloying- or conversion-type anodes. Typical alloying-type anodes include Si¹⁶¹⁻¹⁶⁵, Sn^{166,167}, Ge¹⁶⁸ and Al¹⁶⁹ while promising conversion-type anodes include Co₃O₄, Fe₃O₄ and Cu₂O^{10,170,171}, etc. For example, each Si or Sn atom can alloy with up to 4.4 Li ions, leading to theoretical specific capacities of 4200 mAhg⁻¹ and ~1000 mAhg⁻¹, respectively^{53,172}, which are among anode materials with the highest specific capacities, and are 3-10 times the capacity of graphite. Promising as they are, their applications are limited by mechanical degradation^{17,47,53,173-179}, including severe plasticity, cracking, and pulverization, which is attributed to the phase-transition

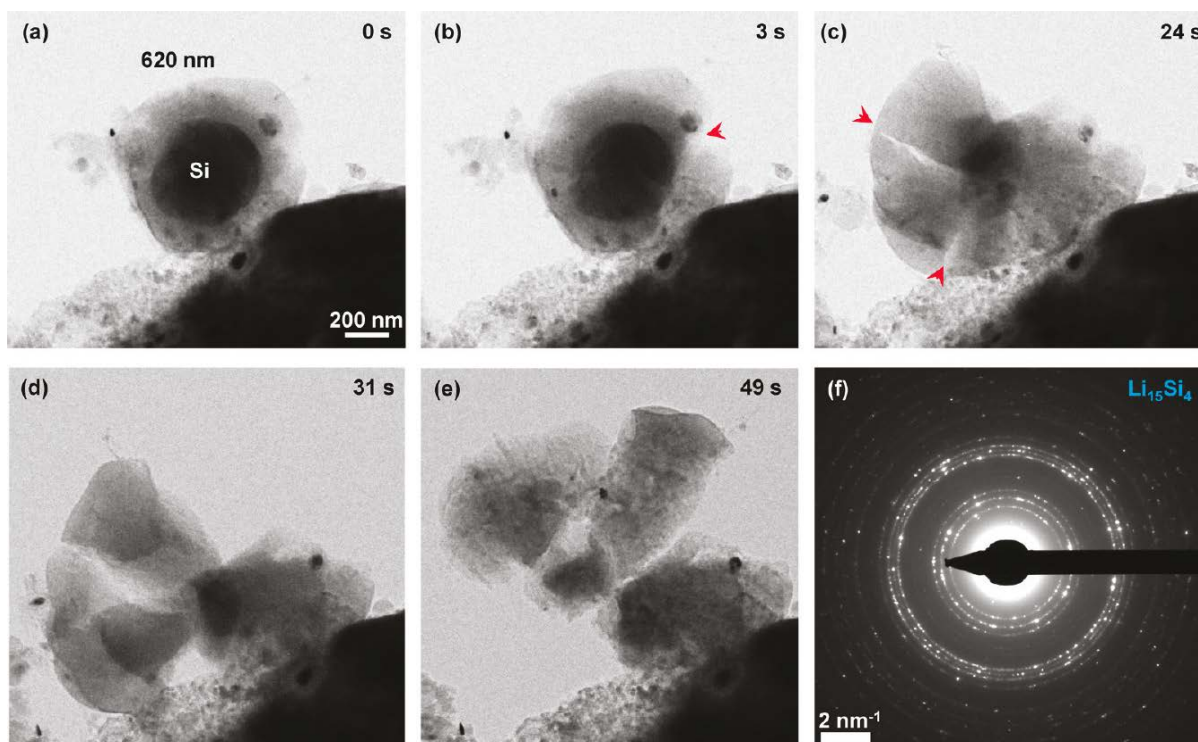


Figure 2.3 Fast fracture of a free-standing 620-nm Si nanoparticle during chemical lithiation in one minute¹⁸⁰. (a-e) Time sequence of crack initiation and growth. (f) EDP indicating formation of polycrystalline $\text{Li}_{15}\text{Si}_4$ as the fully lithiated phase.

induced large volume expansions/contraction upon lithium insertion/removal. When fully lithiated, silicon (Si) and tin (Sn) exhibit as high as ~300% and ~250% volume expansions¹⁸¹, respectively, exhibiting poor cyclabilities with significant pulverization and capacity loss occurring even during the first cycle¹⁸², as is demonstrated in Figure 2.3 where rapid fracture of a Si particle proceeded right upon lithiation¹⁸⁰.

In order to overcome this bottleneck, numerous nanostructured electrodes have recently been designed, including a yolk-shell configuration where Si nanoparticles are encapsulated in relatively larger conductive carbon shells¹⁸³, and a double-walled Si nanotube structure where active Si tubes are surrounded by a silicon oxide layer¹⁸⁴. A basic criterion for these novel designs is to exploit the flexibility and facile strain accommodation in nanomaterials and to rely

on specially-designed configurations to accommodate the huge volume change upon cycling, thus significantly improving the cycle life. Therefore, a mechanistic understanding of the plasticity and volume change upon lithiation/delithiation in the active materials will provide important guidelines for designing advanced nanostructured electrodes.

2.3.2 Phase evolutions in intercalation compounds

Intercalation compounds are the most important materials for cathodes, which largely determine the cost and energy density of LIBs¹⁸⁵. Layered compounds LiMO_2 and olivine compounds LiMPO_4 (M=Co, Ni, Mn, etc.) are two commercialized cathode materials at present, and their performances are found to be closely related to the stability of their phases. Although LiCoO_2 is capable of delivering high capacities, the safety issues due to the instability of its structure in high voltage windows prevent it from being the perfect cathode for LIBs. On the other hand, LiFePO_4 has recently attracted extensive research interests owing to its low-cost, environmental friendliness and superior cycle life. The main drawback of LiFePO_4 lies in its low rate capability due to its one-dimensional lithium diffusion channel as well as the low electronic conductivity. This sluggish lithium insertion, however, was found to be dramatically accelerated by a reduction in the LiFePO_4 particle size^{186,187}. Nevertheless, the origin of this improvement is closely related to the atomic-level lithium intercalation/extraction mechanism, which is still under intense debate¹⁸⁶⁻¹⁹⁰.

Several models concerning the two-phase lithiation mechanism have been proposed, including the shrinking core model where lithiation of LiFePO_4 particles follow a conventional core-shell mechanism¹⁹¹, the mosaic model where lithiation proceeds concurrently at randomly distributed multiple local regions¹⁹², and the domino-cascade model where lithium intercalation,

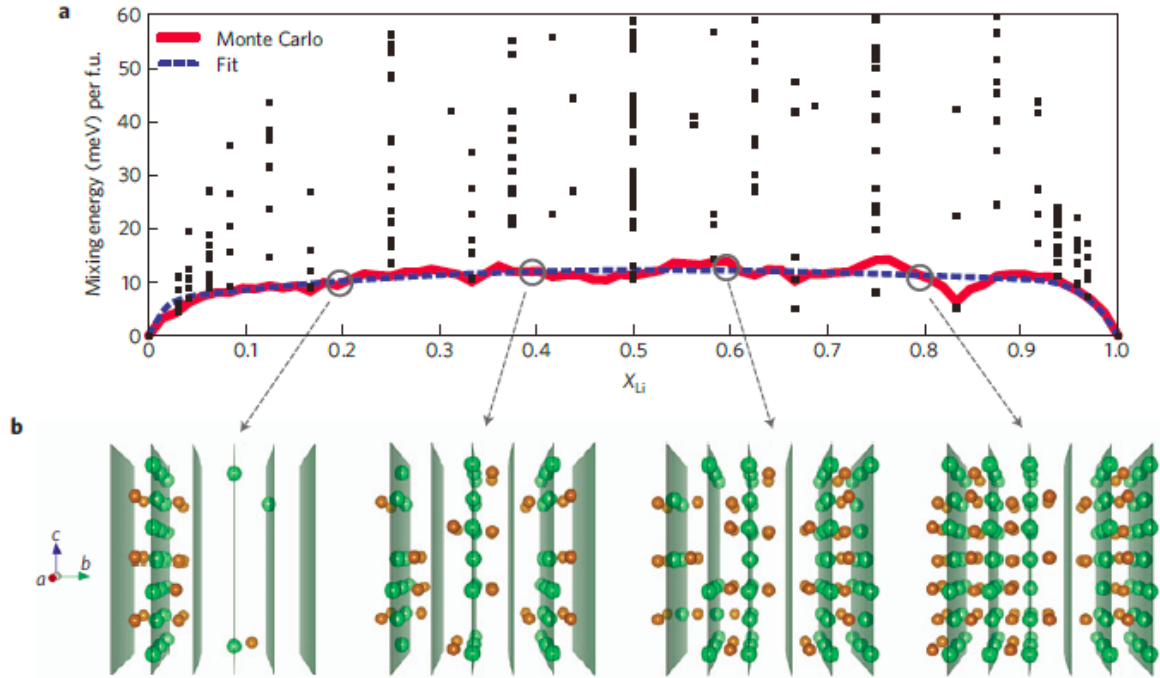


Figure 2.4 Free energy and atomic configurations along the single-phase LiFePO_4 transformation path¹⁸⁶. (a) Zero-temperature mixing energies (black circles) calculated from first principles of 245 different Li/vacancy and electron/hole configurations in Li_xFePO_4 ($0 < x < 1$) show the existence of several low formation energy structures. The non-equilibrium free energy curve at room temperature determined by canonical Monte Carlo simulations (solid red) using small simulation cells ($2 \times 3 \times 3$ unit cells), as well as the least squares cubic spline fit of the Monte Carlo data (dashed blue) both plateau at ~ 15 meV per formula unit (f.u.) within $\sim 0.05 < x_{\text{Li}} < 0.9$. (b) Snapshots of Li (green atoms) and Fe^{2+} (brown atoms) configurations in Monte Carlo simulations at room temperature for $x_{\text{Li}} = 0.2, 0.4, 0.6, 0.8$ show the succession of single-phase states with some local ordering. Adjacent (010) planes containing Li/vacancy are shown in green.

facilitated by the elastic energy of the coherency strains at the two-phase interface, is found to behave like a wave sweeping through the nanoparticle¹⁸⁷. Recently, a non-equilibrium single-phase reaction has been proposed in extremely small LiFePO_4 particles, which is mainly due to the size impact on the thermodynamics of the lithiation process¹⁸⁶. Figure 2.4 demonstrates the formation energy of the intermediate phase Li_xFePO_4 ($0 < x < 1$), which is found to be negligible over the entire compositional range between the stable phases (that is, LiFePO_4 and FePO_4), indicating the possibility of lithiation through a solid-solution path. Such a single-phase reaction

may significantly improve the lithiation kinetics by exempting the need for nucleation of a second phase and, meanwhile, should keep the particle more robust by reducing the strain associated with a two-phase interface. Although phase evolutions in intercalation compounds play an important role for electrochemical performances, they are extremely challenging to reveal inside nanomaterials, due to the subtle morphological and structural changes accompanying lithium intercalation/extraction. As a result, effective methods capable of tracking the lithiation pathway in intercalation compounds are highly appealing.

2.3.3 Previous in-situ studies on LIBs

A mechanistic understanding of the structural instability of electrode materials is important, which can provide important insights for degradation control during cycling. In previous researches, several in-situ techniques have been applied to track the structural evolutions of electrode materials during battery operations. Important in-situ techniques include scanning electron microscopy¹⁹³⁻¹⁹⁷ (SEM), synchrotron X-ray diffraction¹⁹⁸⁻²⁰¹ (XRD), synchrotron X-ray absorption spectroscopy^{119,120} (XAS)^{202,203}, Raman spectroscopy²⁰⁴, mass spectroscopy²⁰⁵⁻²⁰⁷, and nuclear magnetic resonance (NMR) spectroscopy^{176,208}. Among all these techniques, SEM is capable of revealing the surface morphological evolution at a resolution of several nanometers. However, it lacks the ability to provide information on microstructural evolutions inside the active electrode materials. Moreover, to conduct in situ SEM observation requires special design in order to ensure correct functioning of the electrochemical cell inside the high vacuum of an SEM. On the other hand, in-situ XRD and XAS studies allow the cell to work in atmospheric pressures, providing detailed information on crystal structural and electronic structural evolutions. Nondestructive analytical tools, such as MS and NMR, are also widely used to probe

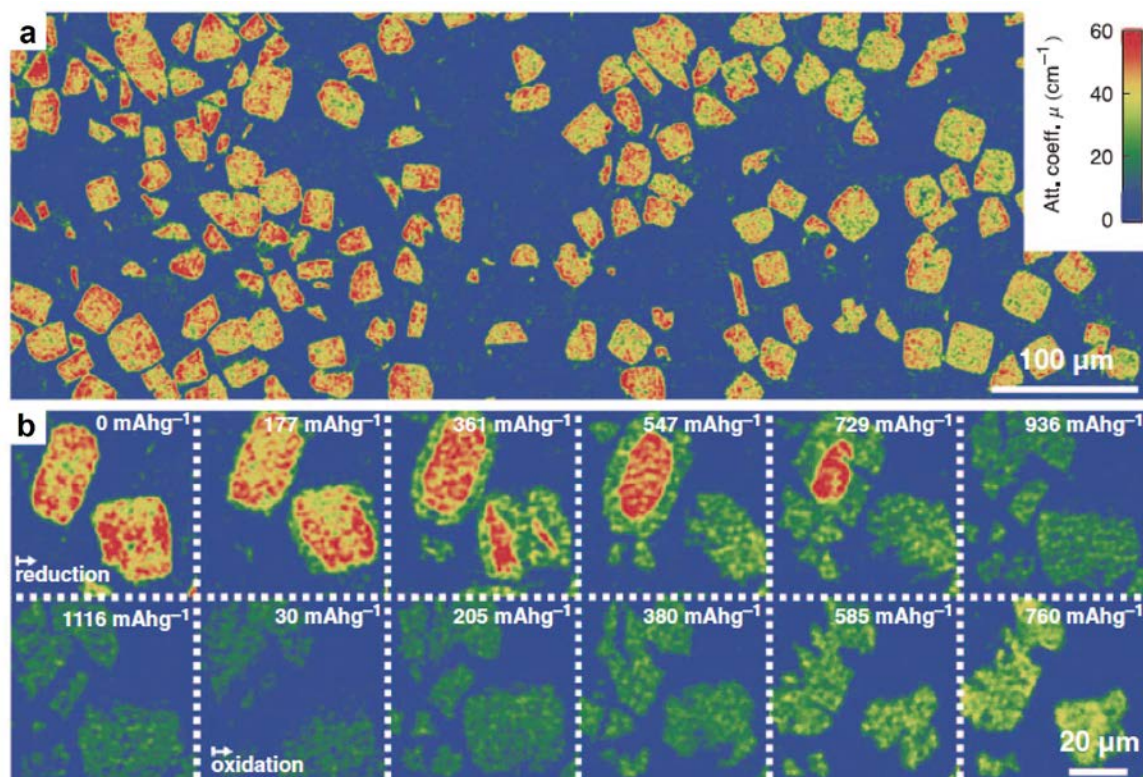


Figure 2.5 X-ray tomography²⁰⁹. (a) Unprocessed cross-sectional tomogram showing individual SnO particles in the electrode with high resolution and good contrast against a low-attenuating carbon black, binder, and electrolyte phase. Att. coeff, attenuation coefficient. (b) A series of cross sections through two particles demonstrates a core-shell process, volume expansion, and particle fracture during the initial reduction and particle redensification during subsequent oxidation. mAhg^{-1} , milliampere hours per gram.

the interfacial processes such as the formation and dissolution of solid electrolyte interfaces (SEIs). Unfortunately, the limited spatial resolution associated with all these analytical methods limit their power to providing only collective information, such as the average structure and composition, from an ensemble of particles composing the electrodes, while a close-up view of the electrochemistry inside individual particles is unattainable. In some cases, such as during a particle-to-particle lithiation process^{187,210}, the spatial limitation may lead to inaccurate interpretation of the mechanisms governing battery operation.

Recently, more and more attempts have been made to visualize the particles during lithiation/delithiation at real time. X-ray tomography^{209,211} and X-ray transmission microscopy²¹² have been performed to reveal the 3-D morphological and structural evolution in micron-sized Sn particles. Figure 2.5 clearly reveals a core-shell lithiation mechanism, along with volume expansion and cracking. However, these approaches still fall short of revealing the atomistic origin of such plasticity and volume change as well as tracking the lithiation pathway in nanosized intercalation compounds.

2.3.4 Difficulties associated with in-situ TEM observation

Despite the long history of batteries, the detailed mechanism of mechanical degradation of electrode materials during electrochemical cycling is still not fully understood due to the complex nature in batteries and the lack of technologies that can visualize the electrochemical reactions on the fly. In-situ TEM technique, with atomic scale spatial and decent temporal resolutions, is a strong tool to overcome such challenges. However, the key technical difficulty to perform in-situ TEM observation on battery operation lies in the choice of a liquid electrolyte with ultralow vapor pressure to survive the high vacuum inside a TEM (typically $\sim 10^{-5}$ Pa). As shown in Table 2.2, the vapor pressure of several most widely used solvents have vapor pressures several orders of magnitude higher than the TEM vacuum pressure²¹³.

One way to protect the liquid electrolyte is to seal it into a liquid-cell device^{64,214-218} with electron beam transparent thin films (typically Si_3N_4 thin films). Such a strategy allows the use of commercialized electrolytes, creating an environment similar to that in practical LIBs. However, the use of thin films and the filled electrolyte in between significantly compromise the

Table 2.2 Vapor pressure of several widely used solvents around RT²¹³.

Solvent	Vapor pressure (Pa)
Ethylene carbonate (C ₃ H ₄ O ₃)	1.33 (20 °C)
Propylene carbonate (C ₄ H ₆ O ₃)	4 (25 °C)
Dimethyl carbonate (C ₃ H ₆ O ₃)	5300 (20 °C)
Diethyl carbonate (C ₅ H ₁₀ O ₃)	1400 (25 °C)

spatial resolution, limiting the microstructural information that can be captured during electrochemical reactions. This configuration also limits the ability to conduct analytical TEM such as electron energy loss spectroscopy (EELS) and energy dispersive spectroscopy (EDS) based composition analysis. Moreover, to fabricate a working liquid cell of LIB also challenges the high-precision nanodevice fabrication and materials assembly (that is, to attach active materials to the designated current collectors), which have become the bottleneck for a technical breakthrough in in-situ liquid-cell studies.

An alternative way is to apply an open-cell configuration by the use of either a nonvolatile ionic liquid electrolyte (ILE) with negligible vapor pressure²¹⁹ or lithium metal covered with a thin Li₂O layer serving as solid electrolyte. This strategy allows facile construction of a nanobattery inside the TEM, atomic scale resolution observation at real time, and great flexibility in selecting and manipulating the desiring electrode materials (e.g., to choose a NW with optimum size and orientation), allowing more room for analytical TEM analysis. Recent development on such an open-cell configuration²²⁰ (see Chapter 5 for details) has promoted numerous in-situ TEM studies on the microscopic processes in LIBs^{169,221-224}.

2.4 MOTIVATION AND OBJECTIVES

Phase transitions are ubiquitously seen in nanomaterials governing their broad applications. A fundamental understanding of the thermodynamics and kinetics during these phase transitions is of both scientific and practical significance. However, very few studies have succeeded in capturing the microscopic processes at real time, owing to the short length-scale and fast kinetics inherently associated with nanomaterials. In this dissertation, an ultrafast nanoscale liquid-quenching system and a nanosized electrochemical cell will be developed inside the TEM to reveal the non-equilibrium processes during rapid solidification as well as the plasticity, strain accommodation and lithiation pathways in nanostructured electrodes. Based on the background review in this chapter, this dissertation will be dedicated to addressing the following critical issues:

1. Is it possible to vitrify melts of pure metals by developing a nanodevice that maximizes the cooling rate? If yes, what are the factors governing the vitrification process in monatomic metallic liquids?
2. What are the atomic-scale processes for mechanical degradation in one-dimensional nanosized high-capacity anodes?
3. What is the reaction pathway in nanosized intercalation compounds? Can the size-dependent competition between an equilibrium two-phase lithiation pathway and a non-equilibrium single-phase reaction pathway be an origin of the size-dependent rate capability observed in nanosized intercalation compounds?

This dissertation aims to gain a fundamental understanding of the phase transition processes during rapid solidification and Li-ion battery operation, which reveals the kinetics and structural behaviors in supercooled liquids far from equilibrium, and uncovers the atomic-scale

mechanisms governing mechanical degradation and size-dependent performances in nanostructured electrodes.

3.0 MATERIALS AND EXPERIMENTAL PROCEDURES

In this chapter, the materials and experimental approaches employed in this dissertation will be introduced. A variety of high-purity body-centered cubic (bcc) and face-centered cubic (fcc) metals are used for the MG formation and processing; a Pd-based MG and $\text{Cu}_{50}\text{Zr}_{50}$ MG are selected for nanoscale tensile mechanical testing; SnO_2 NWs are chosen as a model system for studying the large volume change and strain accommodation in anode materials; both single crystalline and polycrystalline anatase TiO_2 NWs are selected as model systems for tracking the lithiation pathway in intercalation compounds. A novel methodology integrating nanoscale MG fabrication, structural characterization and mechanical testing will be presented, where the ultrafast liquid-quenching approach is a technological breakthrough for rapid solidification. Additionally, an experimental configuration that, for the first time, enables visualization of the atomic-scale electrochemistry in LIB electrodes will also be briefly illustrated.

3.1 MATERIALS

3.1.1 High-purity bcc and fcc metals

A series of high purity bcc and fcc metals were used in this dissertation to study the vitrification process of melts from pure metals, all of which were provided by ESPI Metals. The studied bcc

Table 3.1 Impurities in bcc metals²²⁵.

Impurities	Impurity concentration (ppm)			
	Ta (99.98%)	V (99.9%)	Mo (99.98%)	W (99.98%)
Cr	10	50	10	<20
Nb	10			
Si	10	150		
W	40			
Zr	10			
Mo	10	130		
Mg	10			
Sn	10	<30		
Fe	15	200	20	<50
Ni	15	<50	130	<50
Ti	10	150		
V	10			
Cu	10	<50	<20	<10
Mn	10			
Al	10	50		
Co	10			
Ca		<50		
K			<20	<30

metals include Ta (99.98%), W (99.98%), vanadium (V; 99.9%), and molybdenum (Mo; 99.98%); fcc metals include gold (Au, 99.999%), Silver (Ag, 99.999%), Aluminum (Al; 99.999%), Palladium (Pd; 99.995%), Platinum (Pt; 99.999%), Rhodium (Rh, 99.99%), and Iridium (Ir; 99.99%). Among all these tested materials, only the four bcc metals succeeded in forming monatomic MGs. Since impurities may significantly affect the GFA, they need to be kept minimal. The impurity levels of bcc metals are listed in Table 3.1.

During specimen preparation, one end of a metal rod was flattened by a punch to form a substrate, which was then notched by a tungsten carbide cutter and torn apart with two clamps. This strategy generates many triangle-shaped nano-tips at the fracture edge of the metal pieces

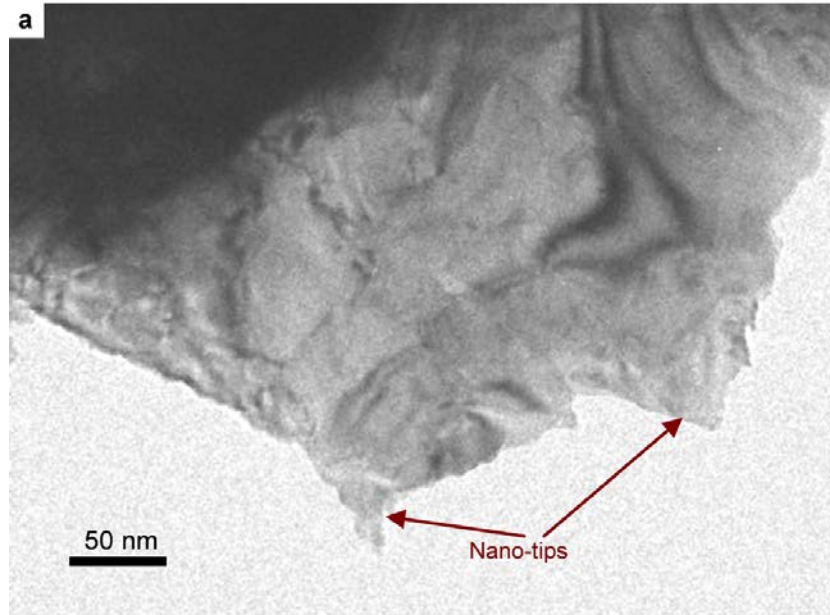


Figure 3.1 Nano-tips as specimens in the liquid-quenching experiment²²⁵.

(Figure 3.1). These nano-tips are the specimens in the liquid-quenching experiments. This strategy allows fabrication of nanosized MGs directly from bulk materials.

3.1.2 $\text{Pd}_{79}\text{Ag}_{3.5}\text{P}_6\text{Si}_{9.5}\text{Ge}_2$ and $\text{Cu}_{50}\text{Zr}_{50}$ metallic glasses

$\text{Pd}_{79}\text{Ag}_{3.5}\text{P}_6\text{Si}_{9.5}\text{Ge}_2$ MG was provided by Dr. Marios Demetriou from California Institute of Technology, which is among the toughest material known at present¹⁰⁵. The glassy ingot was formed by water-quenching the melts inside a quartz tube, and is in the form of a cylinder with a diameter of 3 mm and a height of 2 mm. The detailed experimental procedure is provided in Dr. Marios Demetriou's recent publication¹⁰⁵. $\text{Cu}_{50}\text{Zr}_{50}$ MG ribbons were provided by Yang Zhao from Beihang University with a melting-spinning method. Both MGs were cut and thinned into films, which were then attached to the tip of aluminum rods. Similar to the approach presented in

the section above, the films were notched and torn apart to form nano-tips at the fracture edge for subsequent glass fabrication and mechanical testing.

3.1.3 Single crystalline SnO₂ nanowires

The SnO₂ nanowire were synthesized by Dr. Chongmin Wang's group at Environmental Molecular Sciences Laboratory, Pacific Northwest National Laboratory. The NWs were synthesized by a chemical vapor deposition (CVD) process using activated carbon powder (Ketjen Black, EC600JD, Akzo Nobel Corp. Japan) and SnO₂ nanoparticles (from Aldrich, particle size < 100 nm) as the precursors and Au as the catalyst, based on the synthesis process reported in previous researches^{226,227}. The activated carbon (C) and the SnO₂ nanopowder were combined in a ratio of C:SnO₂ = 1:4 by weight and thoroughly dry mixed using a mortar and pestle. The mixed C and SnO₂ powder was placed into a quartz boat, which was subsequently loaded into a quartz tube furnace. A Si wafer, topped by a 5 nm thick sputter coated Au film, was located next to the quartz boat for the purpose of catalyzing the formation of the SnO₂ nanowires. The carrier gas with high purity nitrogen (99.95%) was flowing in the direction from the mixed powder precursor towards the Si substrate. The nitrogen flow rate was 100 sccm with the pressure in the tube maintained at 200 Torr. The furnace was heated at a rate of 6.5 °C/min to 800 °C and maintained at 800 °C for 6 hours for the growth of the SnO₂ nanowires. Upon completion of the growth, the furnace power was shut off to allow the furnace to cool naturally. Typically, it took ~4 hours for the furnace to cool from 800 °C to room temperature. The diameter of the SnO₂ NWs ranged from several nanometers to ~1 μm and the length of the wires ranged from several hundred nanometers to several hundred micrometers. The cross-section of

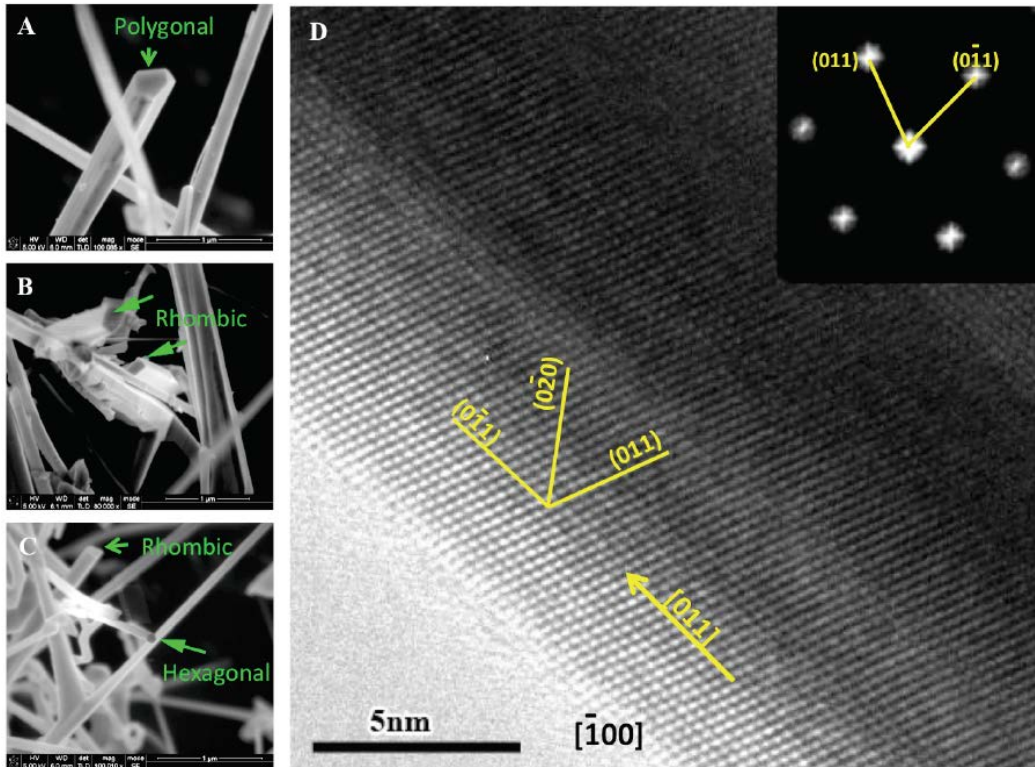


Figure 3.2 Cross-section of the nanowire and their growth direction²²⁰. (A-C) Scanning electron microscopy (SEM) micrographs showing the cross-section of the nanowire is either polygonal (A), or rhombic (B-C), or hexagonal (C). (D) A high resolution transmission electron microscopy (HRTEM) image showing the nanowire growth direction is $[011]$. Inset is a Fast Fourier Transformation of the HRTEM image.

these nanowires is either polygonal, or hexagonal, or rhombic. The growth direction of the nanowires is $[011]$ (Figure 3.2).

3.1.4 Polycrystalline anatase TiO_2 nanowires

The polycrystalline anatase TiO_2 NWs used in this study were obtained from MemPro Ceramics Corporation. They typically have lengths of several micrometers and widths varying between 100-200 nm. Figure 3.3 shows that these NWs are composed of randomly oriented and loosely packed anatase nanoparticles, with most of them being 10–25 nm.

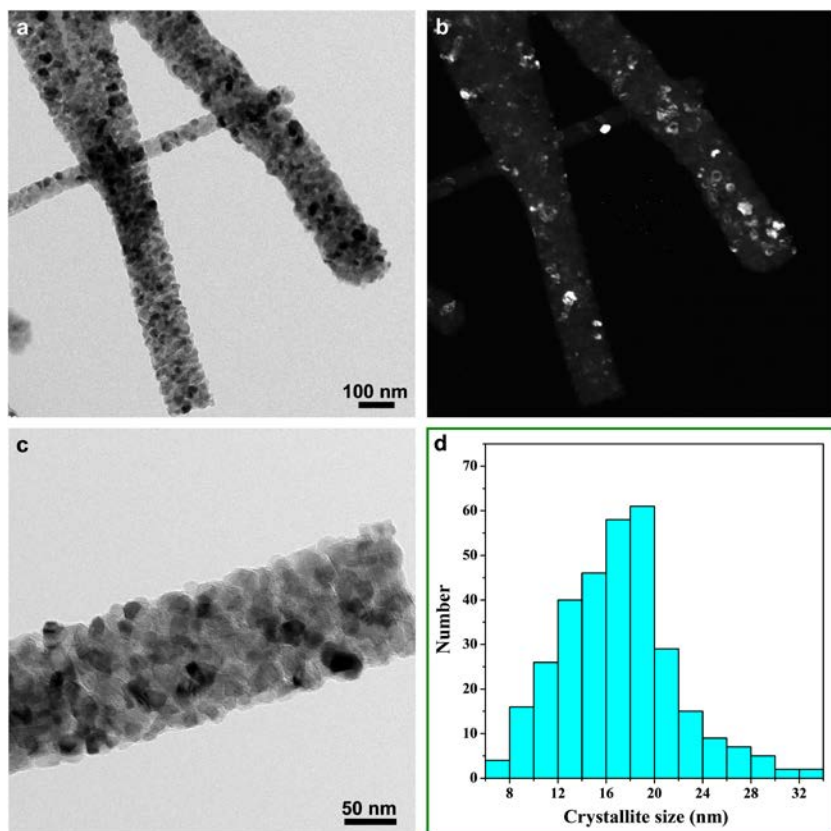


Figure 3.3 Morphology of pristine poly-crystalline anatase TiO₂ nanowires (NWs). (a-b) Bright-field and dark-field TEM images of several poly-crystalline TiO₂ NWs, representing randomly oriented component crystallites. (c) A close-up view of a typical TiO₂ NW, showing that the crystallites are about 20 nm in diameter, randomly oriented, and loosely packed. (d) Size distribution of more than 300 component crystallites with most of them being 10–25 nm.

3.1.5 Single crystalline anatase TiO₂ nanowires

Single crystalline anatase TiO₂ NWs (Figure 3.4) were synthesized by Dr. Weiqiang Han from Brookhaven National Laboratory (Now at Ningbo Institute of Materials Technology and Engineering, Chinese Academy of Sciences). The synthesis process consists of two steps. First H₂Ti₃O₇ nanobelts were produced from a NaOH treatment of anatase TiO₂ particles inside an autoclave at a temperature of 160 °C for 4 days, subsequently followed by acid washing²²⁸. In the second step, the as-grown white H₂Ti₃O₇ nanobelts were put into an alumina boat and heated in a

C_2H_4/H_2 gas mixture²²⁹ at a temperature of 700 °C for 3 minutes. The grey-black product was collected from the boat.

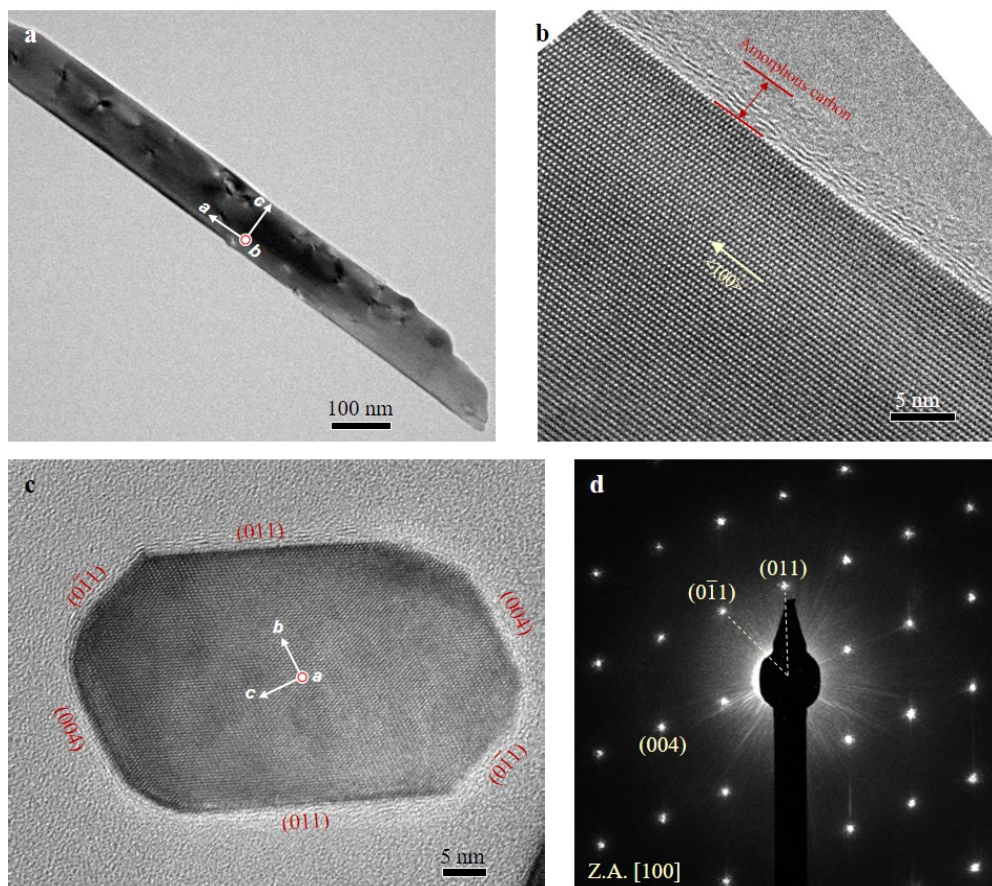


Figure 3.4 Morphology and structure of single crystalline anatase TiO_2 NWs. (a) A typical TiO_2 NW with growth direction of $\langle 100 \rangle$ viewed from the $\langle 010 \rangle$ direction. Some defects are visible. (b) HRTEM showing a well-defined tetragonal phase. A 5-nm-thick amorphous carbon layer was deposited to the surface of the NW to increase the electronic conductivity. (c) Cross-sectional view of one NW along its growth direction (that is, $[100]$). Most of the surface facets are low-index planes such as $\{011\}$ and $\{004\}$. (d) Corresponding EDP of the nanowire cross-section shown in (c).

3.2 EXPERIMENTAL PROCEDURES

3.2.1 Experimental configurations

Most of the work in this dissertation were carried out with an FEI Tecnai F30 TEM at Center for Integrated Nanotechnologies (CINT) in Sandia National Laboratory. The fabrication, structural characterization, and mechanical testing of Pd-based and Cu₅₀Zr₅₀ MGs were performed in an aberration-corrected FEI Titan TEM at Environmental Molecular Sciences Laboratory in Pacific Northwest National Laboratory. Although in-situ TEM technique provides both excellent spatial and temporal resolutions, it, along, does not necessarily lead to success in in-situ investigations. As stated by Ferreira *et al.*, ‘The development in the microelectromechanical systems (MEMS)–based and piezo-actuated in-situ holders are profoundly impacting the way in-situ experiments are performed and the types of observations we are able to make’⁷⁵. By taking advantage of the Nanofactory TEM-STM platform, the present work carried out in-situ TEM observations either under transient electric pulses (for liquid-quenching experiment), or under constant biases (for LIBs investigations).

A schematic illustration of the TEM-STM platform is presented in Figure 3.5. It allows one specimen (specimen 1) to be attached to a metal rod, which is then loaded to the fixed end; and allows another specimen (specimen 2) to be mounted onto the piezo-manipulator, which extends or retrieves under electric field with different magnitudes. By this strategy, specimen 2 can be positioned at an accuracy of ~0.1 nm, which allows precise manipulation to make contact with selected sites (e.g., a NW or a nano-tip) in specimen 1. After that, either transient electric pulses or constant biases can be applied to the specimens for research purpose. This configuration can be slightly modified based on different research demands and objectives.

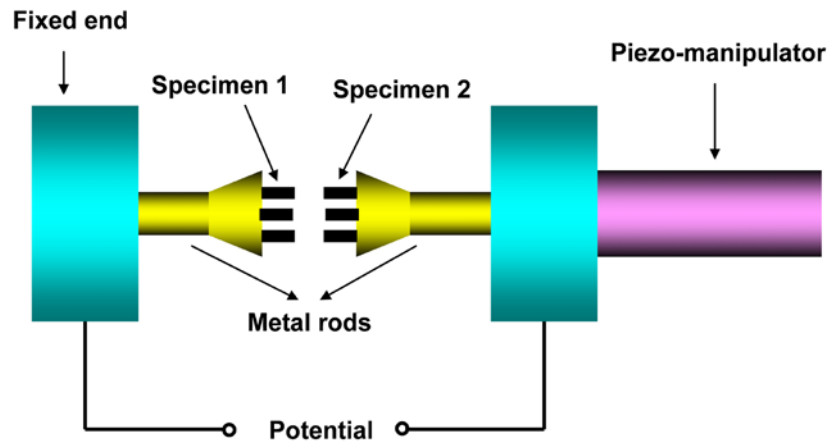


Figure 3.5 Schematic illustration of the Nanofactory TEM-STM platform.

In this dissertation, three configurations have been employed based on Figure 3.5. In Chapter 4, both the fixed end (specimen 1) and the piezo-manipulator (specimen 2) are mounted with metal rods with nano-tips (Figure 3.1) at the front edge, which enables formation of sub-100-nm glassy or crystalline nanostructures directly from bulk substrates. In Chapters 5 and 6, nanowire electrodes are attached to the fix end (specimen 1) and either an ILE droplet on a LiCoO_2 film or a small volume of Li metal with Li_2O surface layer serving as solid electrolyte is mounted onto the piezo-manipulator (specimen 2). These configurations allow development of a nanobattery with either ILE or solid electrolyte inside the TEM for atomic-scale in-situ observations. The detailed configurations and experimental procedures are provided in the experimental approach section in each corresponding chapter.

3.2.2 Calibration of the transient electric pulses

The liquid-quenching experiment started with applying a transient square electric pulse by a Keithley 3401-F pulse generator, creating a melting zone at the contacting nano-tips, followed by ultrafast quenching via rapid heat dissipation through the substrates, leading to the formation of monatomic MGs. Because it is impossible to directly measure the applied voltage on the samples, some calibrations have to be performed outside the TEM. Based on the dimensions of the MG obtained in the liquid-quenching experiment (usually 20–80 in thickness and 30–100 in length), the electric resistance of the sample is about 10–100 Ω . During calibration, resistors with resistance 10-100 Ω , which replace the MG samples, were placed between the fixed end and the current collector on the piezo-manipulator. At the meantime, a Tektronix oscilloscope was connected in parallel to both ends of the resistors in order to measure the actual potential drop on

Table 3.2 Calibration of the applied square electric pulse.

Nominal Voltage (V)	Measured Voltage (V)/Width (ns)			
	Nominal width (ns)	3.2	5.0	10.0
1.0		0.66/3.6	0.89/4.9	0.96/9.9
1.3		0.80/3.6	1.04/5.0	1.21/9.9
1.5		0.91/3.6	1.14/5.1	1.38/10.0
1.8		1.05/3.7	1.30/5.0	1.62/10.0
2.0		1.16/3.7	1.42/5.0	1.78/9.9
2.2		1.26/3.6	1.58/5.1	1.99/10.0
2.5		1.48/3.7	1.80/5.0	2.22/9.8
3.0		1.7/3.7	2.08/5.0	2.7/10.2
3.5		2.0/3.6	2.44/5.1	3.04/9.9
4.0		2.32/3.7	2.82/5.0	3.52/10.2
4.5		2.58/3.6	3.18/5.1	3.92/9.8
5.0		2.82/3.6	3.5/5.0	4.42/9.8

the resistors as well as the pulse width. It was found that the measured potential and width are almost independent of the selected resistors with resistances in the range of 10–100 Ω . Therefore, a 50 Ω resistor was chosen to perform the calibration (Table 3.2). Each value in Table 3.2 is the average of five trials under the same nominal pulse parameters. For simplicity, only the calibrated combinations of voltage and width were used during the liquid-quenching experiments in Chapter 4.

3.2.3 Metallic glass microstructure characterization

The local arrangements of several MGs were investigated using nanobeam diffraction technique^{230,231}, where a nearly parallel coherent electron beam was generated by using a small condenser aperture with a diameter of 10 μm . A small convergence angle of 2–2.5 mrad was selected throughout the experiment, under which the electron beam was focused to spot with a diameter of ~ 0.7 nm. The TEM was operated in scanning transmission electron microscopy (STEM) mode, which allows concurrent imaging and structural characterization, enabling precise pinpointing of the objective regions in the specimen. To gain structural information on the short-to-medium order⁷² in MGs, only the very edge of specimens with a thickness below 5 nm are selected.

3.3 SIMULATION METHODS

To gain a mechanical understanding of the multi-physics during the ultrafast cooling process, the heat transport during the quenching process, as well as the formation mechanism of tantalum

MG was simulated by atoms-to-continuum (AtC) computer simulation with a two-temperature model. This work was performed by my collaborator Dr. Hongwei Sheng from George Mason University. In this method, the classic MD system is coupled to an electron temperature field represented by finite-element meshes to describe the electron transport process. For classic MD, a high-accuracy realistic embedded-atom-method (EAM) potential was developed to describe the interactions between Ta atoms based on first-principles calculations and the force-matching method. The simulation aims to replicate the experimental conditions under which Ta liquids vitrify. The in-silico Ta nanowire is 85 nm×40.8 nm×13.6 nm in dimension, containing up to 2,457,600 atoms, with both ends kept at 300 K. To simulate Joule heating on the nanowire, an electron heat flux was injected to the system, creating a temperature distribution along the nanowire as shown in Figure 4.7a in the next chapter. Quenching processes in scenarios where the heat flux is terminated instantly and within 0.4 ns in a ramp function were simulated.

4.0 FORMATION OF MONATOMIC METALLIC GLASSES THROUGH ULTRAST LIQUID QUENCHING

In this Chapter, a novel ultrafast liquid-quenching methodology will be provided and the atomic-scale vitrification process will be revealed. It has long been conjectured that any metallic liquid can be vitrified into a glassy state provided that the cooling rate is sufficiently high^{156,232-234}. Experimentally, however, vitrification of single-element metallic liquids is notoriously difficult¹⁵⁹. True laboratory demonstration of the formation of monatomic MG has been lacking. Herein we report an experimental approach to vitrify monatomic metallic liquids by achieving an unprecedented high liquid quenching rate of 10^{14} Ks⁻¹. Under such a high cooling rate, melts of pure refractory bcc metals, such as liquid tantalum and vanadium, are, for the first time, successfully vitrified to form MGs suitable for property interrogations. Combining in-situ transmission electron microscopy observation and AtC modeling, we investigated the formation condition and the thermal stability of the as-obtained monatomic MGs. The availability of monatomic MGs being the simplest glass formers offers unique possibilities to study the structure and property relationships of glasses. Our technique also exhibits great control over the reversible vitrification-crystallization processes, suggesting its potential in micro-electro-mechanical applications. The ultra-high cooling rate, approaching the highest liquid-quenching rate attainable in the experiment, makes it possible to explore the fast kinetics and structural behavior of supercooled metallic liquids within the nano- to pico-second regimes.

4.1 INTRODUCTION

Since the first discovery of MG in the 1960s¹¹⁰, the search for new types of MGs has not stopped^{68,155,156}. To date, most MG formers are known to consist of two or more elements with distinct atomic sizes and chemical affinities^{38-41,55}, usually formed by quenching the liquids with techniques varying from conventional die-casting¹⁵⁵ ($\sim 10^{1-3}$ Ks⁻¹), melt-spinning¹⁵⁶ (10^{5-6} Ks⁻¹), liquid splat-quenching¹⁵⁷ ($\sim 10^{9-10}$ Ks⁻¹), to pulsed laser quenching²³⁵ ($\sim 10^{12-13}$ Ks⁻¹). Unfortunately, these solidification techniques can hardly be applied to produce monatomic MGs, mainly due to the extremely low glass forming ability of monatomic metallic liquids resulting from vanishingly small nucleation barriers of supercooled liquids^{43,44} and very fast crystal growth rates^{69,234}. As such, vitrification of pure monatomic MG requires extremely high critical cooling rates far above the experimentally accessible level to suppress crystal growth. Although it has long been conjectured that any metallic liquid can be vitrified into a glassy state provided that the cooling rate is sufficiently high^{40,156,234}, experimental vitrification of single-element metallic liquids is notoriously difficult. True laboratory demonstration of the formation of monatomic metallic glass (MG) has been lacking. The monatomic MG may also be confronted with the thermal stability issue at RT where spontaneous crystallization seems inevitable. Consequently, except for a few special circumstances (e.g., at very thin edges of a splat quenched nickel foil¹⁵⁷), monatomic MGs have not been found to form from pure metal melts by vitrification.

More recently, pure metallic germanium liquid was reported to vitrify under hydrostatic pressure above 7.9 GPa for the first time¹⁵⁹. However, upon releasing pressure to ambient condition, germanium MG quickly transforms to a non-metallic low-density amorphous phase, in which case the tendency and mechanism of liquid vitrification are largely different from those of

most d-block transition metals. Other non-vitrification methods (e.g., vapor deposition²³⁶ and chemical synthesis¹⁵²) have been attempted to produce monatomic amorphous samples, which are often in geometrically confined forms (e.g., substrate-supported thin films and nano-sized powders) and are plagued with either purity¹⁵² or stability problems¹⁴⁶, offering limited potential for broader applications. Therefore, advanced techniques to fabricate high purity monatomic MGs with controllable geometries are highly appealing.

4.2 EXPERIMENTAL APPROACHES

By building an in-situ Joule heating nano-device inside a transmission electron microscope (TEM), we present a unique ultrafast liquid-quenching system to vitrify monatomic metallic liquids. This technique exploits the excellent thermal conductivity of the metals and maximizes the heat conduction rate of the cooling system. As described in Chapter 3, triangle-shaped nano-tips were generated at the fracture surface of the metal piece. Two such metal pieces with nano-tips were mounted to a Nanofactory TEM-STM platform, with one at the fixed end and the other at the piezo-manipulator. All the above specimen preparation and loading procedures were carried out inside a glove box filled with helium (the content of oxygen and water is below 1 ppm). The TEM-STM platform, together with the sample, was quickly transferred to the TEM while being kept in an air-proof environment.

All in-situ experiments were conducted inside an FEI Tecnai F30 TEM operating at an acceleration voltage of 300 kV with column vacuum $\sim 10^{-5}$ Pa. We preferred longer tips with low-index zone axis (i.e., $\langle 111 \rangle$, $\langle 001 \rangle$ and $\langle 110 \rangle$) parallel to the incident electron beam, which can be easily found in our samples. The two chosen nano-tips were brought into contact

by the piezo-manipulator of the STM holder. In order to remove surface contamination, the joined nano-tips were heated to an elevated temperature (close to the melting point) for half an hour by Joule heating. The liquid-quenching experiment started with applying a transient square electric pulse by a Keithley 3401-F pulse generator, creating a melting zone at the nano-tips, followed by ultrafast quenching via rapid heat dissipation through the substrates, leading to the formation of monatomic MGs. Tensile tests on the as-formed tantalum MG were carried out by gradually retracting the substrate mounted on the piezo-manipulator. The strain rate can be controlled by adjusting the speed at which the substrate is retracted, and in the present study, it was controlled to be $\sim 10^{-3} \text{ s}^{-1}$.

4.3 EXPERIMENTAL RESULTS

4.3.1 Formation of monatomic metallic glasses from melts of pure metals

The ultrafast quenching technique in the current study is illustrated in Figure 4.1a-c. First, two protruded nano-tips with clean surfaces are brought into contact with each other (Figure 4.1a) under an ultra-high vacuum condition inside the TEM. A short square electric pulse, typically 0.5–3 V in amplitude and within 3.7 ns in duration, imposes local Joule heating on the joined tips, causing melting of the extrusion tips and formation of a melting zone in the middle (Figure 4.1b). Upon instantaneous cessation of the electric pulse and, consequently, local Joule heating, heat dissipates rapidly through the solidifying piece and the conductive heat reservoir, creating an extremely high cooling rate sufficient to vitrify the melt (Figure 4.1c). In Figure 4.1d-e, we

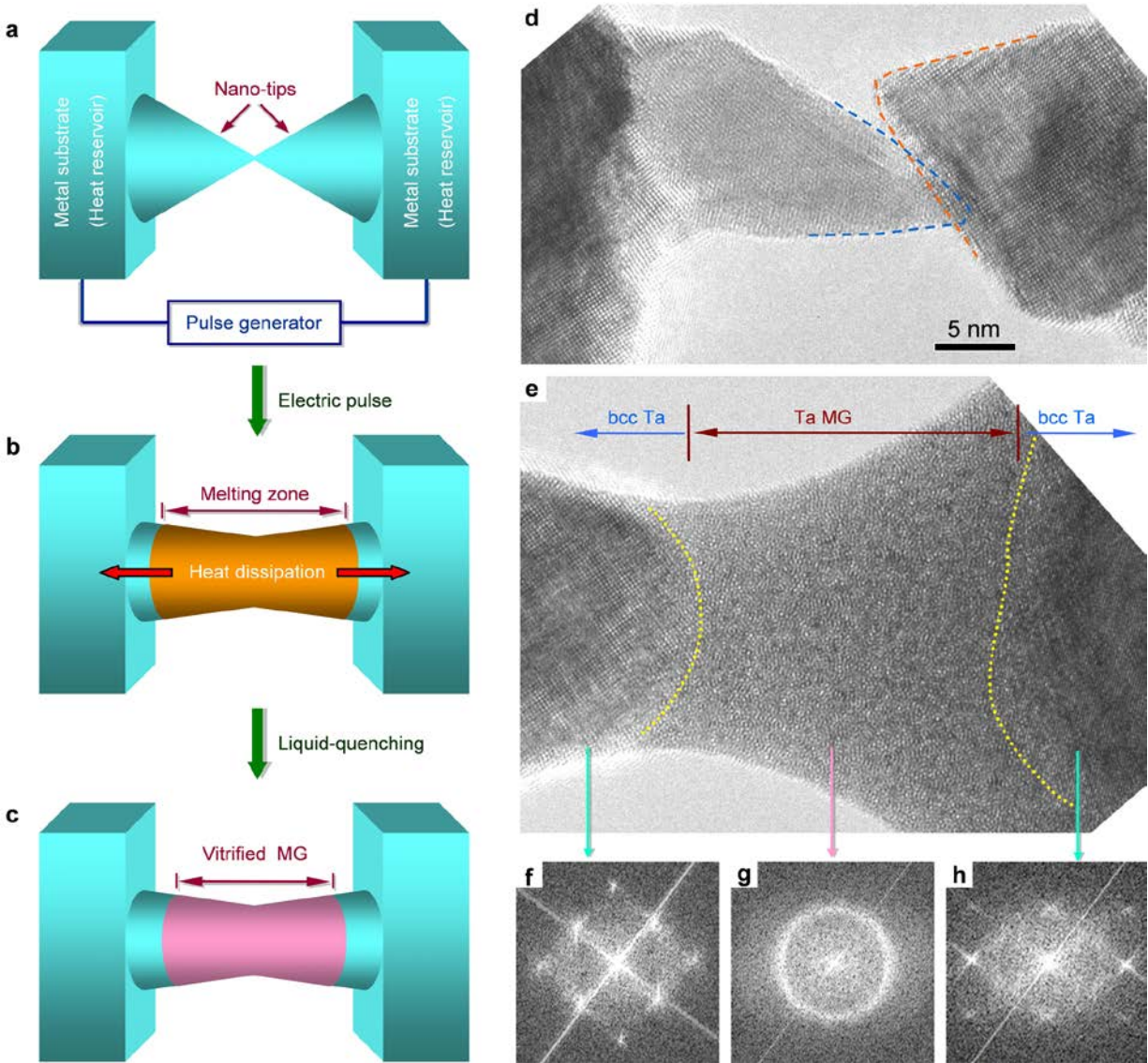


Figure 4.1 Illustration of an ultrafast liquid-quenching approach²²⁵. (a-c) Schematic drawing of the experimental configuration. Two protruded nano-tips are brought into contact with each other (a), which are melted by applying a short square electric pulse with duration around 3.7 ns and voltage in the range of 0.5–3 V (b). Heat dissipates rapidly through the two bulk substrates (indicated by two red arrows), vitrifying the melting zone to form monatomic MGs (c). (d-e) High resolution TEM images showing two contacting tantalum nano-tips (d) forming a tantalum MG (e) after applying a 0.8 V, 3.6 ns electric pulse. The glass-crystal interfaces (GCIs) are denoted by yellow dotted curves. (f-h) FFTs confirming a 20 nm long, 15 nm thick fully vitrified region (g) bounded by two crystalline substrates viewed along the $\langle 100 \rangle$ (f) and $\langle 110 \rangle$ (h) crystallographic orientations, respectively.

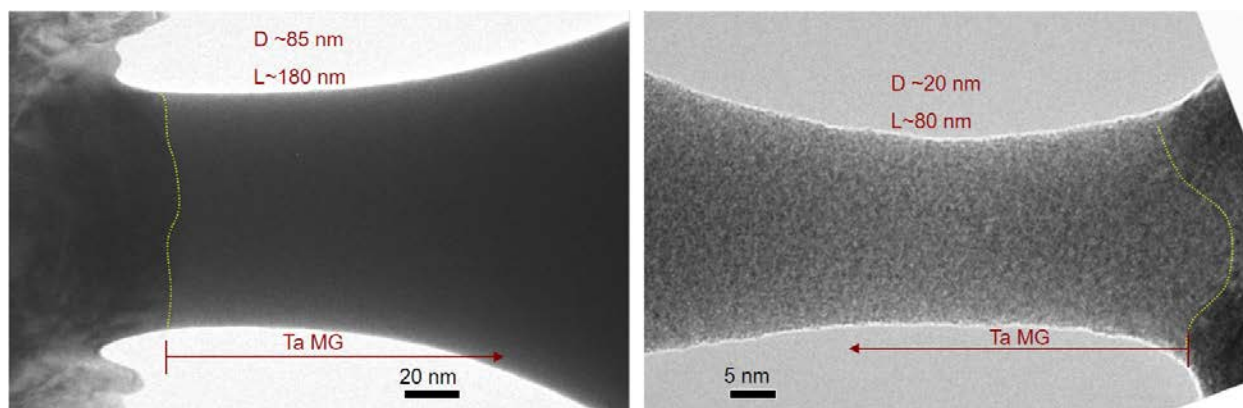


Figure 4.2 Controllable geometries by tuning the electric pulse and by coupling with tensile/compressive stress²²⁵. A tantalum MG with diameter close to 100 nm is obtainable under an electric pulse with voltage above 2 V (left). A nanowire with an aspect ratio of 4 was formed by applying tensile loading during liquid quenching (right). The GCIs are indicated by yellow dotted curves.

demonstrate that a 0.8 V, 3.6 ns electric pulse on two connecting crystalline Ta nano-tips (Figure 4.1d) led to the formation of a 15 nm wide, 20 nm long Ta MG (Figure 4.1e).

The dimensions of the MG samples can be controlled by tuning electric pulse parameters while engaging in-situ tensile/compressive loading. In this way, Ta MG samples with dimensions of 100 nm in diameter or an aspect ratio of ~4 are obtainable (Figure 4.2). The formation of even larger Ta MG samples, which are not electron transparent, has not been pursued in this work. Applying this method, we have systematically tested the vitrification capability of transition metals, and successfully obtained Ta, V (Figure 4.3), Mo (Figure 4.4) and W (Figure 4.5) monatomic MGs (vitrification of V and Mo melts were performed by Dr. Jiangwei Wang from University of Pittsburgh). The materials systems that have been vitrified to form monatomic MGs are typically early transition bcc metals with high melting points and excellent thermal conductivities.

The amorphous nature of the as-obtained MG was confirmed by TEM diffraction patterns. The diffusive diffraction halos in the fast Fourier transformation (FFT) (Figure 4.1g) of the area

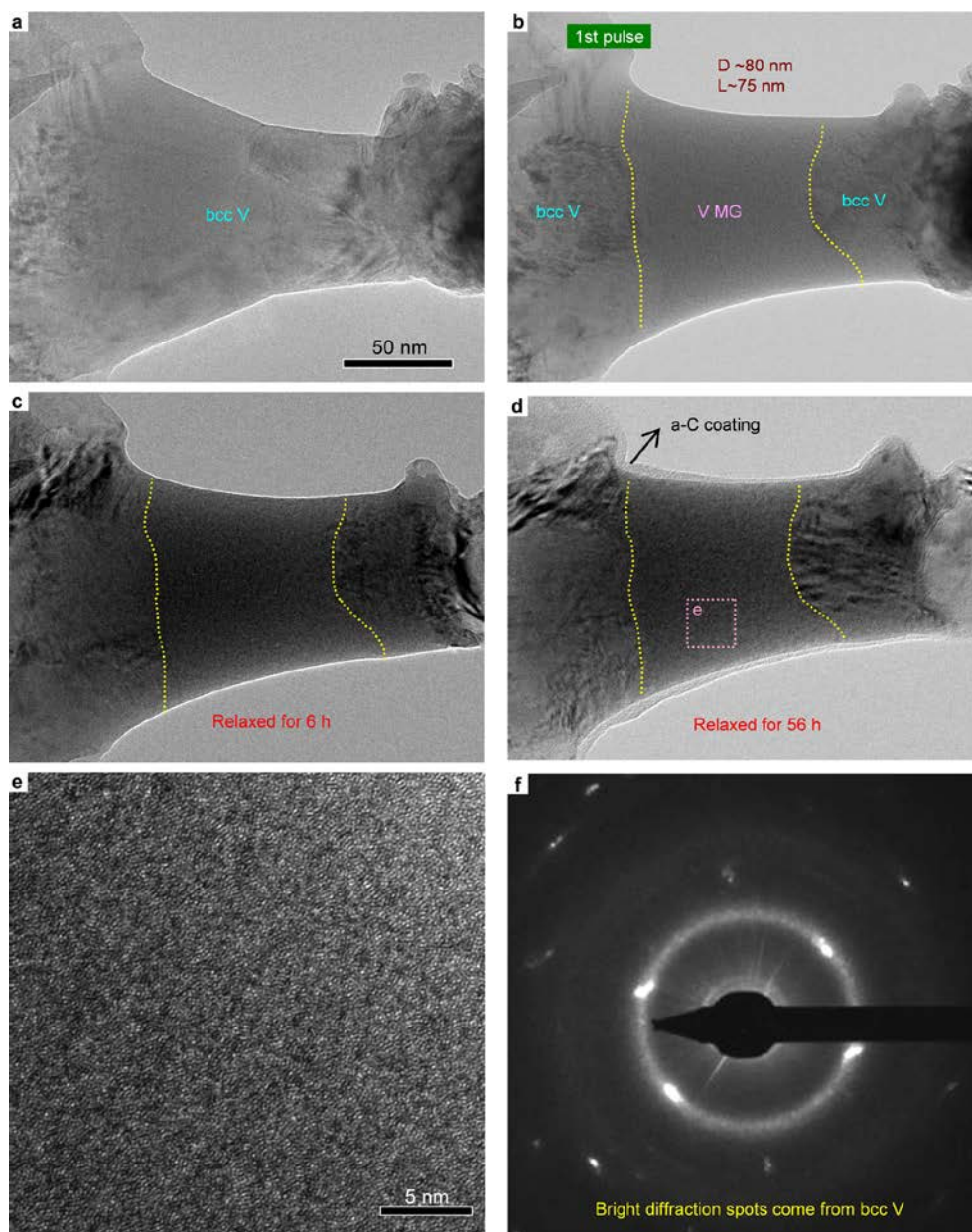


Figure 4.3 Formation and RT stability of vanadium MG²²⁵. (a) TEM image of two crystalline vanadium nano-tips in contact with each other. (b) Formation of a 75 nm long, 80 nm thick vanadium MG under a 1.26 V, 3.6 ns electric pulse. The as-formed vanadium MG was sandwiched by two crystalline substrates with two GCIs (denoted by yellow dotted curves). (c-d) Thermal stability test on vanadium MG at RT, where amorphous vanadium was found stable after 56 hours. In order to protect vanadium from oxidation, a 5 nm thick amorphous carbon layer was coated to the surface of the vanadium MG. The reduced length of the vanadium MG in d is due to a slight change in the viewing angle. (e) High resolution image of the vanadium MG relaxed for 56 h, exhibiting typical amorphous characteristics. (f) Electron diffraction pattern of vanadium MG, showing diffusive amorphous halos and a diffusive background. The bright diffraction spots originate from bcc vanadium due to the fact that the aperture was not small enough to exclude the neighboring crystalline vanadium substrate.

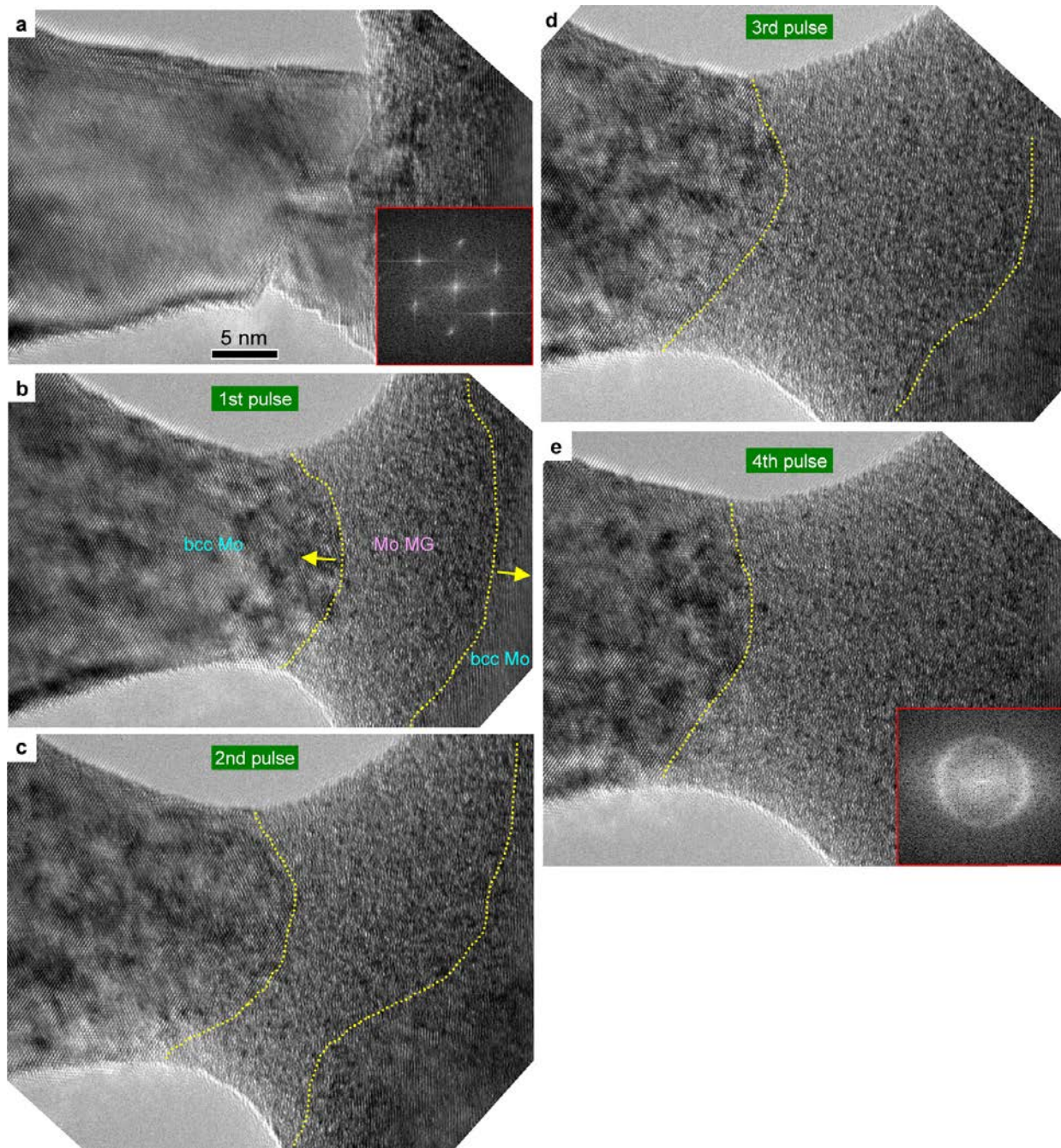


Figure 4.4 Formation of molybdenum MG by ultrafast quenching²²⁵. (a) TEM image of two contacting molybdenum nano-tips with a well-defined bcc structure viewed along the $\langle 111 \rangle$ zone axis (inset in a). (b-e) Mo MG formation and growth under a series of vitrification pulses. The GCIs (indicated by yellow dotted curves) moved a step away from each other after each pulse (denoted by two yellow arrows in b), resulting in the growth of the Mo MG. The amorphous structure is corroborated by the diffuse halos in the FFT (inset in e).

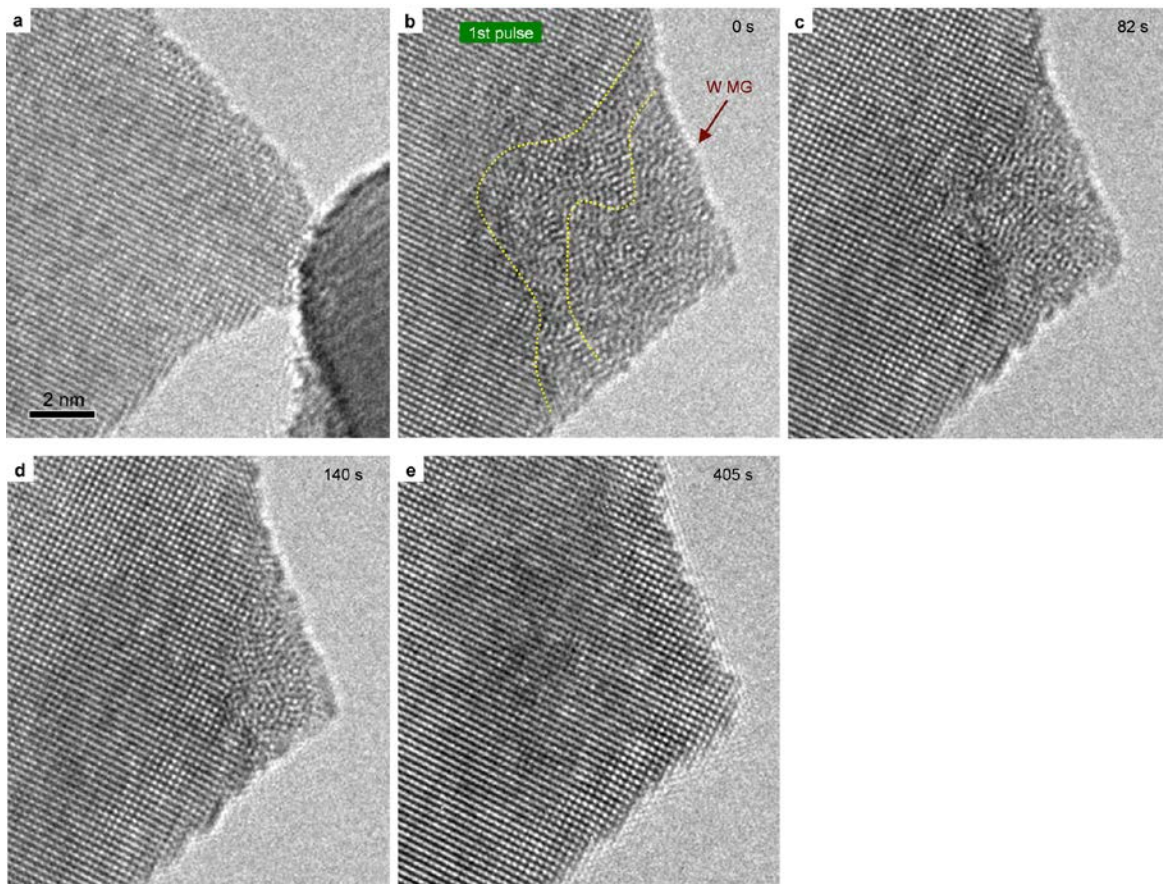


Figure 4.5 Formation and spontaneous crystallization of tungsten MG²²⁵. (a) High resolution TEM image of the original crystalline tungsten nano-tip viewed along $\langle 100 \rangle$ zone axis. (b) Formation of tungsten MG in the tungsten nano-tip under a vitrification pulse. An atomically rough and diffuse GCI was identified, where the transition zone from amorphous to bcc tungsten was about 1–2 nm thick (the region between the two dotted yellow curves) (c-e) In-situ TEM observation of spontaneous crystallization of tungsten MG. Tungsten MG is found to be unstable at RT, undergoing spontaneous crystallization to a well-defined bcc structure.

bounded by two glass-crystal interfaces (GCIs) are characteristic of amorphous structure, contrasting the bright diffraction spots of the Ta substrates with a well-defined bcc structure (Figure 4.1f,h). To confirm the glassy structure and the thermal stability of Ta MG, a sample with 60 nm in diameter and 90 nm in length was relaxed in high vacuum at RT for 8 hours (Figure 4.6a). Electron diffraction patterns (EDPs) of the as-quenched (Figure 4.6b left) and relaxed (Figure 4.6b right) Ta MGs showed similar features characterized by diffuse halos

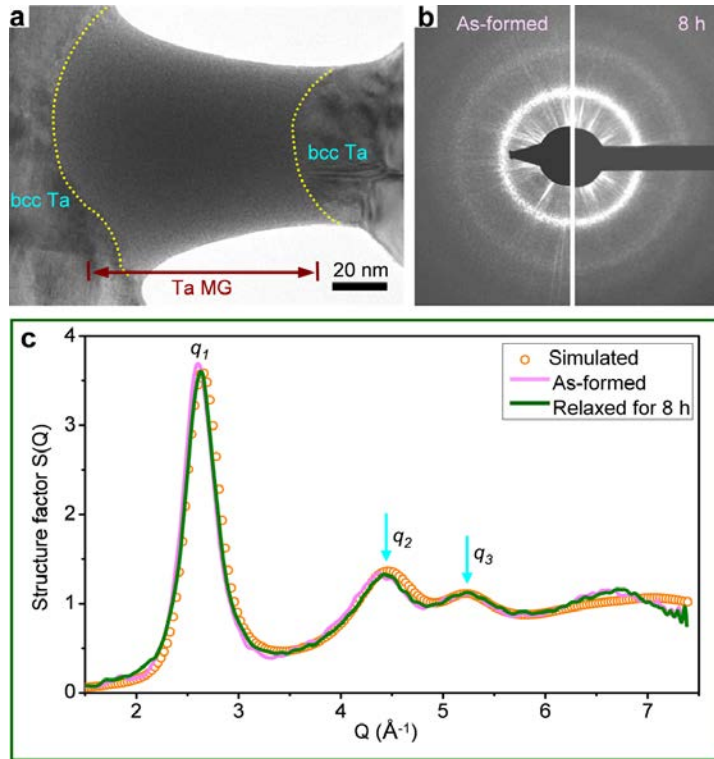


Figure 4.6 Structure and thermal stability of tantalum MG²²⁵. (a) TEM morphology of a typical Ta MG with length of ~90 nm and diameter of ~60 nm. The GCI is indicated by yellow dotted curves. (b) Electron diffraction of Ta MG, as-quenched (b left) versus relaxed for approximately 8 h (b right). (c) A comparison of the structure factors of the as-formed, 8 h relaxed and simulated Ta MGs. All three curves show very similar peak positions, including well separated second (q_2) and third peaks (q_3) (indicated by cyan arrows). The ratios of peak positions are the same for the relaxed and simulated structure, where $q_2/q_1=1.69$ and $q_3/q_1=1.99$.

typical of amorphous structure. The corresponding integrated and optimized 1D static structure factors²³⁷ $S(q)$ (Figure 4.6c) showed similarities in their shape and peak positions, indicating that no major structural changes have occurred in Ta MG after 8 hours. The slight shift to the right in the main peak positions of $S(q)$ may be attributed to structural relaxation in the glass, as expected. The main peak positions of the relaxed MG are measured to be 2.63 \AA^{-1} , 4.42 \AA^{-1} , and 5.23 \AA^{-1} , respectively, corresponding to $q_2/q_1=1.68$ and $q_3/q_1=1.99$, which are almost identical to the simulated structure factor (orange circles in Figure 4.6c) derived by quenching liquid tantalum at a cooling rate of $\sim 10^{13} \text{ Ks}^{-1}$ on the computer. The observed $S(q)$ of tantalum MG also agrees

well with theoretical works on monatomic systems²³⁸⁻²⁴¹, as well as with previous experimental results on amorphous iron²⁴² and cobalt²⁴³ where $q_2/q_1=1.69$ and $q_3/q_1=1.97$.

To understand the vitrification process of the liquid and estimate the cooling rate, atoms-to-continuum simulations²⁴⁴ have been performed where a tantalum nanowire with geometry and size matching the experimental conditions was simulated (This simulation work was performed by Dr. Hongwei Sheng from George Mason University; detailed information about the atoms-to-continuum simulation is presented in Appendix A). Quenching of liquid tantalum starts at the moment when external Joule heating is turned off (Figure 4.7a), during which the temperature evolution in the nanowire depends on rapid heat dissipation through the massive crystalline substrates kept at RT. Due to the large temperature gradient, excellent heat conductivity, and small specimen size, ultrafast cooling is achieved, as evidenced from the evolution of the temperature distribution in the Ta nanowire (Figure 4.7b). The computed cooling rate of the liquid zone (Figure 4.7c) reaches as high as 10^{14} Ks⁻¹ at 4200 K and decreases slightly to 5×10^{13} Ks⁻¹ at the glass transition temperature T_g of liquid tantalum, which is estimated to be around 1650 K (Figure 4.8).

Accompanying the rapid quenching process, the real-time dynamics of the atomic system was revealed by MD simulations, indicating that whether a MG can eventually form is determined by the competition between the liquid-quenching rate and the crystal growth rate from the melt. Under the given experimental condition, a large portion of the original 35-nm-long liquid tantalum zone vitrified after Joule heating was cut off (Figure 4.9a-b), demarcated by atomically rough GCIs (Figure 4.9b inset), corroborating our experimental observations. The effect of a trailing edge in the applied electric pulses is taken into account by modeling liquid-quenching under a heat flux terminated within 0.4 ns in a ramp function rather than instantly. As

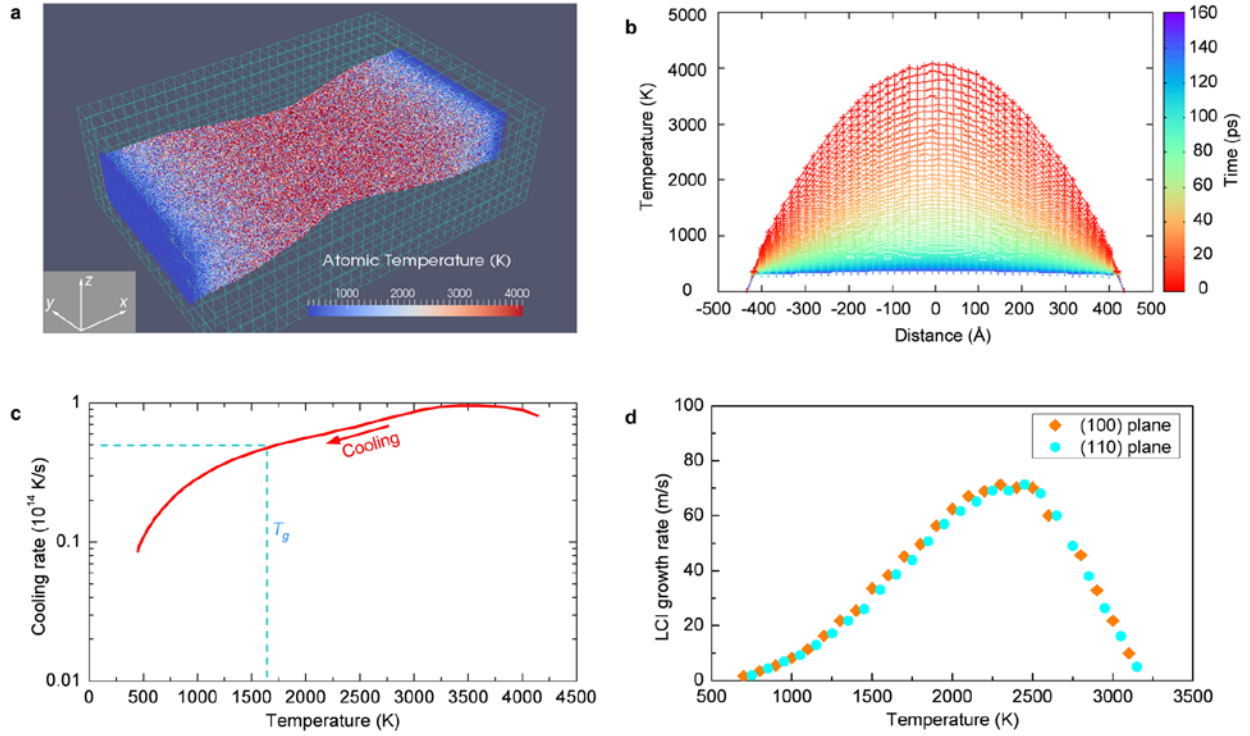


Figure 4.7 Cooling rate and crystal growth rate estimated by AtC computer simulation²²⁵. (a) Atomic temperature distribution of a tantalum nanowire with dimension 85 nm×40.8 nm×13.6 nm at time zero when Joule heating is instantly stopped. The 32×12×6 finite-element meshes were used to simulate the electron temperature field in the TTM. The electron temperature on both sides of the nanowire was kept constant at 300 K. (b) Evolution of atomic temperature distribution along the x direction of the Ta nanowire during the cooling process. (c) Cooling rate as a function of temperature in liquid tantalum (the middle section within 5 nm along the x direction). The highest cooling rate at the initial stage of quenching reaches as high as 10^{14} Ks⁻¹. (d) Crystal growth rate at the LCIs of the (100) (orange squares) and (110) (cyan circles) crystallographic planes, respectively, based on classic MD simulation. The simulation details for crystal growth from the melt are similar to previous research²⁴⁵.

shown in Figure 4.10a-b, 18 nm of the 35 nm Ta liquid was successfully vitrified into MG under a cooling rate varying between 3×10^{13} Ks⁻¹ and 10^{13} Ks⁻¹ (Figure 4.10).

The critical cooling rate \dot{T}_c required for vitrifying liquid tantalum is estimated based on dimensional considerations: $\dot{T}_c \approx T_L v / L$, where T_L is the temperature of the liquid, v is the average moving velocity of the liquid-crystal interface, which is estimated to be ~ 50 ms⁻¹ based on Figure 4.7d, and L is the length of the melting zone. The critical cooling rate is derived by

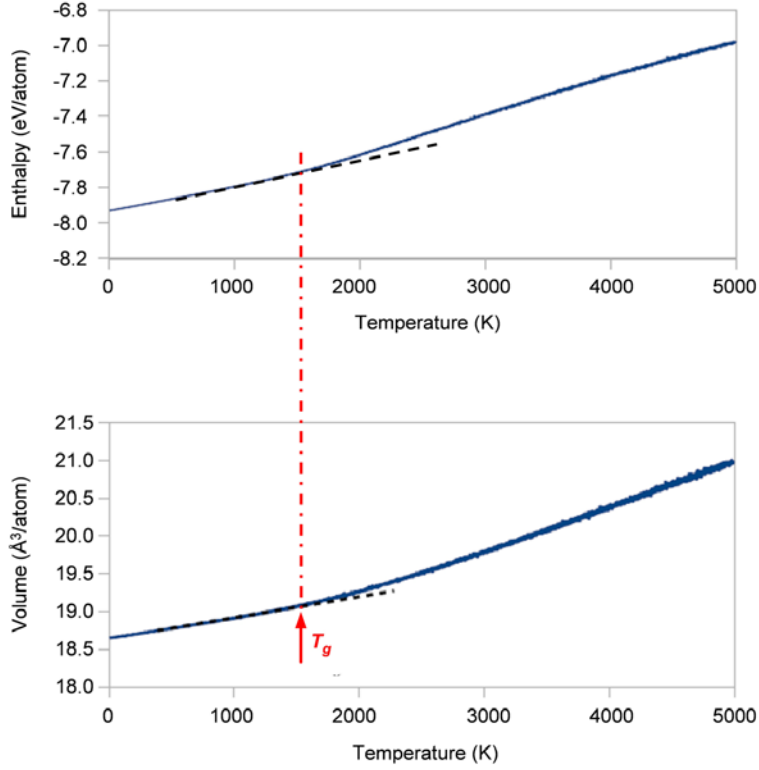


Figure 4.8 Glass transition temperature T_g of tantalum from MD simulation²²⁵. Both the enthalpy change and the volume change as a function of temperature indicate T_g is close to 1650 K.

considering the temperature drop ΔT , which is the temperature interval between T_L and the glass transition temperature T_g , divided by the time t required for complete crystallization. As shown in Figure 4.8 and Figure 4.9, T_g is approximately half of T_L , leading to $\Delta T \approx 0.5 T_L$. Assuming complete crystallization is signified by two glass-crystal interfaces merging in the middle of the melting zone, each interface travels a length of $0.5L$, leading to $t=0.5L/v$. Hence, we have

$$\dot{T}_c = \frac{\Delta T}{t} \approx \frac{0.5T_L}{(0.5L/v)} = \frac{T_L v}{L}. \text{ Under the simulation geometry where } L \text{ is around } 30 \text{ nm, the}$$

estimated critical cooling rate is $\sim 5 \times 10^{12} \text{ Ks}^{-1}$.

The thermal stability of tantalum MG is rationalized by our computation, showing that the crystal growth of low-index faces of bcc Ta is a thermally activated process at RT, with

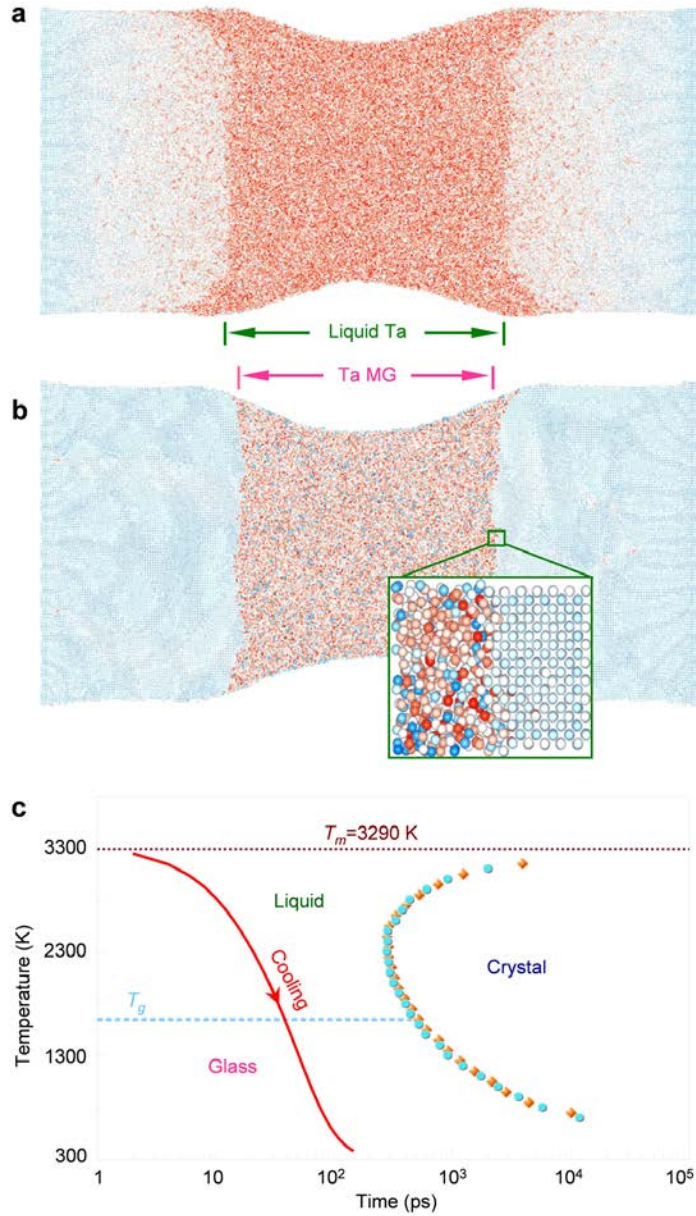


Figure 4.9 Dynamic vitrification process in liquid Ta revealed by atoms-to-continuum computer simulation²²⁵. (a) Atomic configuration showing a 35 nm long liquid zone of tantalum after Joule heating (at $t=0$ ps). The atoms are colored based on their degree of disorder represented by local bond-orientational order parameter²⁴⁶ q_6 . The red color corresponds to liquid tantalum after Joule heating. (b) Atomic configuration showing the formation of a 30 nm long tantalum MG segment after quenching ($t=150$ ps). The average temperature of the tantalum nanowire is close to RT at $t=150$ ps. The inset highlights the interface structure between amorphous and bcc Ta. (c) A Time-Temperature-Transformation diagram derived from isothermal MD simulations, outlining approximately the formation condition of Ta MG. The crystal zone is estimated based on the crystal growth rates of the (100) plane (cyan circles) and the (110) plane (orange squares). The red solid line indicates the temperature evolution of the moving LCI (and later on GCI) during cooling.

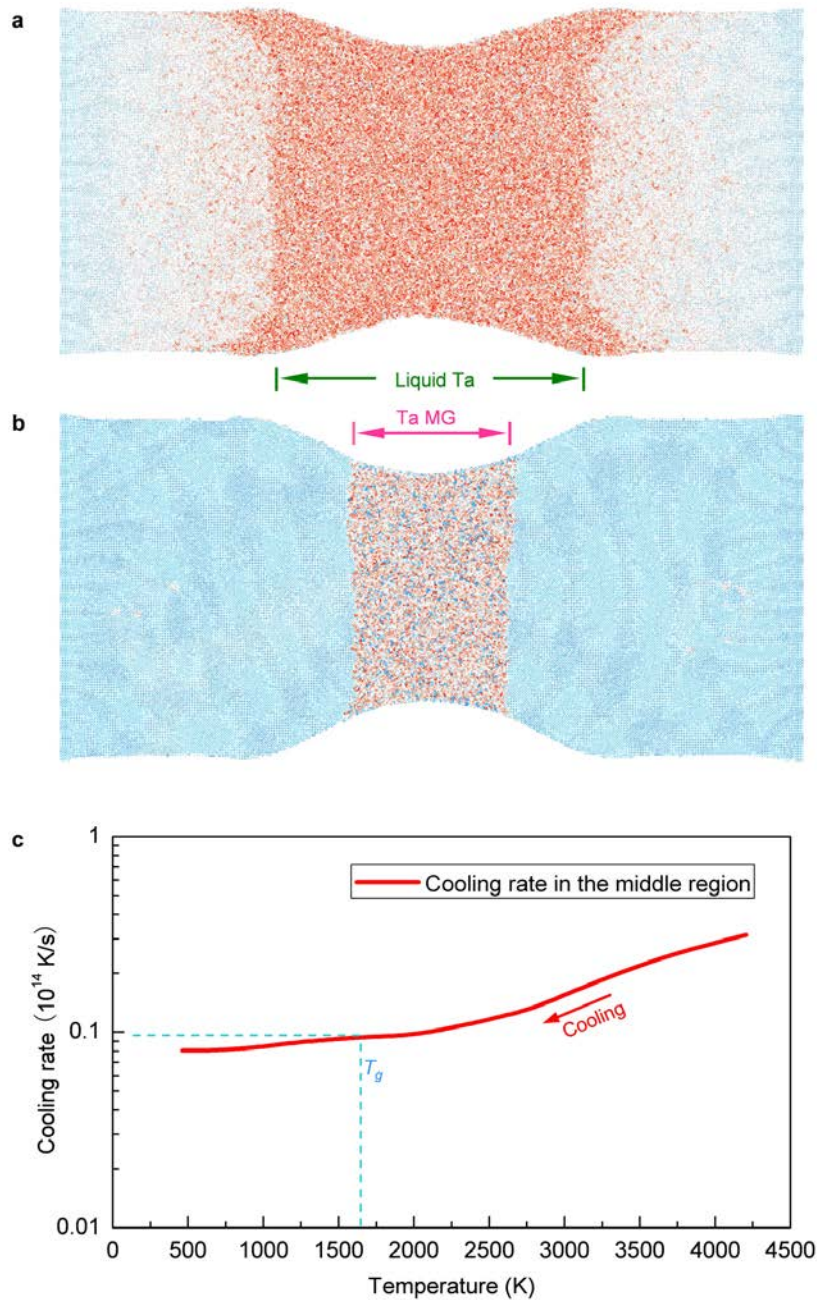


Figure 4.10 Vitrification of liquid tantalum under a heating flux terminated within 0.4 ns by AtC computer simulation²²⁵. (a) Atomic configuration of the tantalum nanowire after Joule heating. A 35 nm long melting zone was formed before quenching (atoms colored with red). (b) A 18 nm region in the middle of the melting zone is vitrified to a glassy state after being quenched to RT. (c) Cooling rate as a function of temperature in the middle region of the melting zone during quenching. The cooling rate varied between $3 \times 10^{13} \text{ Ks}^{-1}$ at 4200 K and 10^{13} Ks^{-1} at T_g .

infinitesimally small growth rates at the GCIs (based on Figure 4.7d). It should be pointed out that the “slow” growth rate of Ta crystals is distinctly different from that of fcc metals, where the growth of crystal interfaces is expected to be spontaneous and fast even at zero temperature^{69,142}. Indeed, we have tried but failed to produce any monatomic MGs from fcc metals (e.g., gold, silver, copper, palladium, aluminum, rhodium, and iridium) using the very same approach.

4.3.2 Controlled competition between vitrification and crystal growth

Interestingly, the competition between vitrification and crystal growth can be experimentally controlled, leading to a novel phase-change phenomenon in the MG. Figure 4.11 illustrates a vitrification-crystallization cycle in a Ta sample controlled by alternately applying two kinds of electric pulses with the same duration (3.6 ns) but different voltages. With the assistance of in-situ TEM observation, the structural and morphological evolutions of the sample can be monitored on the fly. As shown in Figure 4.11a, a 40-nm-thick, 50-nm-long Ta MG obtained with a high-voltage (1.26 V) electric pulse (i.e., the vitrification pulse) was reverted to its original crystalline state after applying a series of low-voltage (0.90 V) electric pulses (i.e., the crystallization pulses), with each pulse reducing the size of the sandwiched amorphous zone (Figure 4.11b-c). The GCIs were identified to be atomically rough and diffuse during both vitrification (Figure 4.11e) and crystallization (Figure 4.11f). After complete crystallization of the Ta MG (Figure 4.11c and its inset), another vitrification pulse again generated a glassy zone of Ta (Figure 4.11d), which exhibits almost identical dimension and morphology with respect to the one shown in Figure 4.11a, demonstrating that a reversible glass-crystal phase-change process is achievable by our approach.

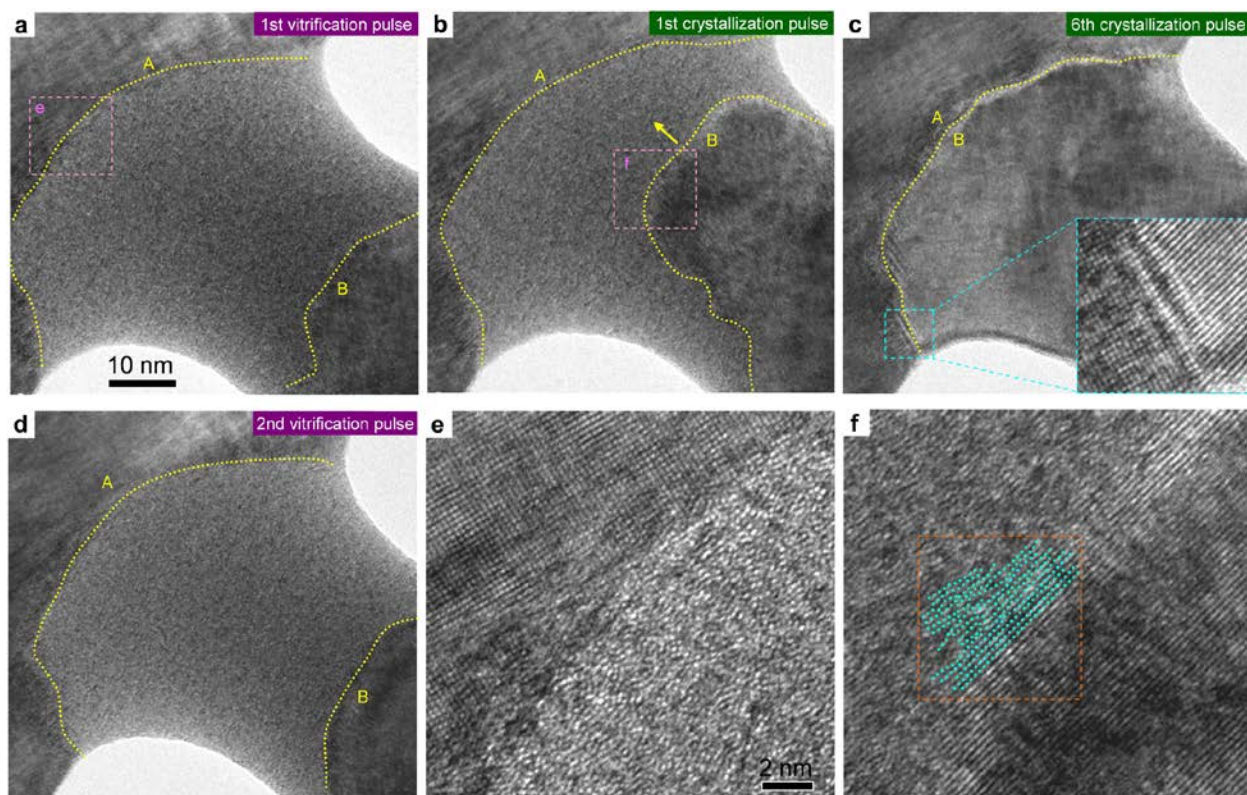


Figure 4.11 Reversible crystallization-vitrification phase changes of tantalum MG²²⁵. (a) Formation of a 40-nm-thick, 50-nm-long tantalum MG under a 3.6 ns, 1.26 V electric pulse. The two GCIs are indicated by yellow dotted curves and labeled as A and B, respectively. (b-c) Controlled gradual crystallization under a series of pulses with 3.6 ns in duration and 0.91 V in amplitude. Crystallization proceeded with crystal growth at GCI B (indicated by a yellow arrow), and completed after 6 crystallization pulses (inset in c). (d) A second vitrification pulse resulted in the formation of a Ta MG similar to (a). (e-f) Close-up views of the atomically rough and diffuse GCIs during a phase-change cycle. A schematic drawing with cyan dotted lines along one set of the (110) planes is presented in f to show the gradual breakdown of the long-range order across the GCI.

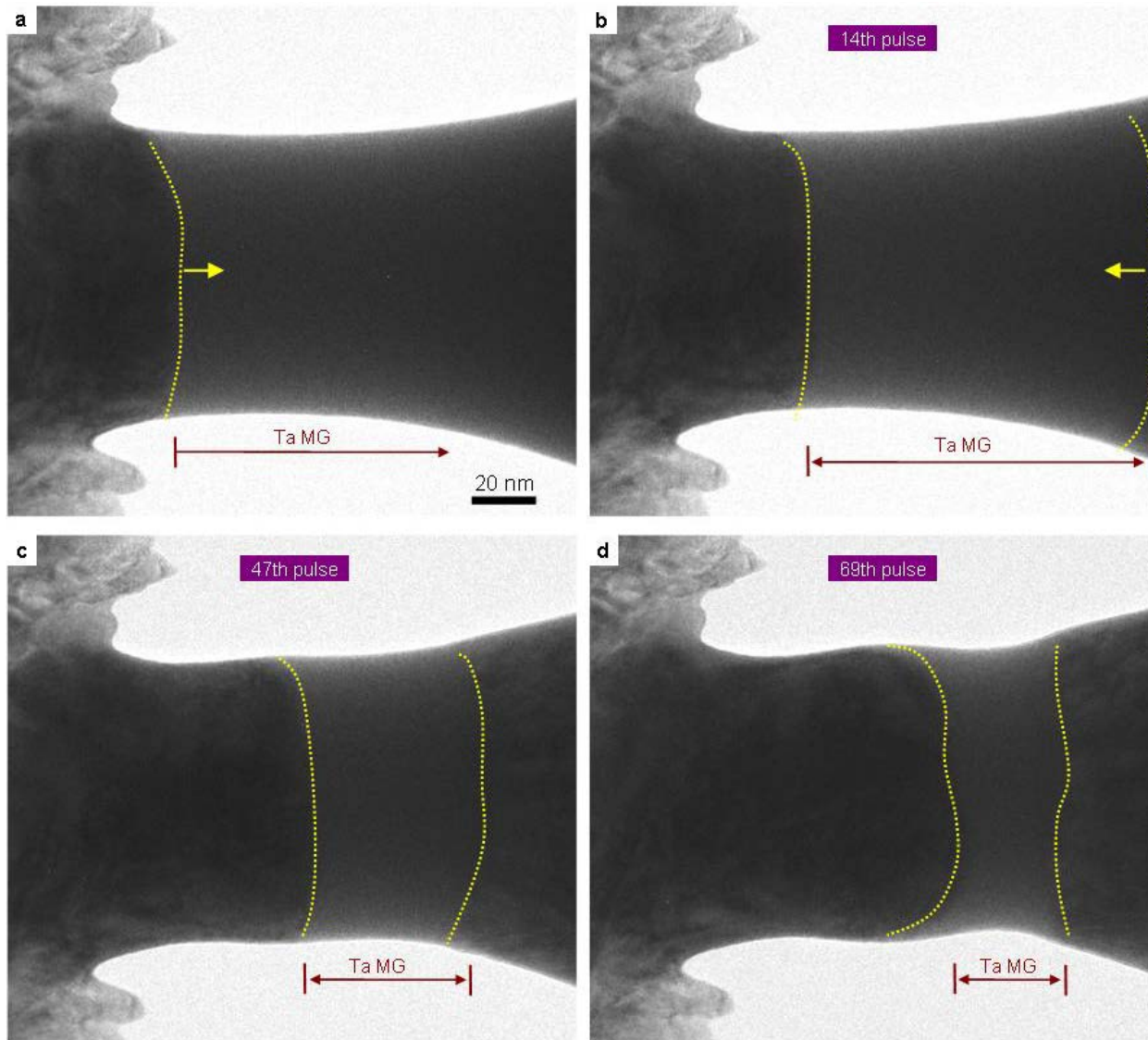


Figure 4.12 Controlled gradual crystallization under a series of crystallization pulses²²⁵. The GCIs are marked with yellow dotted curves their move directions are indicated by yellow arrows.

Another example of controlled phase changes of Ta MG is presented in Figure 4.12. Such reversible phase-change behavior of tantalum, bearing a resemblance to phase-changing chalcogenide glasses^{29,30}, makes it interesting candidates for applications in nano-devices such as phase-change based memristors³⁰ and rewritable data storage devices²⁹.

4.3.3 Tensile deformation of sub-100-nm-sized metallic glasses

With the current ultrafast liquid-quenching approach, the size-dependent tensile behavior of several sub-100-nm-sized MGs were investigated. Figure 4.13 demonstrates a shear-dominated deformation process in a 27-nm-wide Ta MG (that is, the left side of the hybrid Ta NW in Figure 4.13a). One of the GCIs is used as a reference to track the deformation of the Ta MG (pointed out by green arrows in Figure 4.13a-c,g). Premature necking (marked by a pair of purple arrow heads in Figure 4.13c) was observed shortly after yielding at an elastic strain close to 5% (Figure 4.13b), which approaches the elastic limit of MGs²⁴⁷. Further deformation to a strain of ~10% led to nucleation of a major shear with approximately 52° with respect to the loading direction (Figure 4.13d). Unlike in bulk MGs where catastrophic failure is expected after very limited plasticity³⁹, the nanosized Ta MG exhibited gradual growth of a shear offset (Figure 4.13e) until final fracture by cavitation (Figure 4.13f). The length of the deformed region in the original Ta MG is identified by tracking the contour evolution during deformation (Figure 4.13g), which is approximately 28 nm. The stress in the Ta MG are roughly estimated by measuring the lattice strain of the bcc Ta segment (that is, the right side of the hybrid Ta NW), which serve as a strain gauge. The stress-strain curve (Figure 4.13h) demonstrates a yielding strength as high as 4.7 GPa and an elastic modulus of ~110 GPa, which is about half of the elastic modulus of bcc Ta in the

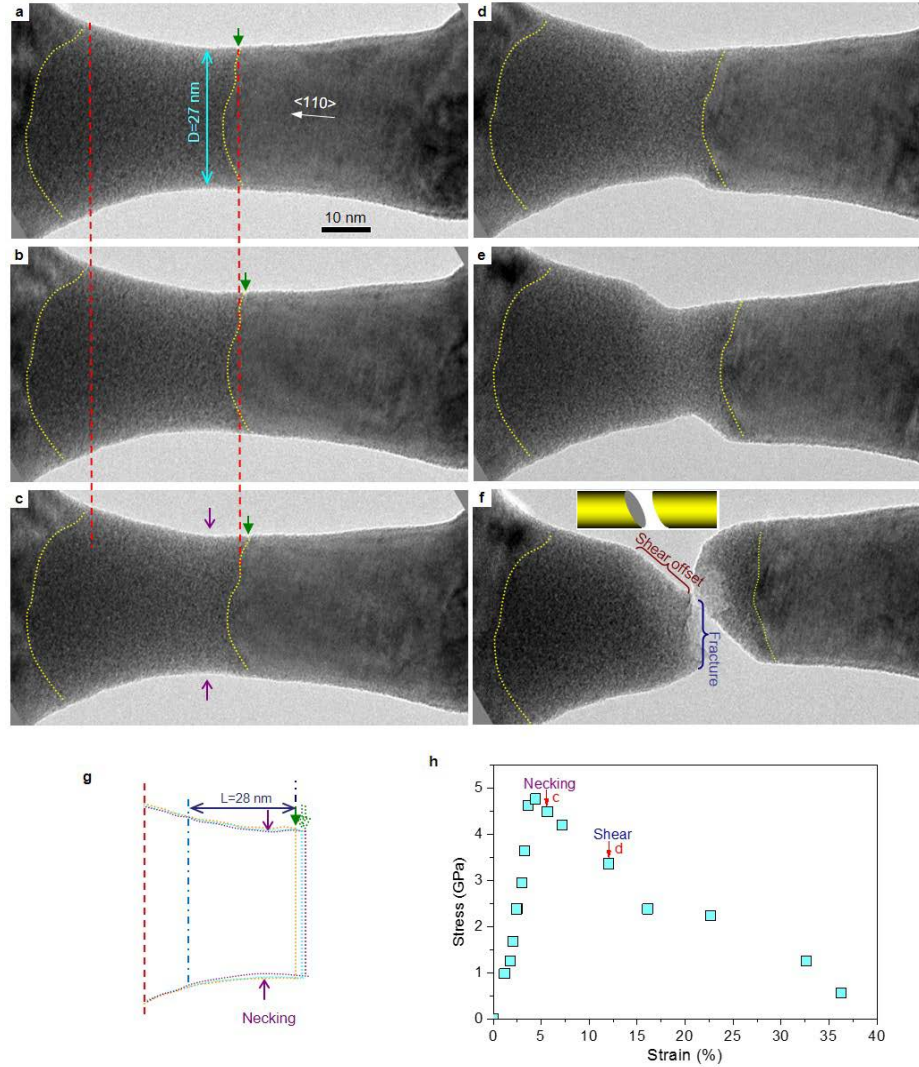


Figure 4.13 Shear-dominated deformation in Ta MG under a strain rate of 10^{-3} s^{-1} . (a) A hybrid Ta nanowire with the left half being Ta MG and the right half being bcc Ta. This hybrid nanowire was fabricated by forming a Ta MG nanowire at first, followed by controlled gradual crystallization to move one of the GCIs (outlined by yellow dotted curves) to the middle of the nanowire (marked by a green arrow), which is used as a reference for tracking the deformation of Ta MG. The strain rate was around $2 \times 10^{-3} \text{ s}^{-1}$. (b) Elastic deformation to a strain close to 5%. (c) Onset of necking shortly after yielding (pointed out by a pair of purple arrow heads). (d) Nucleation of a major shear. (e) Subsequent deformation through gradual growth of a shear offset along $\sim 52^\circ$ off the tensile loading direction. (f) Fracture at an overall strain of 37%. The inset is a schematic drawing of the non-edge-on shear plane. During the whole deformation, no plasticity has been observed in bcc Ta on the right. (g) Contours outlining the shape change of the Ta MG during deformation shown in (a-c) (marked by yellow, cyan and purple contours, respectively). The deformed region in Ta MG is measured to be 28 nm. (h) Stress-strain curve estimated by using crystalline Ta as a strain gauge. The red arrows marked the data points collected from (c) and (d), which correspond to the onset of necking and shear localization, respectively.

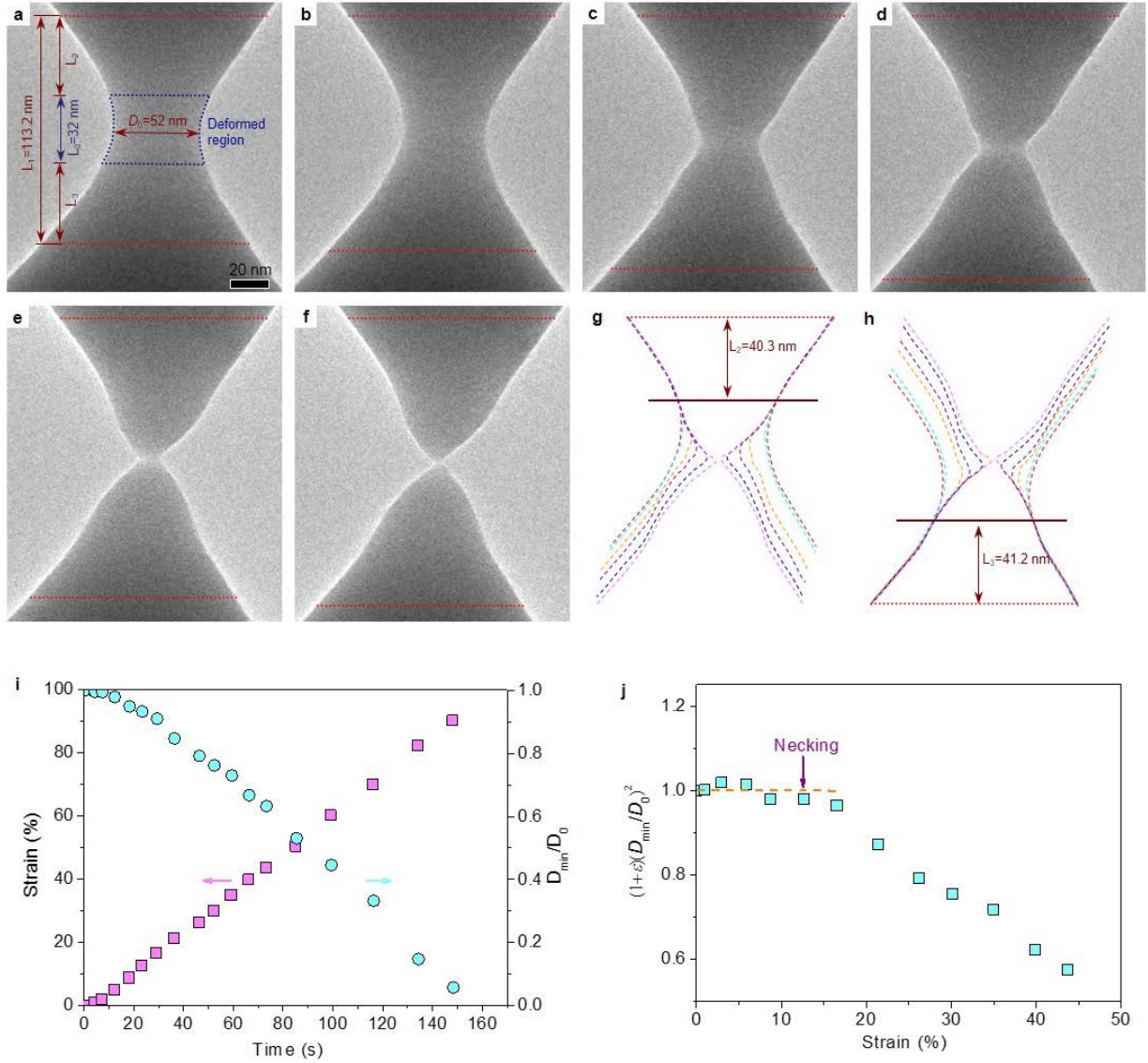


Figure 4.14 Completely ductile necking in Pd₇₉Ag_{3.5}P₆Si_{9.5}Ge₂ MG under a strain rate of $6 \times 10^{-3} \text{ s}^{-1}$. (a) A 52-nm-wide pristine Pd-based MG formed by applying a transient electric pulse on two contacting nanotips. (b) Uniform deformation of the Pd-based MG. (c-f) Completely ductile necking throughout the deformation process. (g-h) Contour evolution during deformation. The length of the deformed region is $L=L_1-L_2-L_3=32$ nm. The contour of the deformed region is outlined by blue dotted lines in (a). (i) Strain (magenta squares) and diameter change (cyan circles) with respect to time. D_0 and D_{\min} represent the minimum diameter of the MG before and during deformation, respectively. (j) $(1+\epsilon)(\frac{D_{\min}}{D_0})^2$ as a function of the overall strain (ϵ). According to equations (4.1) and (4.2), the onset of necking is estimated to be around a strain of 12%.

<110> direction. The stress dropped rapidly after yielding due to the lack of hardening and shear transformation induced softening after the onset of shear banding²⁴⁸.

Unlike Ta MG, a 52-nm-wide Pd₇₉Ag_{3.5}P₆Si_{9.5}Ge₂ MG (referred to as Pd-based MG hereafter) showed extraordinary ductility during deformation. The deformed segment of the Pd-based MG (outlined by blue dotted lines in Figure 4.14a) is identified by tracking the contour change during deformation (Figure 4.14g-h), the length of which is estimated to be about 32 nm. Necking initiated at the early stage of deformation (Figure 4.14c), and proceeded in a completely ductile manner until it was drawn to a point (Figure 4.14d-f). The final strain reached up to 90% (magenta squares in Figure 4.14i), which was accompanied by continuous diminishing in the neck width until it reached zero (cyan circles in Figure 4.14i), indicating an extremely large true strain near the tip region. Due to the non-uniform diameter of the Pd-based MG, the amount of uniform deformation before the onset of necking is not straightforward. During uniform elongation, the diameter and length change accordingly, following a relationship of

$\frac{L_0}{L} = \left(\frac{D_{\min}}{D_0}\right)^2 = \frac{1}{1 + \varepsilon}$, where L_0 and D_0 are the original length and diameter in the narrowest site (Figure 4.14a), while L and D_{\min} represent the length and smallest diameter after deformation.

Therefore, we have:

$$(1 + \varepsilon) \left(\frac{D_{\min}}{D_0}\right)^2 = 1 \quad (4.1)$$

However, after necking, localized deformation causes rapid decrease in D_{\min} , leading to

$$(1 + \varepsilon) \left(\frac{D_{\min}}{D_0}\right)^2 < 1 \quad (4.2)$$

According to equations (4.1) and (4.2), the amount of uniform deformation that the Pd-based MG has carried before necking is about 12% (Figure 4.14j).

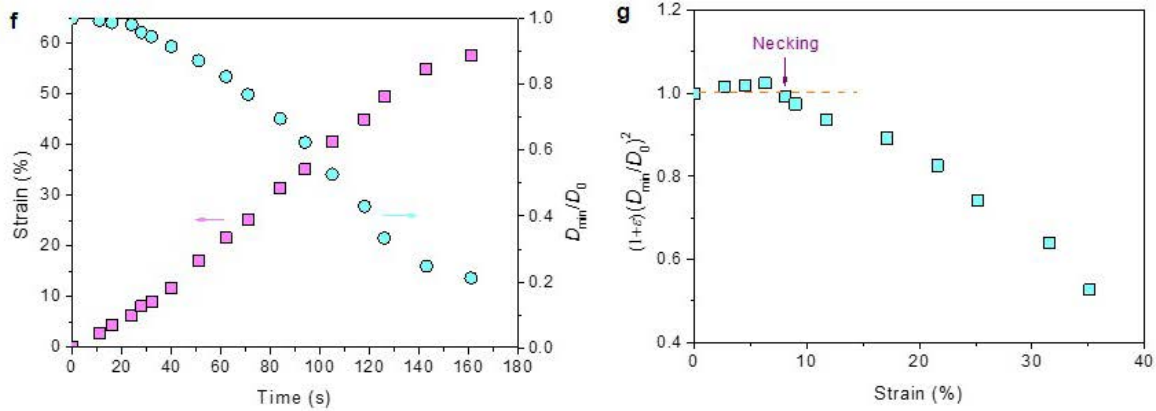
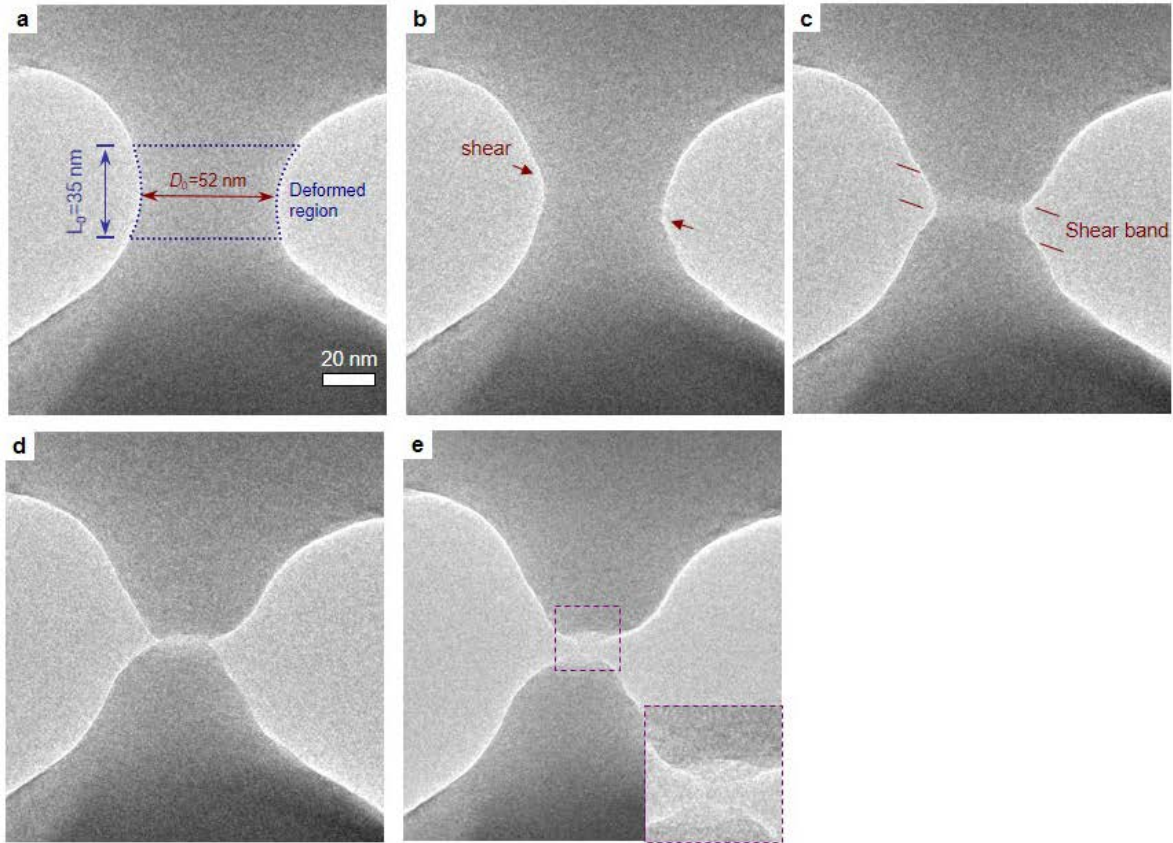


Figure 4.15 Necking in a sense of shear in $\text{Cu}_{50}\text{Zr}_{50}$ MG under a strain rate of $3.5 \times 10^{-3} \text{ s}^{-1}$. (a) Pristine $\text{Cu}_{50}\text{Zr}_{50}$ MG with a diameter of 52 nm and a deformed length of 35 nm. (b-c) Early necking in a sense of shear, where necking proceeded inside a shear band. (d-e) Fracture before being drawn to a point. The inset in (e) is a close-up view of the both tips after fracture. (f) Strain (magenta squares) and diameter change (cyan circles) with respect to time. D_0 and D_{min} represent the minimum diameter of the MG before and during deformation, respectively. (g) Strain at which necking sets in is estimated to be 8% based on equations (4.1) and (4.2).

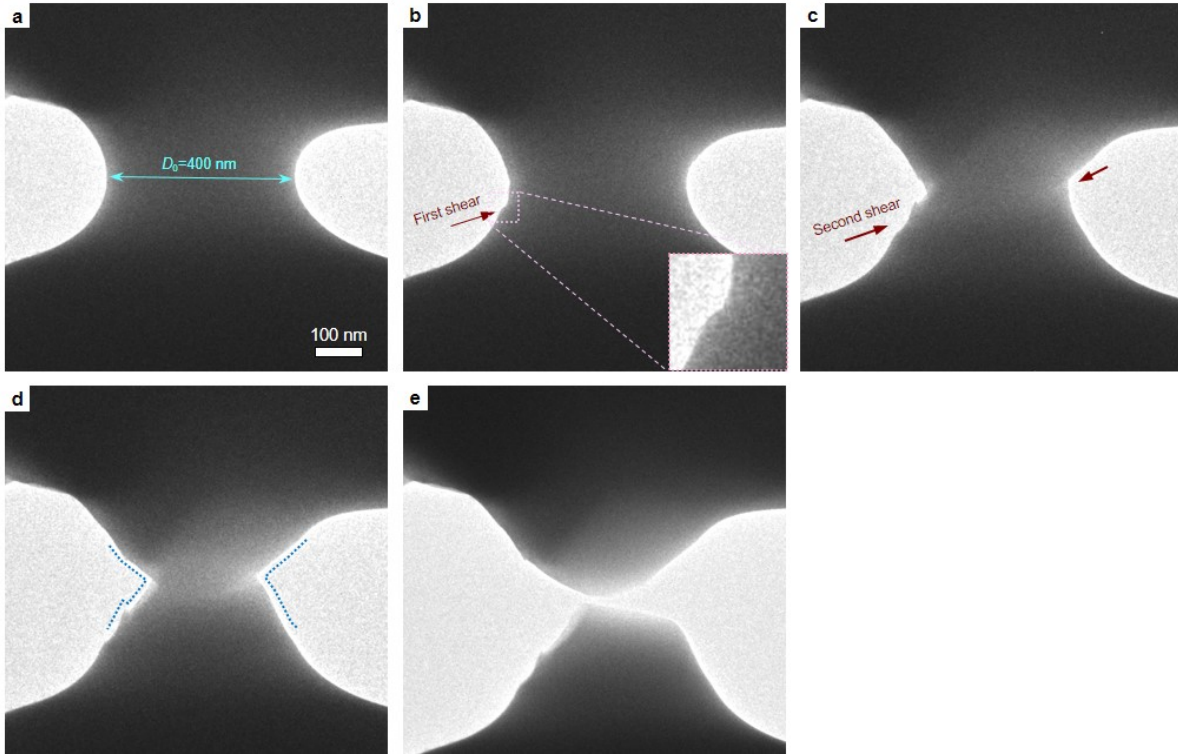


Figure 4.16 Shear localization in Pd-based MG with ‘large’ size under a strain rate of $6 \times 10^{-3} \text{ s}^{-1}$. (a) Pristine Pd-based MG with a diameter of 400 nm. (b-c) Nucleation of multiple shears at the early stage of deformation. The inset in (b) is a close-up view of nucleation of the first shear. (d-e) Fracture by shear along a non-edge-on plane, as evidenced by the abrupt contour of the necking region (outlined by blue dotted curves).

The tensile behavior of a 52-nm-wide $\text{Cu}_{50}\text{Zr}_{50}$ MG was also investigated as shown in Figure 4.15. Necking initiated much earlier compared to the case in Pd-based MG, imparting very limited uniform elongation (Figure 4.15b). Interestingly, necking in $\text{Cu}_{50}\text{Zr}_{50}$ MG proceeded in a sense of shear, which developed inside a shear band (Figure 4.15b-c). Such necking was not completely ductile (Figure 4.15d), and the $\text{Cu}_{50}\text{Zr}_{50}$ MG fractured before being drawn to a point (Figure 4.15e). By using the same approach introduced in Figure 4.14j, we found that the overall strain before fracture reached 57% (Figure 4.15f), and that necking initiated at a strain of 8% (Figure 4.15g).

Size-dependent ductility was observed in all three MGs, which decreases with increasing specimen dimension. A switch in the deformation mode from ductile necking to localized shear was observed in a Pd-based MG with a diameter of 400 nm (Figure 4.16).

4.4 DISCUSSION

4.4.1 Minimization of possible contaminations

The vitrification of pure metallic liquids reported here should not be attributed to the enhanced glass forming ability associated with impurities in the original materials (Table 3.1) and/or oxygen contamination during experimental procedures (Figure 4.17). Some studied materials, such as tantalum, are reactive with the atmosphere, especially oxygen. Here, we made special effort to minimize such contaminations by carrying out our experiment under helium or high vacuum protection and by deoxidization before the liquid-quenching experiment.

First, specimens were prepared and transferred to the microscope in a helium-protected environment with oxygen content below 1 ppm. The specimens were then inserted into the TEM with less than two seconds of exposure to the air. During this short period, oxygen contamination is limited to surface adsorption, as evidenced by the lack of an amorphous oxidation layer on the specimen surface (Figure 4.18). Oxygen absorption on clean Ta surfaces at room temperature was reported to be a self-limiting process where the absorption rate drops exponentially with respect to increasing oxygen coverage²⁴⁹. Therefore, it is expected that limited amount of oxygen is absorbed by our specimen during the specimen loading process.

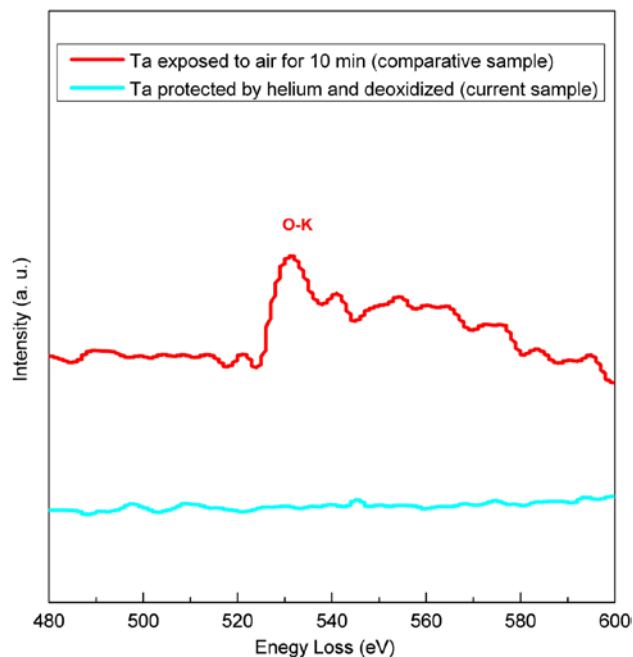


Figure 4.17 Electron energy-loss spectroscopy spectra of oxygen in tantalum²²⁵. An oxygen K-edge was identified around 530 eV energy loss from tantalum that was exposed to air for approximately 10 minutes (red curve). In contrast, no O K-edge was detected in both Ta MG and crystal (cyan curve) when the Ta nano-tips were processed in a helium-protected environment and deoxidized by Joule heating before the liquid-quenching experiment, indicating that the oxygen concentration in the Ta MG was below the detection limit of EELS, which is ~1000 ppm in atomic ratio²⁵⁰ (i.e., ~100 ppm in weight percentage).

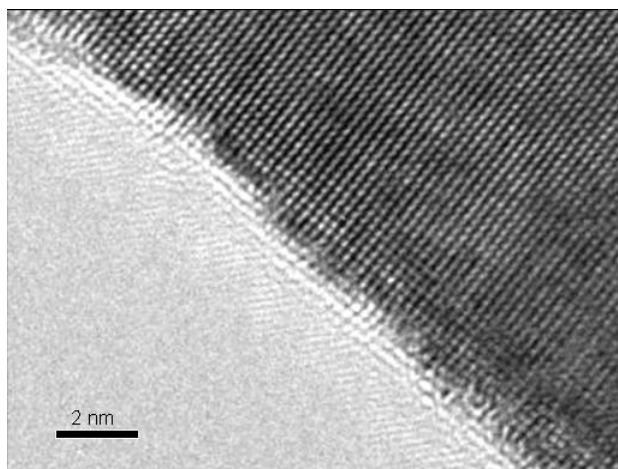


Figure 4.18 High-resolution TEM image showing the clean surface of an original Ta nano-tip specimen²²⁵.

Once specimens are inside the TEM column ($\sim 10^{-5}$ Pa), oxidation becomes negligible as evidenced from the following estimation. If we assume the sticking probability of oxygen molecules is 1.0 (that is, oxygen molecules attach to the surface as soon as they hit the specimen), oxygen adsorption rate can be obtained by calculating the collision frequency between the oxygen molecules and the specimen surface.

In high vacuum as such, the oxygen partial pressure is as low as 2×10^{-6} Pa, in which case the interactions between oxygen molecules are weak. Therefore, oxygen can be treated as an ideal gas. According to $p = nk_B T$, where p is oxygen partial pressure, n is the density of oxygen molecules, k_B is Boltzmann constant, and T is temperature, oxygen molecule density inside the TEM column can be represented as

$$n = p/k_B T. \quad (4.3)$$

According to the Maxwell-Boltzmann distribution theory, the mean speed of oxygen molecules is $\langle v \rangle = \sqrt{\frac{8RT}{\pi M}}$, where R is the gas constant and M is the molar mass of oxygen molecules. In the scenario where collisions occur between oxygen molecules and a flat surface, only the speed along the normal direction of the surface (i.e., x direction) should be considered. Therefore, the mean speed should be recast as

$$\langle v_x \rangle = \frac{2}{\pi} \sqrt{\frac{8RT}{\pi M}}. \quad (4.4)$$

Since oxygen molecules have an equal possibility to travel along all directions, only half of the oxygen molecules move towards the surface. Hence the collision frequency Z on a unit surface area can be calculated as

$$Z = \frac{1}{2} n \langle v_x \rangle. \quad (4.5)$$

Replacing n and $\langle v_x \rangle$ with equations 4.3 and 4.4, we obtain

$$Z = \frac{p}{k_B T \pi} \sqrt{\frac{8RT}{\pi M}}. \quad (4.6)$$

Under a partial pressure of 2×10^{-6} Pa and temperature of 300 K, Z equals 2.16×10^{15} collisions \cdot s $^{-1} \cdot$ m $^{-2}$. Under such a collision rate and a dimension of 85 nm \times 40.8 nm \times 13.6 nm (the size of the tantalum nanowire the computer simulation), approximately 20 collisions take place per second, corresponding to an increase of the oxygen content by 1.4 ppm (weight percentage). In the real experiment, the sticking probability for each collision is less than 1.0, which makes oxidation contamination even more trivial. During our ultrafast quenching experiment on the nanosecond scale, oxygen contamination of the specimens inside the TEM is deemed negligible.

An important procedure to lower the oxygen content is that the specimens were preheated by applying a current on the order of 100 μ A through the joined nano-tips to a temperature close to the melting point for half an hour before the melt-quenching experiment. Such heating in high vacuum expels oxygen from tantalum, which serves as an effective method to obtain tantalum free of oxygen^{45,46}. Although in some cases, complete removal of oxygen was reported to be difficult, the remaining proportion of oxygen is rather small²⁵¹. This is confirmed by electron energy loss spectroscopy where the oxygen K-edge is invisible in the specimen (Figure 4.17), indicating the oxygen concentration in the current specimen is below the detection limit of EELS (that is, below 1000 ppm in atomic ratio).

4.4.2 Opportunity for revealing the structure-ductility relationship in MGs

Superior mechanical properties, such as large accessible elastic strain²⁴⁷, high strength^{32,37}, uniform elongation^{32,252}, and ductile necking^{33,35,36,252} have been frequently reported in sub-

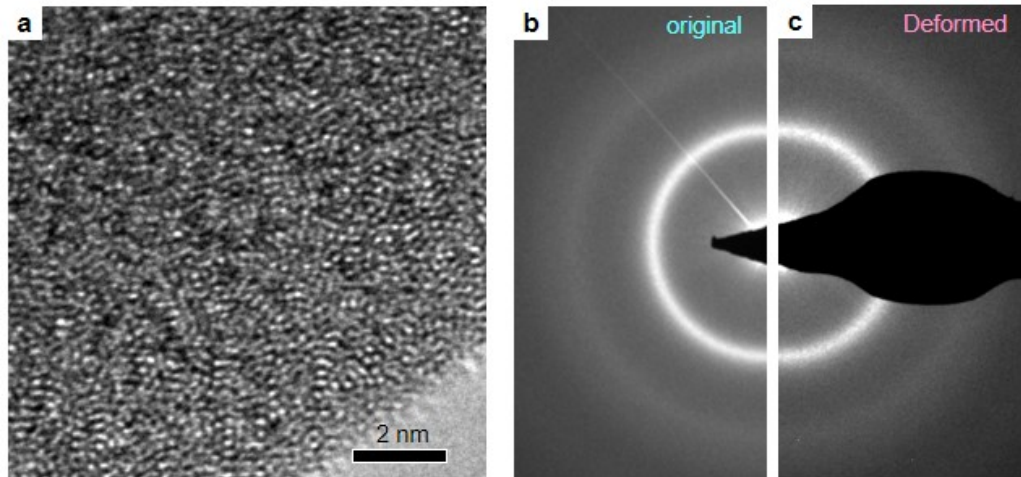


Figure 4.19 Glassy state throughout the deformation. (a) High-resolution TEM image showing a fully amorphous region after deformation. (b-c) Comparison of electron diffraction patterns of Pd-based MG before (b) and after (c) deformation, where no crystallization was identified.

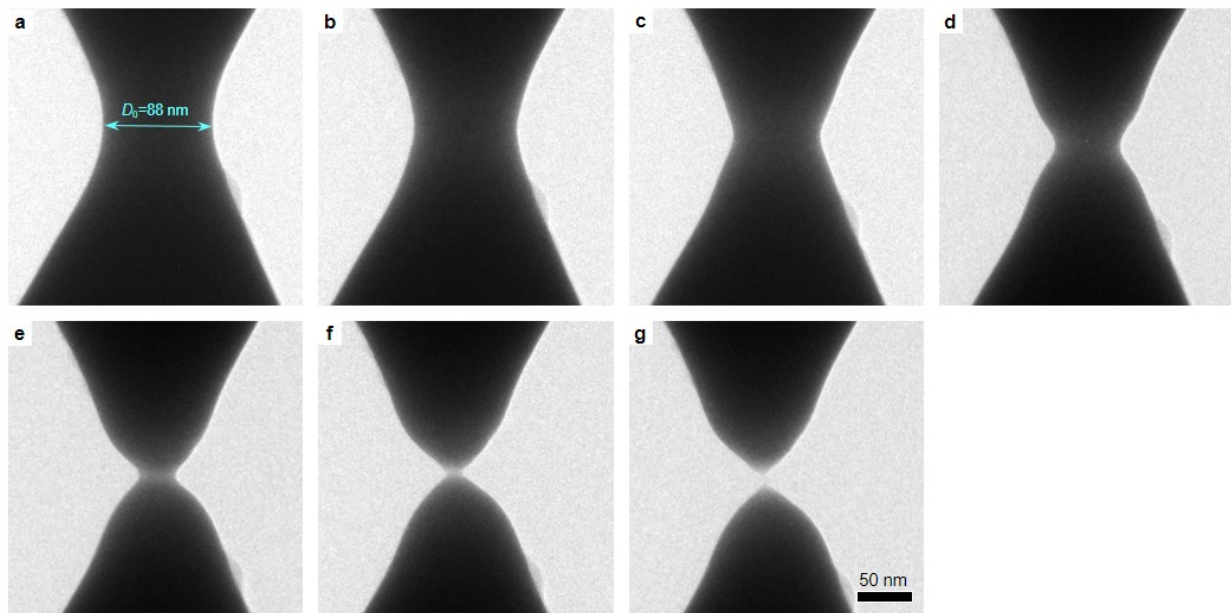


Figure 4.20 Completely ductile necking of an 88-nm-wide Pd-based MG under a strain rate of $3 \times 10^{-3} \text{ s}^{-1}$. The electron beam was blanked throughout the deformation except for recording images every dozens of seconds.

micrometer- and nanometer-sized MGs. However, most of the specimens investigated in previous researches were fabricated by FIB milling^{32,35-37,247}, which is widely known to introduce surface contamination and damage. These extrinsic factors may significantly impact the mechanical behavior of nanosized MGs^{253,254}, therefore complicating the task to gain a fundamental understanding of their intrinsic mechanical properties^{254,255}. Moreover, FIB-fabricated specimens usually have a lower size limit around 100 nm, while further reducing the size is associated with technical difficulties. Here, we demonstrate an experimental approach that overcomes this difficulty and produces extremely small MGs with clean surfaces, enabling an investigation on the intrinsic size-dependence of the mechanical property with accessible sizes covering the entire sub-100-nm regime.

The enhanced ductility observed here cannot be attributed to shear-induced crystallization, which is evidenced by the fully glassy state throughout the deformation process (Figure 4.19). Although electron-beam has been reported to induce super-plasticity in amorphous silica via a bond-switch mechanism, its impact on MGs, however, is expected to be less severe due to the more flexible bonds in MGs (that is, metallic bonding) compared to those in silica glass (that is, ionic bonding). Nevertheless, a low dose electron beam on the order of 10 Acm^{-2} was used throughout the tensile tests in order to minimize possible beam impact. Moreover, tensile tests with electron beam being blanked except for recording images every dozens of seconds have been carried out, where MGs demonstrated identical tensile behaviors compared to those under electron beam exposure. As shown in Figure 4.20, an 88-nm-wide Pd-based MG can be drawn to a point without exposure to the electron beam, indicating that the size dependence of ductility observed in this work is an intrinsic property of MGs. Although the large fracture strain reached in this work is very likely due to the short gauge length, the observed deformation mode (i.e.,

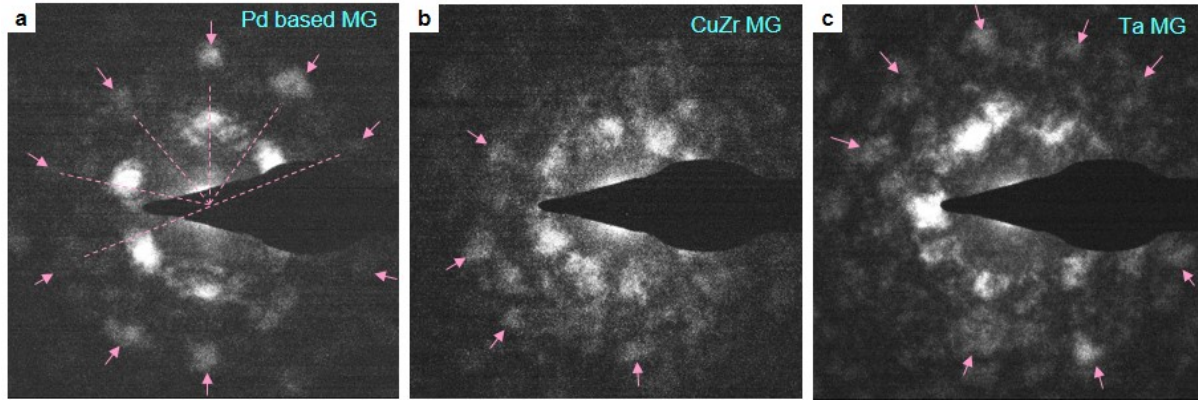


Figure 4.21 Local symmetry of MGs obtained by nanobeam diffraction. Some diffraction spots on the second diffraction ring are highlighted with magenta arrow heads. Pd-based MG exhibits a relatively well-defined 5-fold symmetry compared to the CuZr (b) and Ta (c) MGs.

shear versus ductile necking) provides important insights into the intrinsic ductility of the MGs. Indeed, similar ductile necking has been reported in another Pd-based MG (that is, $\text{Pd}_{40}\text{Cu}_{30}\text{Ni}_{10}\text{P}_{20}$) in the form one dimensional fibers²⁵².

Despite all superior properties of bulk MGs, their applications are usually limited by very small amount of plasticity, if at all. Therefore, gaining a fundamental understanding of the mechanisms governing ductility is of great significance. The ductility of bulk MGs has been related to their elastic stimuli²⁵⁶, where a relatively small elastic shear modulus compared to bulk modulus, and thus a large Poisson's ratio, facilitates shear over dilatation, therefore imparting better plasticity^{104,105,141,257,258}. On the other hand, the better ductility of nanosized MGs compared to their bulk counterparts is often explained as a consequence of suppressed shear band nucleation³⁵⁻³⁷. Though suggestive, both theories remain to be elucidated in terms of the atomic-scale origin of ductility, which is intrinsically related to the local atomic arrangements in MGs^{122,259-261}. Indeed, the tested three MGs that show distinctive ductility also exhibit different local structures, where Pd-based MG demonstrates a better-defined 5-fold symmetry compared to the other two MGs (Figure 4.21). Since the deformation of MG is carried by the operation of

shear transformation zones (STZs)^{262,263}, it is conceivable that the local atomic arrangements will affect the property of STZs and, consequently, the ductility of MGs. Moreover, the atomic-level structure of MGs are not only dictated by their compositions^{118,264}, but also impacted by how fast they are vitrified from the melts¹²². Therefore, with the ability to integrate glass-forming, phase-characterization and mechanical-testing, the present work opens up a new opportunity to interrogate the connection between microstructure and the intrinsic mechanical properties of MGs. Although a clear relationship between them is yet to be uncovered, our work is the first step towards this ultimate goal.

4.5 CONCLUSIONS

A methodology that achieves an ultrafast liquid quenching rate of 10^{14} Ks^{-1} has been developed in this chapter, with which we successfully vitrified monatomic metallic melts and obtained single-element MGs from bcc metals. The forming condition and thermal stability of the as-obtained monatomic MGs were revealed to be determined by the competition between vitrification and crystal growth. The breakthroughs in obtaining monatomic MGs and manipulating their phase behavior are important to both scientific research and technological applications.

The formation of monatomic MGs opens up new opportunities to study the structural dependence of the rheological, thermal, electric, and mechanical properties of MGs, where complications due to chemical effects in multi-component MGs can be isolated. By reaching deep quench under an ultrafast cooling rate, the current work has the potential to advance the fundamental understanding of the fast kinetics and structural properties of supercooled liquids. In

addition, this ultrafast liquid-quenching methodology is a technological break-through in making nano-scale MGs with tunable dimensions. The controllable phase-change phenomenon is promising for micro-electro-mechanical applications, such as phase-changing-based memristors and rewritable data storage devices.

An intrinsic size dependence of ductility was revealed, where MGs with small size can sustain more uniform elongation and deform via ductile necking without catastrophic failure caused by cavitation. More importantly, the current methodology opens up new opportunities to gain a fundamental understanding of the connection between local atomic arrangements and the intrinsic mechanical properties of MGs.

5.0 IN-SITU TEM OBSERVATION ON LITHIATION/DELITHIATION OF TIN DIOXIDE NANOWIRES

In this chapter, the morphological and microstructural evolutions during lithiation/delithiation of individual SnO₂ NWs are revealed at atomic-scale resolution. We report here the successful construction of a nanoscale electrochemical device consisting of a single SnO₂ nanowire anode, an ionic liquid electrolyte, and a bulk LiCoO₂ cathode in a transmission electron microscope. Upon charging, a reaction front propagated progressively along the nanowire, inducing large plastic deformation in the nanowire. A region with a high density of dislocations was identified at the reaction front, where dislocations were continuously nucleated and absorbed at the moving reaction interface. This region is named as ‘dislocation cloud’, which indicates large in-plane misfit stresses and is found to be precursor for electrochemically-driven solid-state amorphization. Because mechanical degradation induced by large volume expansion, plasticity and pulverization of electrode materials during lithiation/delithiation is an important drawback that plagues the performance and lifetime of batteries, our observations provide important implications for the design of advanced batteries.

The atomic scale lithiation mechanism of individual SnO₂ NWs in a flooding geometry with the entire nanowires being immersed in the electrolyte was also revealed by in-situ transmission electron microscopy. Lithiation was initiated by formation of multiple stripes with width of a few nanometers parallel to the (020) plane traversing the entire wires, serving as

multiple reaction fronts for subsequent lithiation. A high density of dislocations and enlarged inter-planar spacing were identified inside the stripes, which provided effective paths for lithium ion transport. The density of the stripes increased with further lithiation, and eventually they merged with one another, causing a large elongation, volume expansion, and the crystalline to amorphous phase transformation. This lithiation mechanism characterized by multiple stripes and multiple reaction fronts was unexpected and differed completely from the expected core-shell lithiation mechanism.

5.1 INTRODUCTION

LIB is one of the most important energy storage devices for hybrid vehicles and portable electronic devices. The next generation of LIBs requires higher capacity, higher power and better cyclability^{45,71,265,266}. However, the performance of LIBs is often plagued by mechanical degradation during electrochemical cycling, including crack, pulverization of the electrode materials and loss of contact between the effective materials and current collectors^{52,53}. Several in-situ techniques, including SEM^{193-197,267}, synchrotron XRD^{167,198}, synchrotron XAS^{119,120}, Raman spectroscopy²⁰⁴, mass spectroscopy²⁰⁵⁻²⁰⁷, and NMR spectroscopy^{176,208}, have been applied to track the structural evolutions of electrode materials during battery operation. Unfortunately, these in-situ techniques fall short of revealing the detailed mechanisms of mechanical degradation, such as strain induced plasticity and strain accommodation, due to either limited spatial and temporal resolution, and the thus lack of ability to visualize the atomic-scale electrochemical processes at real time.

It has been recently reported that electrodes consisting of nanowires demonstrate improved performance and reliability compared to those composed of micron-sized or bulk electrode materials^{47,268-278}. These improvements may be due to the unique one-dimensional geometry of the NWs that shows enough flexibility to accommodate the large volume change during battery operation^{47,279}. In order to reveal the mechanism of such strain accommodation, in-situ TEM study was performed on lithiation/delithiation of SnO₂ NW anode.

5.2 EXPERIMENTAL APPROACHES

To create the test cell, an individual SnO₂ nanowire was attached to a gold rod, which was further attached to a piezo-manipulator. Prior to insertion into the TEM, a drop of ILE [lithium bis (trifluoromethylsulfonyl) imide (LiTFSI) dissolved in 1-butyl-1-methylpyrrolidinium bis (trifluoromethylsulfonyl) imide (P14TFSI)] was placed on the LiCoO₂ cathode surface. The ionic liquid is a molten organic salt with very low vapor pressure, enabling its use in the high vacuum ($\sim 10^{-5}$ Pa) inside the high-resolution TEM while still solvating and transporting Li ions effectively. After loading the battery components into the TEM, an SnO₂ nanowire was manipulated in-situ and partially inserted into the ILE droplet, completing the assembly of the battery (anode, electrolyte, and cathode) (Figure 5.1). When assembled in this manner, the battery is in its discharged state (i.e. with lithium residing in the cathode). The nanowire battery was charged by performing potentiostatic holds at different voltages (up to -4 V) with respect to the LiCoO₂ cathode. These potentials were chosen because the open circuit voltage of SnO₂ vs. LiCoO₂ is about -2.9 V^{280,281}.

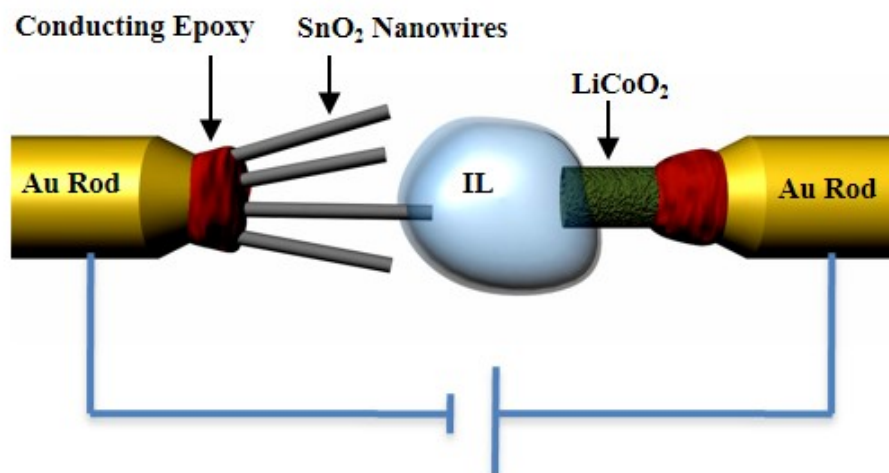


Figure 5.1 Building a nano-battery inside a TEM, which consists of a single SnO₂ nanowire anode, an ionic liquid electrolyte, and a bulk LiCoO₂ cathode²²⁰.

To minimize the effect of the electron beam impinging on the sample, the beam was “blanked” during the charging process except for very short exposures (~1 s) about every five minutes for the purpose of recording images. However, when recording a video, the beam was not blanked. No significant mechanistic differences were found between time lapse imaging with beam blanking and continuous imaging without blanking. In either case, an extremely low electron beam dose ($\sim 10^{-3} \text{ Acm}^{-2}$) was used to minimize possible beam damage artifacts.

Two configurations were applied in this chapter. The first one is in an end-contact geometry, in which the nanowire is barely immersed in the ILE. To create an environment that is close to that in real LIBs, a second configuration in a flooding geometry (i.e., side-contact), where the NWs are immersed in the electrolyte, was also considered.

5.3 EXPERIMENTAL RESULTS

5.3.1 Lithiation/delithiation of SnO₂ NWs in an end-contact geometry

The morphological and structural evolutions in a SnO₂ nanowire during lithiation are presented in Figure 5.2. The pristine NW was barely inserted into the ILE (Figure 5.2a), with a -3.5 V bias being applied to start the lithiation. The reaction started at the contact point between the ILE and NW by propagation of a single reaction front along the axial direction of the NW that continuously moving away from the ILE (pointed out by the small arrow heads) (Figure 5.2a-m). As the reaction front passed by, the NW elongated and became bent, twisted, and spiral, which indicated large plastic deformation and microstructural changes (Figure 5.2o-r). After lithiation for about half an hour, the NW showed up to 60% elongation, 45% diameter change, leading to a 240% volume expansion (Figure 5.2n).

A close-up view and detailed structure characterization at the reaction front are presented in Figure 5.3. The unreacted part was still single crystalline (Figure 5.3b) while the reacted segment right after the reaction front showed a dark grey featureless contrast with corresponding diffusive halos in the EDP (Figure 5.3d), typical of amorphous structure. Between the reacted and unreacted segments of the SnO₂ NW, the amorphous-crystalline interface (ACI) was featured by a high density of dislocations (Figure 5.3a), namely the dislocation cloud, and the EDP corresponding to this region was featured by a spots pattern superimposed on a diffuse scattered background. After further lithiation, the NW was composed of Sn (black indices in Figure 5.3e) and Li_xSn (orange indices in Figure 5.3e) alloy nanocrystals embedded in an amorphous Li₂O matrix (Figure 5.3f).

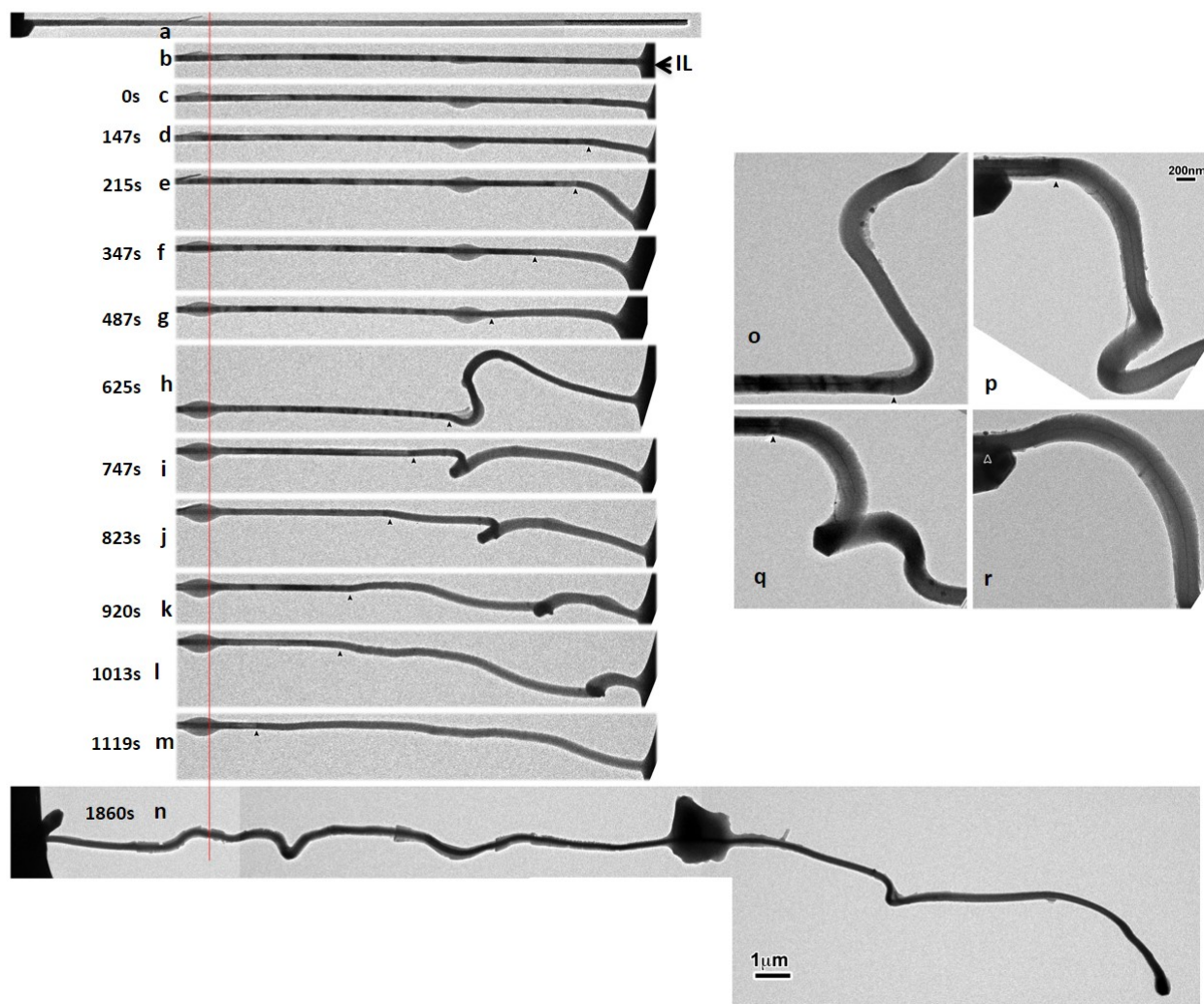


Figure 5.2 Time-lapse structure evolution of a SnO₂ nanowire anode during charging at -3.5 V against a LiCoO₂ cathode²²⁰. The initially straight nanowire (a-b) became significantly twisted and bent after charging (c-r). The chemical reaction front progressed along the nanowire's longitudinal direction, with the front clearly visible, as pointed out by arrowheads in (d) to (r). The red line in (a) to (n) marks a reference point to track the change of the nanowire length. (o) to (r) are sequential high-magnification images showing the progressive migration of the reaction front, swelling, and the twisted morphology of the nanowire after the reaction front passed by. The big dark particle in the middle of (n) is an island of gelled ILE. Because of the long cumulative electron beam exposure time during the recording of TEM images, the ILE front became gelled (with high viscosity) at this spot.

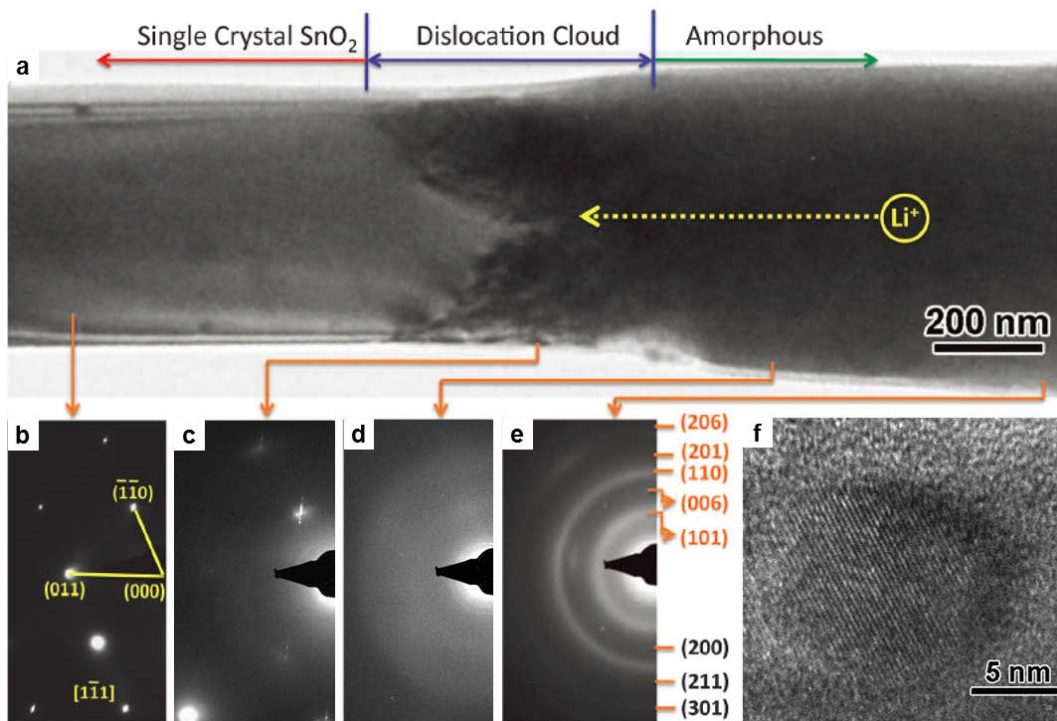


Figure 5.3 Structural and phase characterization of another SnO₂ NW anode during charging at – 3.5 V against the LiCoO₂ cathode²²⁰. (a) TEM micrograph of the nanowire containing a reaction front (dislocation cloud) separating the reacted (amorphous) and non-reacted (single crystal SnO₂) sections. (b-e) EDPs from the different sections of the nanowire. The pristine nanowire was single crystalline and the corresponding EDP (b) can be indexed as the [111] zone axis of rutile SnO₂. The EDP from the dislocation zone (c) shows a spot pattern superimposed on a diffuse scattering background. The EDP from an area immediately after the reaction front (d) shows an amorphous halo. The EDP from an area far away from the reaction front (e) shows diffraction rings superimposed on a diffuse amorphous halo. The diffraction rings can be indexed as tetragonal Sn (black indices) and a Li_xSn compound such as hexagonal Li₁₃Sn₅ (orange indices). (f) A high-resolution TEM image from a charged nanowire showing Sn nanoparticles dispersed in an amorphous matrix.

Unlike brittle bulk SnO₂, SnO₂ NWs showed large dislocation plasticity near the reaction. Although previous ex-situ TEM study has revealed a high density of dislocations in LiCoO₂ cathode after cycling²⁸², it lacks the ability to capture the dynamic dislocation nucleation and migration processes. Figure 5.4 demonstrates that the dislocations were continuously nucleated in crystalline SnO₂ at the vicinity of the ACI and then moved away driven by the high misfit stress at the reaction interface. At the meantime, they were also absorbed by the moving ACI

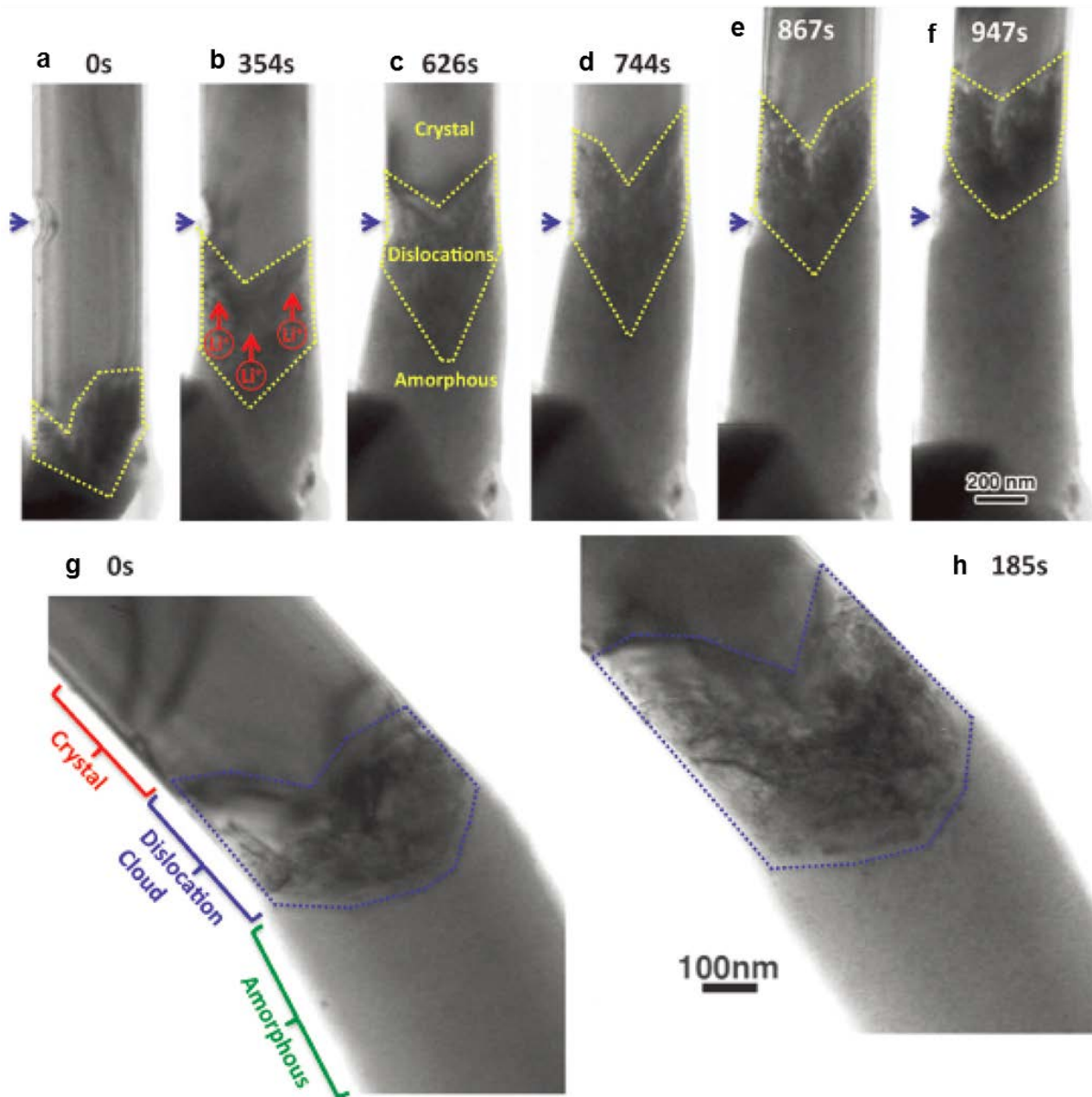
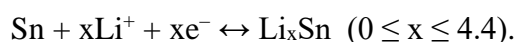
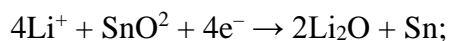


Figure 5.4 TEM images revealed a high density of dislocations emerging from the reaction front (marked by chevron-shaped dotted lines). As the dislocation front propagated, the crystalline contrast changed to gray amorphous contrast instantaneously, and the nanowire diameter increased immediately. (a-f) and (g-h) are two sets of time-lapsed TEM images showing the high density of dislocations that appeared at the reaction front and the migration of the reaction front²²⁰.

from behind²⁸³, thus maintaining a steady volume and a chevron shape in the moving dislocation cloud. Because the old dislocation sources were continuously removed by the advancing ACI, the high density of dislocations have to be emitted from the new dislocation sources continuously generated by the high stress at the reaction front, indicating that a stress close to the ideal strength²⁸⁴ of SnO₂ should exist at the ACI. The large discrepancy (that is, 45% radial expansion in the reacted segment with respect to the original crystalline segment) between the diameters of the reacted and unreacted segment at each side of the reaction interface would generate a large tensile stress near the ACI that leads to spontaneous dislocation nucleation on the unreacted side, as well as a large compressive stress on the reacted amorphous that induce plastic deformation on the amorphous side. The dislocation density in the dislocation cloud was estimated to be on the order of 10^{17} m^{-2} , which is about two orders of magnitude larger than that in heavily work-hardened fcc metals²⁸⁵. Such a high dislocation density drives the crystal far from its equilibrium state and leads to the collapse of the crystal lattices, therefore severing as a precursor toward amorphization.

Delithiation of the lithiated SnO₂ NWs was also performed, during which the Li_xSn alloy nanoparticles were converted back to pure Sn accompanied by a shrinkage in the diameter (Figure 5.5). However, further oxidation of Sn into SnO₂ was not observed, and the amorphous Li₂O matrix formed by the initial lithiation kept stable during the following delithiation processes, resulting in a much less prominent volume change compared to that during the first lithiation half-cycle. Namely, lithiation of SnO₂ is a two-step reaction, which can be expressed as:



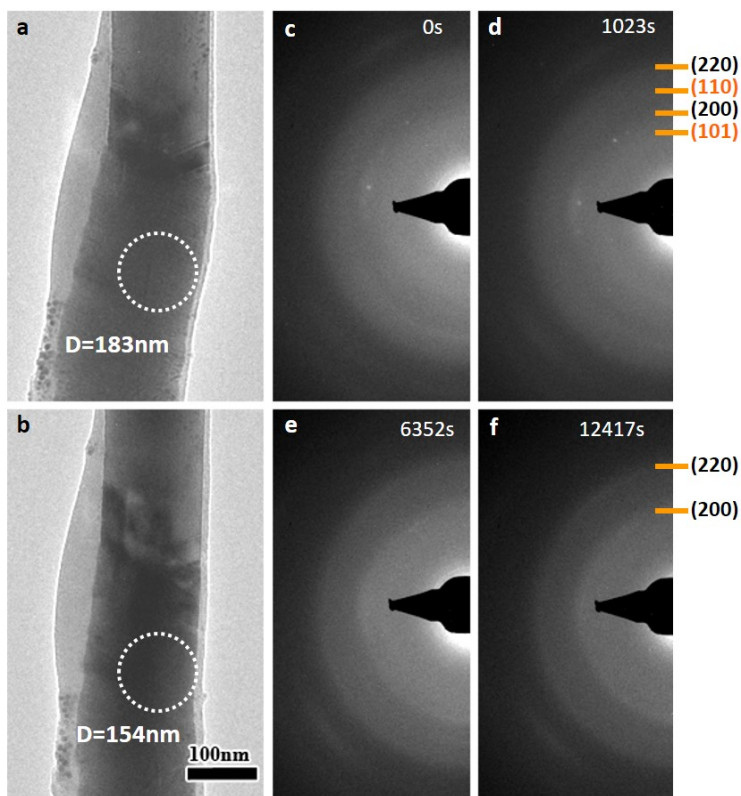


Figure 5.5 TEM images of a lithiated SnO₂ NW before (a) and after (b) delithiation²²⁰. The NW was biased at -0.05 V versus the LiCoO₂ cathode. (c-f) Time-lapse EDPs of the same area as outlined in (a) and (b), showing the structural evolution of the nanowire during delithiation. The initial nanowire consisted of Li_xSn, Sn and Li₂O (c and d). After 12417s of discharging, only Sn (diffraction rings in f) and amorphous Li₂O were present (amorphous halo in f). After discharging, the diameter of the NW was reduced from 183 nm to 154 nm.

5.3.2 Lithiation of SnO₂ NWs in a flooding geometry

The experiment above was conducted in an end contact geometry, in which the nanowire is barely immersed in the ILE (Figure 5.6a). In this setup, the main lithium ion transport channel is inside the nanowire and the reaction front is perpendicular to the nanowire axis. Due to the confinement of the reaction interface, the nanowire undergoes super-elongation (Figure 5.6b). However, in a real battery, the nanowires are immersed in the electrolyte. Then, what will happen in this flooding (i.e., side-contact) geometry (Figure 5.6c)? Will the mechanisms operate

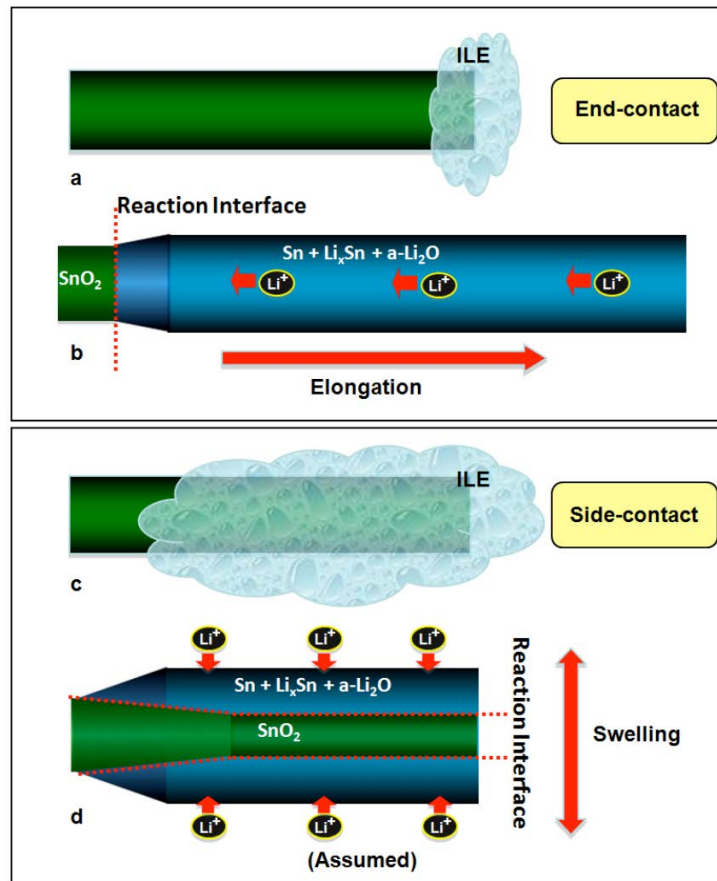


Figure 5.6 Schematic illustration of end-contact and side-contact configurations²⁸⁶.

in an end-contact geometry also operate in a flooding geometry? One guess is that since lithium ions diffuse through the side surface and the nanowire may form a core-shell structure with swelling rather than elongation (Figure 5.6).

To conduct experiments in a flooding geometry, one third of the nanowire was immersed in the electrolyte (Figure 5.7a). When lithiation started, the segment above the electrolyte showed typical lithiation process in an end-contact geometry, which was featured by elongation and a single reaction front propagating along the nanowire (Figure 5.7b-k). Surprisingly, the flooded segment showed similar morphology with large elongation at the ILE was retracted (Figure 5.7l). The EDPs from the non-flooded (Figure 5.7m) and flooded (Figure 5.7n) segments

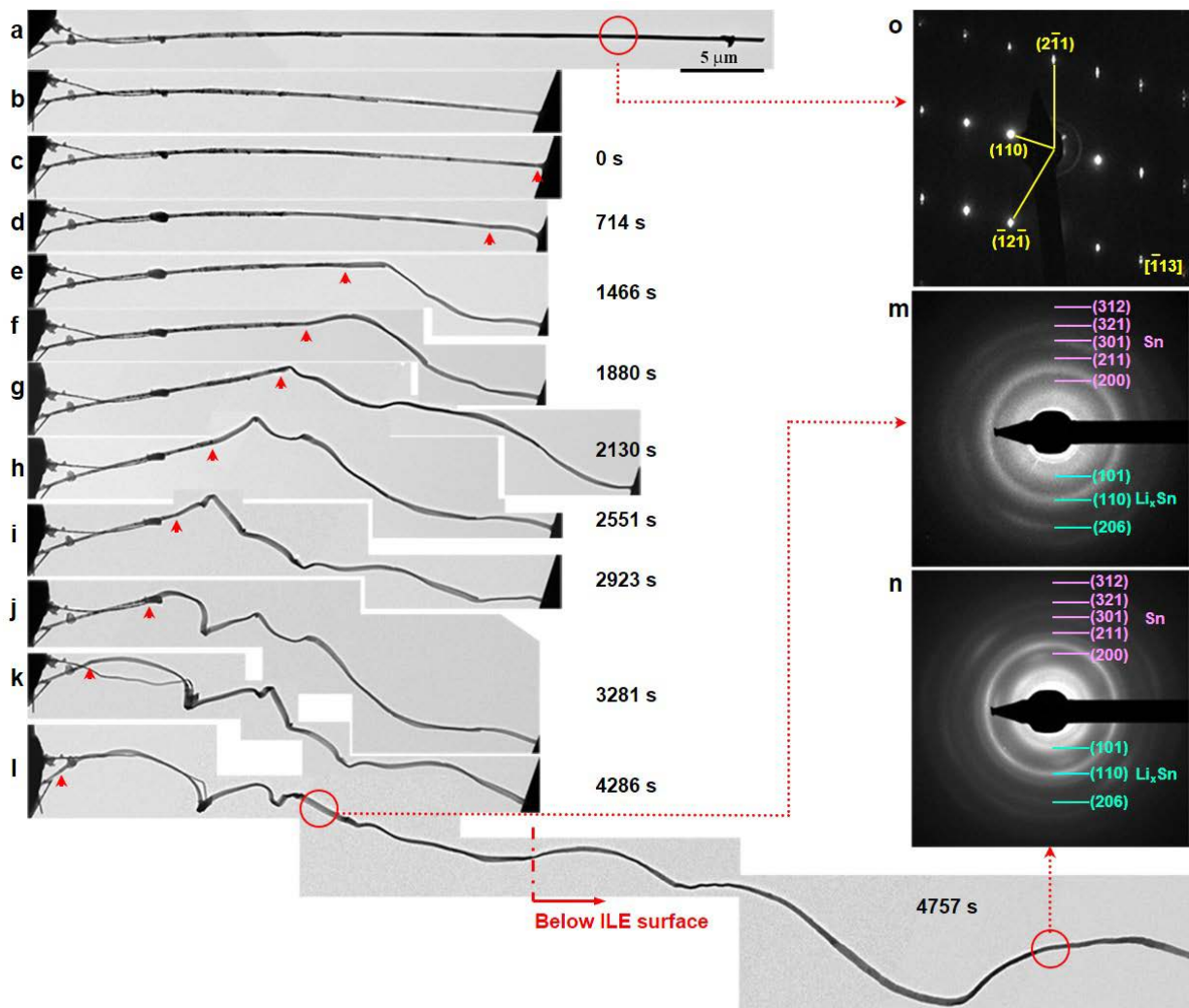


Figure 5.7 Structural evolution of a SnO_2 NW anode in a flooding geometry during charging at -3.5 V with respect to the LiCoO_2 cathode²⁸⁶. (a) A 45- μm -long and 220-nm-thick pristine SnO_2 NW with single crystalline structure (o). (b) Flooding geometry in which about 1/3 of the NW was immersed in the ILE. (c-k) Sequential images showing the morphology change during charging. The reaction front (indicated by the red arrowheads) progressed continuously along the NW's axial direction. (l) Lithiated nanowire after the ILE was withdrawn. Similar morphology was observed for both the flooded and the nonflooded segments. The corresponding EDPs of nonflooded (m) and flooded (n) segments showed almost identical structure after lithiation.

also showed similar microstructure. This is in contrast with the assumed core-shell structure and the swelling in a flooding geometry (Figure 5.6d).

To explain this contradiction, lithiation was stopped at various intermediate stages and the ILE was retracted to inspect the structural evolution of the flooded segment. Figure 5.8 shows morphology and structure changes at different lithiation stages of several SnO₂ NWs in a flooding geometry. A pristine SnO₂ NW was smooth and straight, with a single crystalline rutile structure before lithiation (Figure 5.8a,g). After a -3.5 V bias was applied to the SnO₂ nanowire against a LiCoO₂ cathode, there were no detectable changes until after approximately 90 s, when a set of dark-contrasted stripes inclined 61° with respect to the side surface of the NW emerged (Figure 5.8b). After a few more seconds, the spacing between the stripes became smaller and there was dislocation contrast all over the NW (Figure 5.8c). These stripes were induced by lithiation. The EDP of the striped nanowire (Figure 5.8h) showed single-crystal diffraction spots superimposed on a diffuse scattering background caused by inelastic scattering originating from lithiation induced defects. These strips were likely nucleated from local surface regions with atomic scale defects and each traversed the entire NW. Upon further lithiation, the contrast of these stripes became blurred (red rectangle in Figure 5.8d). In the meantime, some weak arcs around the single-crystal diffraction spots emerged (Figure 5.8i) due to lithiation induced polycrystallization of the NW. With further lithiation (Figure 5.8e-f), the arcs around SnO₂ diffraction spots became much weaker (Figure 5.8j) and finally barely discernible (Figure 5.8k) and the whole nanowire was converted to a Sn, Li_xSn, and Li₂O amorphous matrix.

Figure 5.9a is the morphology of a SnO₂ nanowire with [011] growth direction at the initiation stage of lithiation, showing again multiple stripes inclined to the nanowire axis, and Figure 5.9b is a HRTEM image and an EDP of the same nanowire before lithiation. The stripes

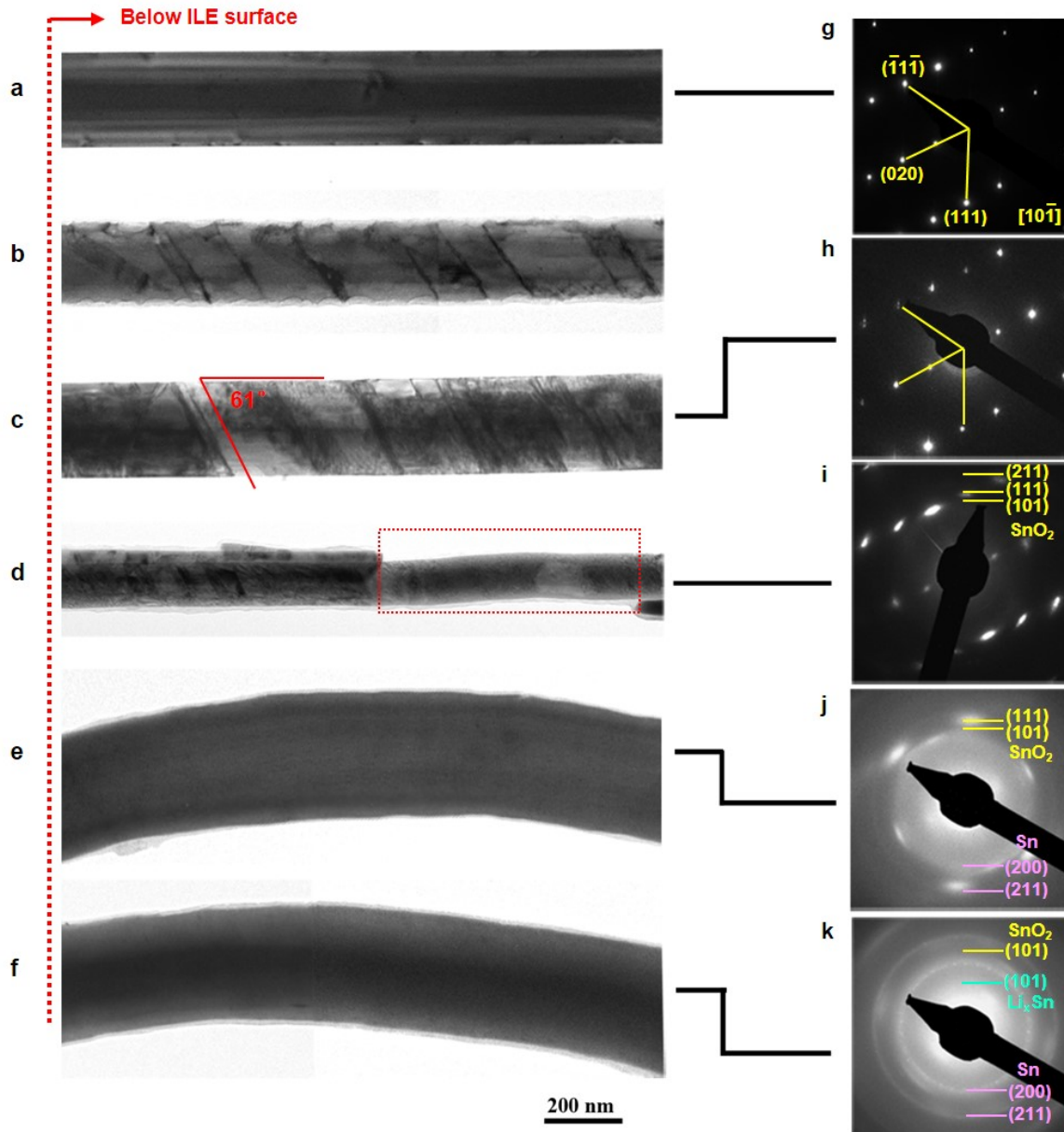


Figure 5.8 Multiple stripes formation in flooded SnO_2 nanowire anodes during charging at -3.5 V against the LiCoO_2 cathode²⁸⁶. (a) Pristine single crystalline nanowire and its corresponding EDP (g) which can be indexed to the $[10\bar{1}]$ zone axis of the rutile SnO_2 . (b-c) Multiple stripes formed after lithiation. A set of parallel stripes with dark contrast inclined 61° to the side surface of the nanowire. The corresponding EDP (h) showed single-crystal diffraction spots superimposed on a diffuse scattering background. Morphology (d-f) and the corresponding EDPs (i-k) after further lithiation. After further lithiation, the stripes disappeared completely and the nanowire underwent both elongation and swelling. The corresponding EDP (j-k) showed that the SnO_2 nanowire has been reduced to $\text{Sn}+\text{Li}_2\text{O}+\text{Li}_x\text{Sn}$. Note the images shown in (b-f) were captured from five different nanowires immersed in the ILE for different periods of time and were all viewed along the $[10\bar{1}]$ direction.

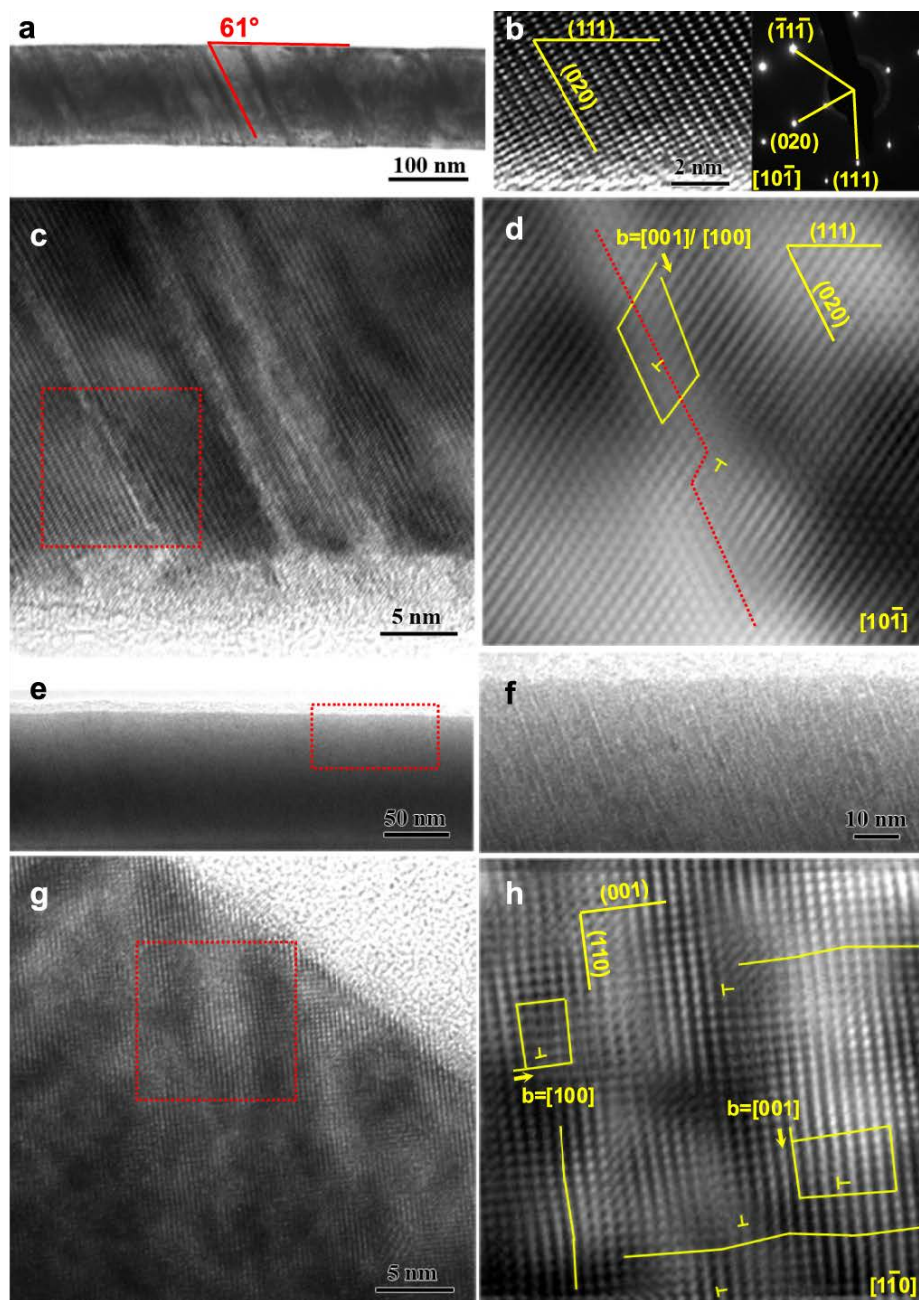


Figure 5.9 Microstructure of the lithiation induced multiple stripes in SnO₂ nanowires²⁸⁶. (a-b) Low and high magnification images of the charged (a) and pristine (b) nanowire. The nanowire was viewed along the $[10\bar{1}]$ zone axis. Stripes inclining 61° to the (111) planes of the nanowire are parallel to the (020) plane. (c-d) Raw and Fourier filtered HRTEM images of the multiple stripes. (d) High magnification image of the framed area in (c), showing dislocations with Burgers vector $[001]$ or $[100]$ in the stripes. (e-f) Images of the nanowire after further lithiation. (f) is a high magnification image of the framed area in (e), showing a high density of stripes formed after prolonged lithiation. (g-h) Raw and Fourier filtered HRTEM images of another nanowire after lithiation, showing a high density of dislocations with Burgers vectors of $[100]$ and $[001]$, and even disordering. The viewing direction was the $[1\bar{1}0]$ zone axis.

are parallel to the (020) plane, which is apparently the preferred lithium insertion plane. HRTEM images (Figure 5.9c-d) of the same nanowire showed lithiation induced dislocations in one of these stripes. Possible Burgers vector of the dislocations was determined to be [001] or [100]. The lithiation induced dislocation cores may act as fast lithium diffusion channels and may increase the lithiation kinetics²⁸⁷. Based on previous studies²⁸⁸⁻²⁹¹, [001] is the diffusion channel in a rutile structural crystal such as SnO₂. Therefore, the initial lithiation process can be interpreted as follows: lithiation initiated at some surface defects, continued along [001] direction in the (020) plane. The lithiation induced stress led to formation of dislocations along the stripes, which further facilitated lithium diffusion into the interior of the NW. The multiple-stripe formation process was rather quick and the density of stripes increased with progression of lithiation (Figure 5.9e-f). HRTEM images (Figure 5.9g-h) from another striped nanowire identified a high density of dislocations with Burgers vectors of [100] and [001]. The crystal lattice became indiscernible at some areas inside the stripes, indicating the beginning of the reaction to form Sn and amorphous Li₂O. The dislocation density was estimated to be $\sim 5 \times 10^{16} \text{ m}^{-2}$ based on Figure 5.9h, similar to that in the dislocation cloud observed in non-flooded NWs²²⁰. Therefore, lithiation-driven dislocation plasticity in the stripes occurred and was a precursor of the crystalline to amorphous phase transition.

Figure 5.10 shows the evolution in the lattice spacing during lithiation obtained from EDPs. When the stripes formed, the (020) diffraction spots were split into two (Figure 5.10c-d, and their insets). The brighter spot corresponded to a d-spacing of 2.36 Å, which matched well with the SnO₂ (020) plane, while the darker spot had a d-spacing of 2.43 Å, which was caused by lithiation induced lattice expansion (Figure 5.10c inset). With further lithiation, the spot from the pristine lattice became much weaker, and the brighter spot corresponded to a d-spacing of 2.49 Å,

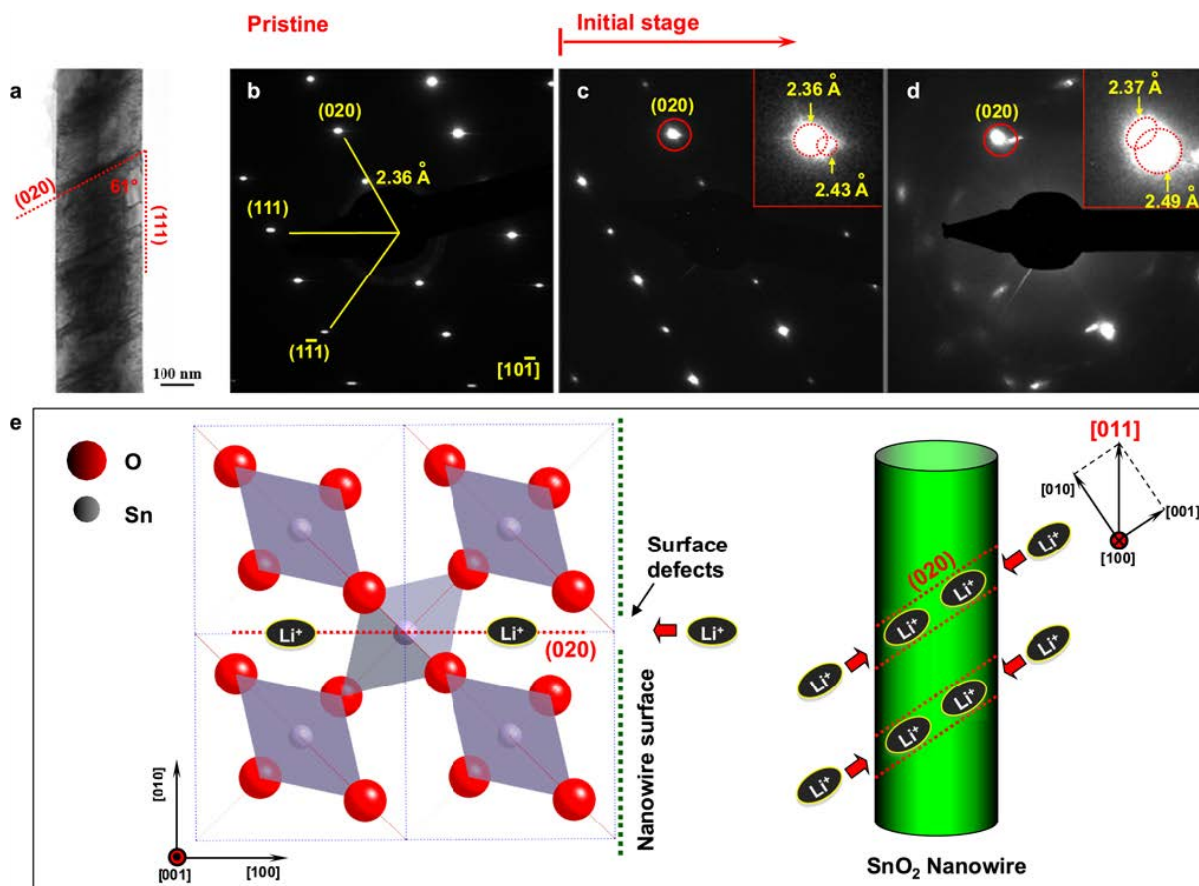


Figure 5.10 EDPs from the striped nanowire indicated lattice expansion caused by lithiation²⁸⁶. Structural evolution was viewed along the $[10\bar{1}]$ zone axis. (a) Stripes parallel to the (020) plane formed after initial lithiation. (b-d) The (020) diffraction spot was split into two with different d-spacings (insets in c and d), with the brighter spot corresponding to a d-spacing of 2.36 Å, matching that of the (020) plane in the pristine structure, while the darker spot having a d-spacing of 2.49 Å, indicating a 5.5% lattice expansion induced by lithiation. (e) Schematic illustration of lithium intercalation along [001] in the (020) plane in a side-contact geometry. The nanowire's growth direction is [011].

a ~5.5% increase with respect to the pristine structure (Figure 5.10d inset). It confirmed that the transverse (020) plane is the preferred lithiation plane, which may be ascribed to the side-contact geometry as shown in Figure 5.10e. Since (020) plane traverses the nanowire, lithium ions diffuse into the [001] channels in the (020) plane inside the nanowire through surface defects. The special one-dimensional geometry of nanowires plays an important role in this multi-stripe lithiation mechanism. The flexibility in the longitudinal direction and the small diameter

facilitate lithium insertion²⁹²⁻²⁹⁴, leading to easier lithium intercalation along (020) plane which traverses the nanowire.

5.4 DISCUSSION

Based on the different lithiation mechanisms in end-contact and side-contact geometries, we demonstrate that experimental configurations can play an important role in determining the mechanisms governing battery operation. An open-cell configuration in the current study allows real-time observation at atomic scale resolution with the capability of concurrent analytical TEM, such as EELS and EDS analysis. However, the choice for the electrolyte is key difficulty in performing an open-cell experiment, because most commercialized electrolytes have high vapor pressure, which cannot survive the high vacuum inside a TEM. Thus commercialized electrolytes have to be replaced by an ILE with ultralow vapor pressure. Moreover, an end-contact geometry is often associated with an open-cell configuration, which is not exactly the same as the electrochemical environment in real batteries, where the electrodes are fully surrounded by electrolyte. Although the use of a side-contact geometry can address this issue, the immersed part of the electrode materials is not visible, which can allow only a quasi-in-situ study. A liquid-cell configuration^{65,214-216,218,295-297}, on the other hand, allows in situ TEM observation on electrode materials that are immersed in real electrolytes, creating an electrochemical environment the same as that in real batteries. However it shows limited resolution compared to that in an open-cell configuration, and imposes difficulties on performing analytical TEM, such as composition analysis. Therefore, in-situ TEM studies complemented by both open-cell and liquid-cell configurations are of scientific and practical importance.

5.5 CONCLUSIONS

In-situ TEM observation on the lithiation/delithiation of SnO₂ NWs was performed in end-contact and flooding geometries, respectively. Lithiation of SnO₂ NW above the ILE is featured by a single reaction front propagating along the axial direction of the NW, accompanied by significant elongation and volume expansion. At the reaction front (i.e., the ACI), a region with a high density of dislocations was identified (i.e., the dislocation cloud), leading to large dislocation plasticity serving as a precursor towards ESA. In a flooding geometry, a unique multiple-stripe multiple-reaction-front lithiation mechanism was discovered, where preferred lithium insertion was found to induce multiple stripes along the (020) plane traversing the nanowire. Lattice expansion and dislocations were observed inside these stripes. This new lithiation process has important implications for the reaction mechanism in practical LIBs where the electrodes are immersed in electrolyte. In both configurations, the SnO₂ NWs successfully accommodate the large strain by elongation in the longitudinal direction without catastrophic failure, which can be attributed to the special 1-D geometry. The results in this chapter provide insights into a fundamental understanding of the plasticity and strain accommodation mechanisms inside SnO₂ NWs, and have significant implications for designing the next-generation LIBs with anode materials demonstrating large volume expansion and contraction during battery operation.

Although this work was carried out by selecting SnO₂ nanowires as a model material, the established methodology is applicable to many other electrode materials for both cathode and anode studies, and thus should provide important insights for a better understanding of the mechanisms governing battery performance and reliability.

6.0 IN-SITU OBSERVATION OF NON-EQUILIBRIUM SINGLE-PHASE LITHIATION IN ANATASE TITANIUM DIOXIDE NANOPARTICLES

In this chapter, the lithiation pathway in single crystalline and polycrystalline anatase TiO₂ NWs are successfully revealed by utilizing both in-situ electron diffraction and HRTEM. Although an equilibrium two-phase lithiation/delithiation path is thermodynamically favored, it requires the nucleation and growth of a second phase, and may thus not be kinetically preferred at the same time^{187,298}. On the other hand, a non-equilibrium single-phase reaction is believed to kinetically improve the reaction rate. However, the possibility of a single-phase reaction replacing a two-phase process is still not conclusive and under intense debate^{186-190,299-301} due to the difficulties in tracking the lithiation/delithiation processes at real time. Here, by conducting in-situ TEM observation, we show direct evidences that the lithiation of anatase TiO₂, previously believed to follow a two-phase reaction path³⁰²⁻³¹⁰, switches to a single-phase reaction with high a rate of 10–60 C when the crystal size goes down to ~20 nm. By demonstrating the significant size impact on the lithiation mechanisms in anatase TiO₂, our results indicate that the observed switch in the lithiation path may also take place in other intercalation compounds whose miscibility gaps are associated with a prominent size effect, therefore providing important guidelines for designing high-power electrodes, especially cathodes.

6.1 INTRODUCTION

An equilibrium two-phase lithiation /delithiation mechanism is quite prevalent among electrode materials for LIBs. For example, intercalation compounds³¹¹⁻³¹³, an important group of electrode materials in LIBs, tend to favor this pathway. These electrode materials exhibit limited bonding and structural modifications upon lithium intercalation/extraction, which tends to mitigate the mechanical degradation during cycling. However, their electrochemical performances are usually limited by their rate capability^{314,315} associated with the slow kinetics in a two-phase reaction mechanism (that is, to form a second phase upon lithiation/delithiation with an interface between the lithium-rich and lithium-poor phases). A non-equilibrium single-phase reaction path (that is, to form a solid solution during lithiation/delithiation) on the other hand, obviates the need for nucleation and growth of a second phase, and therefore may greatly improve the reaction rate. A single-phase reaction further excels in that without the coherency strain at the two-phase interface region, lithiation can proceed more homogeneously inside electrode materials, therefore alleviating the mechanical degradation during cycling. It has been reported that both the thermodynamics and kinetics during lithiation are sensitive to sample size¹⁸⁶. The question is: is this size dependence significant enough to cause replacement of a thermodynamically favored equilibrium two-phase reaction with a non-equilibrium single-phase reaction? And, if yes, what is the threshold size for such a switch to take place?

Although single-phase versus two-phase reaction has been widely discussed, no consensus has been reached. For example, Delmas *et al.*¹⁸⁷ believed that delithiation proceeds by fast migration of a two-phase boundary between the lithium rich and lithium poor phases; while Malik *et al.*¹⁸⁶ proposed a possible non-equilibrium single-phase reaction pathway. Therefore, an approach capable of tracking the electrochemistry at nanoscale is highly desirable. Here, by

conducting in-situ TEM observation on the lithiation of polycrystalline and single crystalline anatase TiO₂ NWs, we demonstrate the significant size impact on the lithiation mechanisms, and report a non-equilibrium single-phase lithiation pathway in anatase TiO₂ nanocrystallites with size of ~20 nm.

6.2 EXPERIMENTAL APPROACHES

To conduct in-situ TEM observation on the lithiation process inside anatase TiO₂ NWs, a nanoscale battery was assembled inside the TEM¹⁸⁰. A positive electrode was made by attaching polycrystalline or single crystalline anatase TiO₂ NWs to an aluminum rod with silver epoxy. This method allows good electrical conductivity between the TiO₂ NWs and the aluminum rod, which serves as a current collector. A tungsten rod was scratched against a lithium metal, so that a small piece of lithium metal was attached to the tip of the tungsten rod, serving as the negative electrode. Both the TiO₂ and lithium electrodes were mounted onto a Nanofactory TEM-STM specimen holder. All the above operations are conducted inside a helium filled glove box with very low content of oxygen and water (both below 1 ppm). Then, the STM holder was quickly transferred to the TEM in a sealed plastic bag filled with helium, which reduces the time of exposure to the air to less than three seconds. A thin surface layer of lithium was oxidized, serving as a solid electrolyte. Inside the TEM, the lithium electrode was brought into contact with the TiO₂ electrode by a piezo-manipulator. At this point, a nanobattery has been successfully assembled. Lithiation occurred under applying a constant 0.5 V bias to the TiO₂ electrode with respect to the lithium electrode.

An FEI Tecnai F30 TEM was used in our experiments, which operates at an acceleration voltage of 300 kV. To reduce electron beam irradiation, an electron beam with intensity as low as 10 Am^{-2} was used throughout the experiment. Due to the small morphology and volume changes before and after lithiation, it is difficult to track lithiation inside individual nanocrystals by conventional bright-field TEM imaging. Employing in-situ electron diffraction, on the other hand, excels in revealing even the slightest changes in the lattice parameters, and is therefore competent to track the structural changes associated with successive lithium incorporation. Most diffraction patterns were recorded at a camera length of 1.2–1.5 m.

6.3 EXPERIMENTAL RESULTS

6.3.1 Lithiation of TiO_2 nanoparticles via a single-phase reaction

Figure 6.1 presents the morphological and structural changes of a poly-crystalline anatase TiO_2 NW during lithiation. The pristine TiO_2 NWs (provided by MemPro Ceramics Corporation) are composed of randomly oriented and loosely packed anatase nanocrystallites with most of them being 10–25 nm (Figure 3.3), creating an environment similar to that in clusters consisting of nano-particles in a real battery electrode. The experiments were carried out using an all-solid electrochemical setup illustrated in Figure 6.1a, consisting of a TiO_2 NW working electrode and a Li metal counter electrode bridged by a thin film of Li_2O solid electrolyte. No significant volume expansion was observed after lithiation, except for a thin layer of Li_2O covering the TiO_2 NW surface, providing a pathway for radial transport of Li ions (Figure 6.1b and Figure 6.2).

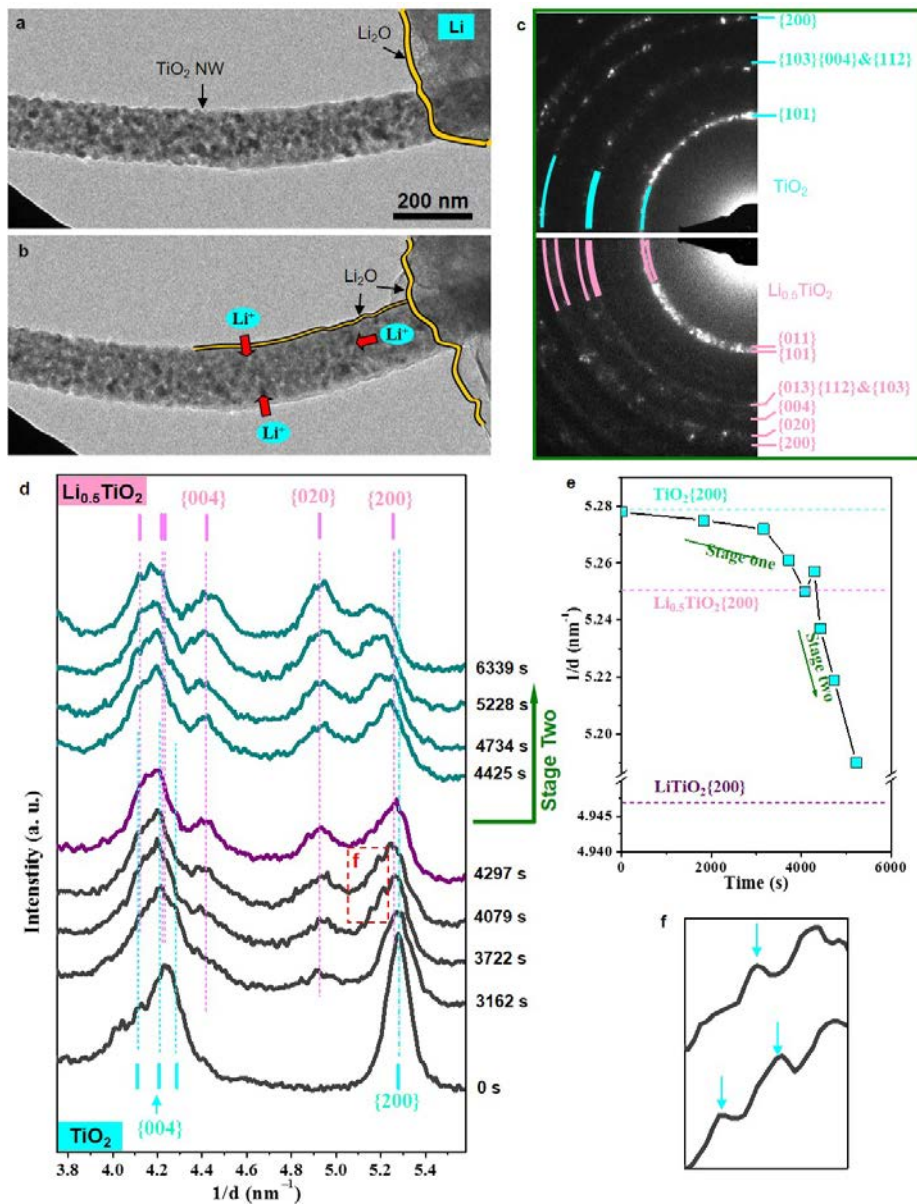


Figure 6.1 Structural evolution of TiO₂ during lithiation. (a-b) Morphology changes of a polycrystalline anatase TiO₂ NW before (a) and after lithiation (b). (c) EDPs of polycrystalline TiO₂ before (top) and after (bottom) lithiation, showing the original tetragonal anatase TiO₂ has been converted to orthorhombic Li_xTiO₂. (d) Integrated intensity from time-lapse EDPs. A two-stage lithiation mechanism was observed. In the first stage (0 s to 4297 s), both diffractions from TiO₂ and Li_xTiO₂ (with x close to 0.5) were detected, indicating the coexistence of two phases. At the end of this stage, the TiO₂ NW has been fully converted to Li_{0.5}TiO₂, corresponding to the purple diffractogram. At the second stage (after 4297 s), the continuous displacement of the Li_xTiO₂ {200} peak was characteristic of a solid solution with increasing lithium content ($0.5 < x < 1$). Cyan and magenta vertical solid lines indicate the expected peak positions of TiO₂ and Li_{0.5}TiO₂, respectively. (e) Displacement of the {200} diffraction peak with respect to time. (f) A magnified view of the {200} diffraction peak (rectangular region in d). Cyan arrows indicate several small peaks at the left edge.

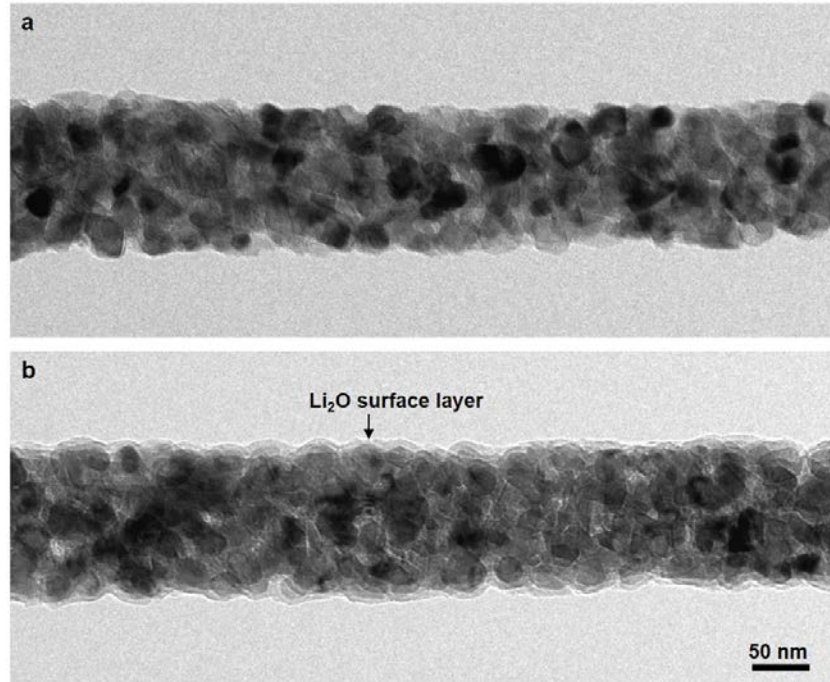


Figure 6.2 Comparison of morphologies before and after lithiation. (a) Pristine TiO₂ NW. (b) After lithiation, the same NW showed similar morphology with no significant changes in the crystallite size. A Li₂O surface layer was formed after lithiation.

The size of the TiO₂ crystallites composing the NW also remained unchanged (Figure 6.2). Nevertheless, EDPs before (Figure 6.1c top) and after (Figure 6.1c bottom) lithiation indicated that the TiO₂ nanoparticles have been converted from the original tetragonal anatase phase (space group $I4_1/amd$) to an orthorhombic Li_xTiO₂ phase (lithium titanate, space group $Imma$)³¹⁶. This phase transition was featured by splits in the TiO₂ {101} and {200} rings to form Li_xTiO₂ ({101}+{011}) and ({200}+{020}) reflections, respectively, as well as the shift in the {004} diffraction ring (Figure 6.1c). Figure 6.1d is derived from a series of EDPs recorded at different periods during lithiation, exhibiting a two-stage lithiation mechanism. In the first stage (before 4297 s), the diffraction intensity came from a juxtaposition of both the anatase and lithium titanate phase, which seems to suggest a well-established two-phase lithiation mechanism. The Li_xTiO₂ {004} and {020} peaks corresponded well with the expected peak positions of Li_{0.5}TiO₂

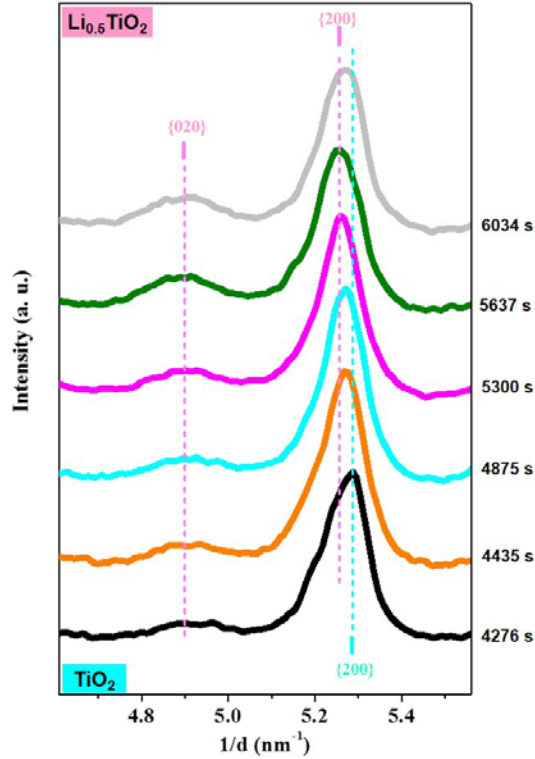


Figure 6.3 Structural evolution of single crystalline anatase TiO_2 NWs during lithiation. Both $\text{Li}_{0.5}\text{TiO}_2$ and TiO_2 phases were detected, with the former growing progressively at the expense of the latter. Unlike the case in polycrystalline TiO_2 NWs, no additional diffraction intensities were captured between $\text{Li}_{0.5}\text{TiO}_2$ {020} and TiO_2 {200}. Cyan and magenta vertical solid lines indicate the expected peak positions of TiO_2 and $\text{Li}_{0.5}\text{TiO}_2$, respectively.

(~7% expansion in b and ~4.8% shrinking in c), indicating x in the obtained lithium titanate phase is close to 0.5. (Hereafter, this metastable phase is referred to as $\text{Li}_{0.5}\text{TiO}_2$.) In the second stage (after 4297 s), continuous displacement of the diffraction peaks was observed, most evident in Li_xTiO_2 {200}, which is characteristic of a single-phase (solid solution) reaction. This displacement is further represented in Figure 6.1e, where the {200} Bragg ring first stayed between TiO_2 {200} and Li_xTiO_2 {200} due to an apparent biphasic nature, then reached the latter at the end of stage one. At this point (4297 s), the polycrystalline TiO_2 NW has been fully converted to $\text{Li}_{0.5}\text{TiO}_2$. Further lithiation led to continuous displacement of the lithium titanate

{200} towards LiTiO_2 {200}, indicating the existence of a solid solution domain when x is above 0.5.

It should be pointed out that the kinetics in the second stage was slow, reflected by the sluggish shift of the lithium titanate diffraction peaks, which almost stopped after prolonged discharge. This means the obtained solid solution above 0.5 lies in a narrow domain, which is possibly a result of crystal size effect³¹⁷ or ordering of Li ions in $\text{Li}_{0.5}\text{TiO}_2$ ³¹⁸. While this solid-solution behavior may be rationalized by previous researches, a careful comparison of the structure changes in stage one between the nanocrystalline NWs and single crystalline NWs (with dimensions of 50–200 nm in diameter and several micrometers in length) reveals one anomaly: the former (Figure 6.1d) showed additional diffraction intensities, such as secondary peaks (Figure 6.1f), between $\text{Li}_{0.5}\text{TiO}_2$ {020} and TiO_2 {200}, which were absent in the latter (Figure 6.3). Since neither the anatase nor the $\text{Li}_{0.5}\text{TiO}_2$ phase has Bragg rings located between $\text{Li}_{0.5}\text{TiO}_2$ {020} and TiO_2 {200}, these additional intensities should not have existed in the structural evolution of a typical two-phase reaction (for example, Figure 6.3). This unexpected phenomenon challenges the validity of the long believed two-phase lithiation mechanism in this classical insertion type anode material when its crystal size comes down to ~20 nm.

Figures 6.4 and 6.5 are close-up views of the evolutions in the Bragg rings obtained from a cluster consisting of 200-300 TiO_2 nanoparticles during the first-stage lithiation. Three bright diffraction spots (labeled with Arabic 1, 2 and 3, respectively) from TiO_2 {004} were presented in Figure 6.4a at 0 s. Based on the randomly oriented nature of these nanoparticles (Figure 3.3a-c) and the limited number of nanoparticles included in the EDP, it is reasonable to treat each diffraction spot as coming from individual crystallites. Surprisingly, the first two Bragg spots, namely 1 and 2, started to shift continuously from the TiO_2 {004} (indicated by a cyan dotted arc)

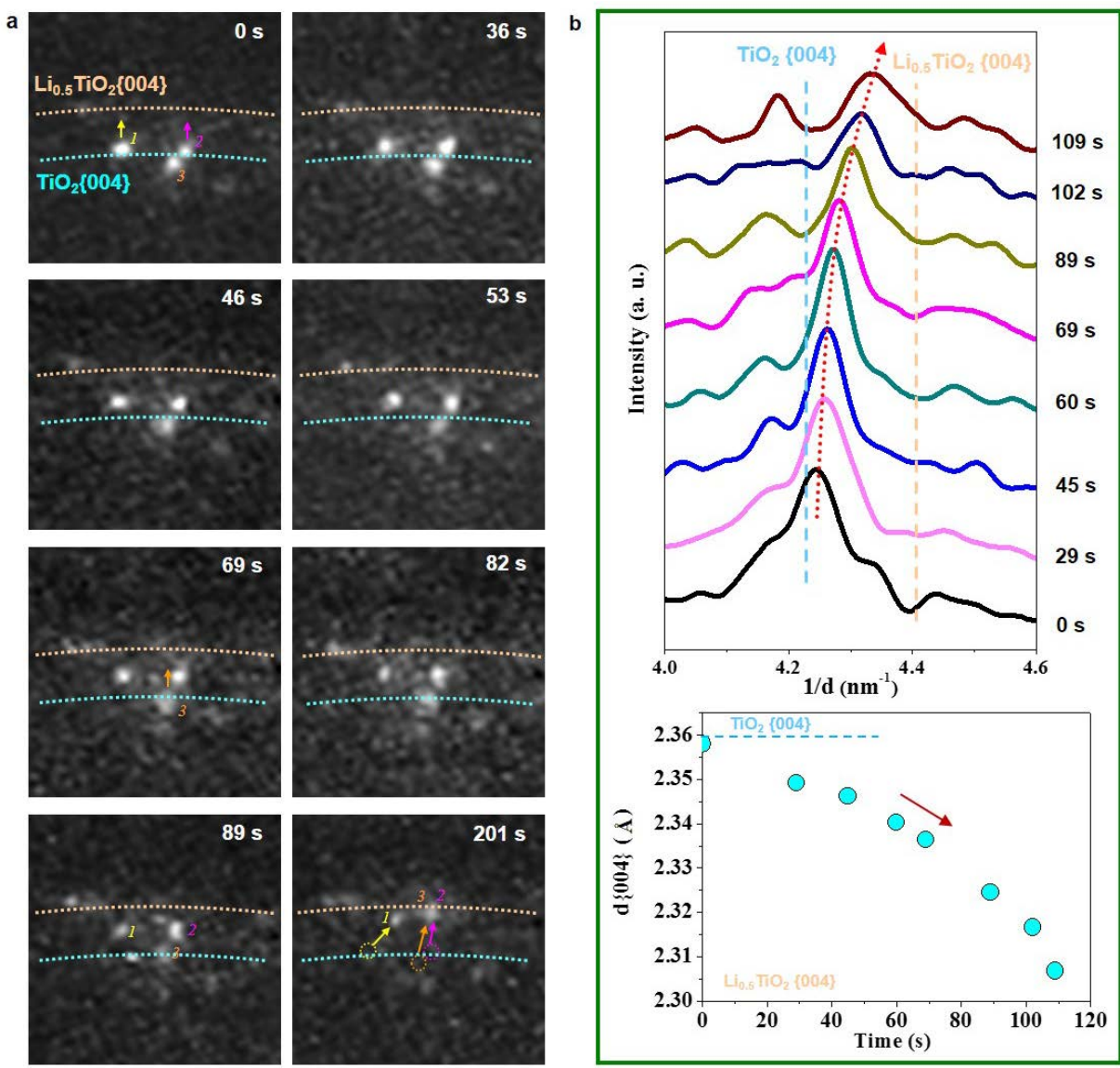


Figure 6.4 Continuous displacement of diffraction intensities from individual TiO₂ particles during the first-stage lithiation. (a) Time-lapse EDPs of {004} diffraction spots from three individual particles (named by Arabic 1, 2, and 3, respectively). Bragg spots 1 and 2 (marked by yellow and magenta arrows, respectively) shifted from the {004} diffraction ring of TiO₂ (Cyan dotted arc) towards that of Li_{0.5}TiO₂ (brown dotted arc) upon progressive lithium incorporation. After 69 s, the third spot also began to shift (indicated by an orange arrow). Finally, all three Bragg spots reached the Li_{0.5}TiO₂ {004} diffraction ring after ~200 s. The circles in the last frame indicate the original positions of the three diffraction spots while arrows indicate the displacement of these diffraction intensities, which are indicative of a single-phase reaction path. (b) Intensity profiles of Bragg spots 1 and 2 (top) and their displacement with respect to time (bottom). It took ~3 minutes to lithiate TiO₂ particles to Li_{0.5}TiO₂, which showed much higher rate compared to the overall lithiation of the poly-crystalline NWs.

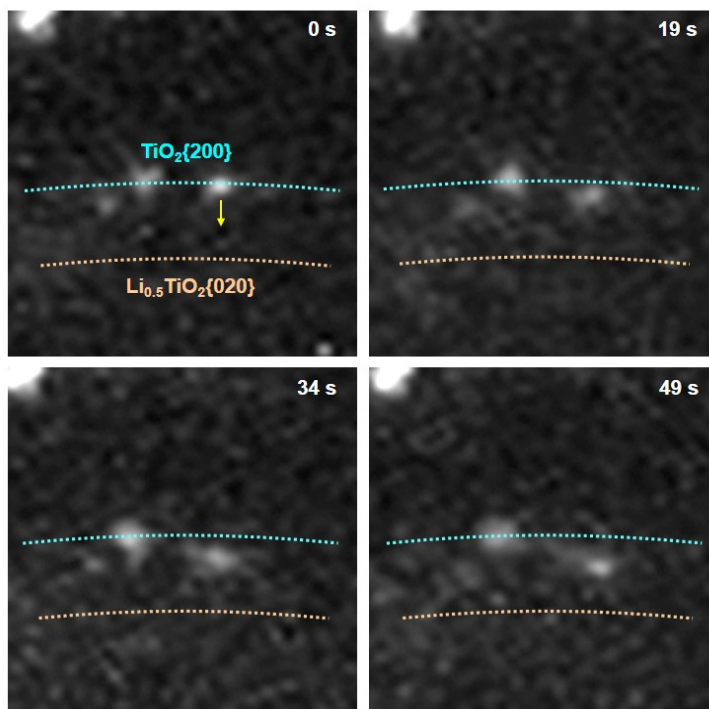


Figure 6.5 Continuous shifting of a diffraction spot from an individual TiO_2 crystallite. The Bragg spot (marked by a yellow arrow) moved from TiO_2 {200} (marked by cyan dotted arc) towards $\text{Li}_{0.5}\text{TiO}_2$ {020} (marked by brown dotted arc). It was half way towards $\text{Li}_{0.5}\text{TiO}_2$ {020} after 49 s.

towards the $\text{Li}_{0.5}\text{TiO}_2$ {004} diffraction ring (indicated by a brown dotted arc) right upon lithiation (pointed out by yellow and pink arrows, respectively). The displacements of these two Bragg spots are also presented in Figure 6.4b, where the intensity shift versus time is clearly visible. After 109 s, an approximately 3% shrinkage along the c axis was observed (Figure 6.4b bottom). The third Bragg spot also began to move towards $\text{Li}_{0.5}\text{TiO}_2$ {004} 69 s behind spots 1 and 2 (marked by an orange arrow). After approximately 200 s, all three Bragg spots have reached the $\text{Li}_{0.5}\text{TiO}_2$ {004} diffraction ring (indicated in the last frame of Figure 6.4a with circles marking the original positions of the three diffraction spots and arrows indicating their displacements). These continuous displacements of the diffraction intensities are a strong indication of Li_xTiO_2 solid solution with successive lithium incorporation. This is also consistent

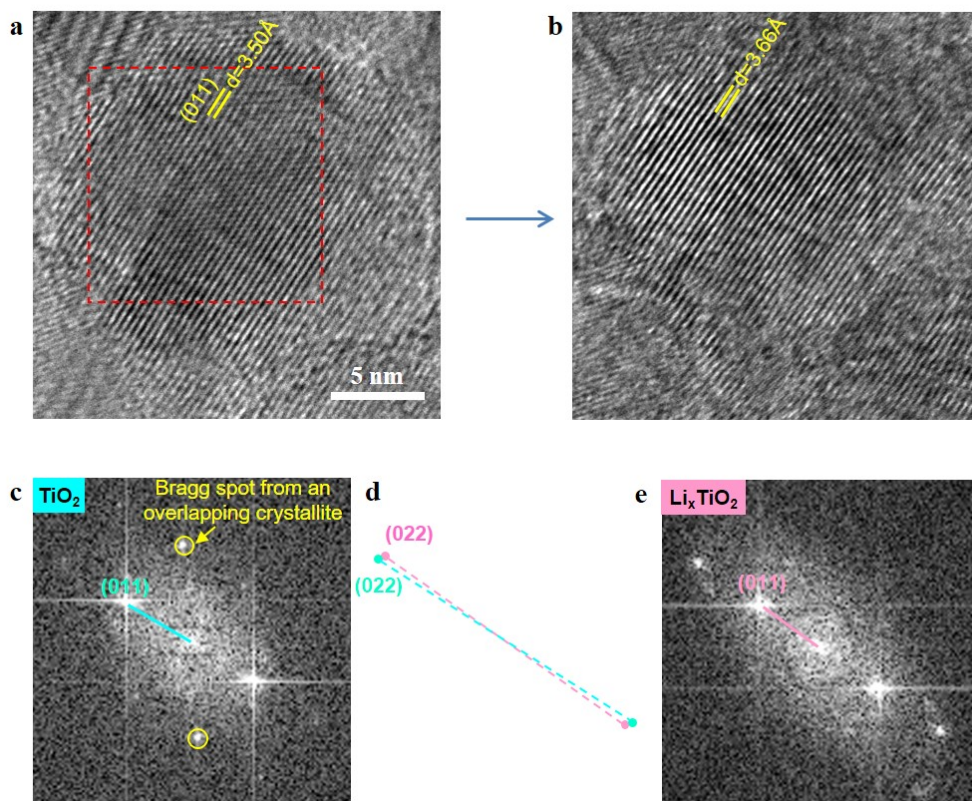


Figure 6.6 Structure changes of a single TiO_2 crystallite induced by lithium insertion. (a-b) High-resolution TEM images of one TiO_2 nanocrystal before (a) and during (b) lithiation, showing a $\sim 5\%$ increase in the $\{011\}$ lattice spacing. c-e, Corresponding fast Fourier transformations (FFTs) before (c) and after (e) lithiation, representing the microstructure changes caused by lithiation. Both an increase in the $\{022\}/\{011\}$ lattice spacing and a slight rotation have been observed (d) by superimposing diffraction patterns before (cyan) and during (magenta) lithiation. Additional diffraction spots (marked by yellow circles in c) came from another overlapping particle.

with the high-resolution TEM images of a single crystallite before and during lithiation where no trace of a two-phase boundary is visible (Figure 6.6). Although nanosize-enhanced solubility in anatase TiO_2 ^{317,319} may have contributed to the shifting of diffraction intensities, the d-spacing changes owing to the formation of solid solutions up to $x=0.25$ in anatase Li_xTiO_2 is very limited^{320,321}, which alone cannot justify the observed large diffraction intensity displacements. It

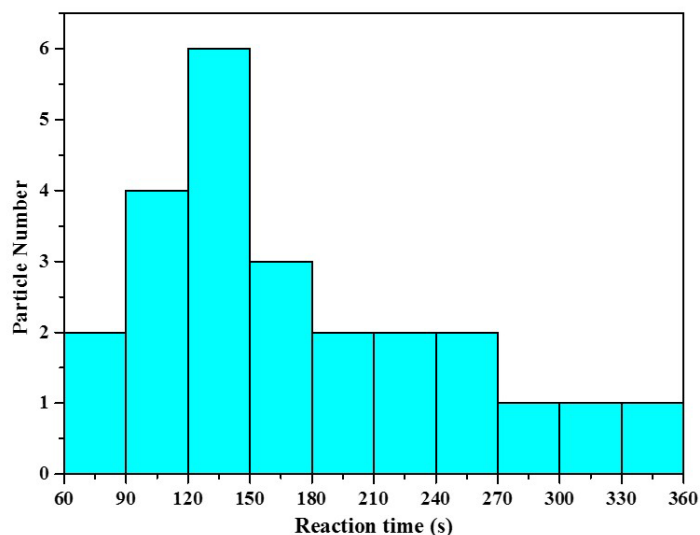


Figure 6.7 Reaction time distribution for individual TiO_2 crystallites to be lithiated to $\text{Li}_{0.5}\text{TiO}_2$ nanocrystals. The examined crystallites were lithiated within 1–6 min, corresponding to a rate of 10–60 C.

can thus be concluded that individual TiO_2 nanoparticles in the present study were lithiated via a single-phase reaction.

The observed single-phase lithiation inside each nanoparticle is rapid, which can be completed within 1–6 min, corresponding to a rate of 10–60 C (Figure 6.7). Under such a rate, the Li^+ diffusion coefficient is estimated to be much larger than $10^{-17} \text{ cm}^2\text{s}^{-1}$ as reported in nano-sized TiO_2 crystals^{322,323}. Instead, it is likely to stay close to $10^{-13} \text{ cm}^2\text{s}^{-1}$, which is expected in micron-scale anatase TiO_2 ^{304,318,324} (see the discussion section for detail). This rapid lithiation of individual particles is more than an order faster compared to the overall lithiation of TiO_2 NWs (Figure 6.1d). In other words, lithiation of the polycrystalline TiO_2 NWs can be treated as an assembly of discrete fast lithiations of individual crystallites, analogous to a jigsaw puzzle which is put together piece by piece. If we consider an observation timescale commensurate with the overall lithiation speed in the polycrystalline NWs, lithiation of individual particles is so rapid that it makes the component crystallites look like either lithiated or unlithiated, therefore

representing an apparent biphasic feature during the first-stage lithiation (Figure 6.1d). Thus the excessive intensities and small peaks between the $\text{Li}_{0.5}\text{TiO}_2$ {020} and TiO_2 {200} can be explained by diffraction intensities originated from nanoparticles with intermediate lithium content ($0 < x < 0.5$), which were captured during their continuous shifting toward the $\text{Li}_{0.5}\text{TiO}_2$ {004} Bragg ring.

Similar rapid lithiation has previously been reported to occur in anatase TiO_2 and LiFePO_4 nanocrystals, leaving the crystallites to appear like either lithiated or unlithiated^{187,317,320}, which was attributed to a shortened diffusion length, enlarged interface area between the electrode materials and electrolyte, and an increased driving force derived from elastic energies at the two-phase interface.¹⁸⁷ In the current study, by conducting in-situ experiment at an adequate temporal resolution, we provide direct evidence to show that the improved kinetics in lithiation of TiO_2 nanoparticles is due to the formation of a solid solution, which eliminates the energy-demanding two-phase interface. The single-phase lithiation process has previously only been reported in amorphous TiO_2 ³²⁵, and is thus unexpected to proceed in a context of an anatase phase. The main driving force for a solid-solution reaction may stem from the large size impact on the lithium solubility in both the anatase and lithium titanate phases³¹⁷. Hence, it is reasonable to think that by reducing the particle size, a single-phase reaction may also take place in other electrode materials whose miscibility gaps are closely related to their crystal sizes.

6.3.2 Two-phase lithiation in single crystalline anatase TiO_2 NWs

If the observed transition from two-phase to single-phase lithiation is intrinsically size-controlled, then a two-phase lithiation is expected when the crystal size increases above a critical threshold. In single crystalline TiO_2 NWs under similar conditions (that is, electron beam irradiation and

identical experimental setups). Indeed, unlike the case in 20 nm TiO₂ crystallites, EDPs collected from an agglomerate consisting dozens of single crystalline TiO₂ NWs (with diameter above 50 nm and length up to several micron-meters) showed no displacements of diffraction intensities during lithiation (Figure 6.3), indicating a two-phase equilibrium reaction. Again, the lithium titanate phase is close to Li_{0.5}TiO₂, as depicted in Figure 6.3.

Direct evidence of a two-phase boundary existing between anatase TiO₂ and lithium titanate has been provided by tracking the microstructural changes during lithiation of an individual single crystalline TiO₂ NW. Figure 6.8a-d shows its formation and migration during lithiation. The pristine TiO₂ NW was about 100 nm in diameter and 1.6 μm in length (Figure 6.8a). A two-phase boundary, presented as two dark-contrasted stripes parallel to the surface (marked by yellow dotted lines in Figure 6.8b; also presented in a close-up view in Figure 6.8j), formed rapidly upon lithiation, and propagated along both the radial and longitudinal directions of the NW (denoted by cyan arrows in Figure 6.8b). The movement of the reaction front was also visible (marked by red arrows in Figure 6.8b-c). The corresponding structural evolution during the two-phase boundary formation and migration was presented in Figure 6.8e-h and their insets, which was featured by the splitting of the {004} Bragg spot into anatase TiO₂ {004} and lithium titanate (Li_{0.5}TiO₂) {004} (denoted by cyan and brown dotted lines, respectively). First, a weak Li_{0.5}TiO₂ {004} Bragg spot appeared at the same time as the formation of a two-phase boundary (Figure 6.8f), which then kept growing at the expense of TiO₂ {004} during the subsequent boundary migration (Figure 6.8g-h). A dark field TEM image illuminated by Li_{0.5}TiO₂ g_{004} reveals a core-shell structure with the interior being TiO₂ and the peripheral being Li_{0.5}TiO₂ (Figure 6.8i). Thus it is clear that lithiation inside individual single crystalline TiO₂ NWs propagated via a two-phase reaction with anatase TiO₂ continuously being replaced by Li_{0.5}TiO₂,

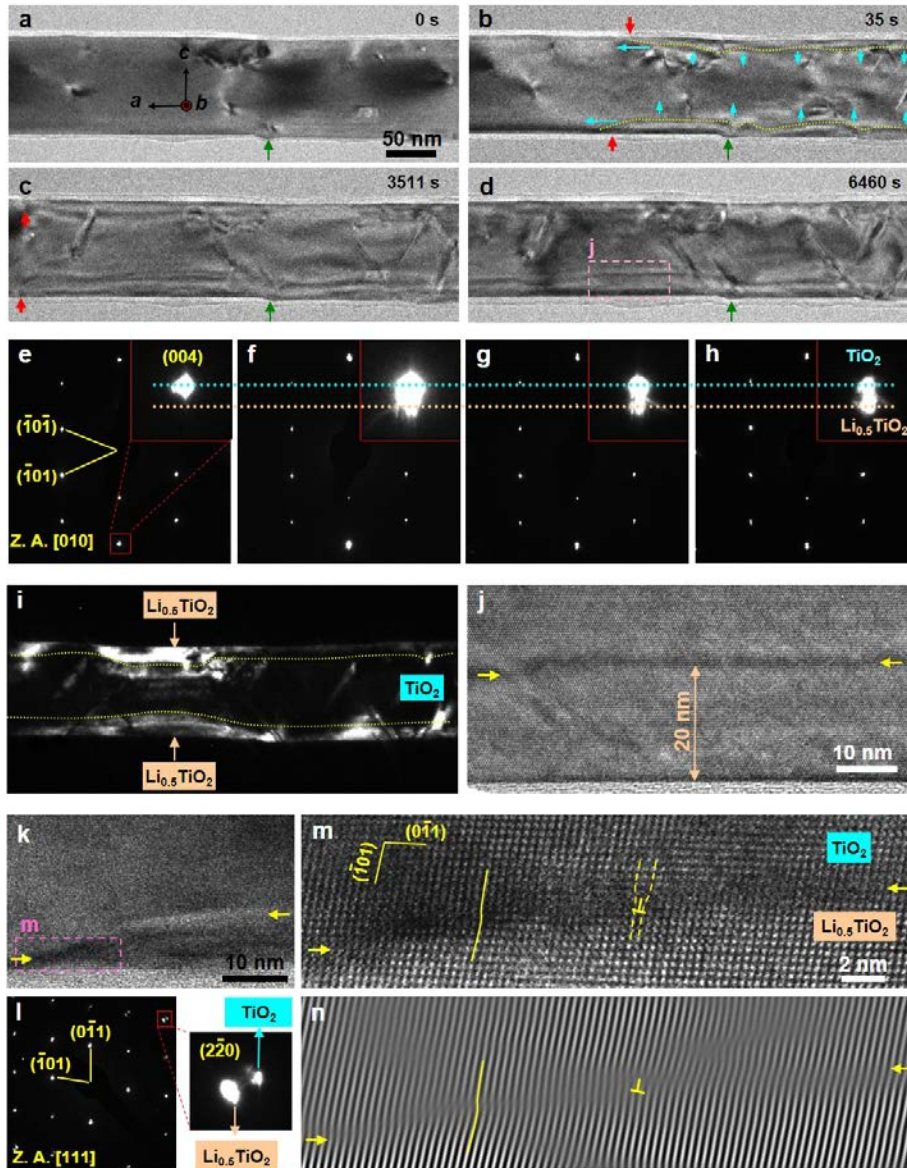


Figure 6.8 Two-phase lithiation in single crystalline TiO₂ NWs. (a) A pristine single crystalline TiO₂ NW diameter around 100 nm. (b-d) Phase boundary migration upon lithiation viewed along the $\langle 010 \rangle$ direction. Red arrow heads mark the reaction front and cyan arrows indicate phase boundary (marked by yellow dotted lines in b) movement upon further lithiation. Olive arrows denote a surface step as a reference for tracking the movement of the interface. (e-h) Structural evolution of the two-phase system corresponding to the lithiation progresses in (a-d). The insets in e-h are magnified views of the {004} diffraction spot. The d-spacing decrease from TiO₂ to Li_{0.5}TiO₂ in the c direction was $\sim 4\%$. (i) Dark-field TEM image of the NW in (d) using Li_{0.5}TiO₂ g_{004} diffraction condition. (j) Close-up view of the phase boundary region (rectangle in d). The thickness of the Li_{0.5}TiO₂ phase was ~ 20 nm. (k-l) Morphology (k) and structure (l) of a reaction front in a partially lithiated TiO₂ NW viewed along $\langle 111 \rangle$ zone axis. The magnified view of the $2\bar{2}0$ diffraction spot (l, right) also reflected both TiO₂ and Li_{0.5}TiO₂. (m-n) Original (m) and Fourier-filtered (n) HRTEM images of the reaction front tip (rectangle in k).

which was accompanied by a two-phase boundary migrating from the surface to the interior of the TiO₂ NW. Another example of a two-phase boundary is represented in Figure 6.8k with a viewing direction of [111]. Splitting of the $\{2\bar{2}0\}$ Bragg spot was observed (Figure 6.8l right), showing, again, the biphasic nature. A HRTEM and its Fourier-filtered image of the reaction front reveal the coexistence of both coherency strains and mismatch dislocations at the two-phase boundary (Figure 6.8m-n). The former is known to significantly contribute to the elastic energy^{186,326,327}, therefore destabilizing the two-phase configuration when the particle size scales down below a critical level, e.g. 20 nm.

6.4 DISCUSSION

An equilibrium two-phase reaction in anatase TiO₂ has frequently been reported based evidences such as a flat potential plateau during galvanostatic lithiation/delithiation^{220,328-330} and the coexistence of both anatase and lithium titanate phases revealed by neutron and X-ray diffractions^{317,331} and by NMR spectra³⁰⁵. The observed single-phase lithiation mechanism, however, is unexpected, even in smallest crystals with size below 20 nm^{317,332}. This discrepancy can be rationalized by Figure 6.9, which is a schematic illustration of the single-phase lithiation process in poly-crystalline TiO₂ NWs. As observed in Figure 6.1d and Figure 6.4, overall lithiation of poly-crystalline TiO₂ NWs proceeds by single-phase lithiation of individual crystallites, with the latter being at least ten times faster than the former. As we know, most in-situ techniques, such as X-ray and neutron diffractions^{307,308} and Raman microscopy^{331,333}, have limited spatial resolution, and are usually conducted under a timescale of minutes, which is incompetent to capture the rapid electrochemistry inside individual particles (reactions enclosed

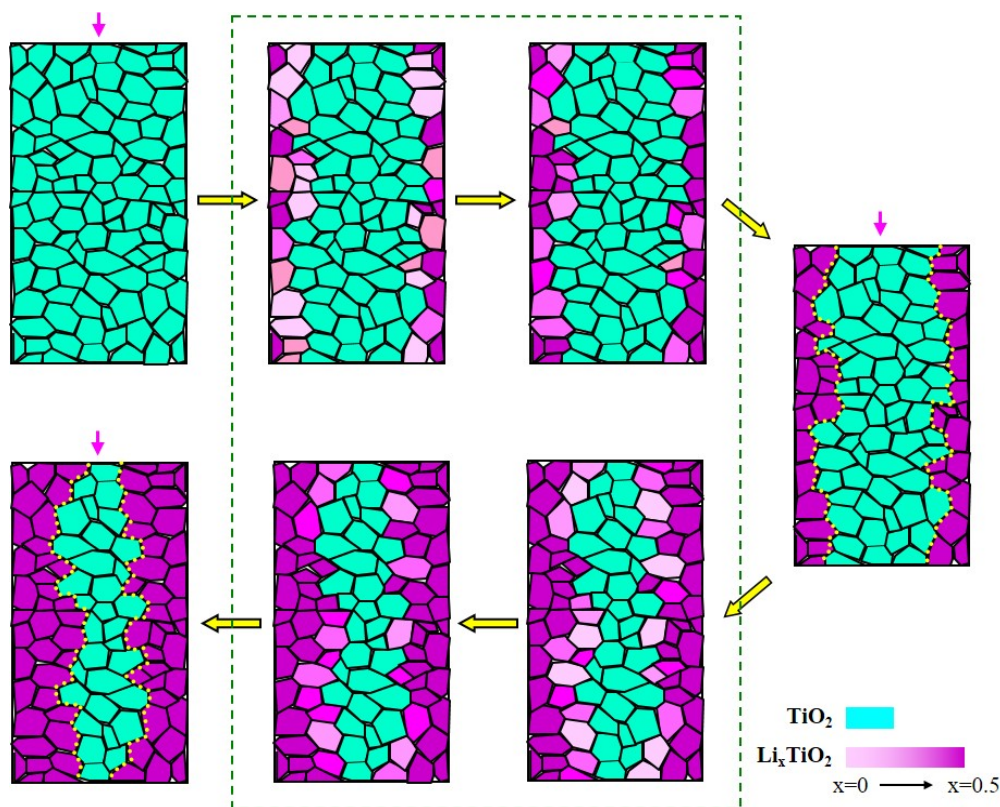


Figure 6.9 Schematic illustration of the single-phase lithiation process in anatase TiO_2 NWs composed of 20 nm crystallites. Cross-sections of the poly-crystalline TiO_2 NWs are depicted. The overall lithiation of the NW is slow (marked by pink arrow heads), proceeding by rapid lithiation of individual crystallites (enclosed in a green rectangle). The single-phase lithiation process inside each nanocrystal is too fast to be revealed by either ex-situ studies or in-situ X-ray and neutron diffractions, which makes TiO_2 crystallites appear to be either lithiated or unlithiated. Therefore, only the sluggish overall lithiation was captured by previous studies. The rapid lithiation inside individual crystallites as well as the metastable nature of $\text{Li}_{0.5}\text{TiO}_2$ makes the overall lithiation of TiO_2 NWs resemble an equilibrium two-phase reaction featured by a two-phase interface (marked by yellow dotted curves).

in a green dotted rectangle). Therefore, only the sluggish overall lithiation of the TiO_2 NWs can be observed (indicated by magenta arrow heads), featured by the coexistence of either TiO_2 or $\text{Li}_{0.5}\text{TiO}_2$ crystallites. On the other hand, In-situ TEM observation, with a 2 \AA spatial resolution and a sub-one-second temporal resolution, is more than adequate to track the single-phase lithiation process inside individual particles (reactions inside the green rectangle), with lithium content continuously increasing from $x=0$ to $x=0.5$. In addition, it can also be noticed that further

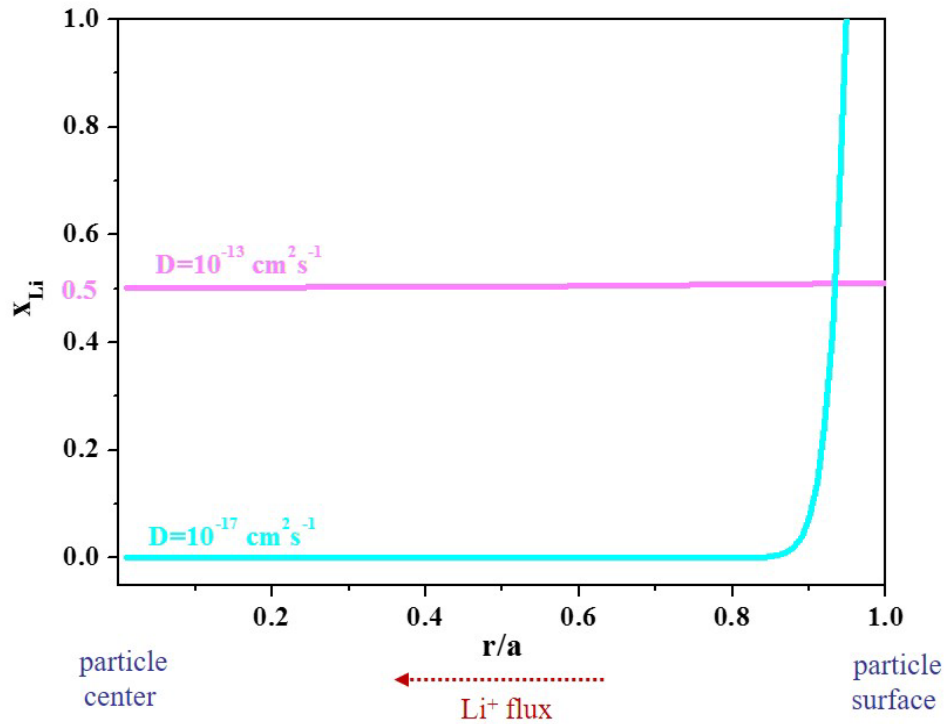


Figure 6.10 lithium concentration distributions in a TiO_2 crystallites (when $t=100$ s) at diffusion coefficients of $10^{-17} \text{ cm}^2\text{s}^{-1}$ (typical for nanosized TiO_2 particles) and $10^{-13} \text{ cm}^2\text{s}^{-1}$ (typical for micron-sized TiO_2 particles), respectively. The former leads to phase separation while the latter enables uniform lithium distribution.

lithiation beyond $x=0.5$ is reluctant (Figure 6.1d), indicating $\text{Li}_{0.5}\text{TiO}_2$ a metastable phase. Compared to the galvanostatic lithiation/delithiation which typically lasts for at least several hours, the transient lithiation of individual crystallites and stable nature of $\text{Li}_{0.5}\text{TiO}_2$ leave the component crystallites in the polycrystalline TiO_2 NWs looking like either $\text{Li}_{0.5}\text{TiO}_2$ (the lithiated shell of NWs) or anatase TiO_2 (the unlithiated core of the NWs). Thus, the overall lithiation in poly-crystalline TiO_2 NWs appear to proceed via migration of a two-phase boundary between TiO_2 and $\text{Li}_{0.5}\text{TiO}_2$ crystallites (marked by yellow dotted curves), resembling an equilibrium two-phase lithiation path. The above scenario is similar to that in a many-particle

electrode model, and therefore both a plateau and a voltage hysteresis are expected in the charge and discharge curves²¹⁰.

The diffusion coefficient can be roughly estimated based on the lithiation rate of individual TiO₂ particles. The displacement of the diffraction spots from TiO₂ {004} to Li_{0.5}TiO₂ {004} proceeded in a more or less uniform manner, indicating a continuous Li⁺ flux into the TiO₂ crystallites. The average Li⁺ flux can be estimated by the following equation:

$$F_0 = \frac{\text{Amount of Li in Li}_{0.5}\text{TiO}_2}{(\text{Reaction time}) \times (\text{Particle surface area})} = \frac{2R}{3abct}, \quad (6.1)$$

where F_0 is the average Li⁺ flux per unit surface area into a TiO₂ particle during progressive lithiation until it reaches Li_{0.5}TiO₂; a , b , c are the unit cell parameters of tetragonal Li_{0.5}TiO₂, respectively; t is the lithiation time; and R is the radius of the a TiO₂ crystallite if we treat it as a sphere. Here, we take 100 s as the reaction time (based on Figure 6.7), and 10 nm as the TiO₂ nanoparticle radius (Figure 3.3d). According to equation (6.1), the corresponding average Li⁺ flux will be $\sim 4.8 \times 10^{17} \text{ m}^{-2}\text{s}^{-1}$. By giving an estimation of this average Li⁺ flux, the Li⁺ diffusion rate in lithiated TiO₂ nanoparticles can be roughly deduced.

By applying the model of diffusion in a sphere with constant surface flux F_0 , we can estimate Lithium concentration distribution in a TiO₂ nanoparticle by³³⁴

$$C = \frac{F_0 R}{D} \left\{ \frac{3Dt}{R^2} + \frac{r^2}{2R^2} - \frac{3}{10} - 2 \frac{R}{r} \sum_{n=1}^{\infty} \frac{\sin(\alpha_n r)}{\alpha_n^2 R^2 \sin(\alpha_n R)} \exp(-D\alpha_n^2 t) \right\}, \quad (6.2)$$

where C is the lithium concentration, r is the distance from a certain spot inside the TiO₂ sphere to the sphere center, D is the diffusion coefficient, and $R\alpha_n$ ($n=1 \rightarrow \infty$) are the positive roots of $R\alpha_n \cot R\alpha_n = 1$. The lithium concentration can be further equalized to x in Li _{x} TiO₂ by

$$x = \frac{Cabc}{4}, \quad (6.3)$$

where the unit cell volume of Li_xTiO_2 ($0 \leq x \leq 0.5$) is treated as the unit cell volume of $\text{Li}_{0.5}\text{TiO}_2$ (that is, $a \cdot b \cdot c$), since the volume change from $x=0$ to $x=0.5$ is only $\sim 4\%$. Combining equations (6.2) and (6.3), the lithium concentration distributions (when $t=100$ s) in a TiO_2 crystallite at diffusion coefficients of $D=10^{-17}$ and $D=10^{-13} \text{ cm}^2\text{s}^{-1}$ are obtained in Figure 6.10. When the diffusion coefficient is on the order of $10^{-17} \text{ cm}^2\text{s}^{-1}$, the lithium flux rate is much faster than the diffusion rate, which will inevitably lead to phase separation with an unlithiated TiO_2 core surrounded by a lithium titanate shell. On the other hand, a diffusion coefficient on the order of $10^{-13} \text{ cm}^2\text{s}^{-1}$ enables almost uniform lithium distribution, which resembles the case in our experiment. Therefore, a reasonable estimation of the diffusion coefficient should be between these two values, and probably very close to $10^{-13} \text{ cm}^2\text{s}^{-1}$.

6.5 CONCLUSIONS

In summary, we have directly revealed that lithiation of individual anatase TiO_2 nanocrystals with size of 20 nm proceeds via a non-equilibrium single-phase reaction. By tracking EDPs from a many-particle system consisting of 200-300 particles, we were able to capture the continuous shifting of diffraction intensities from anatase to lithium titanate phase ($\text{Li}_{0.5}\text{TiO}_2$) in individual TiO_2 nanocrystals. This work captured the size-dependent competition between thermodynamically different lithiation pathways, and unambiguously confirmed the possibility of a single-phase reaction mechanism operating in materials whose miscibility gap is associated with a prominent size impact, which significantly improves the reaction kinetics. These results provide important guidelines for designing high-power LIBs, and demonstrate that precise size-

control of the active electrode materials might be of equal importance compared to searching for new candidate electrode materials.

7.0 SUMMARY AND CONCLUSIONS

Phase transitions are ubiquitously seen to dictate the broad applications of nanomaterials. This dissertation employed state-of-the-art in-situ TEM atomic-scale observation to reveal the rapid solidification processes of metallic liquids and to gain a mechanistic understanding of the mechanical degradation processes, such as volume change and strain accommodation, as well as the reaction pathways in nanostructured electrodes during battery operation.

The stabilities of supercooled metallic liquids are highly dependent on the composition and cooling rate. Melts of pure metals require extremely high cooling rate to be vitrified, due to their intrinsic poor glass-forming ability. In this dissertation, a methodology with the ability to achieve an ultrafast quenching rate of 10^{14} Ks^{-1} has been developed, which successfully vitrified monatomic metallic melts of early transition bcc metals. It was revealed that the formation condition and thermal stability of these novel glasses depend on the competition between the cooling rate and the crystal growth rate at the liquid-crystal interface, and that undercooled metallic liquids from pure fcc metals are intrinsically unstable due to the negligible activation energy and fast kinetics in crystal growth even at room temperature. This work broadens the glass-forming zone by including glass formers with the worst glass-forming abilities. With such a high cooling rate to reach deep quench, the inherent structure of liquids can be accessed, enabling investigations of the fast kinetics of supercooled liquids and the mechanisms for the formation of metastable materials under conditions far away from equilibrium.

By integrating nanoscale fabrication, structural characterization and mechanical testing, this work opens up new opportunities for investigating the connection between the atomic structure and intrinsic mechanical properties of sub-100-nm sized metallic glasses. Unlike crystalline materials whose deformation mechanism has been well established, the deformation of metallic glasses with disordered structures has not yet been fully understood. A mechanistic of the atomic-scale origin of the ductility versus brittleness in metallic glasses warrants further study in the future.

Solid-state amorphization, large expansion/contraction upon reaction, the formation of micro-cracks, and pulverization are common mechanisms that lead to mechanical degradation in lithium-ion battery electrodes, especially in high-capacity anode materials. One-dimensional materials in the form of nanowires are much more robust than their bulk counterparts, due to their special geometry to accommodate large plasticity and volume changes. When immersed in electrolyte, lithiation of SnO₂ nanowires is initiated by preferred lithium insertion along the (020) planes in the transverse direction, which then evolves into multiple reaction fronts with large dislocation plasticity at the vicinity, serving as a precursor towards electrochemically-driven solid-state amorphization. Such mechanism can successfully accommodate a 45% radial expansion and a 90% super-elongation without catastrophic failure. These results provide insights into a fundamental understanding of the plasticity and strain accommodation mechanisms inside one-dimensional materials, and have significant implications for designing nanostructured electrodes with materials exhibiting large volume expansion and contraction during battery operation.

Intercalation compounds with superior rate capabilities are highly desirable. The reaction rate can be significantly dependent on the particle size of the electrode materials, due to not only

the kinetic aspects such as the short diffusion length, but also the change in thermodynamics which dictates the competition between different reaction pathways. Compared to a well-defined two-phase reaction process in bulk TiO₂, lithiation of individual anatase TiO₂ nanoparticles with size of 20 nm proceeds via a non-equilibrium single-phase reaction, which significantly accelerates the reaction kinetics by obviating the need to nucleate a second phase and, at the meantime, effectively alleviates strain by exempting a two-phase boundary. These results demonstrate the significant size impact on both the thermodynamics and kinetics in intercalation compounds and thus provide important guidelines for designing high-power lithium-ion batteries.

In summary, this dissertation develops an ultrafast solidification approach for investigating the fast kinetics and structures of supercooled liquids, and advances the fundamental understanding of the origin of mechanical degradation and size-dependent electrochemical performances in nanostructured electrodes.

8.0 OUTLOOK

The broad application of nanomaterials has attracted extensive research effort to reveal the atomistic origin of their response under different circumstances. For example, a ‘smaller is stronger’ trend has been widely observed among various materials, which aroused a long-lasting pursuit of the underlining mechanisms governing the structural-property relationship in nanosized materials under mechanical loading. At present, the understanding of atomic-scale deformation mechanism is largely based on MD simulations, which are usually subjected to unrealistically fast strain rates and inaccurate atomic potentials, and thus need to be further validated by laboratory efforts. Although several in-situ nanomechanical testing techniques^{335,336} have been developed recently, they usually suffer from limited resolution due to the difficulties in alleviating vibration and reducing the accessible minimum specimen thickness. Moreover, the intrinsic deformation behavior may be shrouded by undesired extrinsic effects such as surface defects and damages induced by FIB milling, therefore significantly hindering a mechanistic understanding of deformation mechanism in nanomaterials. Thanks to the Nanofactory TEM-STM platform, the atomic-scale structural evolution under mechanical loading can be captured at real time, which is thus capable of offering tremendous details that cannot be obtained by alternative approaches. Some examples on the current researches and future planes will be presented and briefly discussed.

8.1 DISPLACIVE VS. DIFFUSIVE PLASTICITY IN NANOCRYSTALS

Displacive plasticity and GB diffusive plasticity are two major deformation mechanisms in nanocrystalline materials at room temperature. These two deformation mechanisms contradict each other in the sense that the former leads to superior strengths but low ductility while the latter contributes to large creep rates with a compromise in hardness. Therefore, the widely reported transition from dislocation dominated to GB-mediated deformation^{337,338} with decreasing crystal size will result in a crossover in the mechanical property of nanocrystalline materials from strong-yet-‘brittle’ to ductile-but-soft. An extreme example of such transition was observed in sub-10-nm Ag nanoparticles, which demonstrate liquid-like behavior even at room temperature⁴. Then a question arises: will the nanocrystalline materials become strong-and-ductile in the crossover regime where both displacive and diffusional activities thrive? Given that GBs become an important dislocation nucleation source in the nanocrystalline regime^{339,340}, it is rational to assume a close interaction between displacive events and GB diffusion, which has recently been reflected in a temperature dependence of the dislocation nucleation strength in Pd nanowires³⁴¹. Nevertheless, the relationship between displacive and GB diffusive plasticity in the crossover regime has often been considered as a size-dependent competition^{337,342}, while their interaction is still poorly understood.

Recently, we focused on the deformation of individual Ag nanocrystals and show that strong-and-ductile nanocrystals can be obtained in the cross-over regime via a special surface diffusional creep, where diffusion at the surface is activated by dislocation slip events, which, in turn, suppresses plastic instability during subsequent displacive deformation (Figure 8.1). Given that the deformation mechanisms found in individual nanocrystals³⁴³ also apply to those bounded by neighboring grains³⁴⁰, the interaction between displacive and diffusive plasticity should thus

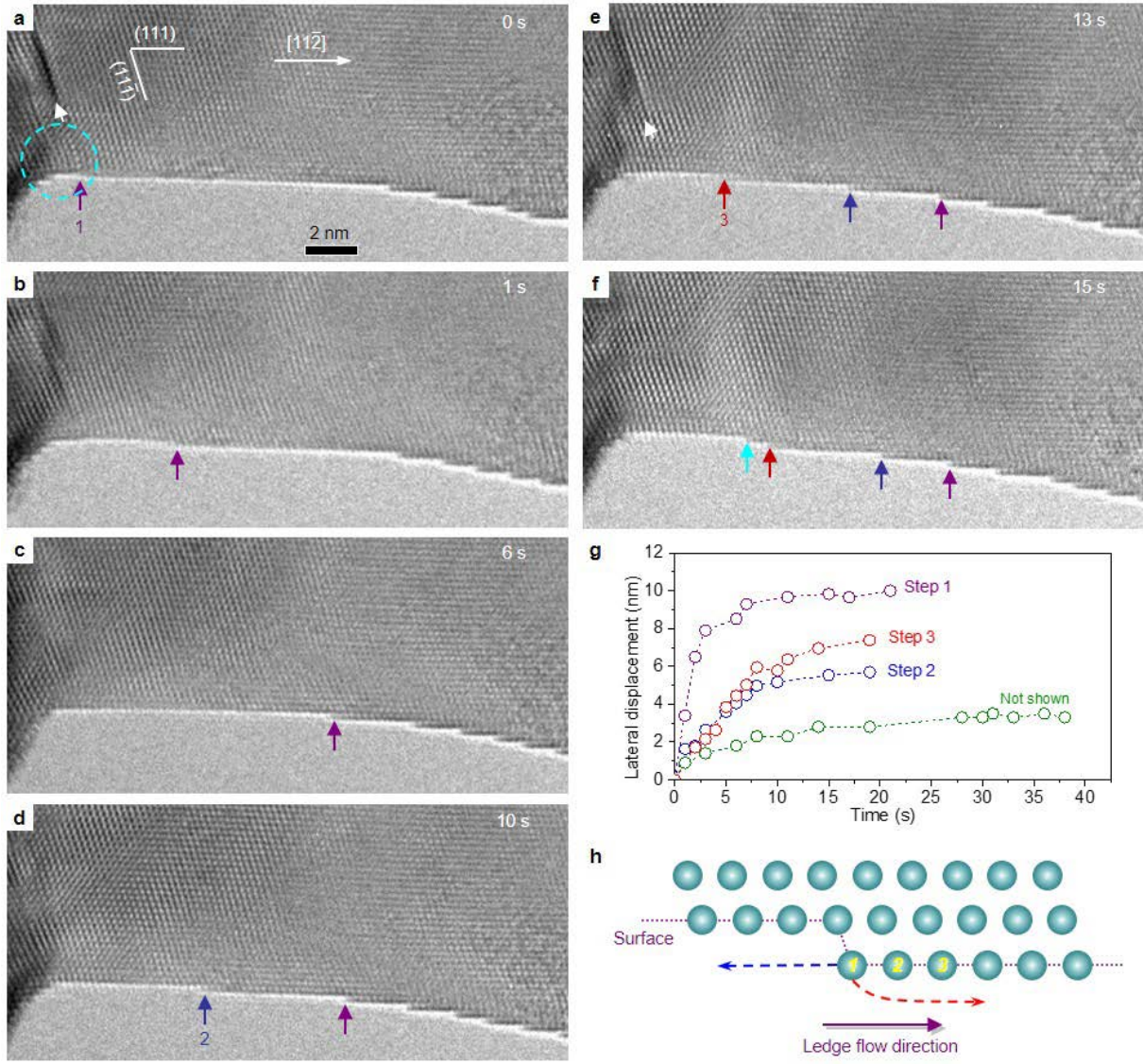


Figure 8.1 Surface diffusive plasticity during tensile deformation of a 20-nm Ag nanocrystal. (a-f) Surface diffusion assisted lateral movement of the steps on a Ag nanocrystal $\{111\}$ surface. Dislocations (pointed by white arrows in a and e) were continuously emitted from the corner enclosed in a cyan circle in a, leading to the formation of surface steps, which quickly moved away from the highly stressed region. Each surface step is tracked by arrows with a specific color. g, Lateral displacement versus time measured from four surface steps, where steps 1-3 correspond to step movements tracked by purple, blue, and red arrows, respectively. The green curve is measured from another surface step that is not shown. (h) Schematic illustration of surface diffusion by sequential hopping of the atoms at a surface step.

also be applicable to bulk nanocrystalline materials. However, the deformation of the later is governed by an ensemble of nanocrystallites, and is thus much more complex than that in an isolated nanocrystal. More effort is still required in the future to explore the impact of this slip-activated interfacial diffusional creep on the mechanical behavior of bulk nanocrystalline materials.

8.2 DEFORMATION TWINNING NUCLEATION AND GROWTH IN BCC NANOCRYSTALS

Unlike fcc metals whose size-dependent deformation map has been well established, the deformation of bcc nanocrystals has been relatively less explored. Due to the complex nature in terms of the non-planar core of screw dislocations and the lack of symmetry in their crystal structure, understandings of the atomistic processes during deformation of bcc metals heavily rely on continuum mechanics models and MD simulations. Recently, direct evidence has been provided to show twinning dominated deformation in bcc W nanocrystals³⁴⁴, however, its nucleation and propagation process, as well as its impact on the ductility are still not clear.

Figure 8.2 demonstrates the nucleation and gradual propagation of a deformation twin in Ta nanocrystal under $\langle 001 \rangle$ tensile loading. The twin embryo was found to have a minimum thickness of 6 $\{112\}$ layers with a twin boundary consisting of steps with a height of 3 $\{112\}$ planes (Figure 8.2 b). The thickening and lateral expansion of the deformation twin were rather reluctant (Figure 8.2c-h). Interestingly, twin boundaries were found to be inclined, which became curved after intersecting the side surface of the Ta NW, causing formation of Moiré patterns by overlapping with the matrix (inset in Figure 8.2d; Figure 8.2i). Such detailed scenario during

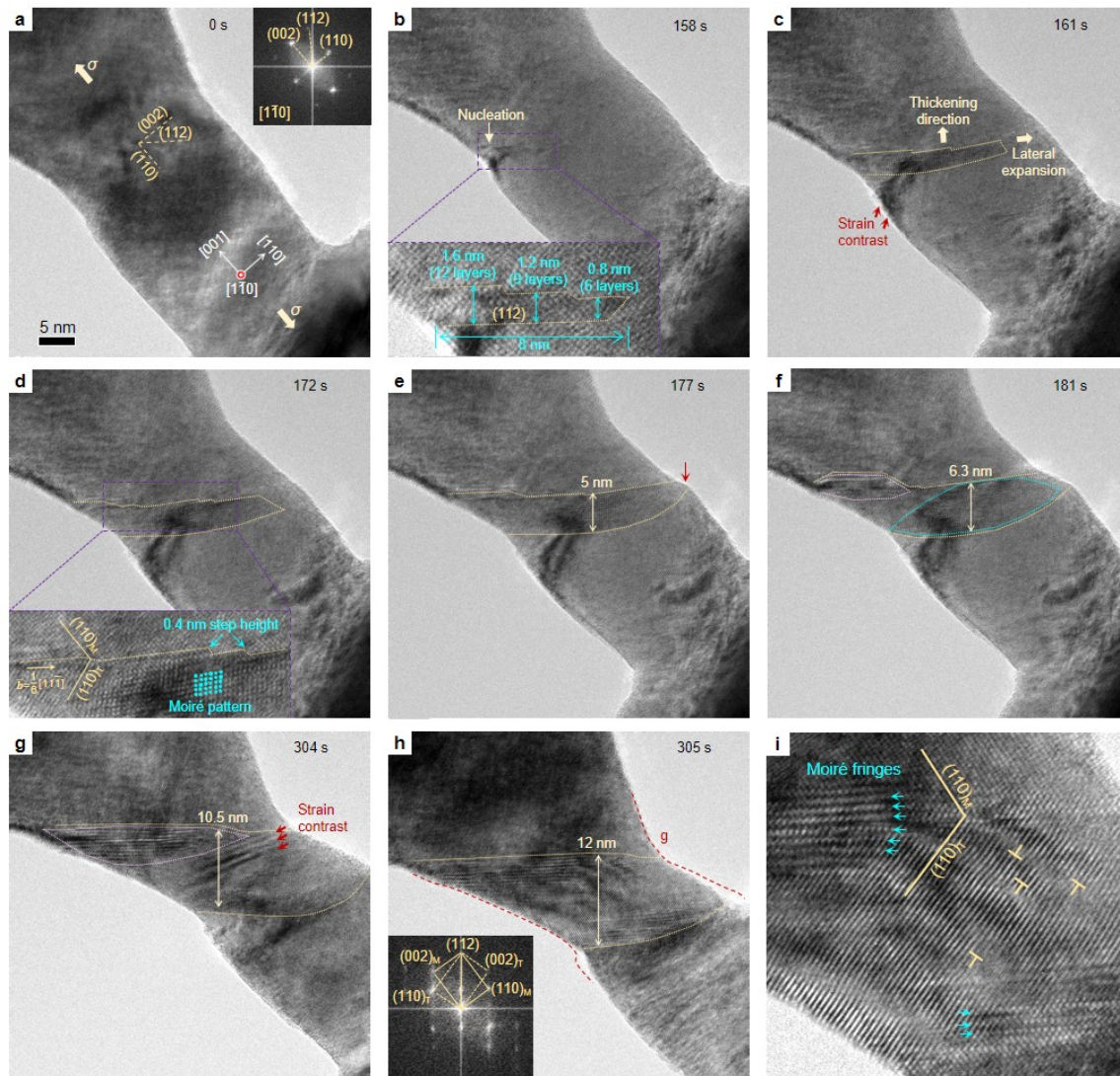


Figure 8.2 Reluctant twin growth in a Ta nanocrystal with size above 20 nm. (a) An as-formed 23-nm wide Ta NW under tensile loading along the [001] direction. (b) Nucleation of a twin embryo with a minimum thickness of six (112) layers and a width of 8 nm (inset in b). (c-h) Slow growth of the deformation twin. The twin boundaries are tracked by yellow dotted lines. Note that the lower twin boundary is inclined, which is curved by intersecting the side surface of the Ta NW. Most regions of the twin lamella exhibited Moiré patterns (cyan dots in d) formed by overlapping of the matrix and the twin. The Moiré-patterned region developed to an approximately elliptical shape (outlined by cyan dotted lines in f), matches the projection of an inclined plane, for example the (101) plane. Meanwhile, a second set of Moiré pattern developed at the upper twin boundary (enclosed by a magenta dotted curves in f and g), due to the formation of an inclined (011) boundary. The lattice strain following twin growth (pointed out by red arrows in c and g) was finally accommodated by penetration of the twin through radial direction of the NW, which was accompanied by an abrupt shape change in the NW (h). The FFT (inset in h) clearly demonstrates a diffraction pattern of a {112} twin. (i) High resolution TEM image of the deformation twin containing a high density of dislocations. Moiré-patterns were found at both twin boundaries (indicated by cyan arrow heads).

deformation twinning in bcc metals has never been revealed before. The formation of inclined twin boundaries is, likely, due to a dislocation-cross-slip-and-dissociation-mediated twin thickening mechanism. Considering that the competition between dislocation plasticity and deformation twinning in bcc metals is highly size dependent, whether further decrease in the crystal size will lead to changes in the deformation twinning nucleation and growth mechanism, as well as the physical origin of this size dependence, is yet to be uncovered.

APPENDIX A

COOLING RATE ESTIMATED BY ATOMS-TO-CONTINUUM SIMULATION

To understand the vitrification process of the liquid and estimate the cooling rate, AtC simulations have been performed by Dr. Hongwei Sheng at George Mason University, where the MD system is coupled to an additional electron temperature field that implements the two-temperature model (TTM)²⁴⁴ for heat transport. It is worth noting that the present experimental approach is capable of vitrifying monatomic metallic liquids on temporal and spatial scales commensurate with those in MD modeling, allowing for a direct comparison between experiment and MD simulation, enabling accurate interpretation of the multi-physics of the cooling process.

A.1 DEVELOPMENT OF A NEW EMBEDDED-ATOM-METHOD (EAM) POTENTIAL FOR TANTALUM

A realistic interatomic potential has been developed for large-scale simulation of Ta. The potential, in the EAM formalism, was developed by fitting the potential energy landscape (PES) of Ta established through extensive *ab initio* calculations based on the density functional theory

(DFT). The interatomic potential was developed in a tabulated form and can be publically obtained from <https://sites.google.com/site/eampotentials/Ta>.

Over 600 reference configurations (typically 96~128 atoms in each configuration) of Ta were employed in the potential fitting process, including equations-of-state of relevant crystal structures, liquid phases, point and interfacial defects, liquid inherent structures, and MGs quenched at various cooling rates, etc., with a special emphasis on the liquid states and phase behavior of Ta. Phonon frequencies and experimental elastic constants of the selected crystals were also taken into account in the fitting. High-precision *ab initio* calculations were performed for each selected atomic configuration, utilizing the pseudopotential and plane-wave method implemented in the Vienna *Ab-initio* Simulation Package (VASP)³⁴⁵. The projector augmented-waves (PAW) method and the generalized-gradient approximation (GGA) were employed in all the VASP calculations, and the Brillouin zone was sampled with $3\times 3\times 3$ Monkhorst-Pack *k*-point grids. The valence electron configuration of Ta in the DFT calculation is $5d^34s^2$.

The EAM potential was optimized by using the force-matching method³⁴⁶ implemented in the potfit package³⁴⁷. The generated EAM parameters were further refined through a recursive method until self-consistent results were reached. Similar techniques have been successfully employed to generate highly optimized EAM potentials for fcc elements and multi-component metallic systems. The as-developed Ta EAM potential accurately predicts the melting temperature of bcc Ta, liquid density, formation of the β -Ta phase as well as many other properties of Ta. More detailed information about the validation and performance of the newly developed EAM potential of Ta will be presented elsewhere.

A.2 ATC SIMULATION OF THE HEAT TRANSPORT

The two-temperature model was used for the AtC computer simulation²⁴⁴. Since heat dissipation is conducted through phonon and electron transport, classic MD is incapable of simulating the electron transport process that dominates the heat transfer in the current setup. In the TTM, the atomistic system, which runs MD simulation, is coupled to an additional electronic system described by the finite-element method. To model the coupling between the electronic system and the atomic system, the following two governing equations are used:

$$\rho_p c_p \dot{T}_p = \kappa_p \nabla^2 T_p - g_{e-p}(T_e - T_p) + \rho_p r_p \quad (\text{A.1})$$

$$\rho_e c_e \dot{T}_e = \kappa_e \nabla^2 T_e - g_{e-p}(T_e - T_p) + \rho_e r_e \quad (\text{A.2})$$

where ρ , c , T , and κ are the density, specific heat, temperature field, and thermal conductivity of phonons (with subscript p) or electrons (with subscript e), respectively. g_{e-p} denotes the electron-phonon coupling parameter, and r is a mass normalized source term, which includes all the external sources of energy exchange events (e.g., the effects of Peltier cooling/heating, laser heating, and Joule heating). Five parameters are needed to implement the AtC model to simulate the vitrification process of Ta. Following the approach of Jones *et al.*²⁴⁴, the five parameters are set as follows.

A.2.1 The phonon heat capacity $\rho_p c_p$

The phonon heat capacity per volume in the classic limit is given by the Dulong-Petit law³⁴⁸:

$$\rho_p c_p = 3k_B/V_\alpha \quad (\text{A.3})$$

where k_B is the Boltzmann constant and V_α is the atomic volume of Ta at a given temperature.

For Ta at 3000 K, $\rho_p c_p$ is calculated to be $2.1 \times 10^6 \text{ J} \cdot \text{m}^{-3} \cdot \text{K}^{-1}$ based on the Dulong-Petit law.

A.2.2 The phonon thermal conductivity κ_p

The thermal conductivity of the phonon system is obtained by conducting classic MD simulation of Ta at desired temperatures (via both the Green-Kubo method, and a direct method employing Fourier's law³⁴⁹). At 3000 K, the thermal conductivity of Ta due to phonons is estimated to be $3.5 \text{ W}\cdot\text{m}^{-1}\cdot\text{K}^{-1}$, which is trivial compared to the experimental thermal conductivity of Ta crystal near its melting point at 3200 K ($67 \text{ W}\cdot\text{m}^{-1}\cdot\text{K}^{-1}$)³⁵⁰. Note that the electron thermal conductivity is about 20 times greater than the phonon conductivity.

A.2.3 The electron heat capacity $\rho_e c_e$

The electron heat capacity per volume is estimated from the free electron density. Assuming the free electrons behave like a kinetic gas:

$$\rho_e c_e = \frac{\pi^2}{2} \frac{n_e k_B}{E_F} T_e = \gamma(n_e) T_e \quad (\text{A.4})$$

where n_e is the number of valence electrons and E_F is the Fermi level. Within the temperature range of interest, $\rho_e c_e$ is assumed to have a constant value of $5.0 \times 10^5 \text{ J}\cdot\text{m}^{-3}\cdot\text{K}^{-1}$. The experimental value³⁵¹ of the electron heat capacity coefficient γ is measured to be $541 \text{ J}\cdot\text{m}^{-3}\cdot\text{K}^{-2}$.

A.2.4 The electron thermal conductivity κ_e

The thermal conductivity of the electron system of Ta is estimated from the Franz–Wiedemann law:

$$\kappa_e = L \sigma T_e = \kappa_0 \frac{T_e}{T_p} \quad (\text{A.5})$$

where σ is the electrical conductivity, and the Lorentz constant is $L=2.443 \times 10^{-8} \text{ W}\cdot\Omega\cdot\text{K}^{-2}$. At 300 K, the electrical conductivity of Ta is about $8.0 \times 10^6 \text{ }\Omega^{-1}\cdot\text{m}^{-1}$, and $\kappa_0=58.6 \text{ W}\cdot\text{m}^{-1}\cdot\text{K}^{-1}$, which

corresponds to the electron thermal conductivity when the electron temperature is at equilibrium with the atomic temperature (i.e., $T_e = T_p$).

A.2.5 The electron-phonon coupling coefficient g_{e-p}

The electron-phonon coupling coefficient is assumed to have a linear relationship with temperature. For Ta, the coupling coefficient is set to be $3.0 \times 10^{17} \text{ J} \cdot \text{m}^{-3} \cdot \text{K}^{-1} \cdot \text{s}^{-1}$, comparable with the experimental electron-phonon coupling parameters for other transition metals³⁵².

A.3 THERMAL CONDUCTIVITY OF TA CRYSTAL AT 3000K BY TTM-MD METHOD

The thermal conductivity is obtained based on the Fourier heat law:

$$\kappa = \frac{-\dot{q}}{\nabla T} \quad (\text{A.6})$$

where \dot{q} is the rate of heat flux. With the parameters prescribed above, the thermal conductivity of Ta at 3000 K is estimated to be $62.6 \text{ W} \cdot \text{m}^{-1} \cdot \text{K}^{-1}$, which is in good agreement with the experimental value³⁵⁰.

A.4 FORMATION OF TA MG BY RAPID LIQUID QUENCHING

The AtC method was used to simulate the cooling process of an $85 \text{ nm} \times 40.8 \text{ nm} \times 13.6 \text{ nm}$ Ta nanowire containing 2,457,600 atoms, without applying periodic boundary conditions. Both ends of the nanowire along the x -axis are connected to heat reservoirs by fixing temperatures (both the atomic temperature and the electronic temperature) to be 300 K. Joule heating is simulated by

injecting electron heat flux into the system, creating a temperature distribution along the nanowire as shown in Figure 4.7a. Quenching processes in scenarios where the heat flux is terminated instantly and within 0.4 ns in a ramp function were simulated. The cooling process starts instantly after Joule heating is zeroed out, which proceeds at a quenching rate on the order of $10^{13-14} \text{ Ks}^{-1}$ (Figure 4.7c and Figure 4.10c). Such an ultrafast cooling rate strongly favors vitrification over crystal growth, leading to the formation of Ta MG.

BIBLIOGRAPHY

- 1 Zaluska, A., Zaluski, L. & Strom-Olsen, J. O. Nanocrystalline magnesium for hydrogen storage. *J. Alloys Compd.* **288**, 217-225 (1999).
- 2 Wang, X. D., Summers, C. J. & Wang, Z. L. Large-scale hexagonal-patterned growth of aligned ZnO nanorods for nano-optoelectronics and nanosensor arrays. *Nano Lett.* **4**, 423-426 (2004).
- 3 Alayoglu, S., Nilekar, A. U., Mavrikakis, M. & Eichhorn, B. Ru-Pt core-shell nanoparticles for preferential oxidation of carbon monoxide in hydrogen. *Nat. Mater.* **7**, 333-338 (2008).
- 4 Sun, J., He, L. B., Lo, Y. C., Xu, T., Bi, H. C., Sun, L. T., Zhang, Z., Mao, S. X. & Li, J. Liquid-like pseudoelasticity of sub-10-nm crystalline silver particles. *Nat. Mater.* **13**, 1007-1012 (2014).
- 5 Zhu, Y., Qin, Q. Q., Xu, F., Fan, F. R., Ding, Y., Zhang, T., Wiley, B. J. & Wang, Z. L. Size effects on elasticity, yielding, and fracture of silver nanowires: In situ experiments. *Phys. Rev. B* **85**, 045443 (2012).
- 6 Ma, E., Wang, Y. M., Lu, Q. H., Sui, M. L., Lu, L. & Lu, K. Strain hardening and large tensile elongation in ultrahigh-strength nano-twinned copper. *Appl. Phys. Lett.* **85**, 4932-4934 (2004).
- 7 Lu, L., Schwaiger, R., Shan, Z. W., Dao, M., Lu, K. & Suresh, S. Nano-sized twins induce high rate sensitivity of flow stress in pure copper. *Acta Mater.* **53**, 2169-2179 (2005).
- 8 Lu, K., Lu, L. & Suresh, S. Strengthening materials by engineering coherent internal boundaries at the nanoscale. *Science* **324**, 349-352 (2009).
- 9 Kawamori, M., Asai, T., Shirai, Y., Yagi, S., Oishi, M., Ichitsubo, T. & Matsubara, E. Three-dimensional nanoelectrode by metal nanowire nonwoven clothes. *Nano Lett.* **14**, 1932-1937 (2014).

- 10 Poizot, P., Laruelle, S., Grugeon, S., Dupont, L. & Tarascon, J. M. Nano-sized transition-metaloxides as negative-electrode materials for lithium-ion batteries. *Nature* **407**, 496-499 (2000).
- 11 Li, H., Huang, X. J., Chen, L. Q., Wu, Z. G. & Liang, Y. A high capacity nano-Si composite anode material for lithium rechargeable batteries. *Electrochem. Solid-State Lett.* **2**, 547-549 (1999).
- 12 Wu, X. L., Jiang, L. Y., Cao, F. F., Guo, Y. G. & Wan, L. J. LiFePO₄ nanoparticles embedded in a nanoporous carbon matrix: superior cathode material for electrochemical energy-storage devices. *Adv. Mater.* **21**, 2710-2714 (2009).
- 13 Simon, P. & Gogotsi, Y. Materials for electrochemical capacitors. *Nat. Mater.* **7**, 845-854 (2008).
- 14 Liu, N., Lu, Z. D., Zhao, J., McDowell, M. T., Lee, H. W., Zhao, W. T. & Cui, Y. A pomegranate-inspired nanoscale design for large-volume-change lithium battery anodes. *Nat. Nanotechnol.* **9**, 187-192 (2014).
- 15 Li, H., Wang, Z. X., Chen, L. Q. & Huang, X. J. Research on advanced materials for Li-ion batteries. *Adv. Mater.* **21**, 4593-4607 (2009).
- 16 Liu, C., Li, F., Ma, L. P. & Cheng, H. M. Advanced materials for energy storage. *Adv. Mater.* **22**, E28-E62 (2010).
- 17 Kasavajjula, U., Wang, C. & Appleby, A. J. Nano- and bulk-silicon-based insertion anodes for lithium-ion secondary cells. *J. Power Sources* **163**, 1003-1039 (2007).
- 18 Arico, A. S., Bruce, P., Scrosati, B., Tarascon, J. M. & Van Schalkwijk, W. Nanostructured materials for advanced energy conversion and storage devices. *Nat. Mater.* **4**, 366-377 (2005).
- 19 Guo, Y. G., Hu, J. S. & Wan, L. J. Nanostructured materials for electrochemical energy conversion and storage devices. *Adv. Mater.* **20**, 2878-2887 (2008).
- 20 Yoo, E., Kim, J., Hosono, E., Zhou, H., Kudo, T. & Honma, I. Large reversible Li storage of graphene nanosheet families for use in rechargeable lithium ion batteries. *Nano Lett.* **8**, 2277-2282 (2008).
- 21 Wu, Z. S., Ren, W. C., Wen, L., Gao, L. B., Zhao, J. P., Chen, Z. P., Zhou, G. M., Li, F. & Cheng, H. M. Graphene anchored with Co₃O₄ nanoparticles as anode of lithium ion batteries with enhanced reversible capacity and cyclic performance. *Acs Nano* **4**, 3187-3194 (2010).

- 22 Ji, L. W., Lin, Z., Alcoutlabi, M. & Zhang, X. W. Recent developments in nanostructured anode materials for rechargeable lithium-ion batteries. *Energy Environ. Sci.* **4**, 2682-2699 (2011).
- 23 Wang, J. Carbon-nanotube based electrochemical biosensors: a review. *Electroanalysis* **17**, 7-14 (2005).
- 24 Sapsford, K. E., Pons, T., Medintz, I. L. & Mattoussi, H. Biosensing with luminescent semiconductor quantum dots. *Sensors* **6**, 925-953 (2006).
- 25 Pumera, M., Ambrosi, A., Bonanni, A., Chng, E. L. K. & Poh, H. L. Graphene for electrochemical sensing and biosensing. *TrAC Trends Anal. Chem.* **29**, 954-965 (2010).
- 26 Pingarron, J. M., Yanez-Sedeno, P. & Gonzalez-Cortes, A. Gold nanoparticle-based electrochemical biosensors. *Electrochem. Acta* **53**, 5848-5866 (2008).
- 27 Yang, J. J., Pickett, M. D., Li, X. M., Ohlberg, D. A. A., Stewart, D. R. & Williams, R. S. Memristive switching mechanism for metal/oxide/metal nanodevices. *Nat. Nanotechnol.* **3**, 429-433 (2008).
- 28 Strukov, D. B., Snider, G. S., Stewart, D. R. & Williams, R. S. The missing memristor found. *Nature* **453**, 80-83 (2008).
- 29 Wuttig, M. & Yamada, N. Phase-change materials for rewriteable data storage. *Nat. Mater.* **6**, 824-832 (2007).
- 30 Siegrist, T., Jost, P., Volker, H., Woda, M., Merkelbach, P., Schlockermann, C. & Wuttig, M. Disorder-induced localization in crystalline phase-change materials. *Nat. Mater.* **10**, 202-207 (2011).
- 31 Lee, S. H., Jung, Y. & Agarwal, R. Highly scalable non-volatile and ultra-lowpower phase-change nanowire memory. *Nat. Nanotechnol.* **2**, 626-630 (2007).
- 32 Jang, D. C. & Greer, J. R. Transition from a strong-yet-brittle to a strong-and-ductile state by size reduction of metallic glasses. *Nat. Mater.* **9**, 215-219 (2010).
- 33 Luo, J. H., Wu, F. F., Huang, J. Y., Wang, J. Q. & Mao, S. X. Superelongation and atomic chain formation in nanosized metallic glass. *Phys. Rev. Lett.* **104**, 215503 (2010).
- 34 Greer, J. R. & De Hosson, J. T. M. Plasticity in small-sized metallic systems: Intrinsic versus extrinsic size effect. *Prog. Mater. Sci.* **56**, 654-724 (2011).
- 35 Tian, L., Shan, Z. W. & Ma, E. Ductile necking behavior of nanoscale metallic glasses under uniaxial tension at room temperature. *Acta Mater.* **61**, 4823-4830 (2013).

- 36 Guo, H., Yan, P. F., Wang, Y. B., Tan, J., Zhang, Z. F., Sui, M. L. & Ma, E. Tensile ductility and necking of metallic glass. *Nat Mater* **6**, 735-739 (2007).
- 37 Shan, Z. W., Li, J., Cheng, Y. Q., Minor, A. M., Asif, S. A. S., Warren, O. L. & Ma, E. Plastic flow and failure resistance of metallic glass: Insight from in situ compression of nanopillars. *Phys. Rev. B* **77**, 155419 (2008).
- 38 Inoue, A., Zhang, T. & Masumoto, T. Al-La-Ni amorphous alloys with a wide supercooled liquid region. *Mater. Trans., JIM* **30**, 965-972 (1989).
- 39 Wang, W. H., Dong, C. & Shek, C. H. Bulk metallic glasses. *Mater. Sci. Eng., R* **44**, 45-89 (2004).
- 40 Cohen, M. H. & Turnbull, D. Composition requirements for glass formation in metallic and ionic systems. *Nature* **189**, 131-132 (1961).
- 41 Inoue, A. Stabilization of metallic supercooled liquid and bulk amorphous alloys. *Acta Mater.* **48**, 279-306 (2000).
- 42 Kim, P., Shi, L., Majumdar, A. & McEuen, P. L. Thermal transport measurements of individual multiwalled nanotubes. *Phys. Rev. Lett.* **87**, 215502 (2001).
- 43 Aga, R., Morris, J., Hoyt, J. & Mendeleev, M. Quantitative parameter-free prediction of simulated crystal-nucleation times. *Phys. Rev. Lett.* **96**, 245701 (2006).
- 44 Trudu, F., Donadio, D. & Parrinello, M. Freezing of a Lennard-Jones fluid: from nucleation to spinodal regime. *Phys. Rev. Lett.* **97**, 105701 (2006).
- 45 Kang, B. & Ceder, G. Battery materials for ultrafast charging and discharging. *Nature* **458**, 190-193 (2009).
- 46 Taberna, L., Mitra, S., Poizot, P., Simon, P. & Tarascon, J. M. High rate capabilities Fe₃O₄-based Cu nano-architected electrodes for lithium-ion battery applications. *Nat. Mater.* **5**, 567-573 (2006).
- 47 Chan, C. K., Peng, H., Liu, G., McIlwrath, K., Zhang, X. F., Huggins, R. A. & Cui, Y. High-performance lithium battery anodes using silicon nanowires. *Nat Nano* **3**, 31-35 (2008).
- 48 Zhou, G. M., Wang, D. W., Li, F., Zhang, L. L., Li, N., Wu, Z. S., Wen, L., Lu, G. Q. & Cheng, H. M. Graphene-wrapped Fe₃O₄ anode material with improved reversible capacity and cyclic stability for lithium ion batteries. *Chem. Mater.* **22**, 5306-5313 (2010).
- 49 Ryu, I., Choi, J. W., Cui, Y. & Nix, W. D. Size-dependent fracture of Si nanowire battery anodes. *J. Mech. Phys. Solids* **59**, 1717-1730 (2011).

- 50 Lee, S. W., McDowell, M. T., Berla, L. A., Nix, W. D. & Cui, Y. Fracture of crystalline silicon nanopillars during electrochemical lithium insertion. *P. Natl. Acad. Sci. USA* **109**, 4080-4085 (2012).
- 51 Ryu, J. H., Kim, J. W., Sung, Y. E. & Oh, S. M. Failure modes of silicon powder negative electrode in lithium secondary batteries. *Electrochem. Solid-State Lett.* **7**, A306-A309 (2004).
- 52 Mukhopadhyay, A. & Sheldon, B. W. Deformation and stress in electrode materials for Li-ion batteries. *Prog. Mater. Sci.* **63**, 58-116 (2014).
- 53 Tarascon, J. M. & Armand, M. Issues and challenges facing rechargeable lithium batteries. *Nature* **414**, 359-367 (2001).
- 54 Brazier, A., Dupont, L., Dantras-Laffont, L., Kuwata, N., Kawamura, J. & Tarascon, J. M. First cross-section observation of an all solid-state lithium-ion “nanobattery” by transmission electron microscopy. *Chem. Mater.* **20**, 2352-2359 (2008).
- 55 Papon, P., Leblond, J. & Meijer, P. H. E. *The physics of Phase Transitions: Concept and Applications*. second edn, (Springer, 2006).
- 56 Donati, C., Douglas, J. F., Kob, W., Plimpton, S. J., Poole, P. H. & Glotzer, S. C. Stringlike cooperative motion in a supercooled liquid. *Phys. Rev. Lett.* **80**, 2338-2341 (1998).
- 57 Vollmayr, K., Kob, W. & Binder, K. Cooling-rate effects in amorphous silica: A computer-simulation study. *Phys. Rev. B* **54**, 15808-15827 (1996).
- 58 Matsumoto, M., Saito, S. & Ohmine, I. Molecular dynamics simulation of the ice nucleation and growth process leading to water freezing. *Nature* **416**, 409-413 (2002).
- 59 Zhang, H. Z., Gilbert, B., Huang, F. & Banfield, J. F. Water-driven structure transformation in nanoparticles at room temperature. *Nature* **424**, 1025-1029 (2003).
- 60 Oh, S. H., Kauffmann, Y., Scheu, C., Kaplan, W. D. & Ruhle, M. Ordered liquid aluminum at the interface with sapphire. *Science* **310**, 661-663 (2005).
- 61 Kim, J. S., LaGrange, T., Reed, B. W., Taheri, M. L., Armstrong, M. R., King, W. E., Browning, N. D. & Campbell, G. H. Imaging of transient structures using nanosecond in situ TEM. *Science* **321**, 1472-1475 (2008).
- 62 Fujita, T., Guan, P. F., McKenna, K., Lang, X. Y., Hirata, A., Zhang, L., Tokunaga, T., Arai, S., Yamamoto, Y., Tanaka, N., Ishikawa, Y., Asao, N., Erlebacher, J. & Chen, M. W. Atomic origins of the high catalytic activity of nanoporous gold. *Nat. Mater.* **11**, 775-780 (2012).

- 63 Boston, R., Schnepf, Z., Nemoto, Y., Sakka, Y. & Hall, S. R. In situ TEM observation of a microcrucible mechanism of nanowire growth. *Science* **344**, 623-626 (2014).
- 64 Liao, H. G., Zherebetsky, D., Xin, H. L., Czarnik, C., Ercius, P., Elmlund, H., Pan, M., Wang, L. W. & Zheng, H. M. Facet development during platinum nanocube growth. *Science* **345**, 916-919 (2014).
- 65 Liao, H. G., Cui, L. K., Whitelam, S. & Zheng, H. M. Real-time imaging of Pt₃Fe nanorod growth in solution. *Science* **336**, 1011-1014 (2012).
- 66 Hemley, R. J., Jephcoat, A. P., Mao, H. K., Ming, L. C. & Manghnani, M. H. Pressure-induced amorphization of crystalline silica. *Nature* **334**, 52-54 (1988).
- 67 Deb, S. K., Wilding, M., Somayazulu, M. & McMillan, P. F. Pressure-induced amorphization and an amorphous-amorphous transition in densified porous silicon. *Nature* **414**, 528-530 (2001).
- 68 Johnson, W. L. Thermodynamic and kinetic aspects of the crystal to glass transformation in metallic materials. *Prog. Mater. Sci.* **30**, 81-134 (1986).
- 69 Broughton, J. O., Gilmer, G. H. & Jackson, K. A. Crystallization rates of a Lennard-Jones liquid. *Phys. Rev. Lett.* **49**, 1496-1500 (1982).
- 70 Goodenough, J. B. & Park, K.-S. The Li-ion rechargeable battery: a perspective. *J. Am. Chem. Soc.* **135**, 1167-1176 (2013).
- 71 Yu, H. C., Ling, C., Bhattacharya, J., Thomas, J. C., Thornton, K. & Van der Ven, A. Designing the next generation high capacity battery electrodes. *Energy Environ. Sci.* **7**, 1760-1768 (2014).
- 72 Sheng, H. W., Luo, W. K., Alamgir, F. M., Bai, J. M. & Ma, E. Atomic packing and short-to-medium-range order in metallic glasses. *Nature* **439**, 419-425 (2006).
- 73 Liu, X. H., Zhang, L. Q., Zhong, L., Liu, Y., Zheng, H., Wang, J. W., Cho, J. H., Dayeh, S. A., Picraux, S. T., Sullivan, J. P., Mao, S. X., Ye, Z. Z. & Huang, J. Y. Ultrafast electrochemical lithiation of individual Si nanowire anodes. *Nano Lett* **11**, 2251-2258 (2011).
- 74 Liu, X. H., Zheng, H., Zhong, L., Huang, S., Karki, K., Zhang, L. Q., Liu, Y., Kushima, A., Liang, W. T., Wang, J. W., Cho, J. H., Epstein, E., Dayeh, S. A., Picraux, S. T., Zhu, T., Li, J., Sullivan, J. P., Cumings, J., Wang, C., Mao, S. X., Ye, Z. Z., Zhang, S. & Huang, J. Y. Anisotropic swelling and fracture of silicon nanowires during lithiation. *Nano Lett.* **11**, 3312-3318 (2011).
- 75 Ferreira, P. J., Mitsuishi, K. & Stach, E. A. *In Situ* transmission electron microscopy. *MRS Bull.* **33**, 83-90 (2008).

- 76 Kodambaka, S., Tersoff, J., Reuter, M. C. & Ross, F. M. Germanium nanowire growth below the eutectic temperature. *Science* **316**, 729-732 (2007).
- 77 Chou, Y. C., Hillerich, K., Tersoff, J., Reuter, M. C., Dick, K. A. & Ross, F. M. Atomic-scale variability and control of III-V nanowire growth kinetics. *Science* **343**, 281-284 (2014).
- 78 Wen, C. Y., Reuter, M. C., Bruley, J., Tersoff, J., Kodambaka, S., Stach, E. A. & Ross, F. M. Formation of compositionally abrupt axial heterojunctions in silicon-germanium nanowires. *Science* **326**, 1247-1250 (2009).
- 79 Kim, B. J., Tersoff, J., Kodambaka, S., Reuter, M. C., Stach, E. A. & Ross, F. M. Kinetics of individual nucleation events observed in nanoscale vapor-liquid-solid growth. *Science* **322**, 1070-1073 (2008).
- 80 Helveg, S., Lopez-Cartes, C., Sehested, J., Hansen, P. L., Clausen, B. S., Rostrup-Nielsen, J. R., Abild-Pedersen, F. & Nørskov, J. K. Atomic-scale imaging of carbon nanofibre growth. *Nature* **427**, 426-429 (2004).
- 81 Oh, S. H., Chisholm, M. F., Kauffmann, Y., Kaplan, W. D., Luo, W. D., Ruhle, M. & Scheu, C. Oscillatory mass transport in vapor-liquid-solid growth of sapphire nanowires. *Science* **330**, 489-493 (2010).
- 82 Nielsen, M. H., Aloni, S. & De Yoreo, J. J. In situ TEM imaging of CaCO_3 nucleation reveals coexistence of direct and indirect pathways. *Science* **345**, 1158-1162 (2014).
- 83 Zheng, H. M., Smith, R. K., Jun, Y. W., Kisielowski, C., Dahmen, U. & Alivisatos, A. P. Observation of single colloidal platinum nanocrystal growth trajectories. *Science* **324**, 1309-1312 (2009).
- 84 Hansen, P. L., Wagner, J. B., Helveg, S., Rostrup-Nielsen, J. R., Clausen, B. S. & Topsoe, H. Atom-resolved imaging of dynamic shape changes in supported copper nanocrystals. *Science* **295**, 2053-2055 (2002).
- 85 Baldi, A., Narayan, T. C., Koh, A. L. & Dionne, J. A. In situ detection of hydrogen-induced phase transitions in individual palladium nanocrystals. *Nat. Mater.* **13**, 1143-1148 (2014).
- 86 Zhang, L. X., Miller, B. K. & Crozier, P. A. Atomic level in situ observation of surface amorphization in anatase nanocrystals during light irradiation in water vapor. *Nano Lett.* **13**, 679-684 (2013).
- 87 Yoshida, H., Kuwauchi, Y., Jinschek, J. R., Sun, K. J., Tanaka, S., Kohyama, M., Shimada, S., Haruta, M. & Takeda, S. Visualizing gas molecules interacting with supported nanoparticulate catalysts at reaction conditions. *Science* **335**, 317-319 (2012).

- 88 Kuwauchi, Y., Yoshida, H., Akita, T., Haruta, M. & Takeda, S. Intrinsic catalytic structure of gold nanoparticles supported on TiO₂. *Angew. Chem. Int. Ed.* **51**, 7729-7733 (2012).
- 89 Kuwauchi, Y., Takeda, S., Yoshida, H., Sun, K., Haruta, M. & Kohno, H. Stepwise displacement of catalytically active gold nanoparticles on cerium oxide. *Nano Lett.* **13**, 3073-3077 (2013).
- 90 Nam, S. W., Chung, H. S., Lo, Y. C., Qi, L., Li, J., Lu, Y., Johnson, A. T. C., Jung, Y. W., Nukala, P. & Agarwal, R. Electrical wind force-driven and dislocation-templated amorphization in phase-change nanowires. *Science* **336**, 1561-1566 (2012).
- 91 Xu, Z., Bando, Y., Wang, W. L., Bai, X. D. & Golberg, D. Real-time in situ HRTEM-resolved resistance switching of Ag₂S nanoscale ionic conductor. *Acs Nano* **4**, 2515-2522 (2010).
- 92 Jung, Y. W., Nam, S. W. & Agarwal, R. High-resolution transmission electron microscopy study of electrically-driven reversible phase change in Ge₂Sb₂Te₅ nanowires. *Nano Lett.* **11**, 1364-1368 (2011).
- 93 Gao, P., Nelson, C. T., Jokisaari, J. R., Zhang, Y., Baek, S. H., Bark, C. W., Wang, E., Liu, Y. M., Li, J. Y., Eom, C. B. & Pan, X. Q. Direct Observations of Retention Failure in Ferroelectric Memories. *Adv. Mater.* **24**, 1106-1110 (2012).
- 94 Gao, P., Nelson, C. T., Jokisaari, J. R., Baek, S. H., Bark, C. W., Zhang, Y., Wang, E. G., Schlom, D. G., Eom, C. B. & Pan, X. Q. Revealing the role of defects in ferroelectric switching with atomic resolution. *Nat. Commun.* **2**, 6 (2011).
- 95 Eswaramoorthy, S. K., Howe, J. M. & Muralidharan, G. In situ determination of the nanoscale chemistry and behavior of solid-liquid systems. *Science* **318**, 1437-1440 (2007).
- 96 Holmberg, V. C., Panthani, M. G. & Korgel, B. A. Phase Transitions, Melting Dynamics, and Solid-State Diffusion in a Nano Test Tube. *Science* **326**, 405-407 (2009).
- 97 Sohn, S., Jung, Y., Xie, Y., Osuji, C., Schroers, J. & Cha, J. J. Nanoscale size effects in crystallization of metallic glass nanorods. *Nat. Commun.* **6**, 8157-8157 (2015).
- 98 Zheng, H. M., Rivest, J. B., Miller, T. A., Sadtler, B., Lindenberg, A., Toney, M. F., Wang, L. W., Kisielowski, C. & Alivisatos, A. P. Observation of transient structural-transformation dynamics in a Cu₂S nanorod. *Science* **333**, 206-209 (2011).
- 99 Lei, Y., Sun, J., Liu, H., Cheng, X., Chen, F. & Liu, Z. Atomic mechanism of predictable phase transition in dual-phase H₂Ti₃O₇/TiO₂ (B) nanofiber: an in situ heating TEM investigation. *Chem. Eur. J.* **20**, 11313-11317 (2014).

- 100 Wang, S. J., Wang, H., Du, K., Zhang, W., Sui, M. L. & Mao, S. X. Deformation-induced structural transition in body-centred cubic molybdenum. *Nat. Commun.* **5**, 3433 (2014).
- 101 Bataillard, L., Bidaux, J. E. & Gotthard, R. Interaction between microstructure and multiple-step transformation in binary NiTi alloys using in-situ transmission electron microscopy observations. *Philos. Mag. A* **78**, 327-344 (1998).
- 102 Zhang, J. X., Xiang, B., He, Q., Seidel, J., Zeches, R. J., Yu, P., Yang, S. Y., Wang, C. H., Chu, Y. H., Martin, L. W., Minor, A. M. & Ramesh, R. Large field-induced strains in a lead-free piezoelectric material. *Nat. Nanotechnol.* **6**, 97-101 (2011).
- 103 Johnson, W. L. Bulk glass-forming metallic alloys: Science and technology. *MRS Bull.* **24**, 42-56 (1999).
- 104 Liu, Y. H., Wang, G., Wang, R. J., Zhao, D. Q., Pan, M. X. & Wang, W. H. Super plastic bulk metallic glasses at room temperature. *Science* **315**, 1385-1388 (2007).
- 105 Demetriou, M. D., Launey, M. E., Garrett, G., Schramm, J. P., Hofmann, D. C., Johnson, W. L. & Ritchie, R. O. A damage-tolerant glass. *Nat. Mater.* **10**, 123-128 (2011).
- 106 Busch, R., Schroers, J. & Wang, W. H. Thermodynamics and kinetics of bulk metallic glass. *MRS Bull.* **32**, 620-623 (2007).
- 107 Inoue, A. High-strength bulk amorphous-alloys with low critical cooling rates. *Mater. Trans. JIM* **36**, 866-875 (1995).
- 108 Busch, R., Liu, W. & Johnson, W. L. Thermodynamics and kinetics of the Mg₆₅Cu₂₅Y₁₀ bulk metallic glass forming liquid. *J. Appl. Phys.* **83**, 4134-4141 (1998).
- 109 Angell, C. A. Formation of glasses from liquids and biopolymers. *Science* **267**, 1924-1935 (1995).
- 110 Klement, W., Willens, R. H. & Duwez, P. Non-crystalline structure in solidified gold-silicon alloys. *Nature* **187**, 869-870 (1960).
- 111 Inoue, A. & Nishiyama, N. Extremely low critical cooling rates of new Pd-Cu-P base amorphous alloys. *Materials Science and Engineering a-Structural Materials Properties Microstructure and Processing* **226**, 401-405 (1997).
- 112 Li, J. H., Dai, Y., Cui, Y. Y. & Liu, B. X. Atomistic theory for predicting the binary metallic glass formation. *Mater. Sci. Eng. R* **72**, 1-28 (2011).
- 113 Inoue, A. & Zhang, W. Formation, thermal stability and mechanical properties of Cu-Zr and Cu-Hf binary glassy alloy rods. *Mater. Trans.* **45**, 584-587 (2004).
- 114 Greer, A. L. Confusion by design. *Nature* **366**, 303-304 (1993).

- 115 Lu, Z. P. & Liu, C. T. A new glass-forming ability criterion for bulk metallic glasses. *Acta Mater.* **50**, 3501-3512 (2002).
- 116 Na, J. H., Demetriou, M. D., Floyd, M., Hoff, A., Garrett, G. R. & Johnson, W. L. Compositional landscape for glass formation in metal alloys. *P. Natl. Acad. Sci. USA* **111**, 9031-9036 (2014).
- 117 Senkov, O. N. Correlation between fragility and glass-forming ability of metallic alloys. *Phys. Rev. B* **76**, 104202 (2007).
- 118 Li, Y., Guo, Q., Kalb, J. A. & Thompson, C. V. Matching glass-forming ability with the density of the amorphous phase. *Science* **322**, 1816-1819 (2008).
- 119 Orava, J. & Greer, A. L. Fast and slow crystal growth kinetics in glass-forming melts. *J. Chem. Phys.* **140**, 214504 (2014).
- 120 Xi, X. K., Li, L. L., Zhang, B., Wang, W. H. & Wu, Y. Correlation of atomic cluster symmetry and glass-forming ability of metallic glass. *Phys. Rev. Lett.* **99**, 095501 (2007).
- 121 Hu, Y. C., Li, F. X., Li, M. Z., Bai, H. Y. & Wang, W. H. Five-fold symmetry as indicator of dynamic arrest in metallic glass-forming liquids. *Nat. Commun.* **6**, 8310 (2015).
- 122 Cheng, Y. Q. & Ma, E. Atomic-level structure and structure-property relationship in metallic glasses. *Prog. Mater. Sci.* **56**, 379-473 (2011).
- 123 Mauro, N. A., Blodgett, M., Johnson, M. L., Vogt, A. J. & Kelton, K. F. A structural signature of liquid fragility. *Nat. Commun.* **5**, 4616 (2014).
- 124 Li, Y., Poon, S. J., Shiflet, G. J., Xu, J., Kim, D. H. & Loffler, J. F. Formation of bulk metallic glasses and their composites. *MRS Bull.* **32**, 624-628 (2007).
- 125 Kui, H. W., Greer, A. L. & Turnbull, D. Formation of bulk metallic glass by fluxing. *Appl. Phys. Lett.* **45**, 615-616 (1984).
- 126 Inoue, A., Nishiyama, N. & Kimura, H. Preparation and thermal stability of bulk amorphous Pd₄₀Cu₃₀Ni₁₀P₂₀ alloy cylinder of 72 mm in diameter. *Mater. Trans. JIM* **38**, 179-183 (1997).
- 127 Peker, A. & Johnson, W. L. A highly processable metallic-glass-Zr_{41.2}Ti_{13.8}Cu_{12.5}Ni_{10.0}Be_{22.5}. *Appl. Phys. Lett.* **63**, 2342-2344 (1993).
- 128 Inoue, A., Zhang, T., Nishiyama, N., Ohba, K. & Masumoto, T. Preparation of 16 mm diameter rod of amorphous Zr₆₅Al_{7.5}Ni₁₀Cu_{17.5} alloy. *Mater. Trans. JIM* **34**, 1234-1237 (1993).

- 129 Xu, D. H., Duan, G. & Johnson, W. L. Unusual glass-forming ability of bulk amorphous alloys based on ordinary metal copper. *Phys. Rev. Lett.* **92**, 245504 (2004).
- 130 Jia, P., Guo, H., Li, Y., Xu, J. & Ma, E. A new Cu-Hf-Al ternary bulk metallic glass with high glass forming ability and ductility. *Scripta Mater.* **54**, 2165-2168 (2006).
- 131 Tan, H., Zhang, Y., Ma, D., Feng, Y. P. & Li, Y. Optimum glass formation at off-eutectic composition and its relation to skewed eutectic coupled zone in the La based La-Al-(Cu,Ni) pseudo ternary system. *Acta Mater.* **51**, 4551-4561 (2003).
- 132 Guo, F. Q., Poon, S. J. & Shiflet, G. J. Metallic glass ingots based on yttrium. *Appl. Phys. Lett.* **83**, 2575-2577 (2003).
- 133 Park, E. S. & Kim, D. H. Formation of Mg-Cu-Ni-Ag-Zn-Y-Gd bulk glassy alloy by casting into cone-shaped copper mold in air atmosphere. *J. Mater. Res.* **20**, 1465-1469 (2005).
- 134 Ma, H., Shi, L. L., Xu, J., Li, Y. & Ma, E. Discovering inch-diameter metallic glasses in three-dimensional composition space. *Appl. Phys. Lett.* **87**, 181915 (2005).
- 135 Shen, J., Chen, Q. J., Sun, J. F., Fan, H. B. & Wang, G. Exceptionally high glass-forming ability of an FeCoCrMoCBY alloy. *Appl. Phys. Lett.* **86**, 151907 (2005).
- 136 Ponnambalam, V., Poon, S. J. & Shiflet, G. J. Fe-based bulk metallic glasses with diameter thickness larger than one centimeter. *J. Mater. Res.* **19**, 1320-1323 (2004).
- 137 Lu, Z. P., Liu, C. T., Thompson, J. R. & Porter, W. D. Structural amorphous steels. *Phys. Rev. Lett.* **92**, 049901 (2004).
- 138 Men, H., Pang, S. J. & Zhang, T. Effect of Er doping on glass-forming ability of Co₅₀Cr₁₅Mo₁₄C₁₅B₆ alloy. *J. Mater. Res.* **21**, 958-961 (2006).
- 139 Guoa, F. Q., Wang, H. J., Poon, S. J. & Shiflet, G. J. Ductile titanium-based glassy alloy ingots. *Appl. Phys. Lett.* **86**, 091907 (2005).
- 140 Park, E. S. & Kim, D. H. Formation of Ca-Mg-Zn bulk glassy alloy by casting into cone-shaped copper mold. *J. Mater. Res.* **19**, 685-688 (2004).
- 141 Schroers, J. & Johnson, W. L. Ductile bulk metallic glass. *Phys. Rev. Lett.* **93**, 255506 (2004).
- 142 Ashkenazy, Y. & Averbach, R. S. Kinetic stages in the crystallization of deeply undercooled body-centered-cubic and face-centered-cubic metals. *Acta Mater.* **58**, 524-530 (2010).

- 143 Chan, W. L., Averback, R. S., Cahill, D. G. & Ashkenazy, Y. Solidification velocities in deeply undercooled silver. *Phys. Rev. Lett.* **102**, 095701 (2009).
- 144 Busch, R., Masuhr, A., Bakke, E. & Johnson, W. L. Bulk metallic glass formation from strong liquids. *Mater. Sci. Forum* **269**, 547-552 (1998).
- 145 Hauser, J. Amorphous nickel films getter sputtered at 25°K. *Phys. Rev. B* **17**, 1908-1912 (1978).
- 146 Hilsch, R. *Non-Crystalline Solids*. 348 (J. Wiley and Sons, 1960).
- 147 Buckel, W. & Hilsch, R. Influence of the condensation at low temperatures on the electric resistance and the superconductivity for different metals. *Z. Phys.* **138**, 109-120 (1954).
- 148 Stella, K., Bürstel, D., Franzka, S., Posth, O. & Diesing, D. Preparation and properties of thin amorphous tantalum films formed by small e-beam evaporators. *J. Phys. D Appl. Phys.* **42**, 135417 (2009).
- 149 Wang, Z., Li, X., Gao, M. & Zeng, X. One-step preparation of amorphous iron nanoparticles by laser ablation. *Power Technol.* **215-216**, 147-150 (2012).
- 150 Holz, M., Ziemann, P. & Buckel, W. Direct evidence for amorphization of pure gallium by low-temperature ion irradiation. *Phys. Rev. Lett.* **51**, 1584-1587 (1983).
- 151 Shimizu, K., Kawakatsut, H. & Kanayat, K. Contamination layers formed by argon ion bombardment. *J. Phys. D Appl. Phys.* **8**, 1453-1459 (1975).
- 152 Suslick, K. S., Choe, S. B., Cichowlas, A. A. & Grinstaff, M. W. Sonochemical synthesis of amorphous iron. *Nature* **353**, 414-416 (1991).
- 153 Koltypin, Y., Katabi, G., Cao, X., Prozorov, R. & Gedanken, A. Sonochemical preparation of amorphous nickel. *J. Non-Cryst. Solids* **201**, 159-162 (1996).
- 154 Han, S., Zhao, L., Jiang, Q. & Lian, J. Deformation-induced localized solid-state amorphization in nanocrystalline nickel. *Sci Rep* **2**, 493 (2012).
- 155 Johnson, W. L. Fundamental aspects of bulk metallic glass formation in multicomponent alloys. *Mater. Sci. Forum* **225-227**, 35-50 (1996).
- 156 Greer, L. A. Metallic glasses. *Science* **267**, 1947-1953 (1995).
- 157 Davies, H. A., Aucote, J. & Hull, J. B. Amorphous nickel produced by splat quenching. *Nature* **246**, 13-14 (1973).
- 158 Ashby, M. F. & Jones, D. R. *Engineering Materials 2: An Introduction to Microstructures, Processing and Design*. (Pergamon, 1986).

- 159 Bhat, M. H., Molinero, V., Soignard, E., Solomon, V. C., Sastry, S., Yarger, J. L. & Angell, C. A. Vitrification of a monatomic metallic liquid. *Nature* **448**, 787-790 (2007).
- 160 Kim, Y. W., Lin, H. M. & Kelly, T. F. Amorphous solidification of pure metals in submicron spheres. *Acta Metall.* **37**, 247-255 (1989).
- 161 Zhao, K. J., Wang, W. L., Gregoire, J., Pharr, M., Suo, Z. G., Vlassak, J. J. & Kaxiras, E. Lithium-assisted plastic deformation of silicon electrodes in lithium-ion batteries: a first-principles theoretical study. *Nano Lett.* **11**, 2962-2967 (2011).
- 162 Zhao, K. J., Tritsarlis, G. A., Pharr, M., Wang, W. L., Okeke, O., Suo, Z. G., Vlassak, J. J. & Kaxiras, E. Reactive flow in silicon electrodes assisted by the insertion of lithium. *Nano Lett.* **12**, 4397-4403 (2012).
- 163 Zhao, K. J., Pharr, M., Wan, Q., Wang, W. L., Kaxiras, E., Vlassak, J. J. & Suo, Z. G. Concurrent reaction and plasticity during initial lithiation of crystalline silicon in lithium-ion batteries. *J. Electrochem. Soc.* **159**, A238-A243 (2012).
- 164 Zhao, K. J., Pharr, M., Cai, S. Q., Vlassak, J. J. & Suo, Z. G. Large plastic deformation in high-capacity lithium-ion batteries caused by charge and discharge. *J. Am. Ceram. Soc.* **94**, S226-S235 (2011).
- 165 Su, X., Wu, Q. L., Li, J. C., Xiao, X. C., Lott, A., Lu, W. Q., Sheldon, B. W. & Wu, J. Silicon-based nanomaterials for lithium-ion batteries: a review. *Adv. Energy Mater.* **4**, 1300882 (2014).
- 166 Idota, Y., Kubota, T., Matsufuji, A., Maekawa, Y. & Miyasaka, T. Tin-based amorphous oxide: A high-capacity lithium-ion-storage material. *Science* **276**, 1395-1397 (1997).
- 167 Courtney, I. A. & Dahn, J. R. Electrochemical and in situ x-ray diffraction studies of the reaction of lithium with tin oxide composites. *J. Electrochem. Soc.* **144**, 2045-2052 (1997).
- 168 Graetz, J., Ahn, C. C., Yazami, R. & Fultz, B. Nanocrystalline and thin film germanium electrodes with high lithium capacity and high rate capabilities. *J. Electrochem. Soc.* **151**, A698-A702 (2004).
- 169 Liu, Y., Hudak, N. S., Huber, D. L., Limmer, S. J., Sullivan, J. P. & Huang, J. Y. In situ transmission electron microscopy observation of pulverization of aluminum nanowires and evolution of the thin surface Al₂O₃ layers during lithiation-delithiation cycles. *Nano Lett.* **11**, 4188-4194 (2011).
- 170 Cabana, J., Monconduit, L., Larcher, D. & Palacin, M. R. Beyond intercalation-based Li-ion batteries: the state of the art and challenges of electrode materials reacting through conversion reactions. *Adv. Mater.* **22**, E170-E192 (2010).

- 171 Lin, F., Nordlund, D., Weng, T. C., Zhu, Y., Ban, C. M., Richards, R. M. & Xin, H. L. Phase evolution for conversion reaction electrodes in lithium-ion batteries. *Nat. Commun.* **5**, 3358 (2014).
- 172 Zhang, W. J. A review of the electrochemical performance of alloy anodes for lithium-ion batteries. *J. Power Sources* **196**, 13-24 (2011).
- 173 Cui, L.-F., Ruffo, R., Chan, C. K., Peng, H. & Cui, Y. Crystalline-amorphous core-shell silicon nanowires for high capacity and high current battery electrodes. *Nano Lett.* **9**, 491-495 (2008).
- 174 Park, M.-H., Kim, M. G., Joo, J., Kim, K., Kim, J., Ahn, S., Cui, Y. & Cho, J. Silicon nanotube battery anodes. *Nano Lett.* **9**, 3844-3847 (2009).
- 175 Zhang, Q., Zhang, W., Wan, W., Cui, Y. & Wang, E. Lithium insertion in silicon nanowires: an ab initio study. *Nano Lett.* **10**, 3243-3249 (2010).
- 176 Key, B., Bhattacharyya, R., Morcrette, M., Seznéc, V., Tarascon, J.-M. & Grey, C. P. Real-time NMR investigations of structural changes in silicon electrodes for lithium-ion batteries. *J. Am. Chem. Soc.* **131**, 9239-9249 (2009).
- 177 Zhou, S., Liu, X. & Wang, D. Si/TiSi₂ heteronanostructures as high-capacity anode material for Li ion batteries. *Nano Lett.* **10**, 860-863 (2010).
- 178 Magasinski, A., Dixon, P., Hertzberg, B., Kvit, A., Ayala, J. & Yushin, G. High-performance lithium-ion anodes using a hierarchical bottom-up approach. *Nat Mater* **9**, 353-358 (2010).
- 179 Shao-Horn, Y., Croguennec, L., Delmas, C., Nelson, E. C. & O'Keefe, M. A. Atomic resolution of lithium ions in LiCoO₂. *Nat Mater* **2**, 464-467 (2003).
- 180 Liu, X. H., Zhong, L., Huang, S., Mao, S. X., Zhu, T. & Huang, J. Y. Size-dependent fracture of silicon nanoparticles during lithiation. *Acs Nano* **6**, 1522-1531 (2012).
- 181 Beaulieu, L. Y., Beattie, S. D., Hatchard, T. D. & Dahn, J. R. The electrochemical reaction of lithium with tin studied by in situ AFM. *J. Electrochem. Soc.* **150**, A419-A424 (2003).
- 182 Limthongkul, P., Jang, Y.-I., Dudney, N. J. & Chiang, Y.-M. Electrochemically-driven solid-state amorphization in lithium-silicon alloys and implications for lithium storage. *Acta Mater.* **51**, 1103-1113 (2003).
- 183 Liu, N., Wu, H., McDowell, M. T., Yao, Y., Wang, C. M. & Cui, Y. A yolk-shell design for stabilized and scalable Li-ion battery alloy anodes. *Nano Lett.* **12**, 3315-3321 (2012).

- 184 Wu, H., Chan, G., Choi, J. W., Ryu, I., Yao, Y., McDowell, M. T., Lee, S. W., Jackson, A., Yang, Y., Hu, L. B. & Cui, Y. Stable cycling of double-walled silicon nanotube battery anodes through solid-electrolyte interphase control. *Nat. Nanotechnol.* **7**, 309-314 (2012).
- 185 Xu, B., Qian, D., Wang, Z. & Meng, Y. S. Recent progress in cathode materials research for advanced lithium ion batteries. *Mater. Sci. Eng. R* **73**, 51-65 (2012).
- 186 Malik, R., Zhou, F. & Ceder, G. Kinetics of non-equilibrium lithium incorporation in LiFePO₄. *Nat Mater* **10**, 587-590 (2011).
- 187 Delmas, C., Maccario, M., Croguennec, L., Le Cras, F. & Weill, F. Lithium deintercalation in LiFePO₄ nanoparticles via a domino-cascade model. *Nat Mater* **7**, 665-671 (2008).
- 188 Gibot, P., Casas-Cabanas, M., Laffont, L., Levasseur, S., Carlach, P., Hamelet, S., Tarascon, J. M. & Masquelier, C. Room-temperature single-phase Li insertion/extraction in nanoscale Li_xFePO₄. *Nat Mater* **7**, 741-747 (2008).
- 189 Sharma, N., Guo, X., Du, G., Guo, Z., Wang, J., Wang, Z. & Peterson, V. K. Direct evidence of concurrent solid-solution and two-phase reactions and the nonequilibrium structural evolution of LiFePO₄. *J Am Chem Soc* **134**, 7867-7873 (2012).
- 190 Bai, P., Cogswell, D. A. & Bazant, M. Z. Suppression of phase separation in LiFePO₄ nanoparticles during battery discharge. *Nano Lett* **11**, 4890-4896 (2011).
- 191 Padhi, A. K., Nanjundaswamy, K. S. & Goodenough, J. B. Phospho-olivines as positive-electrode materials for rechargeable lithium batteries. *J. Electrochem. Soc.* **144**, 1188-1194 (1997).
- 192 Ramana, C. V., Mauger, A., Gendron, F., Julien, C. M. & Zaghib, K. Study of the Li-insertion/extraction process in LiFePO₄/FePO₄. *J. Power Sources* **187**, 555-564 (2009).
- 193 Chen, D., Indris, S., Schulz, M., Gamer, B. & Mönig, R. In situ scanning electron microscopy on lithium-ion battery electrodes using an ionic liquid. *J. Power Sources* **196**, 6382-6387 (2011).
- 194 Raimann, P. R., Hochgatterer, N. S., Korepp, C., Möller, K. C., Winter, M., Schröttner, H., Hofer, F. & Besenhard, J. O. Monitoring dynamics of electrode reactions in Li-ion batteries by in situ ESEM. *Ionics* **12**, 253-255 (2006).
- 195 Orsini, F., Pasquier, A. D., Beaudoin, B., Tarascon, J. M., Trentin, M., Langenhuizen, N., Beer, E. D. & Notten, P. In situ Scanning Electron Microscopy (SEM) observation of interfaces within plastic lithium batteries. *J. Power Sources* **76**, 19-29 (1998).

- 196 Orsini, F., Pasquier, A. d., Beaudouin, B., Tarascon, J. M., Trentin, M., Langenhuizen, N., Beer, E. d. & Notten, P. In situ SEM study of the interfaces in plastic lithium cells. *J. Power Sources* **81-82**, 918-921 (1999).
- 197 Dollé, M., Sannier, L., Beaudoin, B., Trentin, M. & Tarascon, J.-M. Live scanning electron microscope observations of dendritic growth in lithium/polymer cells. *Electrochem. Solid-State Lett.* **5**, A286-A289 (2002).
- 198 Balasubramanian, M., Sun, X., Yang, X. Q. & McBreen, J. In situ X-ray diffraction and X-ray absorption studies of high-rate lithium-ion batteries. *J. Power Sources* **92**, 1-8 (2001).
- 199 Yang, X.-Q., McBreen, J., Yoon, W.-S. & Grey, C. P. Crystal structure changes of $\text{LiMn}_{0.5}\text{Ni}_{0.5}\text{O}_2$ cathode materials during charge and discharge studied by synchrotron based in situ XRD. *Electrochem. Commun.* **4**, 649-654 (2002).
- 200 Tarascon, J. M., Gozdz, A. S., Schmutz, C., Shokoohi, F. & Warren, P. C. Performance of Bellcore's plastic rechargeable Li-ion batteries. *Solid State Ionics* **86-88, Part 1**, 49-54 (1996).
- 201 Baehtz, C., Buhrmester, T., Bramnik, N. N., Nikolowski, K. & Ehrenberg, H. Design and performance of an electrochemical in-situ cell for high resolution full-pattern X-ray powder diffraction. *Solid State Ionics* **176**, 1647-1652 (2005).
- 202 Karan, N. K., Abraham, D. P., Balasubramanian, M., Furczon, M. M., Thomas, R. & Katiyar, R. S. Morphology, structure, and electrochemistry of solution-derived $\text{LiMn}_{0.5-x}\text{Cr}_{2x}\text{Ni}_{0.5-x}\text{O}_2$ for lithium-ion cells. *J. Electrochem. Soc.* **156**, A553-A562 (2009).
- 203 Haas, O., Deb, A., Cairns, E. J. & Wokaun, A. Synchrotron X-ray absorption study of LiFePO_4 electrodes. *J. Electrochem. Soc.* **152**, A191-A196 (2005).
- 204 Kong, F., Kostecki, R., Nadeau, G., Song, X., Zaghbi, K., Kinoshita, K. & McLarnon, F. In situ studies of SEI formation. *J. Power Sources* **97-98**, 58-66 (2001).
- 205 Wuersig, A., Scheifele, W. & Novák, P. CO_2 gas evolution on cathode materials for lithium-ion batteries. *J. Electrochem. Soc.* **154**, A449-A454 (2007).
- 206 Doi, T., Zhao, L., Zhou, M., Okada, S. & Yamaki, J.-i. Quantitative studies on the thermal stability of the interface between graphite electrode and electrolyte. *J. Power Sources* **185**, 1380-1385 (2008).
- 207 Lee, S. H., Jung, J.-M., Ok, J. H. & Park, C.-H. Thermal studies of charged cathode material (Li_xCoO_2) with temperature-programmed decomposition-mass spectrometry. *J. Power Sources* **195**, 5049-5051 (2010).

- 208 Bhattacharyya, R., Key, B., Chen, H., Best, A. S., Hollenkamp, A. F. & Grey, C. P. In situ NMR observation of the formation of metallic lithium microstructures in lithium batteries. *Nat Mater* **9**, 504-510 (2010).
- 209 Ebner, M., Marone, F., Stampanoni, M. & Wood, V. Visualization and quantification of electrochemical and mechanical degradation in Li ion batteries. *Science* **342**, 716-720 (2013).
- 210 Dreyer, W., Guhlke, C. & Huth, R. The behavior of a many-particle electrode in a lithium-ion battery. *Physica D: Nonlinear Phenomena* **240**, 1008-1019 (2011).
- 211 Wang, J. J., Chen-Wiegart, Y. C. K. & Wang, J. In situ three-dimensional synchrotron X-ray nanotomography of the (de) lithiation processes in tin anodes. *Angew. Chem. Int. Ed.* **53**, 4460-4464 (2014).
- 212 Chao, S. C., Yen, Y. C., Song, Y. F., Chen, Y. M., Wu, H. C. & Wu, N. L. A study on the interior microstructures of working Sn particle electrode of Li-ion batteries by in situ X-ray transmission microscopy. *Electrochem. Commun.* **12**, 234-237 (2010).
- 213 Healy, C. J. & Ackland, G. J. Molecular dynamics simulations of compression tension asymmetry in plasticity of Fe nanopillars. *Acta Mater.* **70**, 105-112 (2014).
- 214 Parent, L. R., Robinson, D. B., Cappillino, P. J., Hartnett, R. J., Abellan, P., Evans, J. E., Browning, N. D. & Arslan, I. In situ observation of directed nanoparticle aggregation during the synthesis of ordered nanoporous metal in soft templates. *Chem. Mater.* **26**, 1426-1433 (2014).
- 215 Jungjohann, K. L., Bliznakov, S., Sutter, P. W., Stach, E. A. & Sutter, E. A. In situ liquid cell electron microscopy of the solution growth of Au-Pd core-shell nanostructures. *Nano Lett.* **13**, 2964-2970 (2013).
- 216 Woehl, T. J., Park, C., Evans, J. E., Arslan, I., Ristenpart, W. D. & Browning, N. D. Direct observation of aggregative nanoparticle growth: kinetic modeling of the size distribution and growth rate. *Nano Lett.* **14**, 373-378 (2014).
- 217 Zeng, Z. Y., Liang, W. I., Liao, H. G., Xin, H. L. L., Chu, Y. H. & Zheng, H. M. Visualization of electrode-electrolyte interfaces in LiPF₆/EC/DEC electrolyte for lithium ion batteries via in situ TEM. *Nano Lett.* **14**, 1745-1750 (2014).
- 218 Williamson, M. J., Tromp, R. M., Vereecken, P. M., Hull, R. & Ross, F. M. Dynamic microscopy of nanoscale cluster growth at the solid-liquid interface. *Nat Mater* **2**, 532-536 (2003).
- 219 Galiński, M., Lewandowski, A. & Stępnia, I. Ionic liquids as electrolytes. *Electrochem. Acta* **51**, 5567-5580 (2006).

- 220 Huang, J. Y., Zhong, L., Wang, C. M., Sullivan, J. P., Xu, W., Zhang, L. Q., Mao, S. X., Hudak, N. S., Liu, X. H., Subramanian, A., Fan, H., Qi, L., Kushima, A. & Li, J. In situ observation of the electrochemical lithiation of a single SnO₂ nanowire electrode. *Science* **330**, 1515-1520 (2010).
- 221 McDowell, M. T., Lee, S. W., Harris, J. T., Korgel, B. A., Wang, C. M., Nix, W. D. & Cui, Y. In situ TEM of two-phase lithiation of amorphous silicon nanospheres. *Nano Lett.* **13**, 758-764 (2013).
- 222 Wang, F., Yu, H. C., Chen, M. H., Wu, L. J., Pereira, N., Thornton, K., Van der Ven, A., Zhu, Y. M., Amatucci, G. G. & Graetz, J. Tracking lithium transport and electrochemical reactions in nanoparticles. *Nat. Commun.* **3**, 1201 (2012).
- 223 Wang, X., Tang, D. M., Li, H. Q., Yi, W., Zhai, T. Y., Bando, Y. & Golberg, D. Revealing the conversion mechanism of CuO nanowires during lithiation-delithiation by in situ transmission electron microscopy. *Chem. Commun.* **48**, 4812-4814 (2012).
- 224 Zhong, L., Mitchell, R. R., Liu, Y., Gallant, B. M., Thompson, C. V., Huang, J. Y., Mao, S. X. & Shao-Horn, Y. In situ transmission electron microscopy observations of electrochemical oxidation of Li₂O₂. *Nano Lett.* **13**, 2209-2214 (2013).
- 225 Zhong, L., Wang, J. W., Sheng, H. W., Zhang, Z. & Mao, S. X. Formation of monatomic metallic glasses through ultrafast liquid quenching. *Nature* **512**, 177-180 (2014).
- 226 Budak, S., Miao, G. X., Ozdemir, M., Chetry, K. B. & Gupta, A. Growth and characterization of single crystalline tin oxide (SnO₂) nanowires. *J. Cryst. Growth* **291**, 405-411 (2006).
- 227 Wang, J. X., Liu, D. F., Yan, X. Q., Yuan, H. J., Ci, L. J., Zhou, Z. P., Gao, Y., Song, L., Liu, L. F., Zhou, W. Y., Wang, G. & Xie, S. S. Growth of SnO₂ nanowires with uniform branched structures. *Solid State Commun.* **130**, 89-94 (2004).
- 228 Han, W. Q., Wu, L. J., Klie, R. F. & Zhu, Y. M. Enhanced optical absorption induced by dense nanocavities inside titania nanorods. *Adv. Mater.* **19**, 2525-2529 (2007).
- 229 Han, W. Q. & Wang, X. L. Carbon-coated Magnéli-phase T_nO_{2n-1} nanobelts as anodes for Li-ion batteries and hybrid electrochemical cells. *Appl. Phys. Lett.* **97**, 243104 (2010).
- 230 Hirata, A., Kang, L. J., Fujita, T., Klumov, B., Matsue, K., Kotani, M., Yavari, A. R. & Chen, M. W. Geometric frustration of icosahedron in metallic glasses. *Science* **341**, 376-379 (2013).
- 231 Hirata, A., Guan, P. F., Fujita, T., Hirotsu, Y., Inoue, A., Yavari, A. R., Sakurai, T. & Chen, M. W. Direct observation of local atomic order in a metallic glass. *Nat. Mater.* **10**, 28-33 (2011).

- 232 K., K., Willens, R. H. & Duwez, P. Non-crystalline structure in solidified gold-silicon alloys. *Nature* **187**, 869-870 (1960).
- 233 Cohen, M. H. & Turnbull, D. Molecular transport in liquids and glasses. *J. Chem. Phys.* **31**, 1164-1169 (1959).
- 234 Turnbull, D. Under what conditions can a glass be formed? *Contemp. Phys.* **10**, 473-488 (1969).
- 235 Lin, C.-J. & Spaepen, F. Fe-B glasses formed by picosecond pulsed laser quenching. *Appl. Phys. Lett.* **41**, 721-723 (1982).
- 236 Fujime, S. Electron diffraction at low temperature II. radial distribution analysis of metastable structure of metal films prepared by low temperature condensation. *Jpn. J. Appl. Phys.* **5**, 778-787 (1966).
- 237 Sheng, H. W., Liu, H. Z., Cheng, Y. Q., Wen, J., Lee, P. L., Luo, W. K., Shastri, S. D. & Ma, E. Polyamorphism in a metallic glass. *Nat Mater* **6**, 192-197 (2007).
- 238 Ichikawa, T. The assembly of hard spheres as a structure model of amorphous iron. *Phys. Status Solidi A* **29**, 293-302 (1975).
- 239 Sachdev, S. & Nelson, D. R. Theory of the structure factor of metallic glasses. *Phys. Rev. Lett.* **53**, 1947-1950 (1984).
- 240 Yamamoto, R., Matsuoka, H. & Doyama, M. Structural relaxation of the dense random packing model for amorphous iron. *Phys. Status Solidi A* **45**, 305-314 (1978).
- 241 Dzugutov, M. Glass formation in a simple monatomic liquid with icosahedral inherent local order. *Phys. Rev. A* **46**, R2984-R2987 (1992).
- 242 Ichikawa, T. Electron diffraction study of the local atomic arrangement in amorphous iron and nickel films. *Phys. Status Solidi A* **19**, 707-716 (1973).
- 243 Leung, P. K. & Wright, J. G. Structural investigations of amorphous transition element films I. Scanning electron diffraction study of cobalt. *Philos. Mag.* **30**, 185-194 (1974).
- 244 Jones, R. E., Templeton, J. A., Wagner, G. J., Olmsted, D. & Modine, N. A. Electron transport enhanced molecular dynamics for metals and semi-metals. *Int. J. Numer. Methods Eng.* **83**, 940-967 (2010).
- 245 Tang, C. & Harrowell, P. Anomalously slow crystal growth of the glass-forming alloy CuZr. *Nat. Mater.* **12**, 507-511 (2013).
- 246 Steinhardt, P., Nelson, D. & Ronchetti, M. Bond-orientational order in liquids and glasses. *Phys. Rev. B* **28**, 784-805 (1983).

- 247 Tian, L., Cheng, Y. Q., Shan, Z. W., Li, J., Wang, C. C., Han, X. D., Sun, J. & Ma, E. Approaching the ideal elastic limit of metallic glasses. *Nat. Commun.* **3**, 609 (2012).
- 248 Schuh, C. A., Hufnagel, T. C. & Ramamurty, U. Mechanical behavior of amorphous alloys. *Acta Mater.* **55**, 4067-4109 (2007).
- 249 Bauder, U. & Fromm, E. Absorption of nitrogen and oxygen by vapour-deposited tantalum films. *Surf. Sci.* **52**, 415-425 (1975).
- 250 Egerton, R. F. *Electron Energy-Loss Spectroscopy in the Electron Microscope*. third edn, (Springer, 2011).
- 251 Hopkins, B. J., Leggett, M. & Watts, G. D. A RHEED study of the adsorption of oxygen, hydrogen, nitrogen and water vapour on the (110) face of tantalum. *Surf. Sci.* **28**, 581-597 (1971).
- 252 Yi, J., Wang, W. H. & Lewandowski, J. J. Sample size and preparation effects on the tensile ductility of Pd-based metallic glass nanowires. *Acta Mater.* **87**, 1-7 (2015).
- 253 Gu, X. W., Jafary-Zadeh, M., Chen, D. Z., Wu, Z. X., Zhang, Y. W., Srolovitz, D. J. & Greer, J. R. Mechanisms of Failure in Nanoscale Metallic Glass. *Nano Lett.* **14**, 5858-5864 (2014).
- 254 Liu, Y. H., Zhao, F., Li, Y. L. & Chen, M. W. Deformation behavior of metallic glass thin films. *J. Appl. Phys.* **112**, 063504 (2012).
- 255 Chen, D. Z., Jang, D., Guan, K. M., An, Q., Goddard, W. A. & Greer, J. R. Nanometallic glasses: size reduction brings ductility, surface state drives its extent. *Nano Lett.* **13**, 4462-4468 (2013).
- 256 Lewandowski, J. J., Wang, W. H. & Greer, A. L. Intrinsic plasticity or brittleness of metallic glasses. *Philosophical Magazine Letters* **85**, 77-87 (2005).
- 257 He, Q., Shang, J. K., Ma, E. & Xu, J. Crack-resistance curve of a Zr-Ti-Cu-Al bulk metallic glass with extraordinary fracture toughness. *Acta Mater.* **60**, 4940-4949 (2012).
- 258 Das, J., Tang, M. B., Kim, K. B., Theissmann, R., Baier, F., Wang, W. H. & Eckert, J. "Work-hardenable" ductile bulk metallic glass. *Phys. Rev. Lett.* **94**, 205501 (2005).
- 259 Schall, P., Weitz, D. A. & Spaepen, F. Structural rearrangements that govern flow in colloidal glasses. *Science* **318**, 1895-1899 (2007).
- 260 Pan, D., Inoue, A., Sakurai, T. & Chen, M. W. Experimental characterization of shear transformation zones for plastic flow of bulk metallic glasses. *P. Natl. Acad. Sci. USA* **105**, 14769-14772 (2008).

- 261 Chen, M. W. in *Annual Review of Materials Research* Vol. 38 *Annual Review of Materials Research* 445-469 (Annual Reviews, 2008).
- 262 Argon, A. S. Plastic-deformation in metallic glasses. *Acta Metall.* **27**, 47-58 (1979).
- 263 Falk, M. L. & Langer, J. S. Dynamics of viscoplastic deformation in amorphous solids. *Phys. Rev. E* **57**, 7192-7205 (1998).
- 264 Ma, D., Stoica, A. D. & Wang, X. L. Power-law scaling and fractal nature of medium-range order in metallic glasses. *Nat. Mater.* **8**, 30-34 (2009).
- 265 Goodenough, J. B. & Kim, Y. Challenges for Rechargeable Li Batteries. *Chem. Mater.* **22**, 587-603 (2010).
- 266 Etacheri, V., Marom, R., Elazari, R., Salitra, G. & Aurbach, D. Challenges in the development of advanced Li-ion batteries: a review. *Energy Environ. Sci.* **4**, 3243-3262 (2011).
- 267 Zheng, H., Xiao, D. D., Li, X., Liu, Y. L., Wu, Y., Wang, J. P., Jiang, K. L., Chen, C., Gu, L., Wei, X. L., Hu, Y. S., Chen, Q. & Li, H. New insight in understanding oxygen reduction and evolution in solid-state lithium oxygen batteries using an in situ environmental scanning electron microscope. *Nano Lett.* **14**, 4245-4249 (2014).
- 268 Li, Y. G., Tan, B. & Wu, Y. Y. Mesoporous CO₃O₄ nanowire arrays for lithium ion batteries with high capacity and rate capability. *Nano Lett.* **8**, 265-270 (2008).
- 269 Chan, C. K., Zhang, X. F. & Cui, Y. High capacity Li ion battery anodes using Ge nanowires. *Nano Lett.* **8**, 307-309 (2008).
- 270 Ge, M. Y., Rong, J. P., Fang, X. & Zhou, C. W. Porous doped silicon nanowires for lithium ion battery anode with long cycle life. *Nano Lett.* **12**, 2318-2323 (2012).
- 271 Ruffo, R., Hong, S. S., Chan, C. K., Huggins, R. A. & Cui, Y. Impedance analysis of silicon nanowire lithium ion battery anodes. *J. Phys. Chem. C* **113**, 11390-11398 (2009).
- 272 Cao, Y. L., Xiao, L. F., Sushko, M. L., Wang, W., Schwenzer, B., Xiao, J., Nie, Z. M., Saraf, L. V., Yang, Z. G. & Liu, J. Sodium ion insertion in hollow carbon nanowires for battery applications. *Nano Lett.* **12**, 3783-3787 (2012).
- 273 Wang, K., Huang, J. Y. & Wei, Z. X. Conducting polyaniline nanowire arrays for high performance supercapacitors. *J. Phys. Chem. C* **114**, 8062-8067 (2010).
- 274 Lee, H. W., Muralidharan, P., Ruffo, R., Mari, C. M., Cui, Y. & Kim, D. K. Ultrathin spinel LiMn₂O₄ nanowires as high power cathode materials for Li-ion batteries. *Nano Lett.* **10**, 3852-3856 (2010).

- 275 Liu, B., Zhang, J., Wang, X. F., Chen, G., Chen, D., Zhou, C. W. & Shen, G. Z. Hierarchical three-dimensional ZnCo₂O₄ nanowire arrays/carbon cloth anodes for a novel class of high-performance flexible lithium-ion batteries. *Nano Lett.* **12**, 3005-3011 (2012).
- 276 Wang, Q., Wen, Z. H. & Li, J. H. A hybrid supercapacitor fabricated with a carbon nanotube cathode and a TiO₂-B nanowire anode. *Adv. Funct. Mater.* **16**, 2141-2146 (2006).
- 277 Xia, X. H., Tu, J. P., Mai, Y. J., Wang, X. L., Gu, C. D. & Zhao, X. B. Self-supported hydrothermal synthesized hollow Co₃O₄ nanowire arrays with high supercapacitor capacitance. *J. Mater. Chem.* **21**, 9319-9325 (2011).
- 278 Shaju, K. M., Jiao, F., Debart, A. & Bruce, P. G. Mesoporous and nanowire Co₃O₄ as negative electrodes for rechargeable lithium batteries. *Phys. Chem. Chem. Phys.* **9**, 1837-1842 (2007).
- 279 Nam, K. T., Kim, D. W., Yoo, P. J., Chiang, C. Y., Meethong, N., Hammond, P. T., Chiang, Y. M. & Belcher, A. M. Virus-enabled synthesis and assembly of nanowires for lithium ion battery electrodes. *Science* **312**, 885-888 (2006).
- 280 Reimers, J. N. & Dahn, J. R. Electrochemical and in situ X - ray diffraction studies of lithium intercalation in Li_xCoO₂. *J. Electrochem. Soc.* **139**, 2091-2097 (1992).
- 281 Courtney, I. A. & Dahn, J. R. Key factors controlling the reversibility of the reaction of lithium with SnO₂ and Sn₂BPO₆ glass. *J. Electrochem. Soc.* **144**, 2943-2948 (1997).
- 282 Gabrisch, H., Yazami, R. & Fultz, B. The character of dislocations in LiCoO₂. *Electrochem. Solid-State Lett.* **5**, A111-A114 (2002).
- 283 Wang, Y. M., Li, J., Hamza, A. V. & Barbee, T. W. Ductile crystalline-amorphous nanolaminates. *P. Natl. Acad. Sci. USA* **104**, 11155-11160 (2007).
- 284 Zhu, T. & Li, J. Ultra-strength materials. *Prog. Mater Sci.* **55**, 710-757 (2010).
- 285 Mughrabi, H. Deformation-induced long-range internal stresses and lattice plane misorientations and the role of geometrically necessary dislocations. *Philos. Mag.* **86**, 4037-4054 (2006).
- 286 Zhong, L., Liu, X. H., Wang, G. F., Mao, S. X. & Huang, J. Y. Multiple-stripe lithiation mechanism of individual SnO₂ nanowires in a flooding geometry. *Phys. Rev. Lett.* **106**, 248302 (2011).
- 287 Legros, M., Dehm, G., Arzt, E. & Balk, T. J. Observation of giant diffusivity along dislocation cores. *Science* **319**, 1646-1649 (2008).

- 288 Koudriachova, M., Harrison, N. & de Leeuw, S. Density-functional simulations of lithium intercalation in rutile. *Phys. Rev. B* **65**, 235423 (2002).
- 289 Koudriachova, M. Diffusion of Li-ions in rutile. An ab initio study. *Solid State Ionics* **157**, 35-38 (2003).
- 290 Gligor, F. & Deleeuw, S. Lithium diffusion in rutile structured titania. *Solid State Ionics* **177**, 2741-2746 (2006).
- 291 Reddy, M. A., Kishore, M. S., Pralong, V., Caignaert, V., Varadaraju, U. V. & Raveau, B. Room temperature synthesis and Li insertion into nanocrystalline rutile TiO₂. *Electrochem. Commun.* **8**, 1299-1303 (2006).
- 292 Milne, N. A., Skyllas-Kazacos, M. & Luca, V. Crystallite size dependence of lithium intercalation in nanocrystalline rutile. *J. Phys. Chem. C* **113**, 12983-12995 (2009).
- 293 Larcher, D., Masquelier, C., Bonnin, D., Chabre, Y., Masson, V., Leriche, J. B. & Tarascon, J. M. Effect of particle size on lithium intercalation into α -Fe₂O₃. *J. Electrochem. Soc.* **150**, A133 (2003).
- 294 Bach, S., Pereira-Ramos, J. P. & Willman, P. Investigation of lithium diffusion in nano-sized rutile TiO₂ by impedance spectroscopy. *Electrochem. Acta* **55**, 4952-4959 (2010).
- 295 White, E. R., Singer, S. B., Augustyn, V., Hubbard, W. A., Mecklenburg, M., Dunn, B. & Regan, B. C. In situ transmission electron microscopy of lead dendrites and lead ions in aqueous solution. *Acs Nano* **6**, 6308-6317 (2012).
- 296 Zheng, H. M., Claridge, S. A., Minor, A. M., Alivisatos, A. P. & Dahmen, U. Nanocrystal diffusion in a liquid thin film observed by in situ transmission electron microscopy. *Nano Lett.* **9**, 2460-2465 (2009).
- 297 Evans, J. E., Jungjohann, K. L., Browning, N. D. & Arslan, I. Controlled growth of nanoparticles from solution with in situ liquid transmission electron microscopy. *Nano Lett.* **11**, 2809-2813 (2011).
- 298 Allen, J. L., Jow, T. R. & Wolfenstine, J. Kinetic study of the electrochemical FePO₄ to LiFePO₄ phase transition. *Chem. Mater.* **19**, 2108-2111 (2007).
- 299 Yamada, A., Koizumi, H., Nishimura, S., Sonoyama, N., Kanno, R., Yonemura, M., Nakamura, T. & Kobayashi, Y. Room-temperature miscibility gap in Li_xFePO₄. *Nat Mater* **5**, 357-360 (2006).
- 300 Scharner, S., Weppner, W. & Schmid-Beurmann, P. Evidence of two-phase formation upon lithium insertion into the Li_{1.33}Ti_{1.67}O₄ spinel. *J. Electrochem. Soc.* **146**, 857-861 (1999).

- 301 Wagemaker, M., Simon, D. R., Kelder, E. M., Schoonman, J., Ringpfeil, C., Haake, U., Lützenkirchen-Hecht, D., Frahm, R. & Mulder, F. M. A kinetic two-phase and equilibrium solid solution in spinel $\text{Li}_{4+x}\text{Ti}_5\text{O}_{12}$. *Adv. Mater.* **18**, 3169-3173 (2006).
- 302 Zachau-Christiansen, B., West, K., Jacobsen, T. & Atlung, S. Lithium insertion in different TiO_2 modifications. *Solid State Ionics* **28–30, Part 2**, 1176-1182 (1988).
- 303 Wagemaker, M., Kearley, G. J., van Well, A. A., Mutka, H. & Mulder, F. M. Multiple Li positions inside oxygen octahedra in lithiated TiO_2 anatase. *J. Am. Chem. Soc.* **125**, 840-848 (2003).
- 304 Wagemaker, M., van de Krol, R., Kentgens, A. P. M., van Well, A. A. & Mulder, F. M. Two phase morphology limits lithium diffusion in TiO_2 (anatase): a ^7Li MAS NMR study. *J. Am. Chem. Soc.* **123**, 11454-11461 (2001).
- 305 Wagemaker, M., Kentgens, A. P. M. & Mulder, F. M. Equilibrium lithium transport between nanocrystalline phases in intercalated TiO_2 anatase. *Nature* **418**, 397-399 (2002).
- 306 Morgan, B. J. & Watson, G. W. Role of lithium ordering in the Li_xTiO_2 anatase \rightarrow titanate phase transition. *J. Phys. Chem. Lett.* **2**, 1657-1661 (2011).
- 307 van de Krol, R., Goossens, A. & Meulenkamp, E. A. In situ X - ray diffraction of lithium intercalation in nanostructured and thin film anatase TiO_2 . *J. Electrochem. Soc.* **146**, 3150-3154 (1999).
- 308 Wagemaker, M., van de Krol, R. & van Well, A. A. Nano-morphology of lithiated thin film TiO_2 anatase probed with in situ neutron reflectometry. *Physica B* **336**, 124-129 (2003).
- 309 Koudriachova, M. V., Harrison, N. M. & de Leeuw, S. W. Effect of diffusion on lithium intercalation in titanium dioxide. *Phys. Rev. Lett.* **86**, 1275-1278 (2001).
- 310 Richter, J. H., Henningsson, A., Sanyal, B., Karlsson, P. G., Andersson, M. P., Uvdal, P., Siegbahn, H., Eriksson, O. & Sandell, A. Phase separation and charge localization in UHV-lithiated anatase TiO_2 nanoparticles. *Phys. Rev. B* **71**, 235419 (2005).
- 311 Whittingham, M. S. Electrical energy storage and intercalation chemistry. *science* **192**, 1126-1127 (1976).
- 312 Whittingham, M. S. The role of ternary phases in cathode reactions. *J. Electrochem. Soc.* **123**, 315-320 (1976).
- 313 Gamble, F. R., Osiecki, J. H., Cais, M., R., P., DiSalvo, F. J. & Geballe, T. H. Intercalation complexes of Lewis bases and layered sulfides: A large class of new superconductors. *science* **174**, 493-497 (1971).

- 314 Ottaviani, M., Panero, S., Morzilli, S., Scrosati, B. & Lazzari, M. The electrochromic characteristics of titanium oxide thin film electrodes. *Solid State Ionics* **20**, 197-202 (1986).
- 315 van de Krol, R., Goossens, A. & Schoonman, J. Spatial extent of lithium intercalation in anatase TiO₂. *J. Phys. Chem. B* **103**, 7151-7159 (1999).
- 316 Cava, R. J., Murphy, D. W., Zahurak, S., Santoro, A. & Roth, R. S. The crystal structures of the lithium-inserted metal oxides Li_{0.5}TiO₂ anatase, LiTi₂O₄ spinel, and Li₂Ti₂O₄. *J. Solid State Chem.* **53**, 64-75 (1984).
- 317 Wagemaker, M., Borghols, W. J. H. & Mulder, F. M. Large impact of particle size on insertion reactions. A case for anatase Li_xTiO₂. *J. Am. Chem. Soc.* **129**, 4323-4327 (2007).
- 318 Belak, A. A., Wang, Y. & Van der Ven, A. Kinetics of anatase electrodes: The role of ordering, anisotropy, and shape memory effects. *Chem. Mater.* **24**, 2894-2898 (2012).
- 319 Sudant, G., Baudrin, E., Larcher, D. & Tarascon, J.-M. Electrochemical lithium reactivity with nanotextured anatase-type TiO₂. *J. Mater. Chem.* **15**, 1263-1269 (2005).
- 320 Wagemaker, M., Borghols, W. J., van Eck, E. R., Kentgens, A. P., Kearley, G. J. & Mulder, F. M. The influence of size on phase morphology and Li-ion mobility in nanosized lithiated anatase TiO₂. *Chemistry* **13**, 2023-2028 (2007).
- 321 Tielens, F., Calatayud, M., Beltrán, A., Minot, C. & Andrés, J. Lithium insertion and mobility in the TiO₂-anatase/titanate structure: A periodic DFT study. *J. Electroanal. Chem.* **581**, 216-223 (2005).
- 322 Lindström, H., Södergren, S., Solbrand, A., Rensmo, H., Hjelm, J., Hagfeldt, A. & Lindquist, S.-E. Li⁺ ion insertion in TiO₂ (Anatase). 1. Chronoamperometry on CVD films and nanoporous films. *J. Phys. Chem. B* **101**, 7710-7716 (1997).
- 323 Kavan, L., Rathouský, J., Grätzel, M., Shklover, V. & Zikal, A. Surfactant-templated TiO₂ (Anatase): Characteristic features of lithium insertion electrochemistry in organized nanostructures. *J. Phys. Chem. B* **104**, 12012-12020 (2000).
- 324 Kavan, L., Grätzel, M., Gilbert, S. E., Klemenz, C. & Scheel, H. J. Electrochemical and photoelectrochemical investigation of single-crystal anatase. *J. Am. Chem. Soc.* **118**, 6716-6723 (1996).
- 325 Hibino, M., Abe, K., Mochizuki, M. & Miyayama, M. Amorphous titanium oxide electrode for high-rate discharge and charge. *J. Power Sources* **126**, 139-143 (2004).
- 326 Tang, M., Belak, J. F. & Dorr, M. R. Anisotropic phase boundary morphology in nanoscale olivine electrode particles. *J. Phys. Chem. C* **115**, 4922-4926 (2011).

- 327 Cogswell, D. A. & Bazant, M. Z. Coherency strain and the kinetics of phase separation in LiFePO₄ nanoparticles. *ACS Nano* **6**, 2215-2225 (2012).
- 328 Bonino, F., Busani, L., Lazzari, M., Manstretta, M., Rivolta, B. & Scrosati, B. Anatase as a cathode material in lithium—organic electrolyte rechargeable batteries. *J. Power Sources* **6**, 261-270 (1981).
- 329 Jiang, C., Wei, M., Qi, Z., Kudo, T., Honma, I. & Zhou, H. Particle size dependence of the lithium storage capability and high rate performance of nanocrystalline anatase TiO₂ electrode. *J. Power Sources* **166**, 239-243 (2007).
- 330 Kang, J. W., Kim, D. H., Mathew, V., Lim, J. S., Gim, J. H. & Kim, J. Particle size effect of anatase TiO₂ nanocrystals for lithium-ion batteries. *J. Electrochem. Soc.* **158**, A59 (2011).
- 331 Gentili, V., Brutti, S., Hardwick, L. J., Armstrong, A. R., Panero, S. & Bruce, P. G. Lithium insertion into anatase nanotubes. *Chem. Mater.* **24**, 4468-4476 (2012).
- 332 Lafont, U., Carta, D., Mountjoy, G., Chadwick, A. V. & Kelder, E. M. In situ structural changes upon electrochemical lithium insertion in nanosized anatase TiO₂. *J. Phys. Chem. C* **114**, 1372-1378 (2010).
- 333 Hardwick, L. J., Holzappel, M., Novák, P., Dupont, L. & Baudrin, E. Electrochemical lithium insertion into anatase-type TiO₂: An in situ Raman microscopy investigation. *Electrochim. Acta* **52**, 5357-5367 (2007).
- 334 Crank, J. *The mathematics of diffusion*. second edn, (Clarendon Press, 1975).
- 335 Lu, Y., Peng, C., Ganesan, Y., Huang, J. Y. & Lou, J. Quantitative in situ TEM tensile testing of an individual nickel nanowire. *Nanotechnology* **22**, 355702 (2011).
- 336 Shan, Z. W., Mishra, R. K., Asif, S. A. S., Warren, O. L. & Minor, A. M. Mechanical annealing and source-limited deformation in submicrometre-diameter Ni crystals. *Nat. Mater.* **7**, 115-119 (2008).
- 337 Shan, Z. W., Stach, E. A., Wieszorek, J. M. K., Knapp, J. A., Follstaedt, D. M. & Mao, S. X. Grain boundary-mediated plasticity in nanocrystalline nickel. *Science* **305**, 654-657 (2004).
- 338 Schiotz, J. & Jacobsen, K. W. A maximum in the strength of nanocrystalline copper. *Science* **301**, 1357-1359 (2003).
- 339 Wolf, D., Yamakov, V., Phillpot, S. R., Mukherjee, A. & Gleiter, H. Deformation of nanocrystalline materials by molecular-dynamics simulation: relationship to experiments? *Acta Mater.* **53**, 1-40 (2005).

- 340 Yamakov, V., Wolf, D., Phillpot, S. R. & Gleiter, H. Deformation twinning in nanocrystalline Al by molecular dynamics simulation. *Acta Mater.* **50**, 5005-5020 (2002).
- 341 Chen, L. Y., He, M. R., Shin, J., Richter, G. & Gianola, D. S. Measuring surface dislocation nucleation in defect-scarce nanostructures. *Nat. Mater.* **14**, 707-713 (2015).
- 342 Guo, W., Wang, Z. & Li, J. Diffusive versus displacive contact plasticity of nanoscale asperities: temperature- and velocity-dependent strongest size. *Nano Lett.* **15**, 6582-8585 (2015).
- 343 Zheng, H., Cao, A. J., Weinberger, C. R., Huang, J. Y., Du, K., Wang, J. B., Ma, Y. Y., Xia, Y. N. & Mao, S. X. Discrete plasticity in sub-10-nm-sized gold crystals. *Nat. Commun.* **1**, 144 (2010).
- 344 Wang, J. W., Zeng, Z., Weinberger, C. R., Zhang, Z., Zhu, T. & Mao, S. X. In situ atomic-scale observation of twinning-dominated deformation in nanoscale body-centred cubic tungsten. *Nat. Mater.* **14**, 594-600 (2015).
- 345 Kresse, G. & Hafner, J. Ab initio molecular dynamics for liquid metals. *Phys. Rev. B* **47**, 558-561 (1993).
- 346 Sheng, H. W., Kramer, M. J., Cadien, A., Fujita, T. & Chen, M. W. Highly optimized embedded-atom-method potentials for fourteen fcc metals. *Phys. Rev. B* **83**, 134118 (2011).
- 347 Brommer, P. & Gähler, F. Potfit: effective potentials from ab initio data. *Modell. Simul. Mater. Sci. Eng.* **15**, 295-304 (2007).
- 348 Li, D., Wu, Y., Fan, R., Yang, P. & Majumdar, A. Thermal conductivity of Si/SiGe superlattice nanowires. *Appl. Phys. Lett.* **83**, 3186-3188 (2003).
- 349 Schelling, P. K., Phillpot, S. R. & Keblinski, P. Comparison of atomic-level simulation methods for computing thermal conductivity. *Phys. Rev. B* **65**, 144306 (2002).
- 350 Ho, C. Y., Powell, R. W. & Liley, P. E. Thermal conductivity of the elements. *J. Phys. Chem. Ref. Data* **1**, 279-421 (1972).
- 351 Tari, A. *The Specific Heat of Matter at Low Temperatures* 71 (Imperial College Press, 2003).
- 352 Lin, Z., Zhigilei, L. & Celli, V. Electron-phonon coupling and electron heat capacity of metals under conditions of strong electron-phonon nonequilibrium. *Phys. Rev. B* **77**, 075133 (2008).